

For Reference

NOT TO BE TAKEN FROM THIS ROOM

Ex LIBRIS
UNIVERSITATIS
ALBERTAEISIS





Digitized by the Internet Archive
in 2023 with funding from
University of Alberta Library

<https://archive.org/details/Pani1972>

THE UNIVERSITY OF ALBERTA

FACULTY OF GRADUATE STUDIES AND RESEARCH

THREE DIMENSIONAL TURBULENT WALL JETS

BY



BIDYA SAGAR PANI

A THESIS

SUBMITTED TO THE FACULTY OF GRADUATE STUDIES AND RESEARCH
IN PARTIAL FULFILMENT OF THE REQUIREMENTS FOR THE DEGREE OF
DOCTOR OF PHILOSOPHY

DEPARTMENT OF CIVIL ENGINEERING

EDMONTON, ALBERTA

FALL, 1972

Thesis
721-82D

UNIVERSITY OF ALBERTA
FACULTY OF GRADUATE STUDIES AND RESEARCH

The undersigned certify that they have read, and recommend to the Faculty of Graduate Studies and Research, for acceptance, a thesis entitled "THREE DIMENSIONAL TURBULENT WALL JETS" submitted by Bidya Sagar Pani, in partial fulfilment of the requirements for the degree of Doctor of Philosophy.

ABSTRACT

Based on the experimental observation that in the fully developed flow region of a submerged three dimensional jet, the velocity profiles in the normal and in transverse planes are all similar, a suitable form of nondimensional velocity distribution was introduced. The boundary layer type of equations for the three dimensional free jet was then analysed and relationships for the maximum velocity decay and growth of length scales were established. The approach was then extended for a three dimensional wall jet growing on a smooth wall in a very wide channel, assuming that the forward momentum of the jet was preserved. Flow from deeply submerged outlets of various geometric shapes resting on the bed, to discharge tangentially were investigated experimentally. For each shape of outlet, the velocity profile normal to the wall as well as in the transverse planes were found to be similar. The centerline non-dimensional profile normal to the wall was found to be described closely by the classical wall jet curve, whereas, the transverse profiles were described by Goertler's curve for a free circular jet. The streamwise variation of the velocity and length scales were studied and compared with theoretical laws. From dimensional analysis, the square root of the area of cross-section of the outlet was found to be a characteristic length parameter and was found to be useful in

correlating the experimental data for maximum velocity decay, regardless of the outlet shape. The transverse distribution of bed shear was investigated and was found to be similar. Curves for estimating the centerline bed shear are presented in convenient forms.

Other aspects of practical interest, such as, the effect of the side walls of the channel and the bed roughness, on the growth of a circular wall jet were also investigated. A circular wall jet with swirl was then studied experimentally and was found to be a very effective means of reducing the maximum forward velocity in comparatively shorter distances. Further, the similarity of velocity profiles and the bed shear distribution for the swirling jets were investigated.

The similarity analysis for velocity distribution was found to be useful even in more general types of flows. The turbulent compound annular shear was analysed to establish a relationship for the growth of the half velocity length scale. Experiments were conducted for four different secondary stream to jet velocity ratios, and the results justify similarity of velocity profiles and the growth law. The constant of proportionality in Prandtl's mixing length relationship was found to increase with the velocity ratio, and was far from being a constant as assumed by other investigators (Appendix A).

In Appendix B, some of the available data on three dimensional free jets were analysed for velocity decay and growth rates.

ACKNOWLEDGEMENTS

The author wishes to express his sincere gratitude to Professor N. Rajaratnam for his thoughtful guidance, constructive criticism and advice throughout the course of this investigation.

The assistance of the Hydraulics Laboratory staff in fabricating the apparatus in various phases of the work is greatly appreciated.

The author is grateful to the National Research Council of Canada for the support of this work through a grant to Professor Rajaratnam (A-3365).

TABLE OF CONTENTS

	<u>Page</u>
Title page	i
Approval sheet	ii
Abstract	iii
Acknowledgements	v
Table of Contents	vi
List of Tables	vii
List of Figures	viii
List of Symbols	xv
CHAPTER I INTRODUCTION	1
CHAPTER II THEORETICAL CONSIDERATIONS	8
CHAPTER III EXPERIMENTAL ARRANGEMENTS AND MEASUREMENT TECHNIQUES	35
CHAPTER IV THREE DIMENSIONAL WALL JETS	64
CHAPTER V EFFECT OF SIDE WALLS	94
CHAPTER VI EFFECT OF BOUNDARY ROUGHNESS ON CIRCULAR WALL JETS	107
CHAPTER VII WALL JETS WITH SWIRL	125
CHAPTER VIII CONCLUSIONS AND RECOMMENDATIONS	147
LIST OF REFERENCES	152
APPENDIX A TURBULENT COMPOUND ANNULAR SHEAR LAYERS	A1
APPENDIX B THREE DIMENSIONAL FREE JETS	B1
APPENDIX C VELOCITY PLOTS AND EXPERIMENTAL DATA	C1

LIST OF TABLES

<u>Table</u>		<u>Page</u>
III-1	Swirl Number Measurements	62
IV-1	Nozzle Shapes Studied	67
IV-2	Coordinates of the Similarity Profiles	76
A-1	Experimental Results on Length Scale of Annular Shear Layers	A13
B-1	Velocity and Length Scales for a Free Square Jet	B2
C-1	Important Flow Parameters for Three Dimensional Wall Jets	C13
C-2	Flow Parameters for Circular Wall Jets Diffusing in Channels of Finite Width	C20
C-3	Flow Parameters for Circular Wall Jet on a Rough Boundary	C22
C-4	Flow Parameters for Swirling Wall Jets	C23

LIST OF FIGURES

<u>Figure</u>		<u>Page</u>
2.1	Schematic Representation of Three Dimensional Free Jets	10
2.2	Schematic Representation of Three Dimensional Wall Jets	25
3.1	Experimental Flume 1 (Schematic Representation)	36
3.2	Experimental Flume 2 (Schematic Representation)	38
3.3	Sand Grain Roughness	40
3.4	Definition Sketch for Pitch and Yaw	43
3.5	Calibration Factors K_7 and K_8 for Five Hole Probe	46
3.6	Calibration Factor K_{12} for Five Hole Probe	47
3.7	Calibration Factor K_1 for Five Hole Probe	48
3.8	Calibration Factor K_0 for Yaw Probe	53
3.9	Calibration Factors for Yaw Probe on the Boundary	54
3.10	Pressure-Shear Ratio for Rough Boundaries (Analytical)	56
3.11	Swirl Generator (Schematic Representation)	59
3.12	Swirl Number-Discharge Ratio Relationship	63
4.1	Velocity Distribution in the Center-Plane	68
4.2	Velocity Distribution in the z Direction	69
4.3	Bed Shear Distribution	71

LIST OF FIGURES (continued)

<u>Figure</u>		<u>Page</u>
4.4	Non-Dimensional Velocity Profile Normal to the Wall	72
4.5	Non-Dimensional Velocity Distribution in z Direction	74
4.6	Virtual Origin (Based on Velocity Scale)	77
4.7	Decay of Maximum Velocity Along the Center-Plane (With Hydraulic Radius as a Parameter)	80
4.8	Decay of Maximum Velocity Along the Center-Plane (With the Square Root of the Area of the Nozzle as a Parameter)	81
4.9	Growth of Length Scale Normal to the Wall	83
4.10	Growth of Transverse Length Scale b_z	84
4.11	Growth of the Jet: (a) Along the Transverse Direction; (b) Normal to the Wall	86
4.12	Isovels in the Fully-Developed Region	88
4.13	Bed Shear Stress Along the Center-Plane	90
4.14	Bed Shear Distribution Along the Center-Plane (Alternate Plot)	91
5.1	Virtual Origin for Jets in Finite Width Channels (Based on Velocity Scale)	97
5.2	Jet Velocity Decay in Channels of Finite Width	98
5.3	Growth of Length Scale b_y	100

LIST OF FIGURES (continued)

<u>Figure</u>		<u>Page</u>
5.4	Water Surface Profile	101
5.5	Non-Dimensional Velocity Distribution Normal to the Wall (Center-Plane of Channels)	102
5.6	Skin Friction Coefficient (Along the Center-Plane)	105
5.7	Bed Shear Decay (On the Centerline)	105
6.1	Effect of Bed Roughness on the Maximum Velocity Decay Constant for Plane Jets	110
6.2	Centerline Non-Dimensional Velocity Profile on a Rough Wall	113
6.3	Velocity Distribution-Free Mixing Region	115
6.4	Velocity Distribution in the Boundary Layer (Rough Wall)	116
6.5	Non-Dimensional Velocity Distribution in z Direction (Rough Wall)	118
6.6	Maximum Velocity Decay of a Jet on a Rough Wall	119
6.7	Growth of Length Scales for Free Mixing and Inner Region	122
6.8	Growth of Length Scale b_z (Rough Wall)	122
7.1	Centerline Non-Dimensional Velocity Distribution - Swirling Jets	128
7.2	Non-Dimensional Velocity Distribution in Transverse Planes of Swirling Jets	130

LIST OF FIGURES (continued)

<u>Figure</u>		<u>Page</u>
7.3	v and w Velocity Components - A Typical Plot	131
7.4	Static Pressure Along Center-Plane - A Typical Plot	132
7.5	Maximum Velocity Decay for Swirling Jets	134
7.6	Growth of Length Scale b_y	134
7.7	Growth of Length Scale b_z	136
7.8	Non-Dimensional Bed Shear Distribution	138
7.9	Variation of Length Scale b_τ	139
7.10	Non-Dimensional Bed Shear Distribution (with x' as the Length Scale)	141
7.11	Effect of Swirl on Bed Shear Distribution	142
7.12	Decay of Centerline Shear Stress for Swirling Jets	143
7.13	Yaw Angle for Off-Center Bed Shear Vector	145
A.1	Definition Sketch of Compound Annular Shear Layer	A2
A.2	Variation of the Inner and Outer Edges of the Shear Layer	A10
A.3	Experimental Arrangement	A11
A.4	Typical Velocity Distribution	A14
A.5	Comparison of Experimental Observations with the Cosine Curve	A15
A.6	Similarity in Velocity Distribution	A18
A.7	Growth of the Inner Edge of the Shear Layer	A20

LIST OF FIGURES (continued)

<u>Figure</u>		<u>Page</u>
A.8	Length of Potential Core	A22
A.9	Variation of c^2 with λ	A23
A.10	Growth of Length Scale	A24
A.11	Variation of C_1 with λ	A25
A.12	Growth of the Outer Edge of the Shear Layer	A27
A.13	Angles of the Inner and Outer Edges	A28
B.1	Non-Dimensional Velocity Distribution in y Direction	B3
B.2	Non-Dimensional Velocity Distribution in z Direction	B4
B.3	Maximum Velocity Decay for a Square Nozzle	B6
B.4	Maximum Velocity Decay for Three Dimensional Free Jets	B7
B.5	Growth of Length Scales b_y and b_z	B10
C.1	Non-Dimensional Velocity Distribution in the Center-Plane - Circular Nozzle	C1
C.2	Non-Dimensional Velocity Distribution in the Center-Plane - Square Nozzle	C1
C.3	Non-Dimensional Velocity Distribution in the Center-Plane - Rectangular Nozzle ($e = 1.50$)	C2
C.4	Non-Dimensional Velocity Distribution in the Center-Plane - Triangular Nozzle	C2

LIST OF FIGURES (continued)

<u>Figure</u>		<u>Page</u>
C.5	Non-Dimensional Velocity Distribution in the Center-Plane - Square Nozzle	C3
C.6	Non-Dimensional Velocity Distribution in the Center-Plane - Elliptic Nozzle ($e = 1.62$)	C3
C.7	Non-Dimensional Velocity Distribution in the Center-Plane - Triangular Nozzle	C4
C.8	Non-Dimensional Velocity Distribution in the Center-Plane - Rectangular Nozzle ($e = 0.4$)	C4
C.9	Non-Dimensional Velocity Distribution in the z Direction - Circular Nozzle	C5
C.10	Non-Dimensional Velocity Distribution in the z Direction - Square Nozzle	C6
C.11	Non-Dimensional Velocity Distribution in the z Direction - Rectangular Nozzle ($e = 1.50$)	C7
C.12	Non-Dimensional Velocity Distribution in the z Direction - Triangular Nozzle	C8
C.13	Non-Dimensional Velocity Distribution in the z Direction - Square Nozzle	C9
C.14	Non-Dimensional Velocity Distribution in the z Direction - Elliptic Nozzle	C10
C.15	Non-Dimensional Velocity Distribution in the z Direction - Triangular Nozzle	C11

LIST OF FIGURES (continued)

<u>Figure</u>		<u>Page</u>
C.16	Non-Dimensional Velocity Distribution in the z Direction - Rectangular Nozzle ($e = 0.4$)	C12

LIST OF SYMBOLS

a	inner radius of the stagnation tube
a_1	area under the non-dimensional bed shear distribution curve
a_2	constant of integration
a_{11}, a_{10} and a_{00}	coefficients defined in Eq. A.10
A	area of cross-section of nozzle
A_{11}, A_{10} and A_{00}	coefficients defined in Eq. A.10
b	length scale for co-flowing jets
b_y	length scale normal to the wall and in the center-plane
b_z	length scale in transverse direction, parallel to the wall and at any height y from the wall
b_τ	length scale for shear stress (i.e. $b_\tau = z$ at which $\tau_0 = \tau_{om}/2$)
B	width of the nozzle, also a parameter defined in Eq. A.10
B_s	a function of the roughness Reynolds number
c	an empirical constant in mixing length relationship, Eq. A.6
c_f	skin friction coefficient, defined as $\tau_{om}/\frac{1}{2} \rho u_{mo}^2$
C	constant of proportionality in maximum velocity decay law

LIST OF SYMBOLS (continued)

c_1, c_2, c_3 and c_4	empirical constants
d	diameter of circular nozzle
D	diameter of circular nozzle, also diameter of pipe
e	aspect ratio
f	$= \frac{U}{U_m}$ and is a function of η
f_1	$= \frac{u_m}{u_{m0}}$ and is a function of η_y
F	a function
F_a	ratio of area of primary device opening at flow temperature to that at 60°F
F_m	manometer factor for liquid on mercury
g	$= \frac{\tau}{\rho U_m^2}$, a function of η
$g_1, g_2, g_3,$ g_4 and g_5	functions of η_z representing distribution of non-dimensional quantities
G_f	specific gravity of liquid on mercury
G_ℓ	specific gravity of liquid at base temperature
h	height of nozzle, height of center of stagnation tube or a functional relation, as specified
h_w	operating differential as read on manometer in inches of water
Δh	differential manometric head in inches of water

LIST OF SYMBOLS (continued)

K	roughness height or constant of proportionality as specified
K_s	equivalent sand grain roughness
K_0	calibration coefficient for a yaw probe resting on the boundary
K_1, K_2, K_3 K_4 and K_5	coefficients for a five hole probe, Eq. 3.1
K_6, K_7, K_8 and K_9	coefficients for a five hole probe, Eq. 3.3
K_{10}, K_{20} and K_{30}	coefficients for a yaw prove, Eq. 3.6
K_{12}, K_{13}, K_{14} and K_{15}	coefficients for a five hole probe, Eq. 3.2
λ	mixing length
M	axial momentum of the jet
M_0	momentum flux at nozzle section
n	exponent
N	a constant
p	exponent for variation of velocity scale u_{mo} , also pressure intensity at any point
Δp	dynamic pressure
p_0	static pressure

LIST OF SYMBOLS (continued)

p_1, p_2, p_3	pressure recorded by holes 1, 2, 3 etc.
p_4 and p_5	
P	total pressure in the jet
q	dynamic pressure, also an exponent
q_1	exponent for variation of length scale by
q_2	exponent for variation of length scale b_z
Q_n	rate of flow through orifice meter
Q_s	discharge through the tangential slots of the swirl generator
Q_T	total discharge in the swirl generator
r	radial distance
r_0	radius of the nozzle, also the radius vector of a reference isovvel
r_1	radius of the inner edge of the shear layer
r_2	radius of the outer edge of the shear layer
r'	hydraulic radius of the wall jet (i.e. ratio of the nozzle area to the perimeter of fluid boundary at the nozzle)
R	Reynolds number ($U_0 d/\nu$, $U_0 B/\nu$ or $U_0 \sqrt{A}/\nu$)
R_1	non-dimensional r_1
R_2	non-dimensional r_2
S	swirl number
t	thickness of wall of the stagnation tube

LIST OF SYMBOLS (continued)

T	angular momentum of the jet
u	turbulent mean velocity in x direction
u_m	u in the center-plane of wall jets, also the maximum value of u in a radial plane of axially symmetric jets
u_{mo}	maximum value of u_m at any section
u_*	$= \sqrt{\frac{\tau_0}{\rho}}$ = shear velocity
u'	fluctuating velocity component in x direction
U	velocity relative to the secondary stream
U_0	uniform velocity at exit of the nozzle
U_1	uniform velocity of the secondary stream
v	mean velocity component in y direction
v'	fluctuating component of velocity in y direction
V	resultant velocity vector in a three dimensional flow field
w	mean velocity component in z direction
w'	fluctuating component of velocity in z direction
W	width of channel
x	longitudinal distance from virtual origin
x', \bar{x}	distance measured from the nozzle section
x_0	axial distance from the nozzle to the end of the potential core

LIST OF SYMBOLS (continued)

x_0'	distance from the nozzle to the virtual origin, based on velocity scale
y	normal distance from the wall
z	transverse distance, measured from the center-plane
α	an operating figure in Eq. 3.14
δ	boundary layer thickness in the center-plane
Δ	a quantity of small order
ξ	$= \frac{r_2 - r}{r_2 - r_1}$
η	$= \frac{r - r_1}{b}$
η_y	$= \frac{y}{b_y}$
η_z	$= \frac{z}{b_z}$
η_τ	$= \frac{z}{b_\tau}$
η'	$= \frac{y - \delta}{b_y - \delta}$
$\bar{\eta}$	$= \frac{r - r_1}{r_2 - r_1}$
θ	yaw angle of bed shear vector, also angle of attack
κ	Karman's universal constant
λ	$= \frac{U_1}{U_0} =$ secondary stream to nozzle velocity ratio

LIST OF SYMBOLS (continued)

ν	= kinematic viscosity
ξ	= $\frac{z}{x^4}$
ρ	= mass density of the fluid
τ_0	= shear stress on the bed in x direction
τ_{om}	= bed shear stress along the centerline
τ_0^+	= $\frac{\tau_0 d^2}{4 \rho v^2}$
ϕ	pitch angle
ψ	yaw angle

CHAPTER I

INTRODUCTION

1.1 General

In a number of hydraulic structures a high velocity stream meets an ambient fluid at rest and gets diffused. As the high velocity stream meets the stationary water, the so called surfaces of separation or discontinuity would appear. Tangential separation surfaces are highly unstable and result in eddies that move in a random fashion both along and across the stream, thus bringing about an exchange of momentum between adjoining layers. This results in a region of finite thickness having a continuous distribution of velocity and is termed a shear layer. In most practical cases the Reynolds number of flow is large and the shear layer is turbulent. This turbulent shear layer gradually extends into the non-viscous core of the oncoming jet of fluid and beyond a comparatively short distance the shear layer extends over the entire thickness of flow.

The type of turbulent jet, that has been studied most, is the one diffusing through a medium at rest. The two common types investigated in detail are the two dimensional or the plane jet, and the axially symmetric jet. If the jet diffuses in the absence of any solid boundary, it is called a free jet and if it diffuses near a solid boundary, it is known as a wall jet. A frequently encountered

example of a wall jet is the one with a jet of fluid impinging tangentially on a solid wall and then growing on it.

1.2 Hydraulic Outlets

Control gate structures are frequently encountered in any irrigation and power development project. During certain periods, these control structures operate under submerged tail water conditions and in general the flow from any submerged outlet can be analysed as a turbulent jet. If the boundaries are sufficiently away, the flow can be treated as a free jet problem and the information available on it is quite extensive (Abramovich, 1963). However, in practice, the flow from the outlet issues close to a boundary, normally the bed of a channel, and has to be analysed as a wall jet.

In few cases the outlet might occupy the full width of a channel and could then be treated as a plane wall jet. Considerable amount of information is available on plane wall jets (Schwarz and Cosart, 1961; Meyer et al., 1961) and it has been demonstrated (Rajaratnam and Subramanya, 1967) that the plane wall jet serves as an useful model to describe the flow below sluice gates in hydraulic engineering. However, in most cases the flow emanates from outlets that do not occupy the entire width of the channel and have finite aspect ratios; being situated right on the bed of the channel or at a small height from the bed. Some information on diffusion of wall jets into wider channels is available (Rajaratnam and Subramanya, 1967), but the investigation does not include any shape other than a

rectangle. A preliminary experimental study is available on flow from non-rectangular outlets (Rajaratnam and Muralidhar, 1969).

1.3 Existing Work

The experimental investigations on jets of finite aspect ratio or the three dimensional jets are limited. Yevdjevich (1966) studied the diffusion of three dimensional free jets issuing from rectangular slots having a wide range of aspect ratios. Sforza et al. (1966) and Trentacoste and Sforza (1967) studied the behaviour of free jets emanating from rectangular nozzles having different aspect ratios as well as from other nozzle shapes that include a triangle and an ellipse. The investigation on a three dimensional wall jet was more restrictive and covered only the rectangular nozzle (Viets and Sforza, 1966; Sforza and Herbst, 1967) having a few aspect ratios.

1.4 Present Investigation

An understanding of the flow field and shear stress distribution on the channel bed resulting from the operation of submerged culverts and gated structures will be of great practical use, particularly in designing efficient energy dissipating devices and bed protections. Information on the behaviour of diffusion of wall jets issuing from triangular, elliptical and the more frequently encountered circular shape outlets is not available at present. In addition the available literature on rectangular wall jets is very limited and many aspects of the problem remain unanswered. The present investigation

was undertaken in an effort to understand the mean flow characteristics for a variety of shapes of practical interest and develop relationships that would apply to an outlet irrespective of its shape. Furthermore, the experimental undertaking is also an effort to accumulate sufficient information, which would enable to predict the flow characteristics for engineering design purposes with some degree of confidence.

In the experimental program, to start with, a simple case of a three dimensional wall jet diffusing in a wide channel and a smooth wall with no swirl was studied. However, this ideal case is far from reality and in most practical cases the channel side walls are close to one another. Proximity of the side walls would interfere with the growth of the jet and might significantly alter the behaviour of the jet. In an attempt to study this behaviour, the experimental program was extended to investigate the diffusion of circular wall jets in channels of finite width.

Another significant aspect in which the ideal case considered so far differs from practice is the roughness of the bed or wall. In reality, under most hydraulic outlets the bed is rough. To assess the order to which the ideal case is getting affected by the roughness elements, the present investigation includes the case of a circular outlet on a rough bed.

In a free circular jet, a certain amount of swirl or rotation before it comes out of the nozzle helps the jet to spread more rapidly, and the velocity field decays much faster (Chigier and Chervinsky, 1965).

It is therefore thought that giving a rotation to the circular jet might greatly assist in diffusion of the jet efficiently in a shorter reach and would be useful in reducing the length of apron or protection needed below the outlet. To explore this aspect the investigation was further extended to diffusion of circular wall jets with swirl.

1.5 Presentation of the Program

The following is an arrangement adapted in presenting the details of the present investigation.

A theoretical consideration is presented in Chapter II. Based on the observations that the velocity profiles are similar, the theoretical analysis predicts certain basic relationships for the decay of velocity and the rate of spreading of the jet. Dimensional considerations are also presented to arrive at a number of useful dimensionless parameters, which set the stage for presentation of the experimental results.

Chapter III gives the details regarding the experimental arrangements and the measuring techniques adapted. Certain special types of probes had to be built and tested to measure the three dimensional velocity field and the boundary shear distributions. The calibration techniques and the methods of using the calibration charts are also discussed. The limitations of the measurements are then described.

In Chapter IV, the investigations on three dimensional turbulent wall jets diffusing in a wide channel and on a smooth bed

with no swirl are presented. The shapes studied include a circle, a square, an equilateral triangle, an ellipse and rectangles of different aspect ratios. The results are presented in convenient forms that would predict the velocity decay, the growth of the jet and the bed shear distribution in the channel.

Investigations on the effects of side walls on circular wall jets, growing on a smooth bed, are presented in Chapter V.

Experimental findings on the diffusion of a circular wall jet in a very wide channel, but growing on a rough bed, are reported in Chapter VI. One type of bed roughness was tested and gives useful hints on the decay of the maximum velocity along the centerline of the jet.

In Chapter VII, a preliminary investigation on a circular wall jet with swirl is presented. The velocity scale is found to decay faster when subjected to a swirling motion. Results on the growth rates of the swirling jets and the bed shear distribution are also presented in the same chapter.

Based on the present studies, general conclusions are presented in Chapter VIII. Some recommendations are then made for further studies in this field.

During the course of this investigation, it was found that a similarity analysis can successfully be applied to more complicated flows. In the developing zone of a co-flowing circular jet, it leads to some simple and interesting results. The analytical results were

then verified by experiments, and are presented in Appendix A.

The present experimental investigations were carried out at the hydraulics laboratory of the University of Alberta, Edmonton, Canada, during the years 1970 and 1971.

CHAPTER II

THEORETICAL CONSIDERATIONS

2.1 Introduction

This chapter presents a theoretical analysis for a particular class of three dimensional jets in which the dimensions of the nozzle producing the jet are roughly the same in the major and minor axis directions. A circular free jet has axial symmetry, but when the circular jet diffuses close to a solid boundary the axial symmetry is entirely lost, and the flow is three dimensional in nature. As the present investigation is primarily on wall jets, any jet of circular, square, triangular, elliptic or some other geometrical shape having aspect ratio not very different from unity is referred to as a three dimensional wall jet. First a simple rectangular free jet is considered for analysis and based on observation of other investigators, the Reynolds equations of motion are simplified. These simplified or the boundary layer type of equations are then analysed to establish the growth rate and velocity decay laws. This approach is then extended to the case of three dimensional wall jets. To supplement the analysis, and to get the distribution of wall shear, a dimensional consideration is presented. As the geometry of the flow field does not suggest readily any suitable co-ordinate system, the cartesian system is adopted for the sake of simplicity and it

also helps to maintain a clear picture of the physical nature of the problem.

2.2 Equations of Motion

The Reynolds equations in the cartesian coordinates (Schlichting, 1968) can be written as

$$u \frac{\partial u}{\partial x} + v \frac{\partial u}{\partial y} + w \frac{\partial u}{\partial z} = - \frac{1}{\rho} \frac{\partial p}{\partial x} + v \left[\frac{\partial^2 u}{\partial x^2} + \frac{\partial^2 u}{\partial y^2} + \frac{\partial^2 u}{\partial z^2} \right] - \left[\frac{\partial}{\partial x} \overline{u'^2} + \frac{\partial}{\partial y} \overline{u'v'} + \frac{\partial}{\partial z} \overline{u'w'} \right] \quad (2.1)$$

$$u \frac{\partial v}{\partial x} + v \frac{\partial v}{\partial y} + w \frac{\partial v}{\partial z} = - \frac{1}{\rho} \frac{\partial p}{\partial y} + v \left[\frac{\partial^2 v}{\partial x^2} + \frac{\partial^2 v}{\partial y^2} + \frac{\partial^2 v}{\partial z^2} \right] - \left[\frac{\partial}{\partial x} \overline{u'v'} + \frac{\partial}{\partial y} \overline{v'^2} + \frac{\partial}{\partial z} \overline{v'w'} \right] \quad (2.2)$$

$$u \frac{\partial w}{\partial x} + v \frac{\partial w}{\partial y} + w \frac{\partial w}{\partial z} = - \frac{1}{\rho} \frac{\partial p}{\partial z} + v \left[\frac{\partial^2 w}{\partial x^2} + \frac{\partial^2 w}{\partial y^2} + \frac{\partial^2 w}{\partial z^2} \right] - \left[\frac{\partial}{\partial x} \overline{u'v'} + \frac{\partial}{\partial y} \overline{v'w'} + \frac{\partial}{\partial z} \overline{w'^2} \right] \quad (2.3)$$

and

$$\frac{\partial u}{\partial x} + \frac{\partial v}{\partial y} + \frac{\partial w}{\partial z} = 0 \quad (2.4)$$

where x axis is in the axial direction of flow (Figure 2.1), y and z axes are normal to the x axis and are along the minor and major axes of the nozzle respectively,

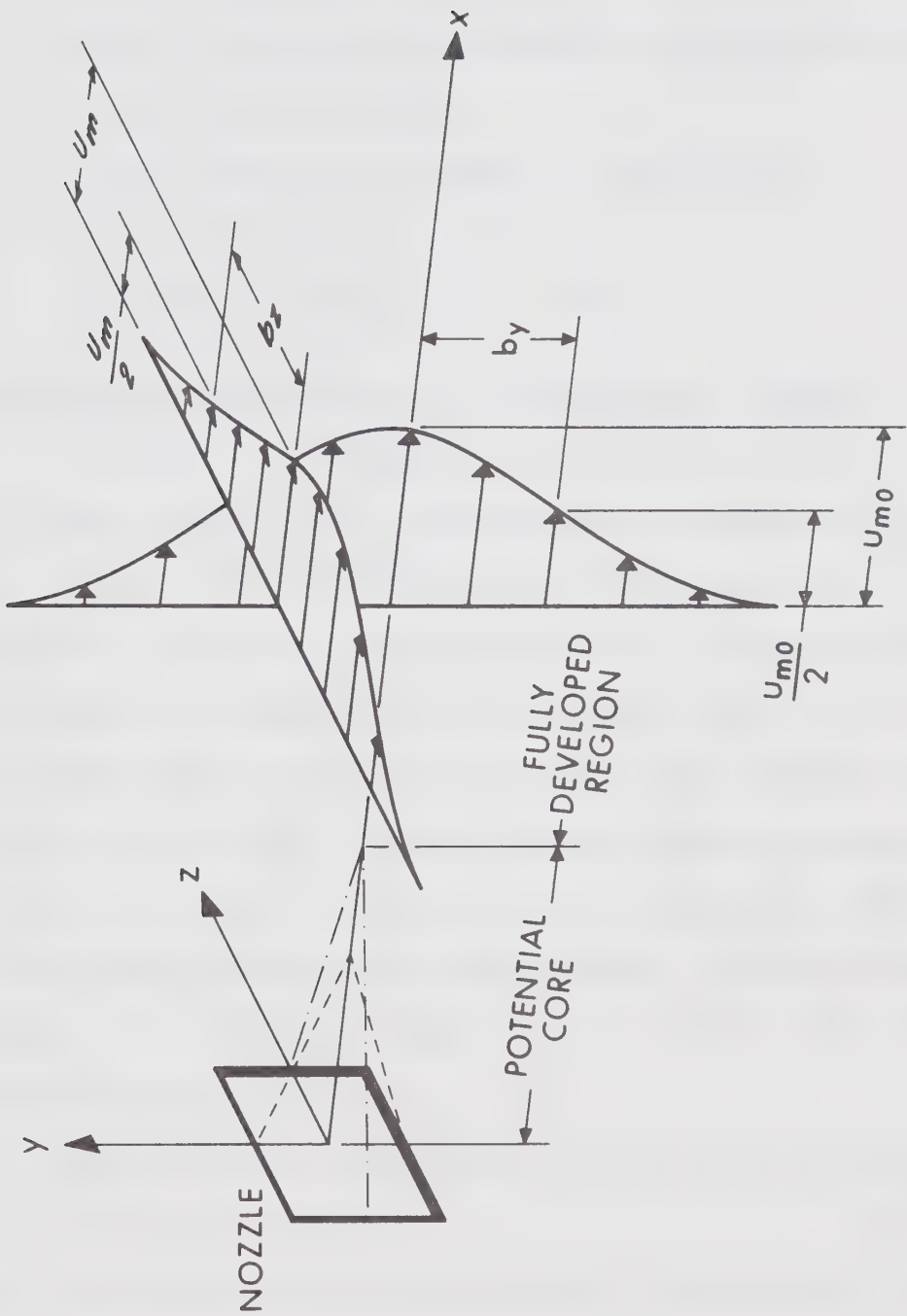


FIGURE 2.1 SCHEMATIC REPRESENTATION OF THREE DIMENSIONAL FREE JETS

u, v, w = the turbulent mean velocity components in the x, y and z direction respectively

u', v', w' = the fluctuating component of the velocities in x, y and z directions

p = mean pressure at the point of consideration

ρ = mass density of the fluid, and

ν = kinematic viscosity of the fluid.

2.3 Boundary Layer Simplification of the Equations of Motion

A characteristic feature of turbulent jets is the limited extent of the thickness in the transverse direction where the solution is sought. Because of the limited extent in the transverse direction, jets expanding into infinite regions filled with a quiescent fluid have negligibly small pressure gradients in the x direction. This otherwise means that, the constant pressure in the surrounding fluid impresses itself on the jet. Another typical feature of submerged jet is the smallness of the transverse velocity components, which are usually neglected for engineering studies on jets. Based on these observations, it is possible to simplify the equations of motion by assuming the following.

- (i) Beyond a certain initial reach from the nozzle outlet,
 $y \ll x$ and $z \ll x$.
- (ii) In a major portion of the flow, $u \gg v$ and $u \gg w$. Also the fluctuating components are much smaller compared to the mean values.

- (iii) The gradients in the y and z directions are much larger than the corresponding gradients in the x direction.
- (iv) The pressure gradients in the x , y and z directions are all small.

The desired simplification of the equations of motion was achieved by estimating the order of magnitude of each term in the equations of motion (Schlichting, 1968). For this, Eqs. 2.1 to 2.4 were considered in the dimensional form and the order of magnitudes were assigned as,

$$u \sim 1, \quad x \sim 1, \quad y \sim \Delta \quad \text{and} \quad z \sim \Delta$$

where Δ is a small quantity, which is at least an order less than unity.

Since $\partial u / \partial x$ was of the order of 1, it can be shown from Eq. 2.4 that $\partial v / \partial y \sim 1$ and $\partial w / \partial z \sim 1$. Furthermore, from the geometry of flow, as y and z become zero on the axis, v and w also become zero. Hence in the jet boundary, $v \sim \Delta$ and $w \sim \Delta$, which was postulated in assumption (ii).

Writing down the order of magnitude of individual terms in Eq. 2.1 through Eq. 2.3, it can be shown that the entire equation of motion in the y and z directions are of the order of Δ , and can be dropped altogether as an approximation. The turbulent shear stresses are usually very large compared to the viscous shear stress and hence the viscous terms were neglected. Deleting terms of smaller order

in Eq. 2.1, the simplified equations of motion are,

$$u \frac{\partial u}{\partial x} + v \frac{\partial u}{\partial y} + w \frac{\partial u}{\partial z} = - \left(\frac{\partial}{\partial y} \overline{u'v'} + \frac{\partial}{\partial z} \overline{u'w'} \right) \quad (2.5)$$

and

$$\frac{\partial u}{\partial x} + \frac{\partial v}{\partial y} + \frac{\partial w}{\partial z} = 0 . \quad (2.6)$$

These would be referred to as the boundary layer type of equations for a three dimensional jet. During this course of analysis, the assumption of negligible pressure gradients leads us to the result that, the effect of all turbulent stress components other than $\overline{u'v'}$ and $\overline{u'w'}$ are negligible.

2.4 Similarity Analysis

The present studies and those of Trentacoste and Sforza (1967) showed that the velocity profiles of the three dimensional jet continually broaden. A plot of velocity profile in the physical coordinates (presented in Chapter IV) for different x stations and $z = 0$ plane for example, look so very different. This is because, the velocity on the axis decreases whereas the profiles get wider. However, interesting results are obtained by plotting the ratio of the local velocity to the velocity on the jet axis and the ratio of the local distance to a characteristic length of the jet. One obvious characteristic length of the jet would be the thickness of the jet at the section under consideration. Exact demarcation of the jet boundary would be a difficult task, and alternative length parameters need to be considered. One

such parameter, widely accepted in the study of jets, is the distance between the axis and the point at which the velocity is equal to half the axial velocity. This is usually referred to as the half width.

When the velocity profiles at various sections are non-dimensionalised by appropriate choice of velocity and length scales, all the profiles collapse into a single curve. This behaviour is what we term as "similarity of the velocity profiles". Thus, in a major part of the flow field, the non-dimensional velocity profile is completely defined by the non-dimensional distance and is independent of the streamwise coordinate x . This is a very important and most useful property that is encountered for most of the jet flows.

For the $z = 0$ plane, based on the above observations, let us assume

$$\frac{u_m}{u_{mo}} = f_1\left(\frac{y}{b_y}\right) = f_1(n_y) \quad (2.7)$$

where u_m is the turbulent mean velocity in the x direction at a distance y from the axis of the jet (see Figure 2.1), u_{mo} is the maximum value of u_m , b_y is a length scale equal to y where $u_m = u_{mo}/2$, n_y is non-dimensional ordinate and f_1 represents a functional relation.

Further in the $z - x$ planes, based again on experimental observations (of Sforza and et al. and those to be presented in this thesis), we can write

$$\frac{u}{u_m} = g_1\left(\frac{z}{b_z}\right) = g_1(n_z) \quad (2.8)$$

where u is the turbulent mean velocity in x direction at a distance z from the axis, b_z is the length scale in the z or transverse direction being equal to z where $u = u_m/2$ (Figure 2.1), η_z is non-dimensional distance and g_1 is a functional relation. Combining Eq. 2.7 and 2.8, the local mean velocity at any point can be re-written in the following form.

$$\frac{u}{u_{mo}} = f_1(\eta_y) \cdot g_1(\eta_z) . \quad (2.9)$$

Experience on plane and circular jets show that v and w velocity components can be non-dimensionalised by the u velocity scale (Anwar and Weller, 1969) and the cumbersome operation of getting the dimensionless v and w components from the continuity equation can be avoided. Hence it is assumed that

$$\frac{v}{u_m} = g_2(\eta_z) \quad (2.10)$$

and

$$\frac{w}{u_m} = g_3(\eta_z) . \quad (2.11)$$

Combining Eq. 2.10 and 2.11 with Eq. 2.7, we can write

$$\frac{v}{u_{mo}} = f_1 g_2 \quad (2.12)$$

$$\frac{w}{u_{mo}} = f_1 g_3 \quad (2.13)$$

where η_y and η_z have been dropped in Eq. 2.12 and 2.13, with the understanding that f is a function of η_y and g is a function of η_z .

Similarly in any $x-z$ plane, from experience on self-preserving jets (Wygnanski and Fiedler, 1969), the turbulent shear stress components can be written as

$$\frac{\overline{u'v'}}{u_m^2} = g_4(\eta_z) \quad (2.14)$$

and

$$\frac{\overline{u'w'}}{u_m^2} = g_5(\eta_z) . \quad (2.15)$$

Combination of these two equations with Eq. 2.7, would give us

$$\frac{\overline{u'v'}}{u_{mo}^2} = f_1^2 g_4 \quad (2.16)$$

$$\frac{\overline{u'w'}}{u_{mo}^2} = f_1^2 g_5 . \quad (2.17)$$

In addition let us suppose that

$$\begin{aligned} u_{mo} &\propto x^p \\ b_y &\propto x^{q_1} \\ b_z &\propto x^{q_2} \end{aligned} \quad (2.18)$$

and

where p , q_1 and q_2 are the unknown exponents. To evaluate these exponents, one relationship is obtained from the boundary layer Eq. 2.5, using the set of assumptions made so far, and following the simplifications enumerated below,

$$u = u_{mo} f_1 g_1 \quad (2.19)$$

$$\frac{\partial u}{\partial x} = f_1' g_1 u_{mo} - \frac{u_{mo} b_y'}{b_y} n_y g_1 f_1' - \frac{u_{mo} b_z'}{b_z} f_1 n_z g_1' \quad (2.20)$$

where

$$u_{mo}' = \frac{\partial u_{mo}}{\partial x} = \frac{du_{mo}}{dx}$$

$$b_y' = \frac{\partial b_y}{\partial x} = \frac{db_y}{dx}$$

$$b_z' = \frac{\partial b_z}{\partial x} = \frac{db_z}{dx}$$

and the prime on the f function denotes differentiation with respect to n_y and that on the g functions denotes differentiation with respect to n_z .

$$u \frac{\partial u}{\partial x} = u_{mo} u_{mo}' f_1^2 g_1^2 - \frac{u_{mo}^2 b_y'}{b_y} n_y f_1 f_1' g_1^2 - \frac{u_{mo}^2 b_z'}{b_z} n_z f_1^2 g_1 g_1' \quad (2.21)$$

$$\frac{\partial u}{\partial y} = -\frac{u_{mo} g_1}{b_y} f_1' \quad (2.22)$$

$$v \frac{\partial u}{\partial y} = \frac{u_{mo}^2}{b_y} f_1 f_1' g_1 g_2 \quad (2.23)$$

$$\frac{\partial u}{\partial z} = \frac{u_{mo}}{b_z} f_1 g_1' \quad (2.24)$$

$$w \frac{\partial u}{\partial z} = \frac{u_{mo}^2}{b_z} f_1^2 g_1' g_3 \quad (2.25)$$

$$\frac{\partial}{\partial y} \overline{u'v'} = \frac{2u_{mo}^2}{b_y} f_1 f_1' g_4 \quad (2.26)$$

$$\frac{\partial}{\partial z} \overline{u'w'} = \frac{u_{mo}^2}{b_z} f_1^2 g_5' \quad . \quad (2.27)$$

Substituting these expressions into Eq. 2.5, we get

$$\begin{aligned} & u_{mo} u_{mo}' f_1^2 g_1^2 - \frac{u_{mo}^2 b_y'}{b_y} \eta_y f_1 f_1' g_1^2 - \frac{u_{mo}^2 b_z'}{b_z} \eta_z f_1^2 g_1 g_1' \\ & + \frac{u_{mo}^2}{b_y} f_1 f_1' g_1 g_2 + \frac{u_{mo}^2}{b_z} f_1^2 g_1' g_3 = -\frac{2u_{mo}^2 f_1 f_1' g_4}{b_y} - \frac{u_{mo}^2 f_1^2 g_5'}{b_z} \end{aligned} \quad (2.28)$$

multiplying right through by b_y/u_{mo}^2 and rearranging,

$$\begin{aligned} 2f_1 f_1' g_4 &= -\frac{b_y}{b_z} f_1^2 g_5' - \frac{b_y u_{mo}'}{u_{mo}} f_1^2 g_1^2 + b_y' \eta_y f_1 f_1' g_1^2 \\ &+ \frac{b_y b_z'}{b_z} \eta_z f_1^2 g_1 g_1' - f_1 f_1' g_1 g_2 - \frac{b_y}{b_z} f_1^2 g_1' g_3 . \end{aligned} \quad (2.29)$$

From the definition of the similarity of velocity profiles, the left

hand side of Eq. 2.29 is independent of x . In order that the equation be valid at any section and is nontrivial, the right hand side of Eq. 2.29 should also be independent of x . So we have,

$$b_y' \propto x^0$$

or

$$q_1 = 1 \quad (2.30)$$

$$\frac{b_y}{b_z} \propto x^0$$

or

$$q_2 = q_1 = 1. \quad (2.31)$$

Further,

$$\frac{b_y b_z'}{b_z} \propto x^0$$

i.e.

$$x^{(q_1+q_2-1-q_2)} \propto x^0$$

or

$$q_1 = 1 \quad (2.32)$$

$$\frac{b_y u_{mo}'}{u_{mo}} \propto x^0$$

i.e.

$$x^{(q_1+p-1-p)} \propto x^0$$

or

$$q_1 = 1. \quad (2.33)$$

To evaluate the other unknown exponent, we would use the integral momentum equation. Since the pressure in the jet is virtually

constant and equal to the pressure in the surrounding medium, a jet issuing into an infinite medium will have the total momentum in the x direction preserved and would be independent of the distance from the orifice. That is

$$\frac{d}{dx} \int_{-\infty}^{\infty} \int_{-\infty}^{\infty} \rho u^2 dy dz = 0 \quad (2.34)$$

i.e.

$$\frac{d}{dx} \int_{-\infty}^{\infty} \int_{-\infty}^{\infty} \rho u_{mo}^2 f_1^2 g_1^2 b_y b_z d\eta_y d\eta_z = 0$$

or

$$\frac{d}{dx} \rho u_{mo}^2 b_y b_z \int_{-\infty}^{\infty} \int_{-\infty}^{\infty} f_1^2 g_1^2 d\eta_y d\eta_z = 0 \quad (2.35)$$

In Eq. 2.35, the integrand is a finite quantity and is a constant.

Hence

$$\frac{d}{dx} [\rho u_{mo}^2 b_y b_z] = 0 . \quad (2.36)$$

That is

$$x^{2p+q_1+q_2} \propto x^0$$

or $2p + q_1 + q_2 = 0 . \quad (2.37)$

From Eqs. 2.31 and 2.37, $p = -1$, so that

$$u_{mo} \propto x^{-1}$$

$$b_y \propto x \quad (2.38)$$

$$b_z \propto x$$

2.5 Velocity Distribution

The distribution of velocity for a plane source and axially symmetric jet are given by the analytical expressions of Tollmien and Goertler (Abramovich, 1963). Tollmien's solutions are based on Prandtl's mixing length theory, whereas, Goertler's solutions are based on Prandtl's constant eddy viscosity model. The two solutions give the velocity distribution with approximately the same accuracy. Discrepancies are however observed between the two, near the boundary of the jet.

The analytical solution for three dimensional turbulent jets is not well established and the only attempt published in literature is that of Sforza (1969). Experimentally it was observed that in the far field, the contours describing constant values of streamwise mean velocity components in the $y-z$ plane were satisfactorily described by ellipses. Also the distribution of streamwise components of the mean velocity were similar and identical in various planes, when plotted in the nondimensional form. This led to the adaptation

of cylindrical coordinates as an appropriate system, and the elliptic isovels were transformed to circular isovels by taking the ratio of the radius vector r of any isovel to the radius vector r_0 of a reference isovel. The radius vector r_0 would then be a function of both x and the orientation θ .

The simplified equations of motion were then solved by assuming a suitable form for eddy viscosity in terms of r_0 . Generally speaking, the form of the equations were similar to the one found for axisymmetric jets and the approximate solution worked out to be identical with the one given by Schlichting (1968) for the axisymmetric case. However, this analysis incorporates the three dimensional jet data in determining the constants of integration and the distribution follows very closely Goertler's curve (Abramovich, 1963) for a free circular jet.

2.6 Extension to Three Dimensional Wall Jets

2.6.1 Effect of Viscosity

In the presence of a solid boundary, the molecular viscosity cannot be neglected completely. Near the wall the velocity gradients are large, and so, for a low-viscosity fluid flowing past a solid boundary, the flow field can be divided into two regions: a comparatively thin layer of fluid located close to the solid wall where viscosity is important and the outer part in which viscous effects can be neglected.

Glauert (1956) considered the laminar and turbulent, radial and plane wall jets, and showed that a complete similarity in velocity

profile in the wall region and the outer free turbulence region is not feasible as a result of the viscosity model being different in the two regions. It was also shown that the concept of constancy of the flux of exterior momentum flux is not applicable for a turbulent wall jet. Glauert's simple power laws, which express the local rates of change with x of maximum velocity and the jet width, have the exponents themselves varying slowly with x . In later experiments (Schwarz and Cosart, 1960), it was found that a single velocity scale and a single length scale correlate all the velocity data; and leads to the concept that it is possible to have experimental similarity, if not theoretical similarity, over the entire turbulent thickness of the jet. The equation of motion indicate the single length scale to vary as $x^{1.0}$, and the velocity scale to vary as x^p . The exponent p was determined empirically, since a second relationship could not be found out for the plane turbulent wall jet.

In view of the difficulties encountered, to account for the viscosity in a plane wall jet, no simple approach is at sight for a three dimensional case. In the hope of establishing the exponents which might serve as a good approximation and provide reasonable answers for engineering calculations, the shear stress on the bed of the channel is neglected. This expectation seems to be borne out in the light of agreement between the predicted laws and the experimental results.

2.6.2 Simplification of the Equations of Motion

Following the line of argument presented for a free jet, the equations of motion (Eq. 2.1 through Eq. 2.4) for a three dimensional wall jet can be simplified as

$$\begin{aligned} u \frac{\partial u}{\partial x} + v \frac{\partial u}{\partial y} + w \frac{\partial u}{\partial z} &= v \left[\frac{\partial^2 u}{\partial y^2} + \frac{\partial^2 u}{\partial z^2} \right] \\ - \left[\frac{\partial}{\partial y} \bar{u}'v' + \frac{\partial}{\partial z} \bar{u}'w' \right] \end{aligned} \quad (2.39)$$

and

$$\frac{\partial u}{\partial x} + \frac{\partial v}{\partial y} + \frac{\partial w}{\partial z} = 0 . \quad (2.40)$$

2.6.3 Similarity Analysis

The non-dimensional velocity distributions are represented by the forms given in Eq. 2.7 and Eq. 2.8, with an exception regarding the definition of the length scale b_y . For wall jet studies the length scale b_y equals y , the height measured from the wall, where $u_m = u_{mo}/2$ and $\partial u_m / \partial y$ is negative (Figure 2.2). All other assumptions and forms of representation remain identical with the free jet case.

Substituting for the terms in Eq. 2.39, it can be shown, as in Section 2.4, that the following expressions will be obtained.

$$\begin{aligned} 2f_1 f_1' g_4 &= \frac{v}{u_{mo} b_y} g_1 f_1''' + \frac{v}{u_{mo} b_y} \left(\frac{b_y}{b_z} \right)^2 f_1 g_1''' - \frac{b_y}{b_z} f_1^2 g_5' \\ - \frac{b_y u_{mo}'}{u_{mo}} f_1^2 g_1'^2 + b_y' n_y f_1 f_1' g_1'^2 + \frac{b_y b_z'}{b_z} n_z f_1^2 g_1 g_1' \\ - f_1 f_1' g_1 g_2 - \frac{b_y}{b_z} f_1^2 g_1' g_3' . \end{aligned} \quad (2.41)$$

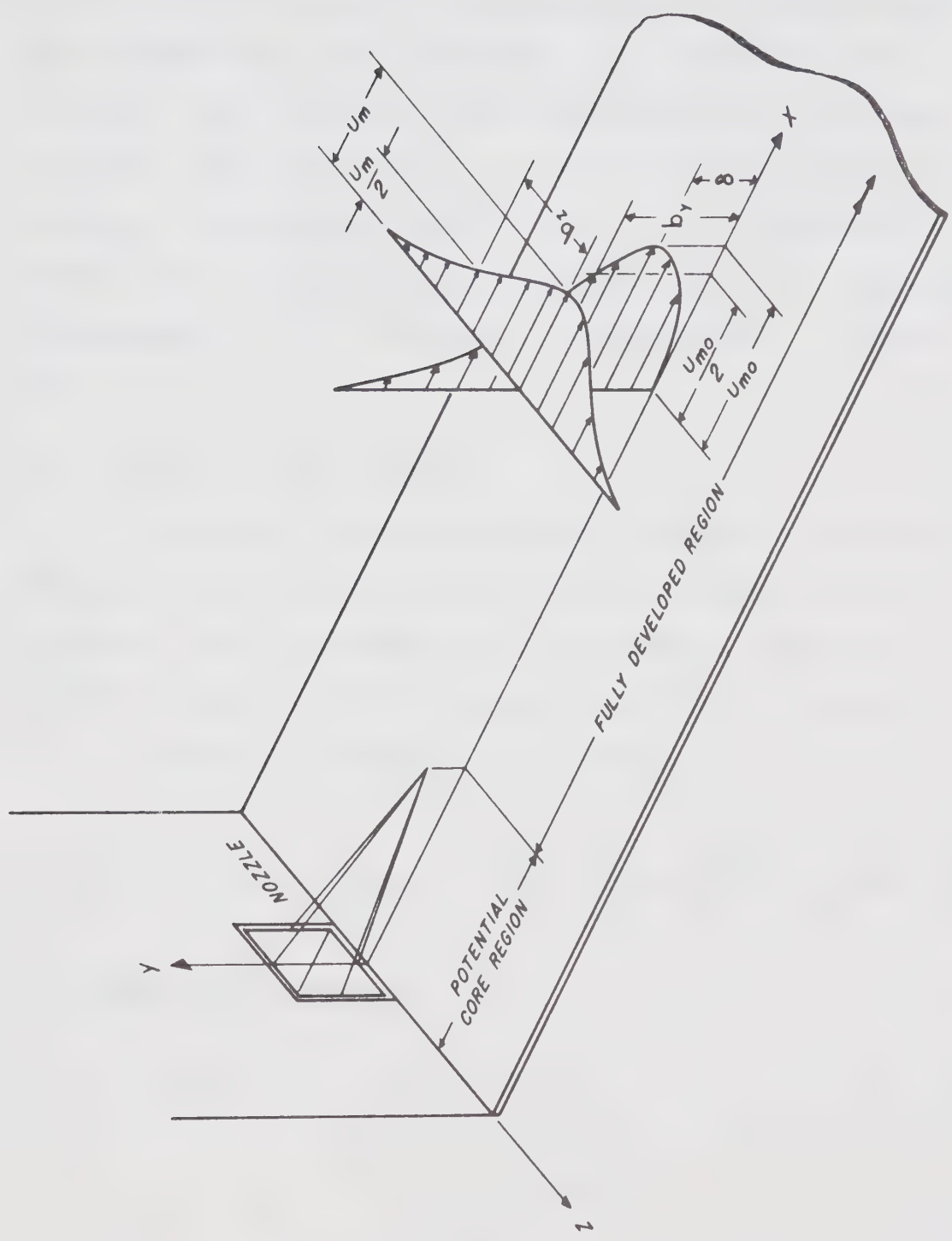


FIGURE 2.2 SCHEMATIC REPRESENTATION OF THREE DIMENSIONAL WALL JETS

For turbulent jets $u_{\text{mo}} b_y / v$ is generally large, so that the first term on the right side could be neglected and this assumption would run into trouble only close to the wall in the laminar sublayer. Further for a wall jet b_y / b_z is less than unity, so that the second term on the right hand side of Eq. 2.41 can as well be dropped. For similarity, since the left hand side of Eq. 2.41 is independent of x , the right hand side should also be independent of x . This would give the exponents $q_1 = q_2 = 1$, the details being worked out in Section 2.4.

2.6.4 Momentum Integral Equation

First of all, the momentum integral equation is worked out taking into account the wall shear. The loss in momentum because of the wall shear is estimated, which then leads to a simplified momentum integral equation that successfully gives the exponent p .

From Eqs. 2.39 and 2.40, we can write

$$\frac{\partial}{\partial x} (u^2) + \frac{\partial}{\partial y} (uv) + \frac{\partial}{\partial z} (uw) = v \left(\frac{\partial^2 u}{\partial y^2} + \frac{\partial^2 u}{\partial z^2} \right) - \left(\frac{\partial}{\partial y} \bar{u}'v' + \frac{\partial}{\partial z} \bar{u}'w' \right) \quad (2.42)$$

The boundary conditions are,

$$\text{at } y = 0, \quad u = v = w = 0$$

$$u' = v' = w' = 0$$

$$y = \infty, \quad u = 0 \quad \frac{\partial u}{\partial y} = 0$$

$$u' = 0$$

$$\text{and, at } z = \pm \infty \quad u = 0 \quad \frac{\partial u}{\partial z} = 0$$

$$u' = 0$$

Equations 2.42 is integrated over the space bounded by $y = 0$ plane and reduces to

$$\int_{-\infty}^{\infty} \int_0^{\infty} \frac{\partial}{\partial x} (u^2) dy dz = v \int_{-\infty}^{\infty} \left(\frac{\partial u}{\partial y} \right)_0^{\infty} dz$$

i.e.

$$\frac{d}{dx} \int_{-\infty}^{\infty} \int_0^{\infty} u^2 dy dz = - \frac{1}{\rho} \int_{-\infty}^{\infty} \tau_0 dz \quad (2.43)$$

where τ_0 is the shear stress on the boundary. To evaluate the integrand on the right hand side of Eq. 2.43, it is rewritten as

$$- \frac{1}{\rho} \int_{-\infty}^{\infty} \tau_0 dz = - \frac{1}{\rho} \tau_{om} x' \int_{-\infty}^{\infty} \left(\frac{\tau_0}{\tau_{om}} \right) d\xi \quad (2.44)$$

where

$$\xi = \frac{z}{x'},$$

x' = streamwise distance measured from the nozzle section

τ_{om} = boundary shear stress on the centerline and is in the x direction.

At this stage let us assume

$$\int_{-\infty}^{\infty} \frac{\tau_0}{\tau_{om}} d\xi = a_1 \quad (2.45)$$

$$\frac{\tau_{om}}{\frac{1}{2} \rho u_{mo}^2} = c_f \quad (2.46)$$

and

$$\frac{u_{mo}}{U_0} = \frac{C}{(x'/\sqrt{A})} . \quad (2.47)$$

Here, a_1 , c_f and C are empirical constants, provided from experiment. U_0 is the efflux velocity at the nozzle outlet and A is the area of cross section of the outlet. The form of Eq. 2.47 is a simplified version that fits the experimental data with no high degree of accuracy. More elaborate expressions are presented for the maximum velocity decay in Eq. 4.1. However, the final answers for momentum loss do not differ very much even when the more precise expressions are used. Making use of Eqs. 2.45 to 2.47 in Eq. 2.44, we have

$$-\frac{1}{\rho} \int_{-\infty}^{\infty} \tau_0 dz = \left(-\frac{a_1 c_f C^2}{2\rho}\right) \frac{M_0}{x'}$$

i.e. from Eq. 2.43

$$\frac{d}{dx'} \int_{-\infty}^{\infty} \int_0^{\infty} \rho u^2 dy dz = \left(-\frac{a_1 c_f C^2}{2\rho}\right) \frac{M_0}{x'} \quad (2.48)$$

where, $M_0 = \rho A U_0^2$ = efflux momentum of the nozzle.

Integration of Eq. 2.48, would give

$$\int_{-\infty}^{\infty} \int_0^{\infty} \rho u^2 dy dz = \left(-\frac{a_1 c_f C^2}{2}\right) M_0 \ln x' + a_2 .. \quad (2.49)$$

The constant of integration a_2 is found from the condition

that at the virtual origin $x' = x_0'$, and the integrand on the left hand side of Eq. 2.49 is equal to the efflux momentum flux M_0 . Hence, Eq. 2.49 can be written as

$$\int_{-\infty}^{\infty} \int_0^{\infty} \rho u^2 dy dz = M_0 \left[1 - \frac{a_1 c_f C^2}{2} \ln \frac{x'}{x_0} \right] \quad (2.50)$$

Based on the present experimental data (discussed in Chapter IV), the empirical constants involved in the above expression are given as

$$C = 8.4 \text{ (approximate value)}$$

$$a_1 = 0.206$$

$$a_2 = 0.0065$$

Equation 2.50 is then simplified to

$$\int_{-\infty}^{\infty} \int_0^{\infty} \rho u^2 dy dz = M_0 \left(1 - 0.0476 \ln \frac{x'}{x_0} \right) . \quad (2.51)$$

Noting that x_0' is approximately ten times the nozzle thickness, the loss in momentum in a distance of one hundred times the nozzle thickness is around 11% of the efflux value. This is very close to the value estimated for the case of a plane turbulent wall jet (Newman, 1969). This demonstrates that as a rough approximation the three dimensional wall jet momentum is conserved and the integral equation (Eq. 2.51) simplifies to

$$\int_{-\infty}^{\infty} \int_0^{\infty} \rho u^2 dy dz = M_0 . \quad (2.52)$$

From Eq. 2.52 and the values of q_1 and q_2 determined in Section 2.6.3, the exponent $p = -1$.

Hence, for a three dimensional wall jet, we have

$$u_{mo} \propto x^{-1}$$

$$b_y \propto x \quad (2.53)$$

$$b_z \propto x$$

For three dimensional wall jets no analytical solution for the distribution of velocity is available at the present time and is established from experiments.

2.7 Dimensional Consideration

The velocity decay and the growth of the jet can conveniently be predicted from simple dimensional considerations. Experience with the plane jet (Newman, 1961) diffusing in an stationary ambient show that the efflux velocity and the thickness of the slot do not affect the problem individually. The two independent variables can be replaced by one variable, the efflux momentum flux M_0 . This leads to the hypothesis that even for a three dimensional jet, the one variable M_0 would be a dominant parameter.

In most practical cases the Reynolds number is greater than 10^4 and it would be reasonable to neglect the effect of viscosity. Hence, the maximum mean velocity along the centerline would be determined

by the momentum flux at the nozzle section, the fluid density and the streamwise distance x measured from the virtual origin (discussed in detail in Chapter IV).

i.e.

$$u_{mo} = \phi(M_0, \rho, x) . \quad (2.54)$$

Using the Pi theorem, Eq. 2.54 can be written as

$$\frac{u_{mo}}{\sqrt{M_0/\rho x^2}} = C \quad (2.55)$$

where, C is an empirical constant.

Expressing the momentum flux in terms of A , the area of cross-section of the nozzle, and the efflux velocity U_0 , Eq. 2.55 may be rewritten in the following form

$$\frac{u_{mo}}{U_0} = \frac{C}{(x/\sqrt{A})} . \quad (2.56)$$

The form of Eq. 2.56 looks very general, and suggests that this would be valid for any arbitrary shape as long as the aspect ratio of the nozzle does not differ very greatly from unity.

For a circular jet of diameter d , Eq. 2.56 becomes

$$\frac{u_{mo}}{U_0} = \frac{C_1}{(x/d)} \quad (2.57)$$

and for a square orifice of side B,

$$\frac{u_{mo}}{U_0} = \frac{C_2}{(x/B)} \quad (2.58)$$

where, C_1 and C_2 are empirical constants.

On similar lines of argument, the problem regarding the length scales can be stated as

$$b_y, b_z = \phi(M_0, \rho, x) \quad (2.59)$$

and would lead to

$$b_y = C_3 x \quad (2.60)$$

$$b_z = C_4 x \quad (2.61)$$

Here again, C_3 and C_4 are empirical constants. For a three dimensional wall jet, the effect of the viscosity is predominant in the laminar sub-layer close to the wall and may not affect the relationships 2.56, 2.60 and 2.61 to any great extent. However, the shear stress on the wall is a result of the viscosity of the fluid, and should therefore be considered. The shear stress in the center-plane can then be expressed as

$$\tau_{om} = \phi(M_0, \rho, x, v) \quad (2.62)$$

where τ_{om} = shear stress on the wall for $z = 0$ values,
 ν = kinematic viscosity of the fluid.

Using dimensional considerations, Eq. 2.62 can be reduced to a general form

$$\frac{\tau_{om}}{\rho U_0^2} \left(\frac{x}{\sqrt{A}}\right)^2 = F\left(\frac{U_0 \sqrt{A}}{\nu}\right) \quad (2.63)$$

Further, Eq. 2.63 may be represented as

$$\frac{\tau_{om}}{\rho U_0^2} \left(\frac{x}{d}\right)^2 = F\left(\frac{U_0 d}{\nu}\right) \quad (2.64)$$

for the circular nozzle, and

$$\frac{\tau_{om}}{\rho U_0^2} \left(\frac{x}{B}\right)^2 = F\left(\frac{U_0 B}{\nu}\right) \quad (2.65)$$

for the square nozzle.

Summary

An order of magnitude study is presented to simplify the equations of motion. Based on the observations that the velocity profiles in the x-y and x-z planes are similar, the velocity decay and growth rate laws for a three dimensional free jet are established in simple exponential forms. From experimentally derived constants, an estimate for the loss in momentum flux of a three dimensional wall jet

is presented showing that there would be a loss of about 11% in a distance of 100 times the nozzle size. Therefore, as an approximation, the momentum of a three dimensional wall jet is assumed to be preserved. Based on this approximation, the velocity decay and growth rate laws are seen to be identical with the free jet case and are given as

$$u_{mo} \propto x^{-1}, \quad b_y \propto x \quad \text{and} \quad b_z \propto x.$$

A dimensional consideration for the flow is also presented taking into account that the outlet velocity and the area of cross-section of the jet do not appear as two separate variables, and rather combine to give a single variable—the efflux momentum flux. The variation of the velocity scale and the length scales, found from dimensional considerations, are in agreement with the relationships established from the equations of motion. A form for the variation of the bed shear stress along the centerline of the jet is also presented.

To check the predicted relationships, some of the available data on three dimensional free jets are analysed in Appendix B. The wall jet investigations are, however, presented in great detail in the subsequent chapters.

CHAPTER III
EXPERIMENTAL ARRANGEMENT AND
MEASUREMENT TECHNIQUES

3.1 Introduction

This chapter describes the experimental arrangements adopted and the limitation of the measurements. A set of preliminary experiments were conducted in a readily available 12.5" wide flume and an extensive investigation was later carried out in a wider flume. The narrow flume would be designated as flume 1 and the wide one as flume 2. Effects of the bed roughness, side walls and the swirl were all studied in flume 2. Probes for the measurement of bed shear and the velocity vector in three dimensional flow field had to be built and calibrated when standard calibration charts were not available. The swirl generating mechanism, used in the present experiments, is also discussed in detail.

3.2 Experimental Flume 1

This flume is 12.5" wide, 18" deep and 15'-6" long, with a horizontal aluminum bottom and plexiglass sides. Figure 3.1 gives a schematic representation of the flume. There is a flap gate at the downstream end of the channel which controls the tailwater depth, and discharges into the laboratory sump. A constant head was maintained

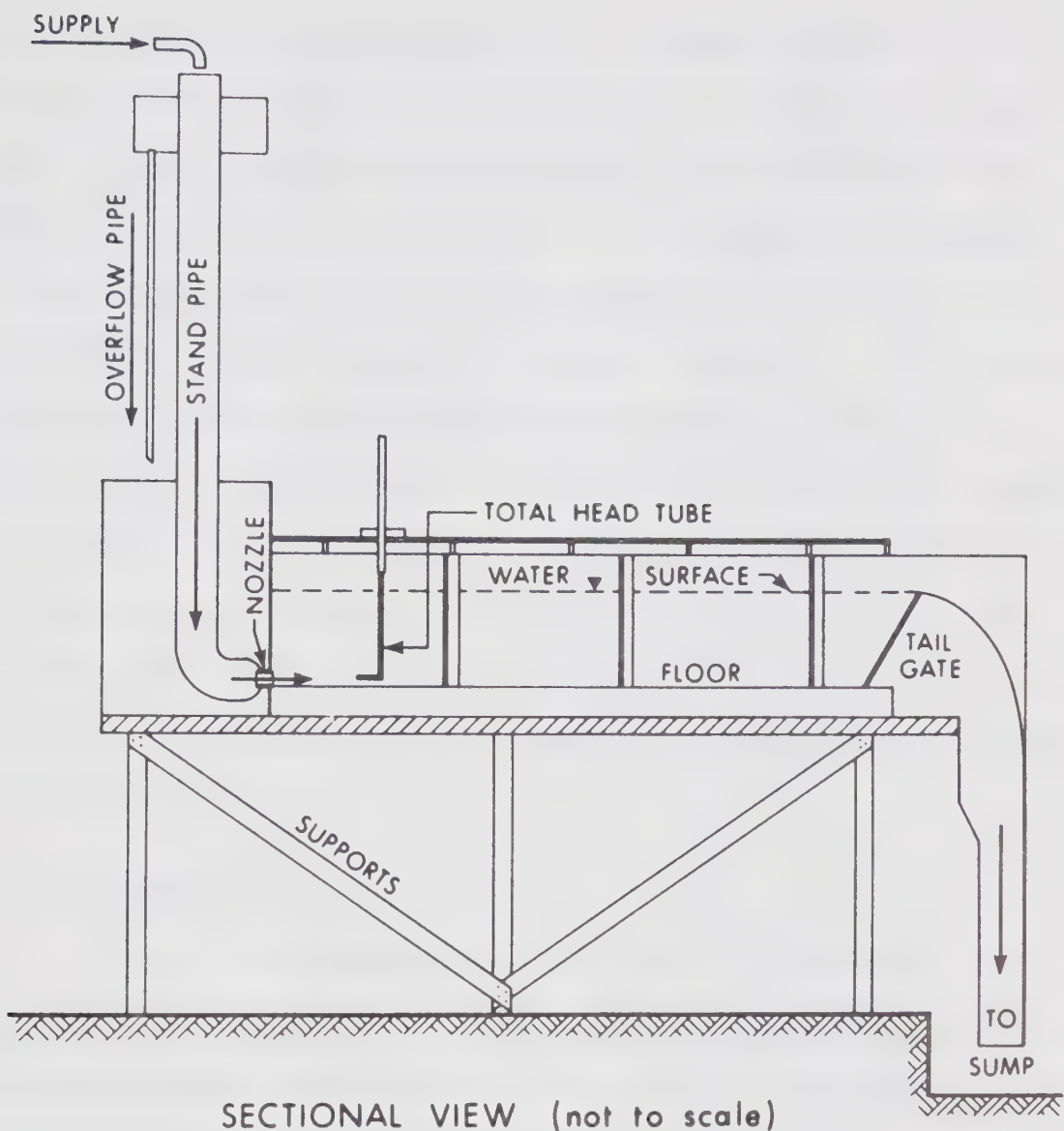


FIGURE 3.1 EXPERIMENTAL FLUME 1 (SCHEMATIC REPRESENTATION)

at the nozzle by a vertical stand-pipe 6" diameter and about 11'-6" high having an overflow device. The stand-pipe was fed by the city water supply. Near the bottom, the stand-pipe is turned through 90° by an elbow, and connected to a contraction. The contraction was prepared by joining two commercially available reducers of 6" x 2" and 2" x 1" size and the flow was contracted in a short length of 8". Test nozzles of the desired shapes were turned from solid brass cylinders 1" in diameter and of a short length of 2" to keep the boundary layer growth to a minimum. As far as possible, bell-mouth entries were provided in the nozzle and were fixed in the contraction without any leak. The test nozzle that fits the contraction, rests symmetrically at the upstream end of the channel and after some trials the nozzle was located tangentially to the bed.

3.3 Experimental Flume 2

This is a rectangular tank 43" wide, 48" deep and 11'-4" long with plexiglass sides. To conduct wall jet experiments, a false bed was provided at a depth of 26.5" from the top. The smooth aluminum plate forming this bed was 43" wide and 9'-0" long, resting on rigid channel sections and a system of jacks that allowed to level the bed as closely as possible (Figure 3.2). The flow in the system was recirculated by a centrifugal pump having its intake in the downstream end wall of the tank. A constant head at the test nozzle was maintained by an arrangement similar to the one described in flume 1. However, to maintain a constant depth of flow in the flume during

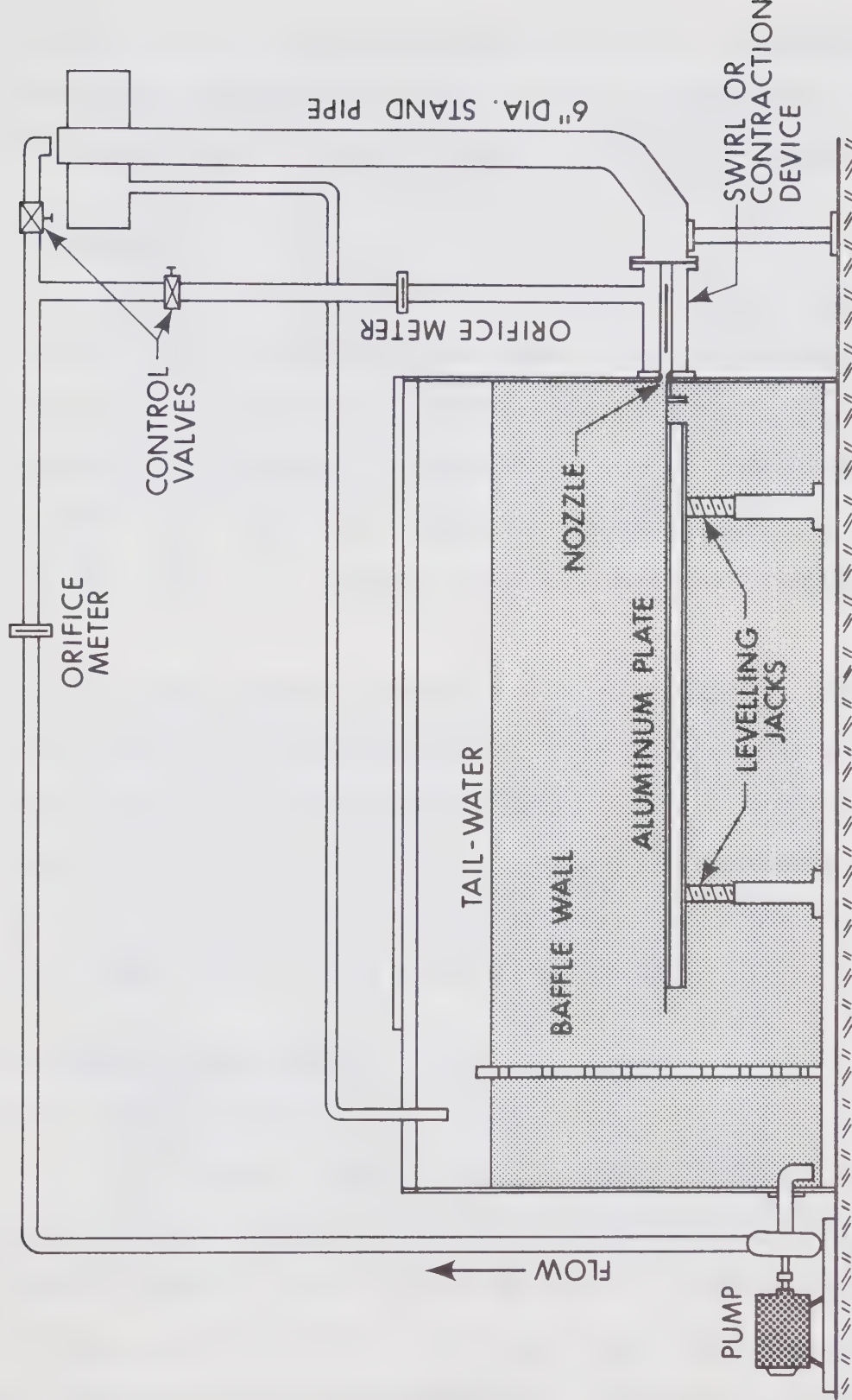


FIGURE 3.2 EXPERIMENTAL FLUME 2 (SCHEMATIC REPRESENTATION)

the tests, the overflow pipe discharges back into the experimental tank behind a baffle wall. The contraction arrangement and the details of the nozzle were in general identical with those in flume 1.

3.4 Roughness Studied

A continuous strip of #36 aluminum oxide wet-or-dry cloth manufactured by the 3M company was glued to the smooth boundary. The grains of this cloth were very angular and are shown in Figure 3.3. The grains were imbedded in a water-proof glue to varying depths. The grain size ranges from 0.38 mm to 0.70 mm, with a median size of 0.56 mm(0.00183 ft.). This was taken as the nominal roughness height K.

While measuring bed shear on rough boundaries, Hollingshead (1972) found that the equivalent sand grain roughness for this particular cloth is 3.3 times the nominal height (i.e. $K_s = 0.0061$ ft.). A high ratio of $K_s/K = 3.3$ resulted as the grains were very angular and many grains that had their long axis about twice the sieve size were oriented with the axis normal to the boundary.

3.5 Velocity Measurements

3.5.1 Total Head Tube

The velocity field for jets on smooth wall and no swirl was explored by a total head tube 0.05" in external diameter and 0.033" internal diameter. During some of the tests in flume 1, the static pressures were measured by a Pitot-static probe and the distribution was essentially found to be hydrostatic. Therefore, in most of the



FIGURE 3.3 SAND GRAIN ROUGHNESS

experiments a static pressure tapping was located on the side wall of the flume and was assumed to indicate the static pressure throughout the jet thickness. For lower range of velocities, the total head tube and the static pressure tapping were connected to a manometer board that was inclined at a slope of 1:2 and read to the nearest $\pm 0.05"$ of water. For higher range of velocities, the two pressure leads were connected to a U tube mercury manometer and the pressure differential was measured with an accuracy of $\pm 0.1"$ of mercury.

During the investigations on the effect of side walls, the water surface was not level, and the static pressure had to be sensed by a Pitot-static probe stationed close to the total head tube. In all cases, the probe was mounted on a traversing mechanism that could be located to the nearest 1/1000 of a foot in the transverse and vertical direction, and to the nearest 1/8 of an inch in the streamwise direction. The corrections to account for the turbulent fluctuations, the viscous effects and the displacement of the effective center were generally believed to be small and no correction was applied to the measured velocity. The reading of a Pitot tube is very insensitive to yaw and an angular displacement of 20° would affect the reading by less than 0.5 percent of $\rho u^2/2$ (Rosenhead, 1963). Hence, in a major part of the jet, the correction for angle of attack would be very small and no attempt is made to correct the present velocity measurements.

3.5.2 Fixed Direction Five Hole Probe

For velocity measurements in swirling jets, the conventional Pitot tube would not suffice as the angles of attack will be very large. In addition the present investigation was aimed at measuring all the three components of a velocity vector which would require the measurement of the yaw and pitch angles. In order to find the unknown quantities - the static pressure, the total pressure and the two angles of inclination of the velocity vector with a reference direction, a five hole probe was used. The five hole probe can be used as a null probe by rotating it, till its principal plane coincides with one of the planes containing the velocity vector. This type of operation was not possible in all cases, and insensitivity of the probe to angles of attack combined with the slow response of the manometers, particularly for small size tubes, makes it hard to align the probe accurately with the velocity vector. Hence, a fixed direction five hole probe was preferred inspite of its complex calibration curves.

In the present case the probe was prepared from stainless steel tubes 0.05" outside diameter and 0.033" inside diameter and has a 45° chamfer. Lewis (1965) has given calibration curves for a hemispherical nosed five hole probe, but the curves are not standardised and any change in the nose shape would change the calibration curves significantly. Hence, the present probe was calibrated and the principle involved is outlined below, following in general the line of thought adopted by Lewis. Let p_1 , p_2 , etc. be the pressures recorded by the five holes (numbered as shown in Figure 3.4) and p_0 be the static pressure. Then

$$p_i = p_0 + K_i q, \quad i = 1, 2, 3, 4, 5 \quad (3.1)$$

where q is the dynamic pressure.

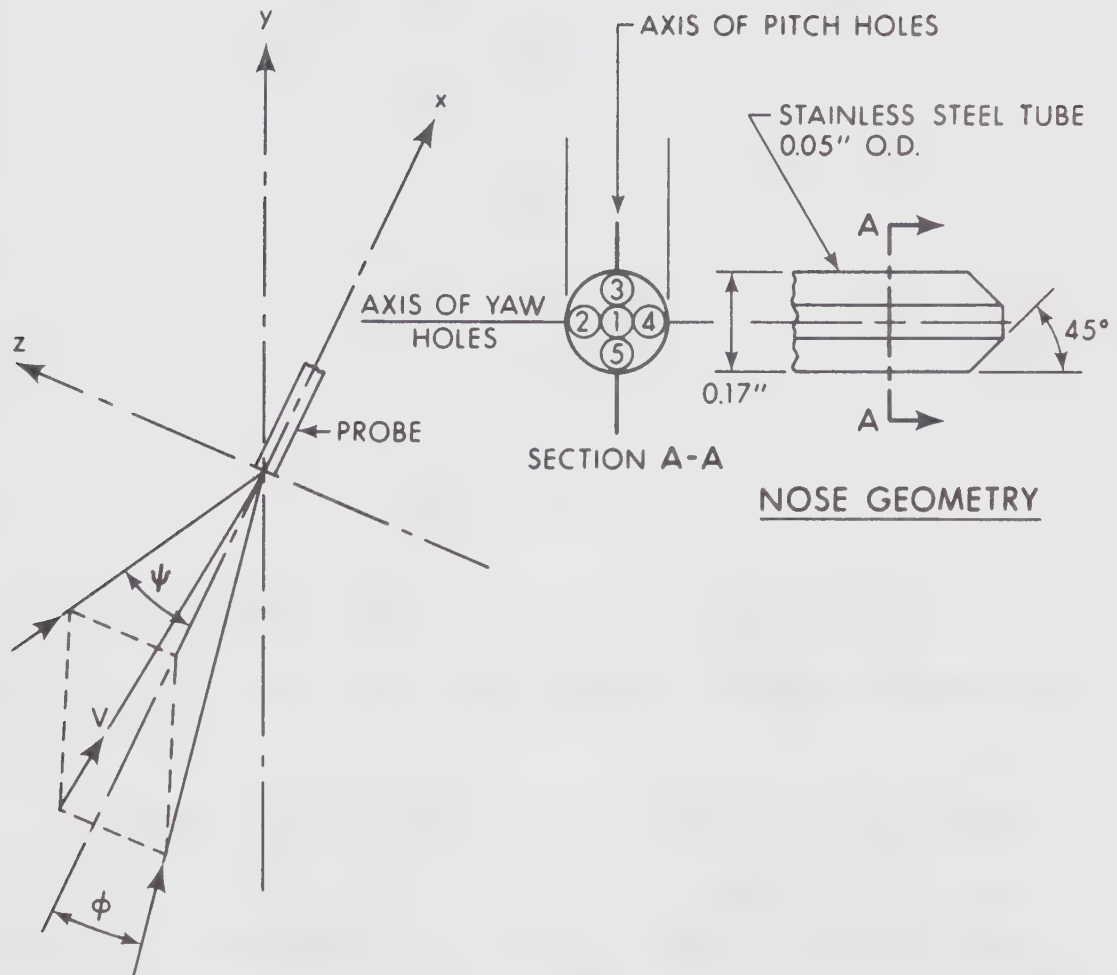


FIGURE 3.4 DEFINITION SKETCH FOR PITCH AND YAW

Using Eq. 3.1, the following coefficients were defined

$$\begin{aligned}
 k_{12} &= \frac{p_1 - p_2}{q} \\
 k_{13} &= \frac{p_1 - p_3}{q} \\
 k_{14} &= \frac{p_1 - p_4}{q} \\
 k_{15} &= \frac{p_1 - p_5}{q}
 \end{aligned} \tag{3.2}$$

$$\begin{aligned}
 k_6 &= \frac{p_1 - p_2}{p_1 - p_4} \\
 k_7 &= \frac{p_1 - p_3}{p_1 - p_5} \\
 k_8 &= \frac{p_1 - p_4}{p_1 - p_2} \\
 k_9 &= \frac{p_1 - p_5}{p_1 - p_3}
 \end{aligned} \tag{3.3}$$

It was assumed that all these coefficients were only functions of the pitch angle ϕ and the yaw angle ψ , and can be represented in an unique manner.

The probe was calibrated in the potential core of a plane wall jet having a velocity of 6 ft./sec. The dynamic pressure was measured by a standard Pitot-static probe. During calibration, values of ψ up to $\pm 55^\circ$ could be attained, but the test facility restricted the values of ϕ to a maximum of 45° . Both ϕ and ψ could be set to the nearest degree and were varied at intervals of 5° . For each combination of ϕ and ψ , the pressure sensed by all the five holes were recorded. Because of the restrictions on setting negative ϕ angles, it was assumed that the probe is symmetrical about a plane passing

through the centers of tube 2, 1 and 4. Thus, in the typical calibration charts presented in Figure 3.5, K_8 for negative ϕ is a mirror image of the values for positive ϕ about the zero pitch axis. However, for the K_7 coefficient the values for negative ϕ were the reciprocals of the corresponding quantities for positive ϕ angles. The other two coefficients K_{12} and K_1 were symmetrical about the $\phi = 0$ axis (Figures 3.6 and 3.7).

At the point of measurement the five pressure readings are known, and K_7 and K_8 are computed. From the calibration curve (Figure 3.5) the corresponding ϕ and ψ angles were noted. From Figure 3.6, K_{12} value for the noted angles is read out and the dynamic pressure q found from Eq. 3.2. The value of q should work out to be a positive quantity. A negative q would indicate that there are other possible pairs of ψ and ϕ , that correspond to the known K_7 and K_8 , needing a new estimate. K_1 is then read from Figure 3.7 and with p_1 and q known, p_0 can easily be computed.

In certain parts of the chart (Figure 3.5) the coefficient K_7 and K_8 become infinity and makes it impossible to estimate the angles ϕ and ψ . However, this can be overcome by plotting charts for the other coefficients and using the one that gives finite values for reliable interpolation.

The three velocity components in terms of ϕ and ψ are given by

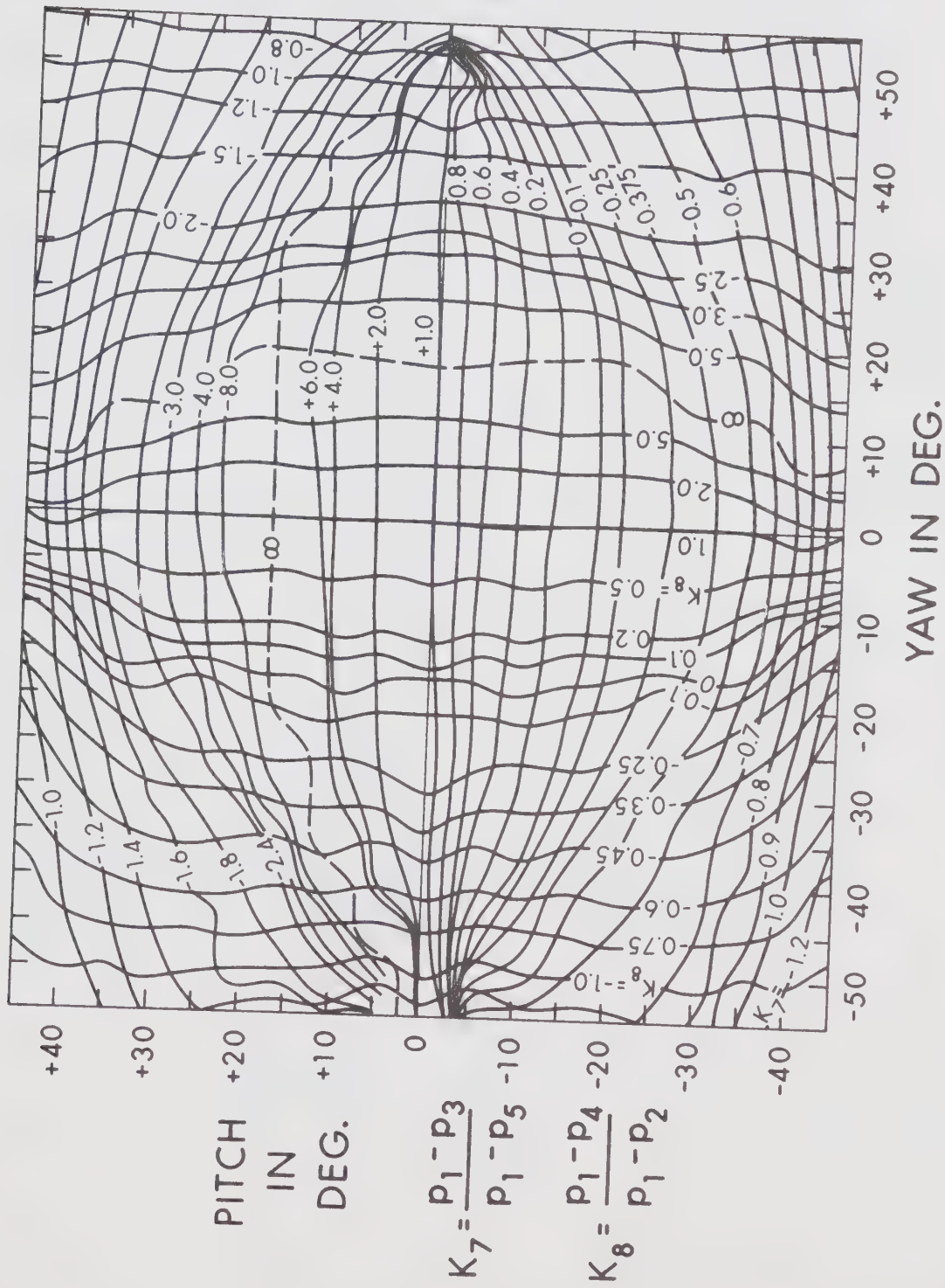


FIGURE 3.5 CALIBRATION FACTORS K_7 AND K_8 FOR FIVE HOLE PROBE

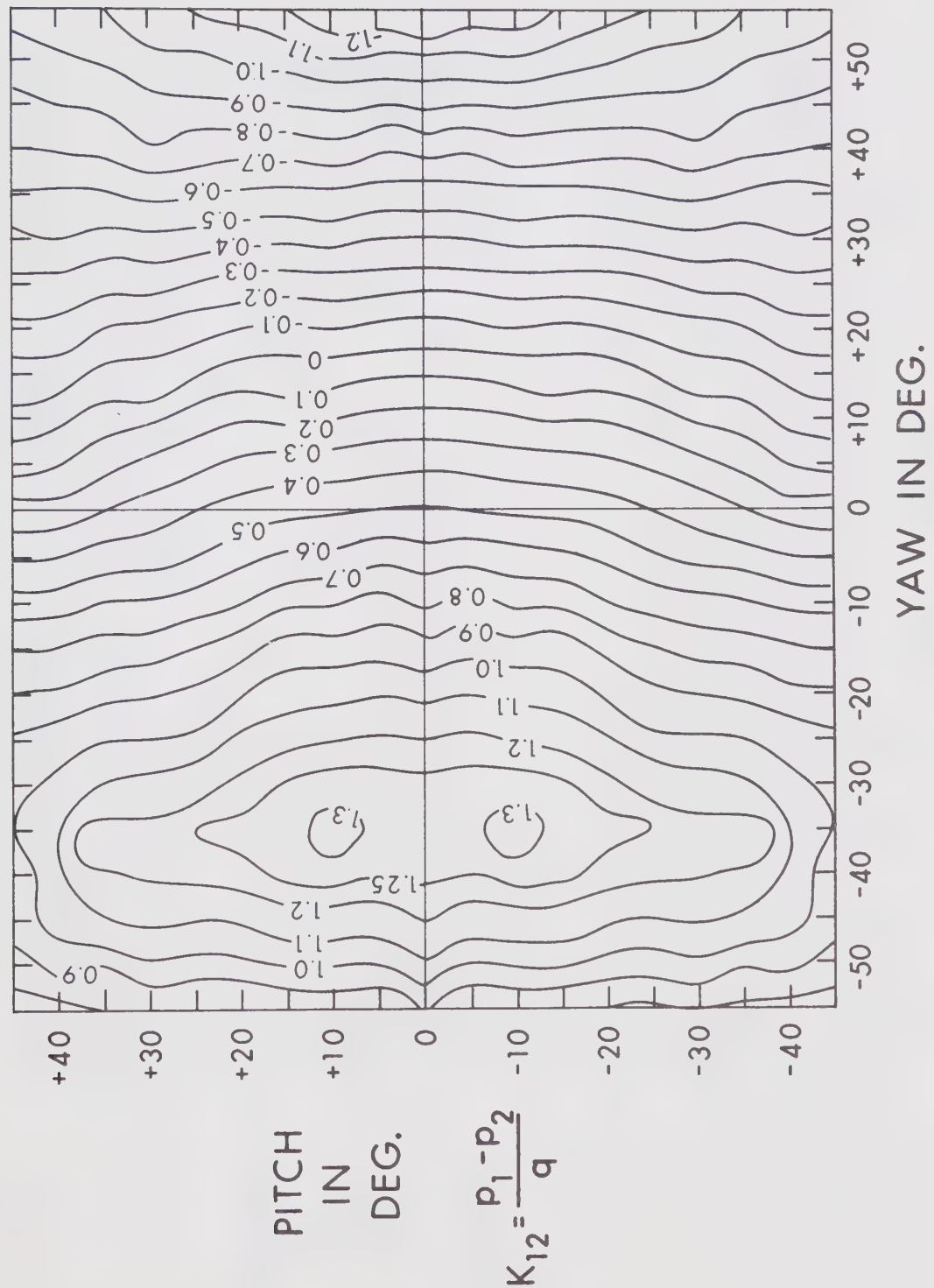
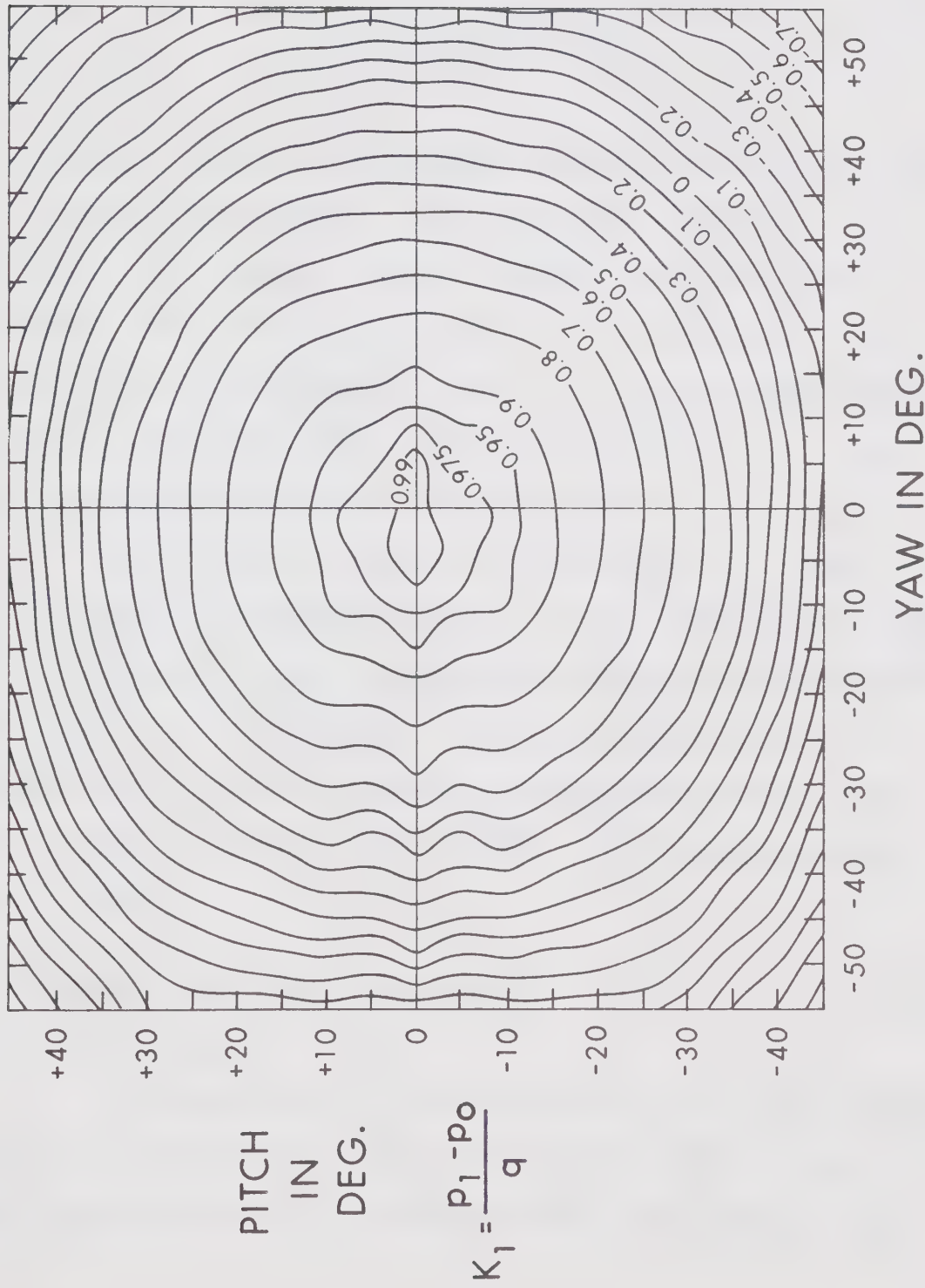


FIGURE 3.6 CALIBRATION FACTOR K_{12} FOR FIVE HOLE PROBE



$$\begin{aligned}
 u &= V(1+\tan^2\psi+\tan^2\phi)^{-1/2} \\
 v &= V \tan\phi(1+\tan^2\psi+\tan^2\phi)^{-1/2} \\
 w &= V \tan\psi(1+\tan^2\psi+\tan^2\phi)^{-1/2}
 \end{aligned} \tag{3.4}$$

The probe was calibrated in an uniform velocity field away from the wall, whereas the conditions during measurement happen to be quite different. The probe was used in a velocity field having large gradients and would introduce errors. This was particularly acute in a field close to the nozzle section. The viscous effects and the proximity of the wall would introduce additional errors in measurement and there seems to be no information available to account for this. There is also a limitation on the smallest size of probe that can be made from the available tubes. In view of the complex nature of the calibration curves, no comment was made on the order of errors involved. It is believed that the probe can measure ϕ and ψ to an accuracy of $\pm 2^\circ$ and the u component can be measured very reliably. The accuracy in the measurement of small v and w components seems to be limited.

3.6 Boundary Shear Stress Measurements

3.6.1 Preston Tube

The Preston tube is a total head tube resting on a boundary and held against the flow. This is a convenient method of measuring the boundary shear when the direction of the flow is known. The

stagnation pressure was found from the sensing device connected to the total head tube, and the static pressure was found by different means. The difference between the two pressures Δp is correlated with the boundary shear stress τ_0 . The correlation was developed by Preston (1954), mainly from similarity considerations and the existence of the law of the wall. This correlation is given in the form

$$\frac{\Delta p d^2}{4\rho v^2} = F\left(\frac{\tau_0 d^2}{4\rho v^2}\right) \quad (3.5)$$

where Δp = dynamic pressure

d = outer diameter of the total head tube

ρ = mass density of the fluid

v = kinematic viscosity of the fluid

The principle of the method has been confirmed by Head and Rechenberg (1962), and Rajaratnam (1965) derived calibration curves theoretically by assuming a suitable velocity distribution in the wall region. The Preston tube technique is found to be valid even in regions with milder pressure gradients and have been investigated extensively by Patel (1965). In the present investigation, Patel's curves have been adopted. The calibration curves available are for cylindrical Preston tubes with square ends, having a ratio of the internal to the external diameter of about 0.6. Even though this ratio is not very critical, to use the available curves with high accuracy, the diameter ratio should be between 0.5 and 0.7, preferably equal to 0.6.

In the present measurements, the total head tube used for taking velocity profiles was also serving as the Preston tube and had 0.05" outside diameter and 0.033" inside diameter. The static pressure tap was located on the side wall of the flume. Temperature of water was around 66°F and $v = 1.11 \times 10^{-5}$ ft.²/sec.

The method requires that the size of the tube be small compared to the boundary layer thickness so that it would lie in a zone where the law of the wall is valid. However, in many of the present measurements the tube was larger than the wall law region and in some instances the tube occupied around 35% of the boundary layer thickness, casting some doubt on the accuracy of the boundary shear results. Sigalla's (1958) investigations on the effect of instrument size on the measurement of skin friction in a boundary layer showed that the results would be within 4% accuracy, even when the diameter of the tube was about 40% of the boundary layer thickness, and therefore, the present measurements were acceptable.

3.6.2 Yaw Probe as a Preston Tube

When the direction of shear stress is at some unknown angle with the free-stream, in principle its magnitude and direction can still be obtained by rotating the Preston tube till the maximum dynamic pressure is indicated. Since the dynamic pressure recorded was very insensitive to the angle of yaw θ , particularly when the angle was less than 20°, this approach is very limited. Further, installing a mechanism to rotate the tube would be an added inconvenience and time consuming. In order to overcome these difficulties, Rajaratnam and

Muralidhar (1967) used a yaw probe on the boundary and gave the necessary calibration curves for shear computation. The nose of the probes was chamfered at 45°. The principle involved in this method of shear measurement is described briefly in the following paragraphs.

The yaw probe was placed on the boundary facing in the reference direction, the x axis. If the shear stress was at an angle θ with the reference direction and if the center tube was designated as number 2, with the tube on the side of shear stress as number 3 and the remaining tube as number 1, the total pressure recorded by them would be,

$$p_1 = p_0 + K_{10} \Delta p$$

$$p_2 = p_0 + K_{20} \Delta p \quad (3.6)$$

$$p_3 = p_0 + K_{30} \Delta p$$

where K_{10} , K_{20} , K_{30} are the respective calibration factors and are only functions of θ , p_0 is the static pressure and Δp is the dynamic pressure. Combining the various expressions in Eq. 3.6 and 3.5 the following can be written

$$\begin{aligned} p_1 &= p_0 + K_{10} \frac{4\rho v^2}{d^2} f(\tau_0^+) \\ p_2 &= p_0 + K_{20} \frac{4\rho v^2}{d^2} f(\tau_0^+) \\ p_3 &= p_0 + K_{30} \frac{4\rho v^2}{d^2} f(\tau_0^+) \end{aligned} \quad (3.7)$$

where

$$\tau_0^+ = \frac{\tau_0 d^2}{4\rho v^2} .$$

By suitably combining the expressions in Eq. 3.7, one can write

$$\frac{p_3 - p_2}{p_1 - p_2} = \frac{K_{30} - K_{20}}{K_{10} - K_{20}} = K_0 . \quad (3.8)$$

The above expression indicates that K_0 is only a function of θ and can be conveniently calibrated. (Figure 3.8).

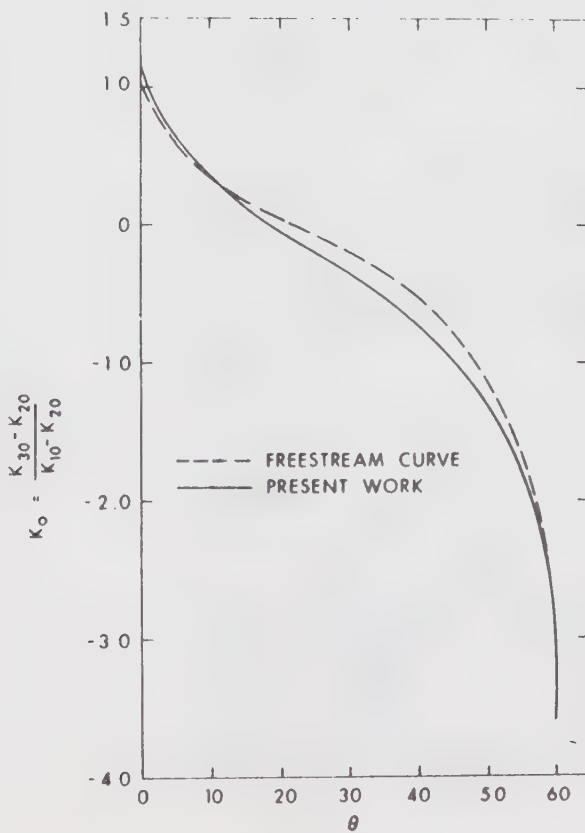


FIGURE 3.8 CALIBRATION FACTOR K_0 FOR YAW PROBE
(Rajaratnam and Muralidhar, 1968)

From Eq. 3.6, it is possible to write,

$$\frac{(p_2 - p_1) d^2}{4 \rho v^2} \frac{1}{K_{20} - K_{10}} = f(\tau_0^+) . \quad (3.9)$$

In measuring shear stress at any point, p_1 , p_2 and P_3 are known quantities so that K_0 can be computed. From Figure 3.8 the corresponding θ , and then K_{10} and K_{20} from Figure 3.9 were noted.

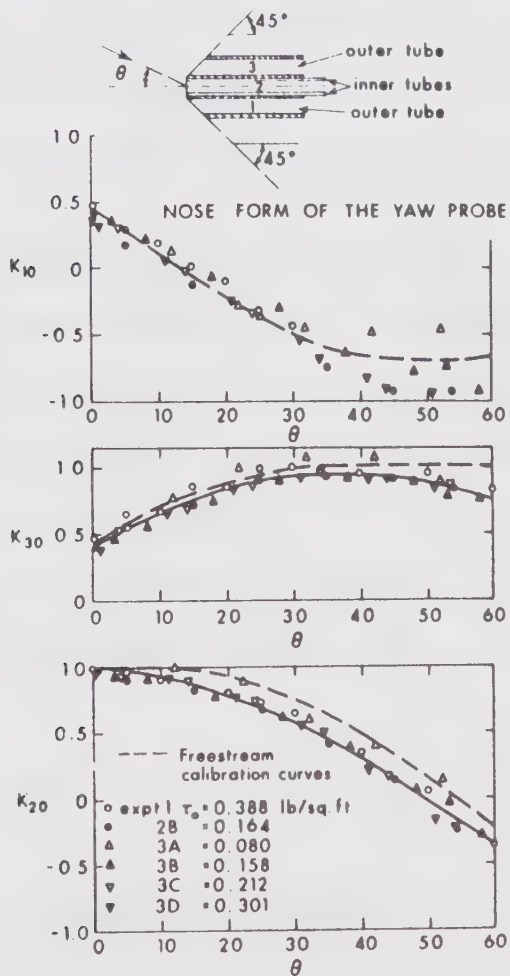


FIGURE 3.9 CALIBRATION FACTORS FOR YAW PROBE ON THE BOUNDARY
(Rajaratnam and Muralidhar, 1968)

Since all the quantities on the left hand side of Eq. 3.9 were known, $f(\tau_0^+)$ was determined. Using Patel's calibration curves τ_0^+ and hence τ_0 were computed.

It is to be noted that the law of the wall for a three dimensional boundary layer seems to be valid in a much smaller region than the corresponding two dimensional case, and therefore, the tubes should be as small as possible. Stainless steel tubes having an outside diameter of 0.045" and an inside diameter of about 0.6 times the outside were used in the present investigation. The nose shape was made geometrically similar to the one calibrated by Rajaratnam and Muralidhar (1967) and hence their curves have been used.

3.6.3 Preston Tube Technique Applied to Rough Walls

Hwang and Laursen (1963) extended the Preston tube technique to measure shear on rough boundaries. A relationship between the dynamic pressure acting on a Pitot tube in contact with a rough boundary and the local boundary shear was worked out analytically using logarithmic velocity distribution with Nikuradse's constants. For the fully developed rough flows the final relationship worked out as,

$$\frac{\Delta p}{\tau_0} = 16.531 \left\{ \left[\log \frac{30h}{K_s} \right]^2 - \log \frac{30h}{K_s} \left[0.25 \left(\frac{a}{h} \right)^2 + 0.0833 \left(\frac{a}{h} \right)^4 + \right] \right. \\ \left. + \left[0.25 \left(\frac{a}{h} \right)^2 + 0.1146 \left(\frac{a}{h} \right)^4 + \right] \right\} \quad (3.10)$$

where h = height of center of stagnation tube from zero datum

a = inner radius of the stagnation tube

K_s = equivalent sand roughness.

The above equation converges rapidly for small values of a/h . The pressure to shear ratio which depends on the roughness size a/K_s and the relative position of the tube $(h-a)/K_s$ is indicated in Figure 3.10.

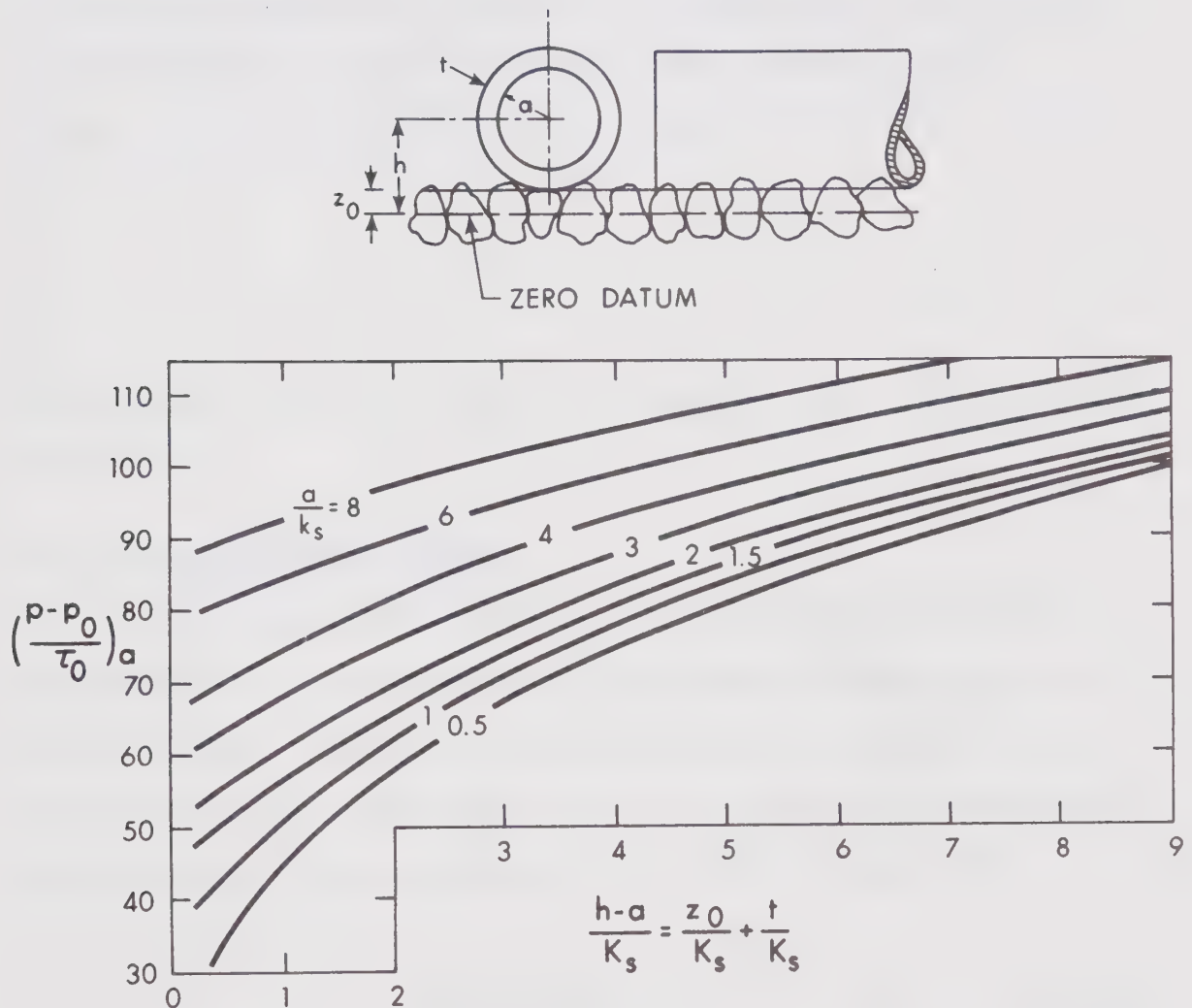


FIGURE 3.10 PRESSURE SHEAR RATIO FOR ROUGH BOUNDARIES (ANALYTICAL)
(Hwang and Laursen, 1963)

For measurement in the hydraulically smooth and transition region ($u_* K_s / v < 70$) empirical curves for applying correction are given.

In the present measurements a stagnation tube having outside diameter 0.11" and inside diameter 0.085" was used. The boundary had an equivalent roughness $K_s = 0.0061$ ft. Assuming $z_0/K_s = 0.15$, where z_0 is the height of bottom of stagnation tube from zero datum, $(h-a)/K_s = 0.33$ and $a/K_s = 0.575$. From Figure 3.10,

$$\frac{\Delta p}{\tau_0} \approx 31.0 . \quad (3.11)$$

This expression was used to compute the boundary shear in hydraulically rough flows.

3.6.4 Velocity Profile Method

For a two dimensional boundary layer, the wall shear stress was assumed to be very nearly equal to the turbulent shear outside the laminar sublayer. Further, on the assumption that this shear stress remains constant in a small zone close to the wall, an expression for the velocity distribution can be derived as (Schlichting, 1968)

$$\frac{u}{u_*} = \frac{1}{\kappa} \ln \frac{y}{K_s} + B_s \quad (3.12)$$

where κ = Karman's universal constant

$$u_* = \sqrt{\frac{\tau_0}{\rho}} , \text{ and}$$

B_s is a function of the roughness Reynolds number $u_* K_s / v$. For hydraulically

rough boundaries (i.e. $u_* K_s / v > 70$), $B_s = 8.5$. Regardless of whether the flow is hydraulically smooth, transitional or rough, adopting a value of 0.4 for κ , the above equation can be rewritten as

$$\sqrt{\frac{\tau_0}{\rho}} = u_* = \frac{1}{5.75} \frac{u_2 - u_1}{\log \frac{y_2}{y_1}} \quad (3.13)$$

This is a convenient expression for boundary shear computation as a knowledge of K_s and B_s are not needed.

To use this method, it would be necessary to determine the correct datum from which y is to be measured. The datum selection was generally made by trial and error by plotting u versus $\log y$, y being measured from an assumed datum, till a straight line plot was obtained.

The displacement of the effective center of the Pitot tube was another important aspect that needed consideration, particularly for measurements taken very close to the wall. The exact correction applicable for a Pitot tube resting on a rough boundary is open to question, although for a smooth boundary it is around 0.18 times the tube diameter (Macmillan, 1957).

3.7 Swirl Generation

3.7.1 Swirl Generator

The experimental layout for producing swirling jets is schematically represented in Figure 3.11. The generator had an outer casing 6" in diameter and an inner steel pipe having a inside diameter of 1" and 0.5" thick wall. The inner pipe was 18" long and had four tangentially cut slots 0.19" thick extending for a length of 4.5".

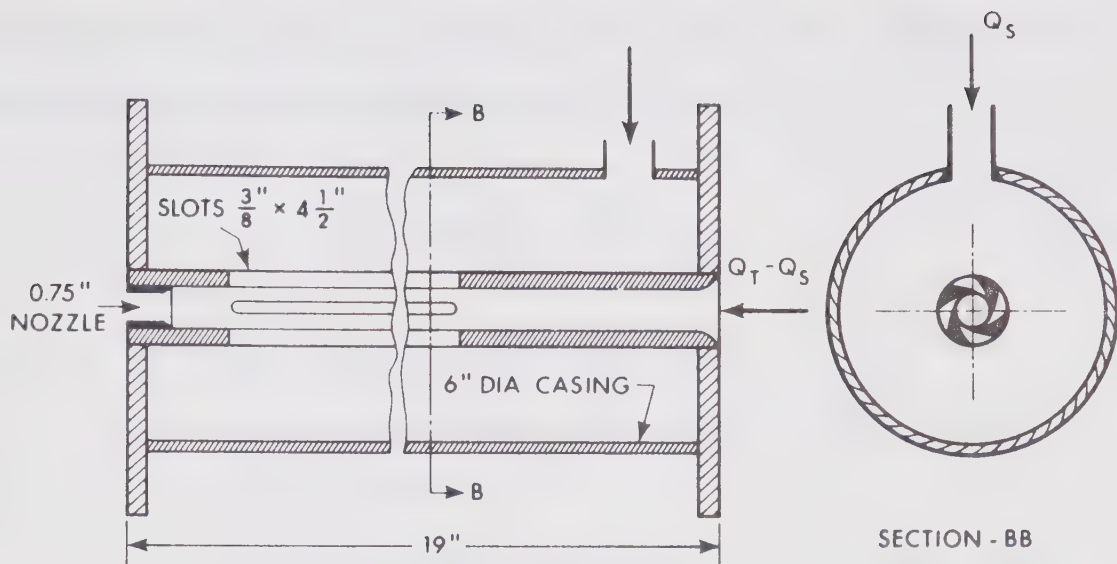


FIGURE 3.11 SWIRL GENERATOR (SCHEMATIC REPRESENTATION)

At the exit end of the inner pipe, a 0.75" nozzle having rounded entrance was provided. Quantities of water let into the axial and the tangential supply pipe could be varied. The highest swirl was produced when the entire flow was led through the tangential slots, whereas, lower swirls could be produced by diverting only a part of the flow through the slots. However, in all cases the stand pipe was made to overflow so as to maintain a constant head.

3.7.2 Discharge Measurement

The discharge rate through the tangential slots as well as the total discharge in the main line were measured by sharp edged orifice meters 1" in diameter, with pressure taps located at 1.5" up-

stream and 1.0" downstream of the orifice plate. The discharge was computed from the flow equation (Spink, 1958)

$$Q_n = \alpha N D^2 F_a F_m \sqrt{\frac{G_f}{G_\ell}} \sqrt{h_w} \quad (3.14)$$

where Q_n = rate of flow, units same as N

α = an operating figure, depending on ratio of orifice and pipe diameter

N = a constant which takes care of units of measurement

D = diameter of the pipe in inches

F_a = ratio of area of primary device opening at flow temperature to that at 60°F

F_m = manometer factor for liquid on mercury

G_f = specific gravity of liquid at flowing temperatures

G_ℓ = specific gravity of liquid at base temperature

h_w = operating differential as read on the differential gauge in inches of water

In the present setup $D = 1.5"$, hence $\alpha = 0.3074$, $N = 0.01263$, $F_a = 1$, $\sqrt{G_f/G_\ell} = 1$ and Eq. 3.14 can be simplified to

$$Q_n = 0.00875 \sqrt{\Delta H} \text{ cfs ...} \quad (3.15)$$

where ΔH = differential manometric head in inches of water.

3.7.3 Measurement of Swirl Number

For a circular jet, dimensional analysis (Chigier and Chervinsky, 1967) and integration of the equations of motion show that, the degree of the swirl can be characterised by a single parameter,

$$S = \frac{T}{(P+M)r_0} \quad (3.16)$$

where S = swirl number

T = angular momentum of the jet

P = total pressure in the jet

M = axial momentum of the jet

r_0 = radius of the nozzle

The form of Eq. 3.16 is based on the fact that the quantities T and $(P+M)$ are preserved for a free jet. Further it can be shown that

$$T = \int_0^\infty \rho r^2 u w dr \quad (3.17)$$

and

$$P+M = \int_0^\infty \rho(u^2 - \frac{w^2}{2}) r dr . \quad (3.18)$$

The swirl number defined in Eq. 3.16 can be varied by changing the ratio of the discharge through the tangential slots to the discharge in the axial direction of the generator. This relationship was primarily guided by the geometry of the slot and the size of other components of the chamber. There seems to be no way of establishing the

swirl number that could be generated for different discharge ratios, except by direct measurements. The ratio was set at four different values in the range of 0 to 1 and for each ratio, velocity profiles in a radial plane of the free jet was measured by the five hole probe. From the measured values of u , w and r , the quantities on the right hand side of Eqs. 3.17 and 3.18 were computed graphically. For a particular discharge ratio, the measurements were conducted at distances of 2" and 4" from the nozzle section. Theoretically the swirl number should be the same for any section, but the present results showed some variation (Table III-1) and is perhaps because of experimental errors.

TABLE III-1
SWIRL NUMBER MEASUREMENTS

Discharge ratio Q_s/Q_t	Swirl No. S $x' = 2.0"$	Swirl No. S $x' = 4.0"$	Average S
1.0	0.275	0.256	0.265
0.877	0.205	0.197	0.201
0.59	0.10	0.10	0.10
0.358	0.0725	0.0535	0.063

Q_s = discharge through the slots

Q_t = total discharge

The average values of the swirl numbers are plotted in Figure 3.12 as a function of the discharge ratio and serves as a calibration curve for the swirl generator used in the present investigation.

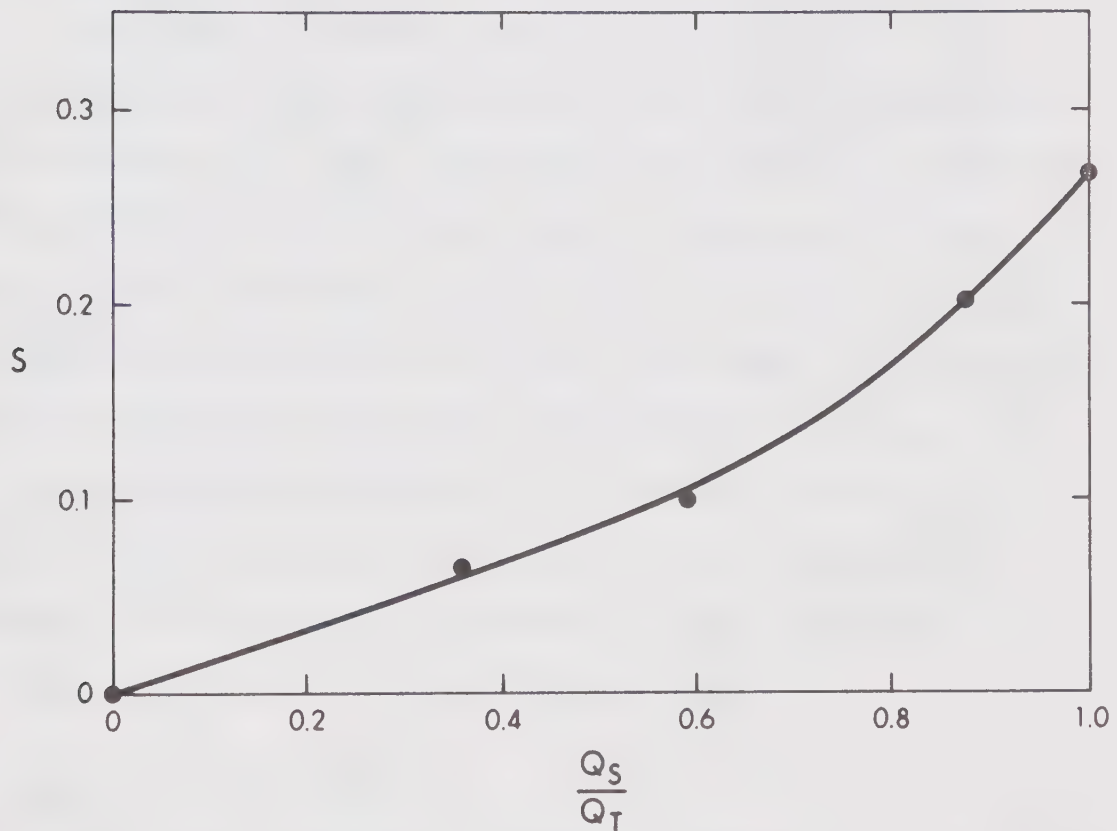


FIGURE 3.12 SWIRL NUMBER-DISCHARGE RATIO RELATIONSHIP

CHAPTER IV

THREE DIMENSIONAL WALL JETS

4.1 Introduction

Wall jets of circular, rectangular, triangular or other similar geometrical shape, having finite aspect ratio are denoted as three dimensional wall jets. Experimental investigations on three dimensional wall jets in wide channels and on a smooth wall (or bed) having no swirl is presented in this chapter. The other experimental investigations are those of Sforza and his associates at the Polytechnic Institute of Brooklyn (1966, 1967) and are limited to rectangular outlets. Based on present observations, relationships for the decay of maximum velocity, growth of the jet and bed shear distribution are presented in suitable forms. Experimentally found relationships are then compared with theoretically established laws.

4.2 Review of Existing Work

The bulk properties of turbulent, incompressible, rectangular wall jets with air as the media, issuing into a quiescent ambient have been experimentally studied by Viets and Sforza (1966) and Sforza and Herbst (1967). Depending on how the maximum velocity decays, the flow field was divided into three distinct regions - the potential core, the characteristic decay region and the radial type decay region.

- (a) Potential core region (P.C.): The maximum velocity remains almost constant and is close to the exit velocity. This

region extends from the nozzle section to a distance of about ten times the nozzle height.

- (b) Characteristic decay region (C.D.): The maximum velocity decays as a constant power of x . Although the mixing from the near boundaries of the outlet has reached the center of the flow region, the mixing from the far boundaries that are on the sides have not extended over the entire flow field. Hence, in this region the velocity decay was related to the aspect ratio of the nozzle. The centerline velocity profiles normal to the wall was found to be similar.
- (c) Radial type decay region (R.D.): In this region, the velocity decays as $x^{-1.1}$ and the mixing from all boundaries of the nozzle extend over the entire flow field. The flow tends to loose memory about the nozzle geometry. The centerline velocity profile taken normal to the wall and the profiles in the transverse direction were found to be similar.

Other important features noticed were that the growth of the mixing layer normal to the wall was independent of the orifice shape. Further, the near-field growth in the transverse direction was found to be affected by the nozzle geometry and the transverse growth rate happened to be larger than the growth in the normal direction.

Irregularities in velocity profile of the C.D. region were observed in transverse planes and was believed to be caused by the induced velocity connected with a system of vortex rings surrounding the jet.

4.3 Experiments

Two series of experiments were conducted. The first series of four experiments were conducted in flume 1 and the second series of six were conducted in flume 2. Descriptions of the two flumes are given in Chapter III. In the second series, the fifth run was for a free square jet and the results are presented in Appendix B. The shapes studied include a circle, a square, an ellipse, an equilateral triangle with its base resting on the bed and two rectangles. The significant details are given in Table IV-1.

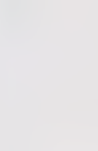
In all experiments, the nozzle was deeply submerged so that the water surface was level thereby ensuring a negligible longitudinal pressure gradient on the wall jet. The velocity field was explored with a total head probe 0.05" external diameter and in most cases, the static pressures were obtained from a side wall tap. The boundary shear along the centerline of the jet was explored by the same total head tube, used as a Preston tube. The off-center shear stress distributions were, however, measured by a yaw probe 0.045" thick.

4.4 Typical Experimental Results

A typical distribution of velocity (u_m) in the center-plane is shown in Figure 4.1, where the distance x' is measured from the nozzle section. It is seen that the velocity distribution assumes the wall jet shape very quickly. Figure 4.2 shows another typical plot of variation of velocity u with z in different horizontal planes for a number of x stations. In any one plane, the maximum velocity that occurs on the centerline decays as the distance from the nozzle

TABLE IV-1

NOZZLE SHAPES STUDIED

Expt. No.	Shape	h or D in.	B or D in.	U_0 FPS	$R = \frac{U_0 h}{v}$	M_0 lbs.	Series No.	Remarks
1	Circular	0.375	0.375	25.95	6.5×10^4	0.997	I	
2	Square	0.388	0.388	25.95	6.7×10^4	1.365	I	
3	Rectangular	0.375	0.563	25.95	9.75×10^4	1.91	I	
4	Triangular	0.50	0.567	25.89	8.6×10^4	1.285	I	
5	Square	0.388	0.388	24.16	6.25×10^4	1.28		
6	Square	0.388	0.388	25.15	6.5×10^4	1.278	II	
7	Elliptic	0.375	0.607	24.55	5.95×10^4	1.445	II	
8	Circular	0.375	0.375	24.34	6.07×10^4	0.878	II	
9	Triangular	0.50	0.567	24.41	8.15×10^4	1.14	II	
10	Rectangular ($e = 0.4$)	0.62	0.25	24.41	1.02×10^5	1.25	II	

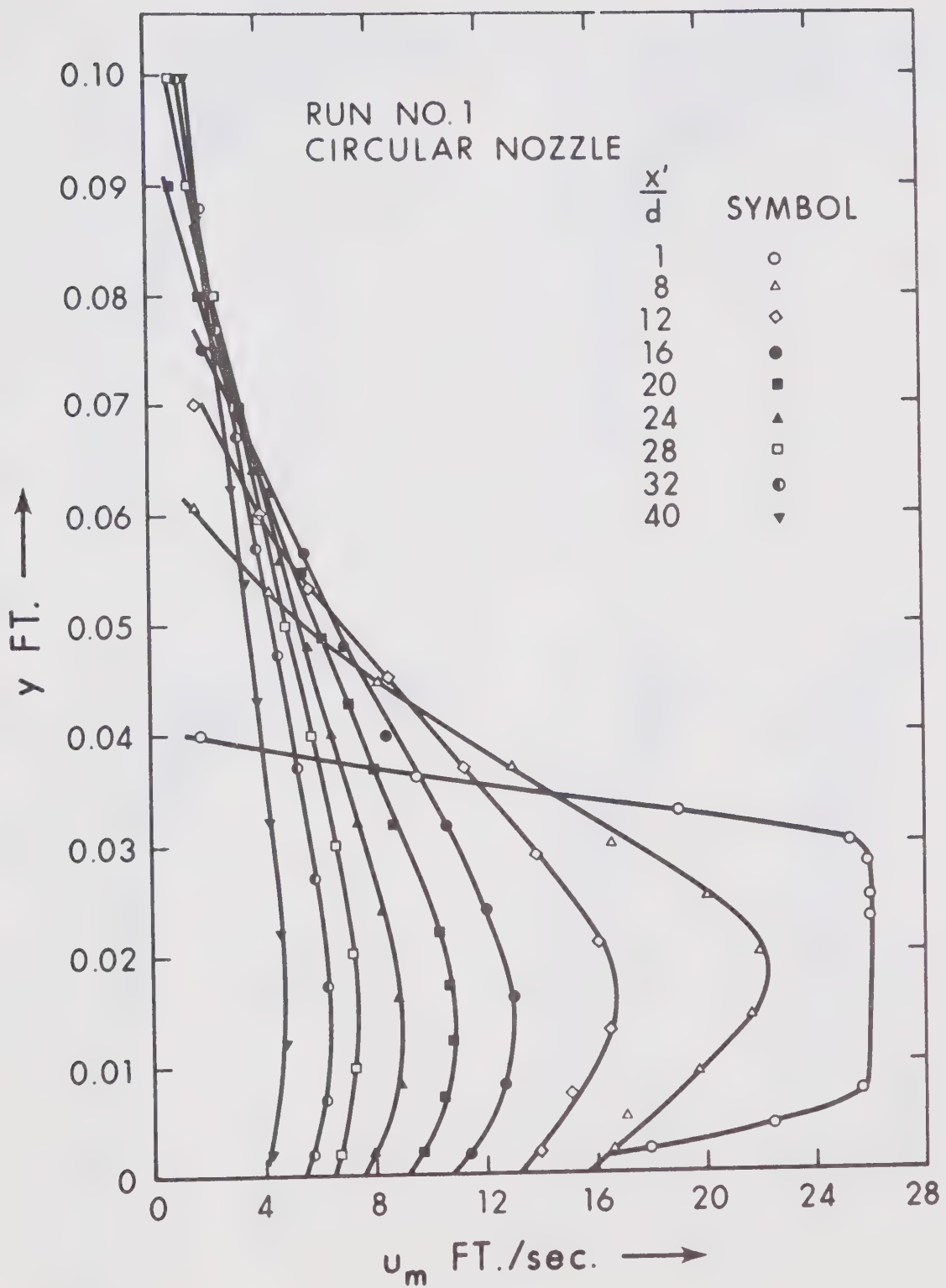
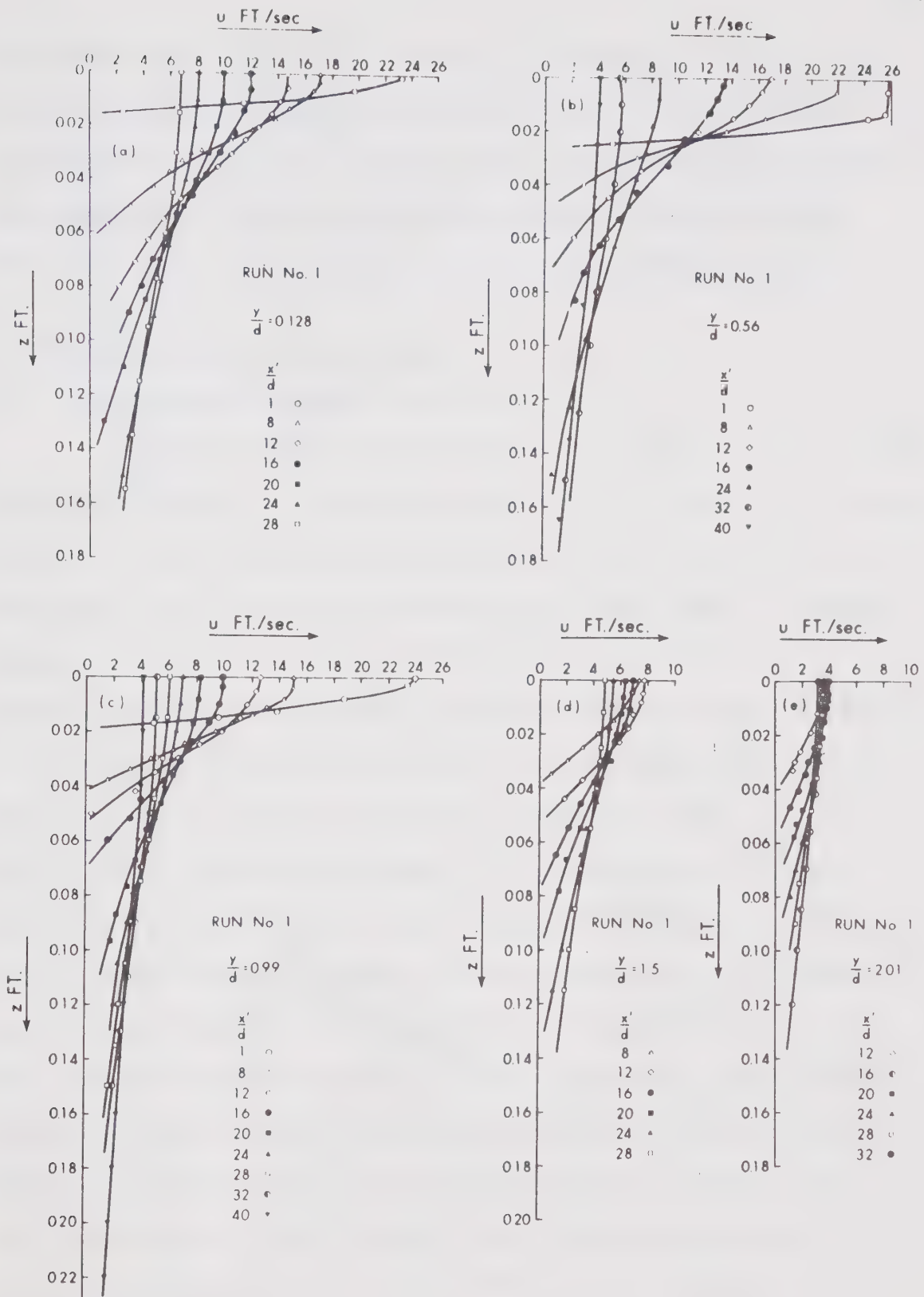


FIGURE 4.1 VELOCITY DISTRIBUTION IN THE CENTER-PLANE

FIGURE 4.2 VELOCITY DISTRIBUTION IN THE z DIRECTION

is increased and simultaneously there is a continuous widening of the profile. The distribution of wall shear is given in Figure 4.3 and its behaviour is in general similar to the transverse velocity profile. The boundary shear stress along the centerline is found to decrease with x and some of the significant results are tabulated in Appendix C.

4.5 Analysis of Experimental Results

4.5.1 Velocity Distribution in the Center-Plane

For all the shapes tested, the velocity profiles in the center-plane were checked for similarity by plotting u_m/u_{m0} versus η_y . A typical plot for the run #8 is shown in Figure 4.4. It was found that for every case studied, the velocity distributions are similar after a streamwise distance of about 15 times the nozzle height. The rest of the non-dimensional velocity distribution for other shapes are given in Appendix C. The curve of the plane turbulent wall jet on smooth walls with zero pressure gradient, denoted for the sake of brevity as the classical wall jet (CWJ), is plotted in Figure 4.4 for comparison. Although the experimental points could be well compared with Glauert's (1956) analytical solution by selecting a proper value of α , it is thought that a proper selection of α is somewhat arbitrary and hence the CWJ curve derived from most available two dimensional wall jet experimental data would be more reliable. The classical wall jet curve describes the present data reasonably well and there appears to be some scatter for large values of η_y and is mostly because of the large errors involved in measuring small velocities. There is also scatter in the data for η_y less than 0.1, indicating that a single length scale

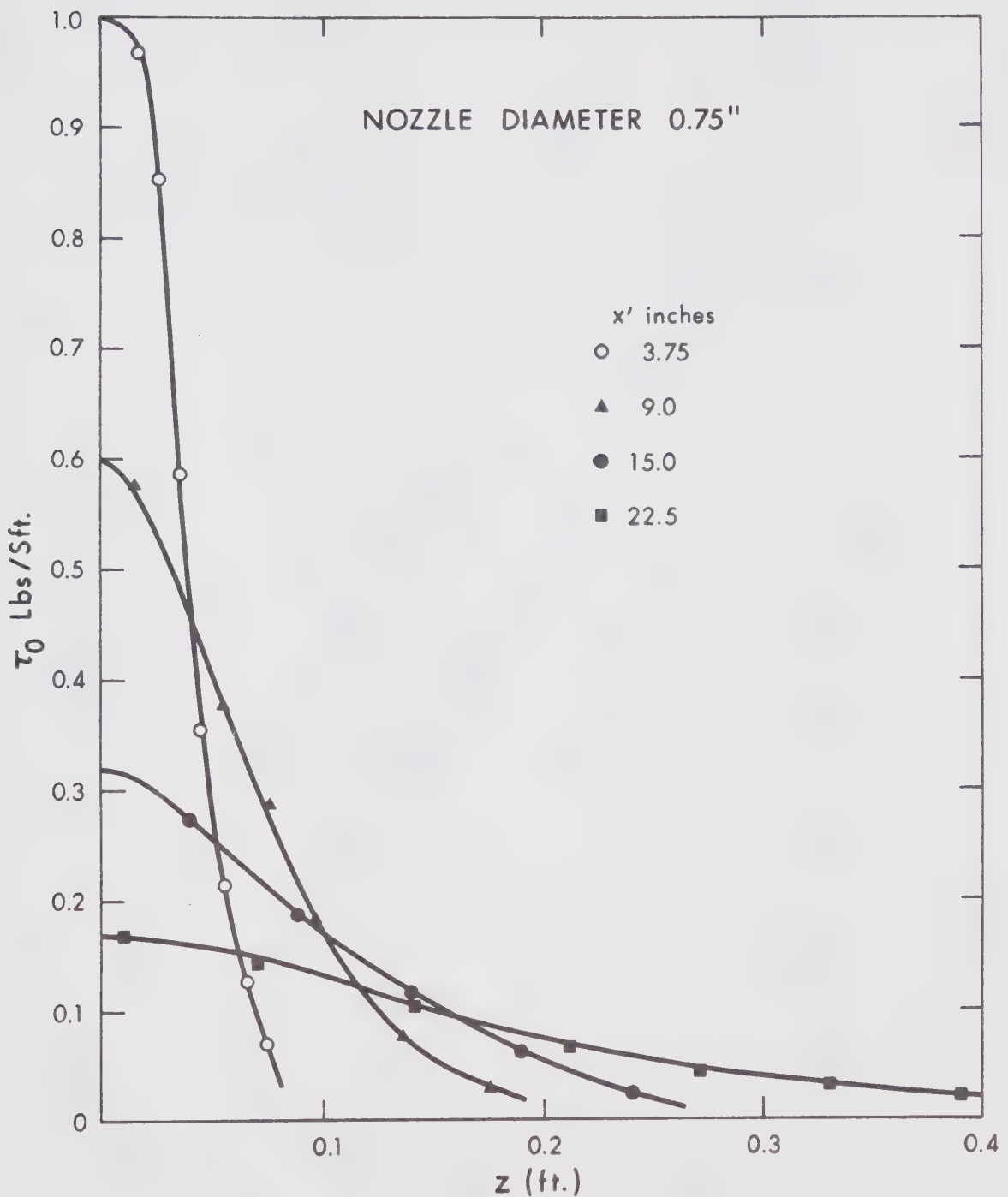


FIGURE 4.3 BED SHEAR DISTRIBUTION

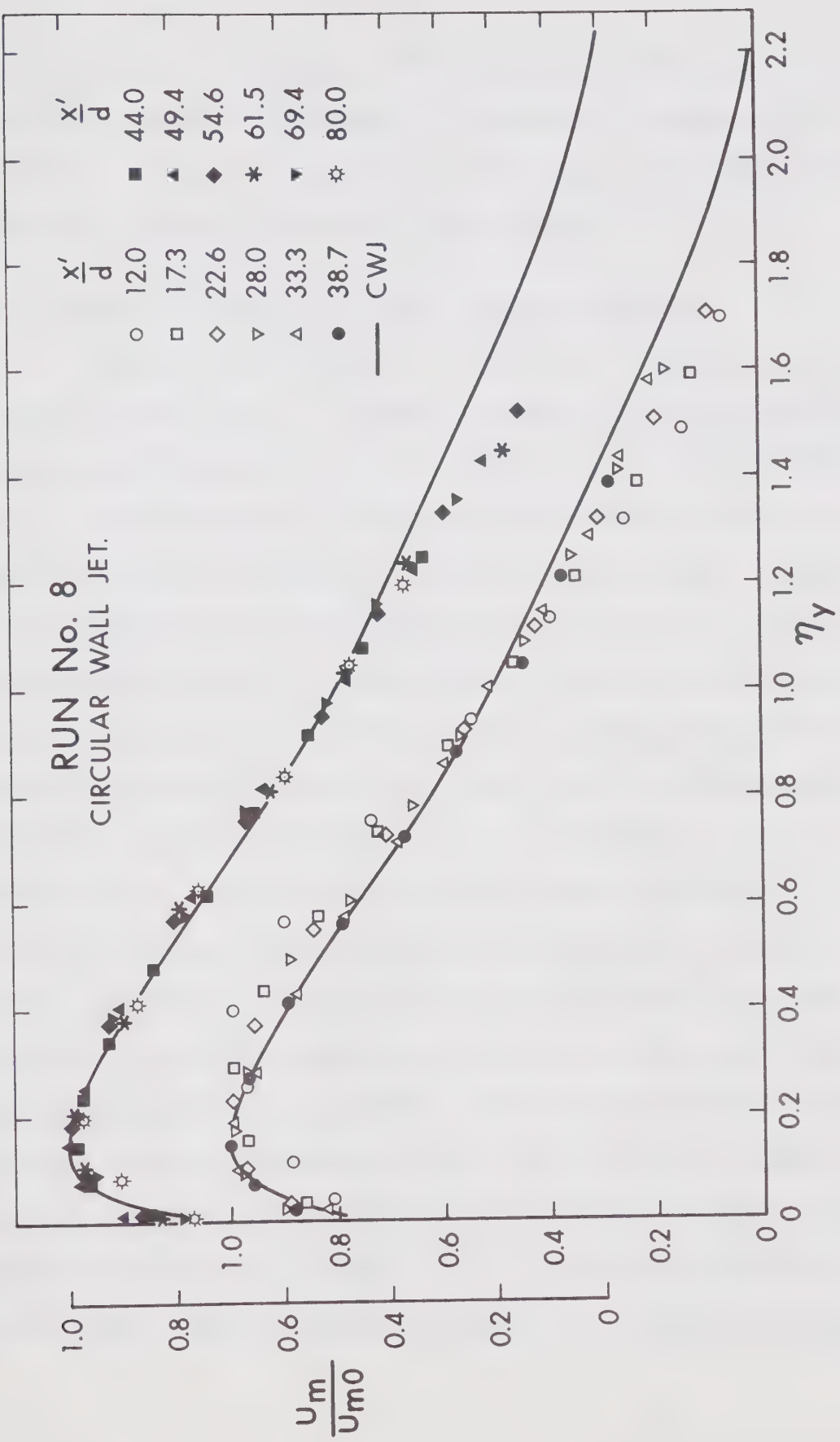


FIGURE 4.4 NON-DIMENSIONAL VELOCITY PROFILE NORMAL TO THE WALL.

is not adequate. For large x , this scatter gets small and for all practical purposes the CWJ curve is satisfactory over the entire thickness. Further it is seen that in all cases, the maximum velocity occurs at about 0.16 times b_y from the wall.

4.5.2 Velocity Distribution in the Transverse Planes

Consider the velocity profiles in any horizontal plane, at a height y from the wall. To check the similarity of these profiles, u/u_m was plotted against n_z for different x stations. It was found that the velocity profiles in the transverse plane were all similar beyond a distance of about 6 to 8 times the nozzle height. Further, the distributions in different planes parallel to the wall behave alike and are similar. A typical non-dimensional distribution is given in Figure 4.5. It can be seen that the data can very well be described by Goertler's curve for a free circular jet (Abramovich, 1963). Figure 4.5 also shows that for planes close to the wall, the scatter is small and as we go higher, the scatter becomes appreciable. This again is attributed to the inaccuracies in measurement of low velocities. The data for all the shapes investigated behave very much alike, which is rather remarkable, and curves for the various cases studied are presented in Appendix C. The data are also compared with Tollmien's solution (Abramovich, 1963) for a free axially symmetric jet and an exponential curve. From Figure 4.5, one can see the Goertler's curve to be in closest agreement with the present experiments and therefore the same curve would be adopted in all future considerations.

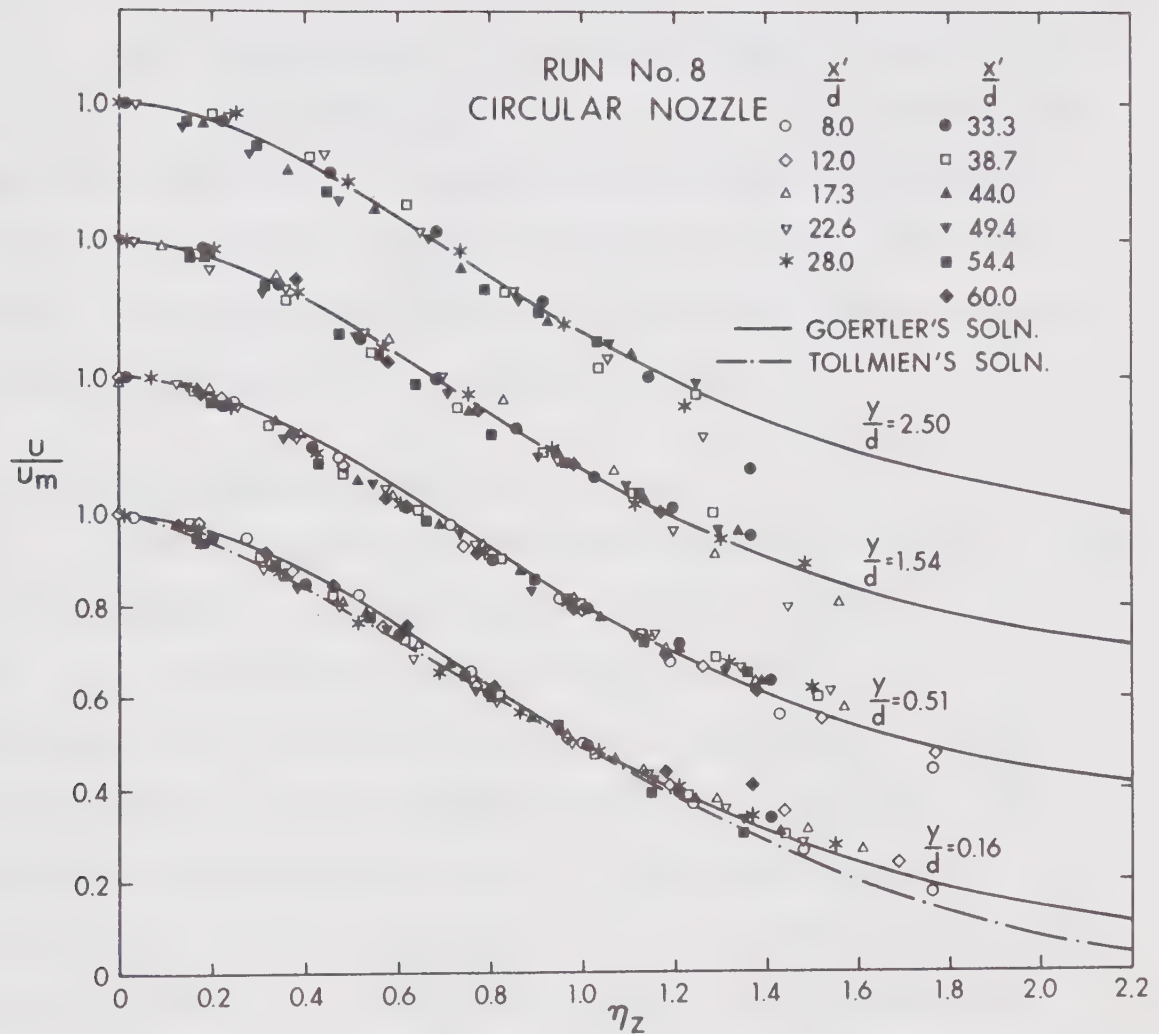


FIGURE 4.5 NON-DIMENSIONAL VELOCITY DISTRIBUTION IN z DIRECTION

Drawing isovels in a future section would need the coordinates of the classical wall jet and the Goertler's curve, which are therefore given in Table IV-2 for ready reference.

The irregularities in the transverse velocity profiles, reported by Sforza and Herbst (1967) for slender orifices could not be detected for these tests. The reason could be that in the present tests the aspect ratios were not too large so that the velocity dip caused by the induced velocities of the surrounding vortex ring would be small and undetected by the present apparatus.

4.5.3 Decay of Maximum Velocity

Before attempting to find the maximum velocity at any section which incidentally is also the velocity scale, an important aspect - the virtual origin should be considered. The virtual origin is a fictitious point at which the velocity of flow approaches infinity in order to maintain a finite momentum flux from a point source. To establish this hypothetical point, $1/u_{mo}$ is plotted against x'/h (or x'/d) as shown in Figure 4.6, where x' is the distance measured from the nozzle section. For test runs in series I, measurements were carried to limited distances of $x'/h \leq 64$ and the results indicate that the virtual origin could lie anywhere between 2 to 8 times the nozzle height downstream of the nozzle. As the velocity profiles should indeed approach similarity at very large distances from the nozzle, more extensive measurements were carried out in series II tests conducted in the wide flume for distances of $x'/h \leq 107$. This series of tests also eliminated the side wall effects inherent in narrow flumes. The

TABLE IV-2
COORDINATES OF THE SIMILARITY PROFILES

<u>Classical Wall Jet</u>		<u>Circular Free Jet (Goertler)</u>	
η	$f(\eta)$	η	$f(\eta)$
0.02	0.79	0	1.000
0.05	0.90	0.10	0.990
0.08	0.95	0.20	0.964
0.10	0.98	0.30	0.930
0.16	1.00	0.40	0.875
0.20	0.995	0.50	0.820
0.30	0.95	0.60	0.754
0.40	0.890	0.70	0.692
0.50	0.825	0.80	0.626
0.60	0.760	0.90	0.565
0.70	0.690	1.00	0.500
0.80	0.625	1.10	0.450
0.90	0.560	1.20	0.400
1.00	0.500	1.40	0.310
1.10	0.450	1.60	0.240
1.20	0.405	1.80	0.187
1.30	0.360	2.00	0.145
1.40	0.310	2.20	0.155
1.50	0.260	2.40	0.090
1.60	0.220		
1.70	0.170		
1.80	0.125		
1.9	0.085		
2.0	0.055		
2.2	0.005		

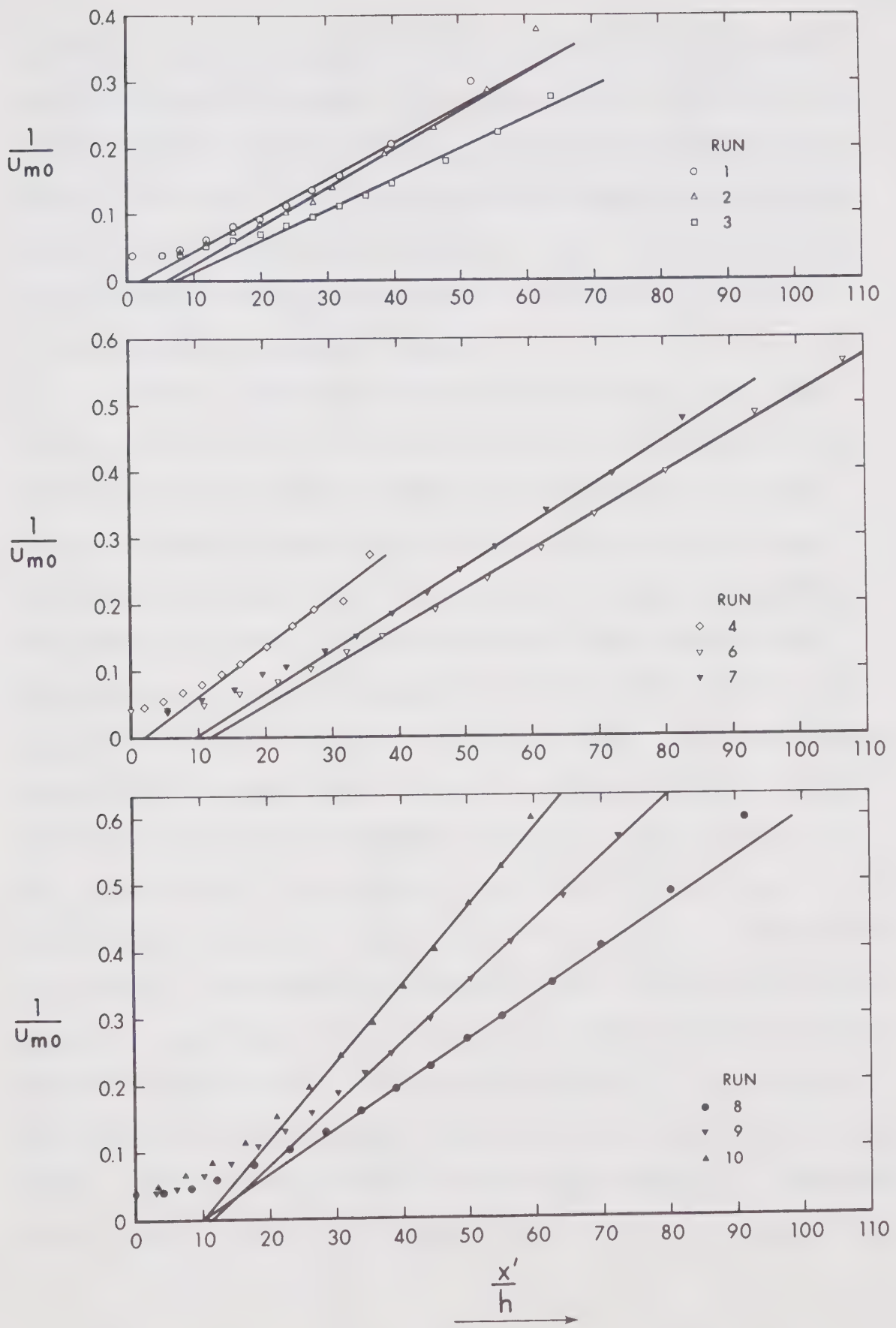


FIGURE 4.6 VIRTUAL ORIGIN (BASED ON VELOCITY SCALE)

results of the series II tests are also shown in Figure 4.6 and it can be seen that the virtual origin based on the far field data lies between 10 to 12 times the nozzle height downstream of the nozzle. Further, Figure 4.6 reveals that in the fully developed zone $u_{mo}^{\alpha x^{-1}}$, where x is the distance from the virtual origin. This relationship is in agreement with the one predicted from dimensional considerations and similarity analysis (Chapter II).

Often investigators do not take into account the virtual origin, which might be justified to the extent that it avoids introduction of another unknown variable - the location of the virtual origin. However, it would not be right to compare the experimental results with any theoretical law, unless the distances are measured from the virtual origin. Sforza and Herbst (1967) presented their data making no provision whatsoever for virtual origin and found that $u_{mo}^{\alpha(x')^{-1.1}}$ for all conventional orifices tested. The present results when plotted in a form similar to that of Sforza and Herbst, indicate that the exponent would lie between -1.14 and -1.20. The fact that the virtual origin is not located at the nozzle section is an inherent property observed in most jets of finite size. As its location can vary over a wide range, the exponent of the velocity decay law too would vary accordingly. This seems to explain the reason why different exponents are reported for different investigations. The location of the virtual origin would depend on the nozzle contraction and to a greater degree on the level of turbulence in the approaching flow. Information on this aspect of the wall jet seems to be nonexistent, although, some

experimental results for plane free jets are available (Flora and Goldschmidt, 1969).

From a practical point of view, it would be very useful to show the variation of u_{mo} with distance (x') measured from the nozzle section. In an attempt to establish a relationship which would in general be valid for any shape, u_{mo}/U_0 is plotted against x'/r' , where r' is the hydraulic radius of the wall jet, defined as the ratio of the nozzle area to the perimeter of the fluid boundary at the nozzle (Subramanya, 1967). The results are plotted in Figure 4.7 and it can be seen that some noticeable shape effect still exists. An examination of Eq. 2.56 suggests that if the streamwise distances are non-dimension- alised by a length parameter \sqrt{A} , where A is the area of cross-section of the nozzle, a unique relationship independent of the outlet shape should result. The experimental data are replotted in Figure 4.8 as u_{mo}/U_0 versus x'/\sqrt{A} and it can be seen that a single curve corre- lates the data extremely well. The curve is described by the follow- ing set of empirical relationships.

$$\frac{u_{mo}}{U_0} = 1.0 \quad 0 < \frac{x'}{\sqrt{A}} \leq 5.8$$

$$\frac{u_{mo}}{U_0} = 2.46 \left(\frac{x'}{\sqrt{A}} \right)^{-0.511} \quad 5.8 < \frac{x'}{\sqrt{A}} \leq 10 \quad (4.1)$$

$$\frac{u_{mo}}{U_0} = 4.14 \left(\frac{x'}{\sqrt{A}} \right)^{-0.735} \quad 10 < \frac{x'}{\sqrt{A}} \leq 22$$

$$\frac{u_{mo}}{U_0} = 16.4 \left(\frac{x'}{\sqrt{A}} \right)^{-1.18} \quad 22 < \frac{x'}{\sqrt{A}}$$

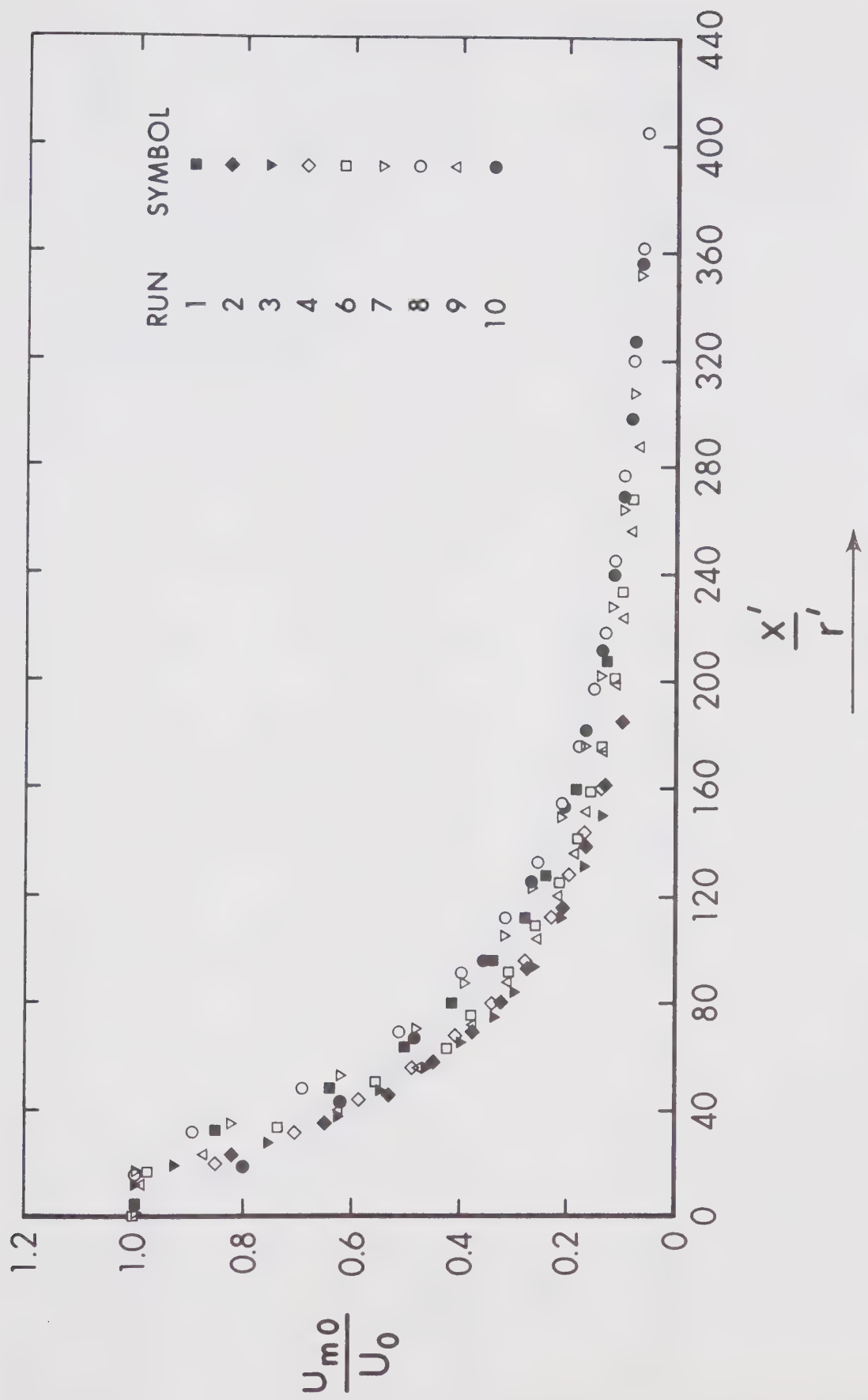


FIGURE 4.7 DECAY OF MAXIMUM VELOCITY ALONG THE CENTER-PLANE
(WITH HYDRAULIC RADIUS AS A PARAMETER)

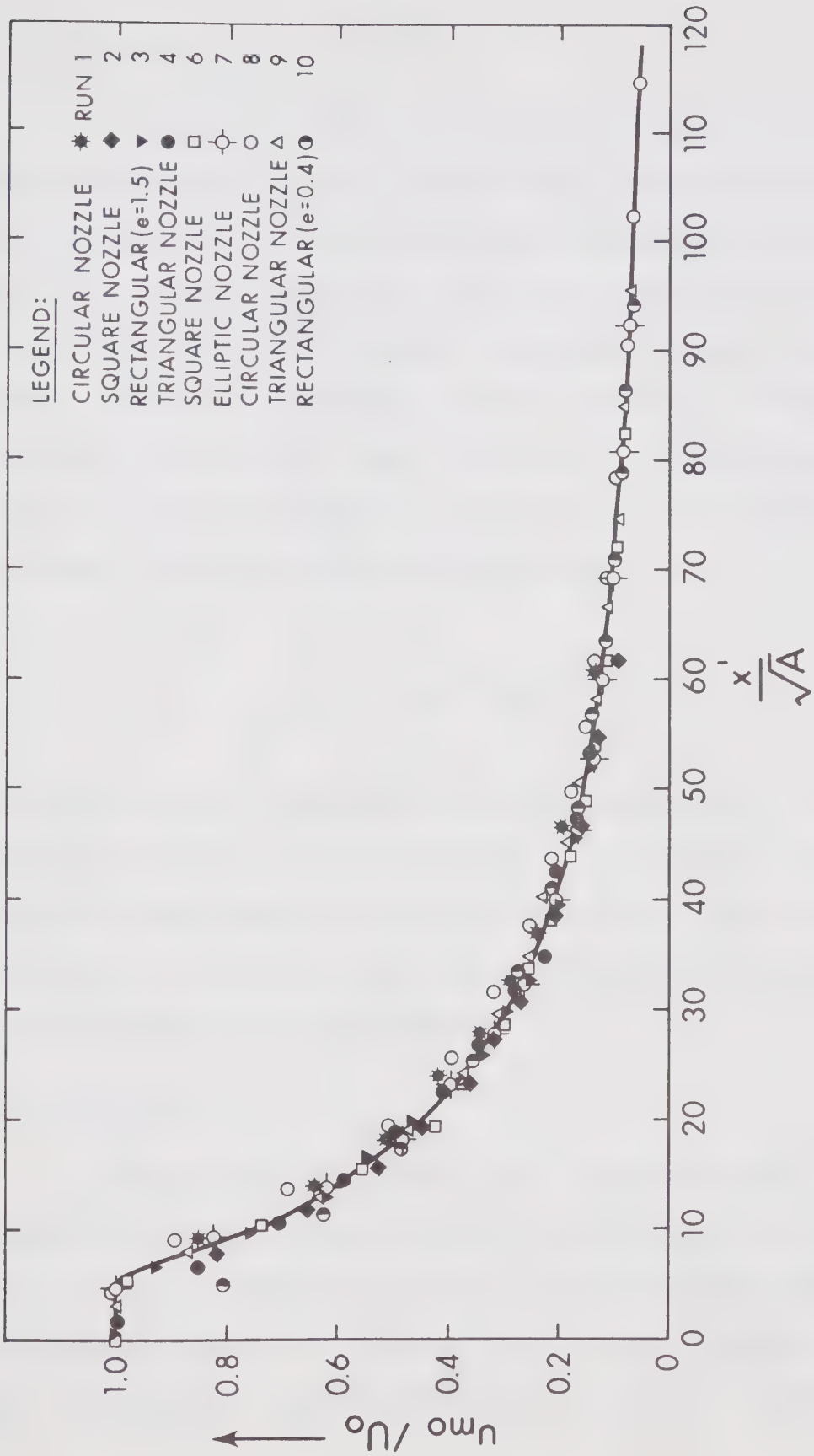


FIGURE 4.8 DECAY OF MAXIMUM VELOCITY ALONG THE CENTER-PLANE
(WITH THE SQUARE ROOT OF THE AREA OF THE NOZZLE AS A PARAMETER)

4.5.4 Length Scale b_y

The variation of the length scale is shown in Figure 4.9. For both series of tests, b_y grows linearly with the streamwise distance and is represented by a single relationship regardless of the nozzle shape. The virtual origin for b_y would be an imaginary point where it tends to be zero, and in general it would be different from the velocity virtual origin discussed earlier. The results indicate that the virtual origin for the normal length scale is located behind the outlet at a distance of about 20 times the height of the nozzle. The data shown in Figure 4.9 can be represented by,

$$\frac{b_y}{h} = 0.90 + 0.045 \frac{x'}{h} \quad (4.2)$$

This rate of growth is comparable with that of Newman et al. (1971), found for a circular wall jet with air as the test media. From Eq. 4.2, the rate of growth normal to the wall is seen to be almost half that of a free jet and is because of the boundary restraint on the growth of large size eddies normal to the wall.

4.5.5 Length Scale b_z

From the velocity profiles taken in any particular plane parallel to the bed, the length scale b_z was determined and its variation is given in Figure 4.10. A total of four different planes were considered and Figure 4.10 indicates that b_z grows linearly with x . This is particularly true for planes close to the wall. In addition,

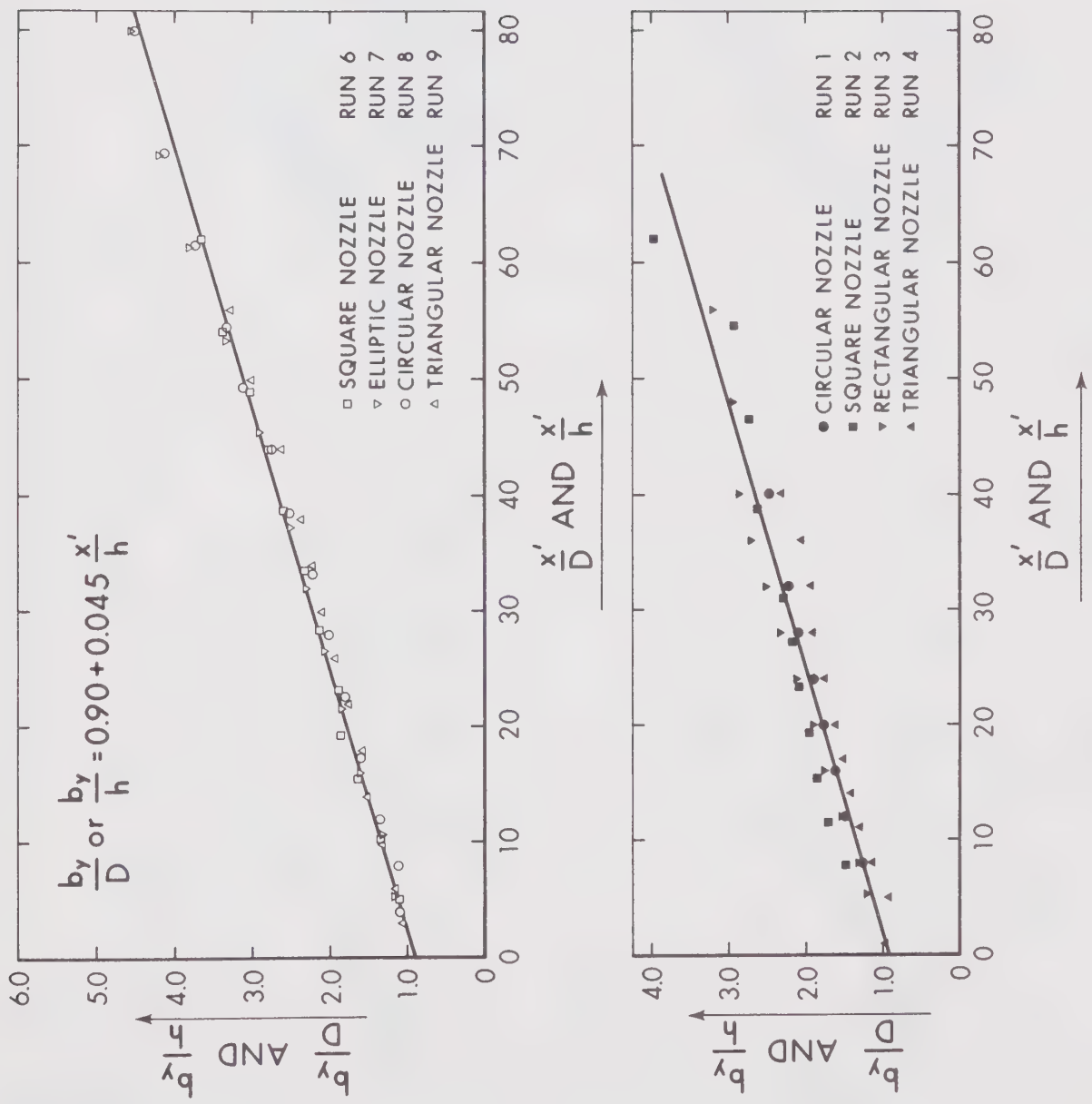


FIGURE 4.9 GROWTH OF LENGTH SCALE NORMAL TO THE WALL

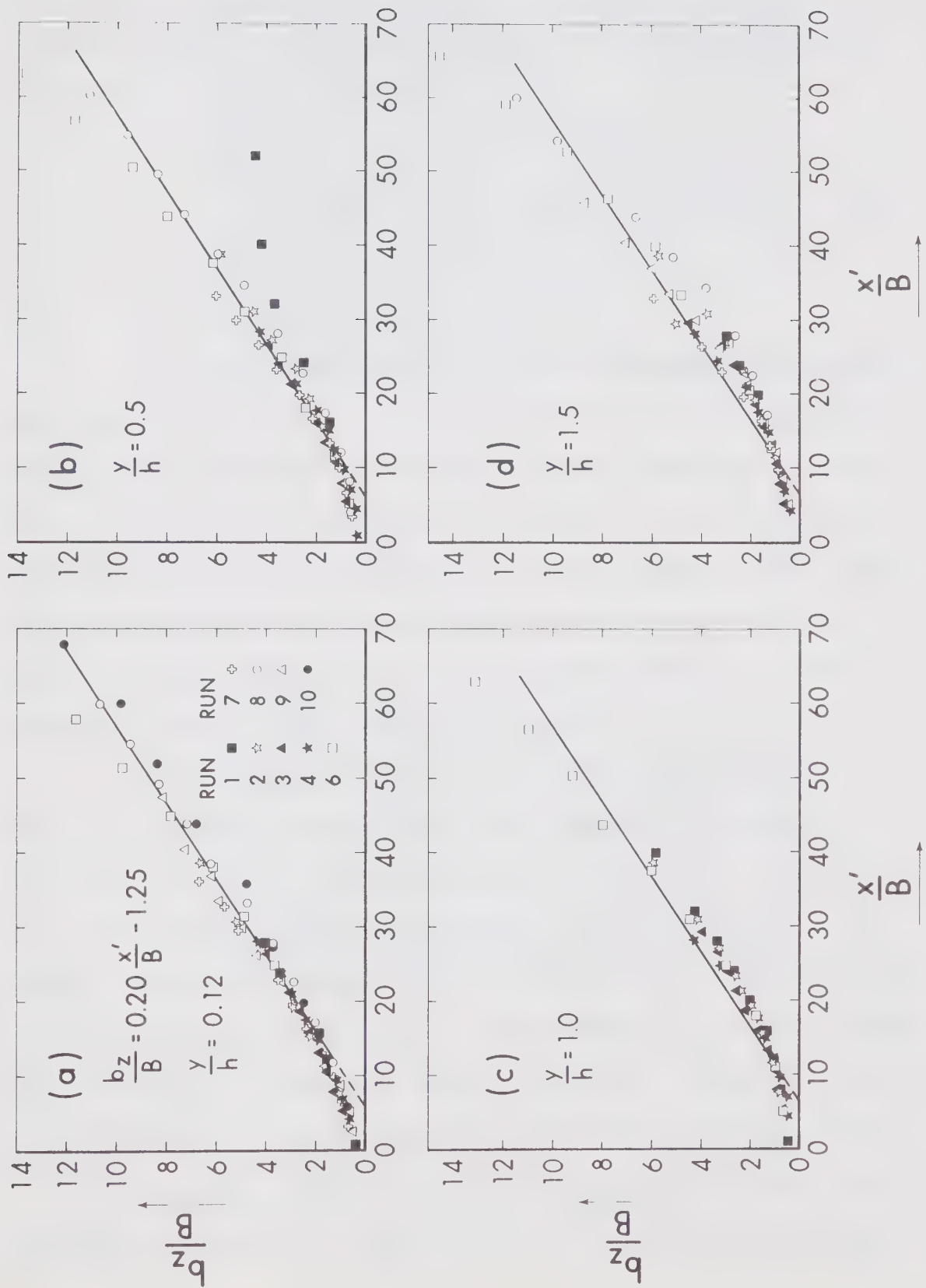


FIGURE 4.10 GROWTH OF TRANSVERSE LENGTH SCALE b_z

the virtual origin for b_z is located in the downstream direction at a distance of about 6 times the nozzle width. The straight line variation is represented by the equation,

$$\frac{b_z}{B} = 0.20 \frac{x'}{B} - 1.25 \quad (4.3)$$

where B = width of the nozzle.

The above expression describes the experimental observations reasonably well for $y/h = 0.5$, whereas for higher values of y/h there appears to be some departure from this. Thus, b_z depends on x as well as on y , although the y dependence is very weak. A high percentage of the total mass flow and momentum is contained within a small height from the bed, and therefore represents the zone of interest from a practical point of view. Hence, it is recommended that Eq. 4.3 be adopted to cover the whole range of y/h values.

It is important to note that b_z grows almost 4.5 times as fast as b_y . Further illustration of this aspect is in Figure 4.11, which was obtained by injecting dye into the main stream. Newman et al. (1971) have also indicated this peculiarity for an air jet, the growth rates being comparable with the present values. For the series II tests, the water is recirculated and eliminates any possible temperature difference and consequent density differences. Therefore, the observed difference in growth rates of b_y and b_z are attributed to the effect of the wall. The data from series I and II are in good agreement, giving an indirect indication that there was not any accountable



(a)



(b)

FIGURE 4.11 GROWTH OF THE JET: (a) ALONG THE TRANSVERSE DIRECTION; (b) NORMAL TO THE WALL

temperature difference for the first series of tests as well.

4.5.6 Isovols

In the earlier discussions, the form of the functional relations f_1 and g_1 were found to agree closely with the classical wall jet and the Goertler's curve respectively. From an examination of Eq. 2.9, one can see that, u/u_{mo} could be represented as a function of η_y and η_z and would be independent of x coordinate. From the coordinates of f_1 and g_1 given in Table IV-2, u/u_{mo} at a number of grid points were established. Isovols or lines of constant u/u_{mo} were drawn by interpolation, and the resulting curves are given in Figure 4.12. If a region near the wall is neglected, the isovols could be approximated by ellipses. This type of behaviour has been noticed earlier by Trentacoste and Sforza (1967) for three dimensional free jets.

4.5.7 Centerline Boundary Shear

The jet Reynolds number defined as $U_0 / A/v$ is generally large for most cases encountered in practice. Hence, the right hand side of Eq. 2.63 can approximately be considered as a constant quantity. Combining Eq. 2.63 and Eq. 2.56, it can be shown that $\tau_{om}/\rho u_{mo}^2/2$ is a constant for the fully developed flow region. The same conclusion can also be arrived at from a different type of analysis presented by Sforza and Herbst (1967). On the assumption that the bed shear distribution in the transverse direction was similar, they derived an expression for the skin friction from the equations of motion as,

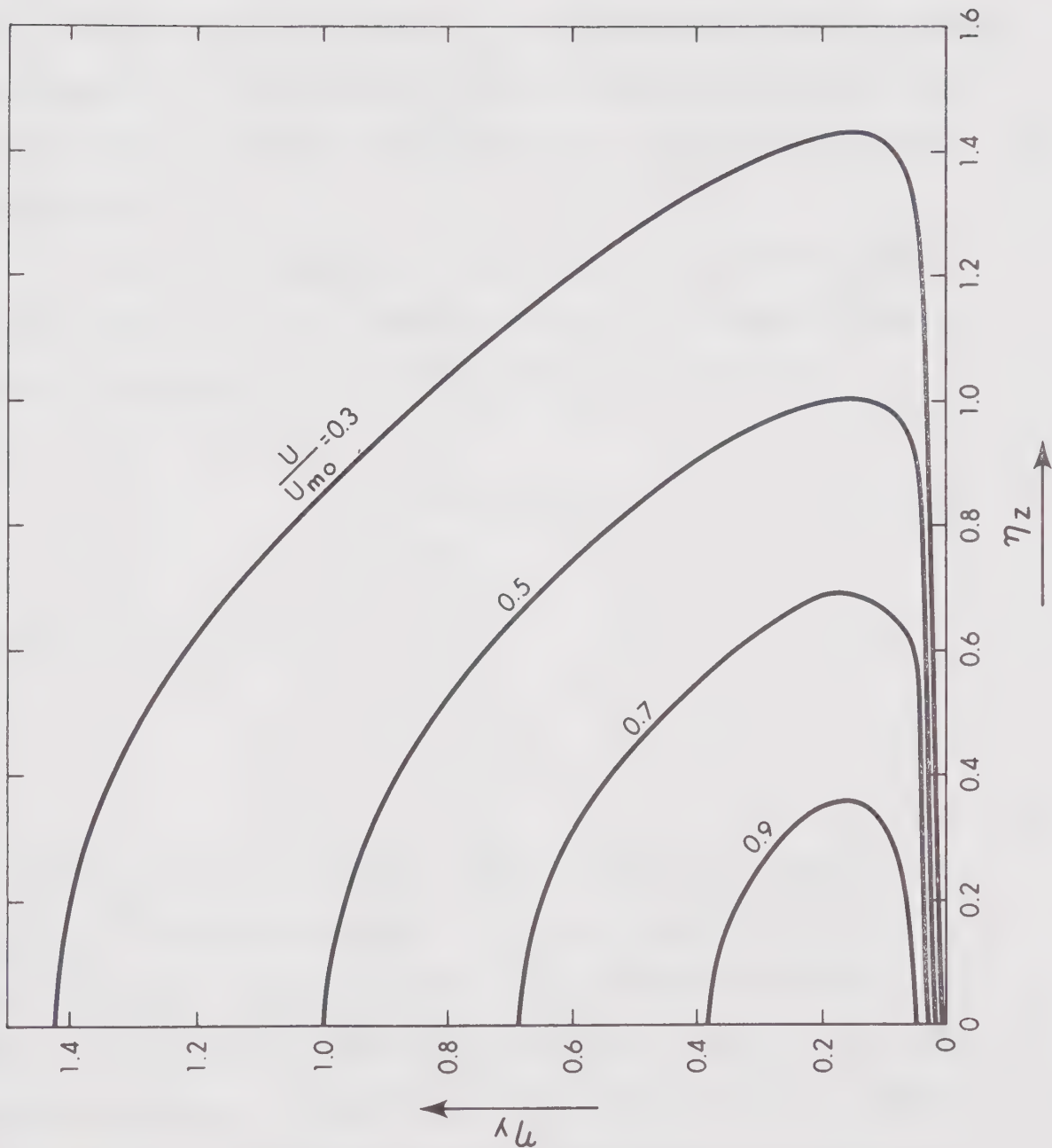


FIGURE 4.12 ISOVELS IN THE FULLY-DEVELOPED REGION

$$\frac{\tau_{om}}{\frac{1}{2} \rho u_{mo}^2} = K \frac{b_y}{x} \sim Kx^{q_1-1} \quad (4.4)$$

where, K is an empirical constant, q_1 is the exponent in the x^{-b_y} growth relationship. At large distances from the nozzle, q_1 approaches unity, and hence the skin friction coefficient in eq. 4.4 tends to attain a constant value.

Figure 4.13 presents the experimental data for the various shapes studied. For x'/\sqrt{A} greater than 50, for the range of Reynolds numbers investigated, the following is seen to be satisfied.

$$\frac{\tau_{om}}{\frac{1}{2} \rho u_{mo}^2} \approx 0.0065 \quad (4.5)$$

Hence, in this region

$$\tau_{om} \propto \frac{1}{x} \quad (4.6)$$

A more convenient type of plot is shown in Figure 4.14 in which $\tau_{om}/\frac{1}{2} \rho u_0^2$ is plotted against x'/\sqrt{A} , and a single curve is easily drawn through all data points. This plot is believed to be more useful as it avoids the virtual origin, and gives a clearer picture about the absolute values of shear stress close to the nozzle. In effect, the area close to the nozzle would need more elaborate consideration for protection against scour, since the intensity of shear stress drops

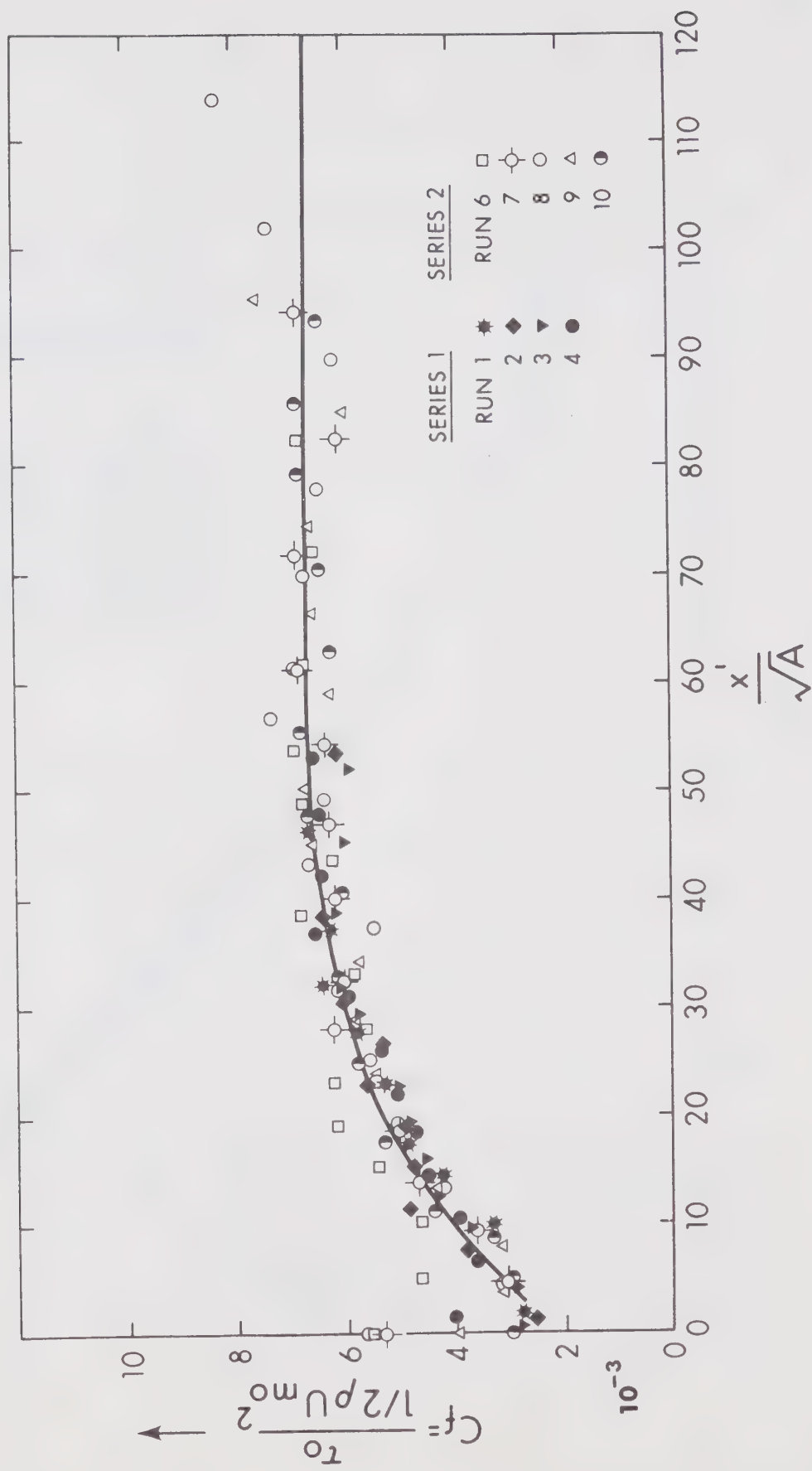


FIGURE 4.13 BED SHEAR STRESS ALONG THE CENTER-PLANE

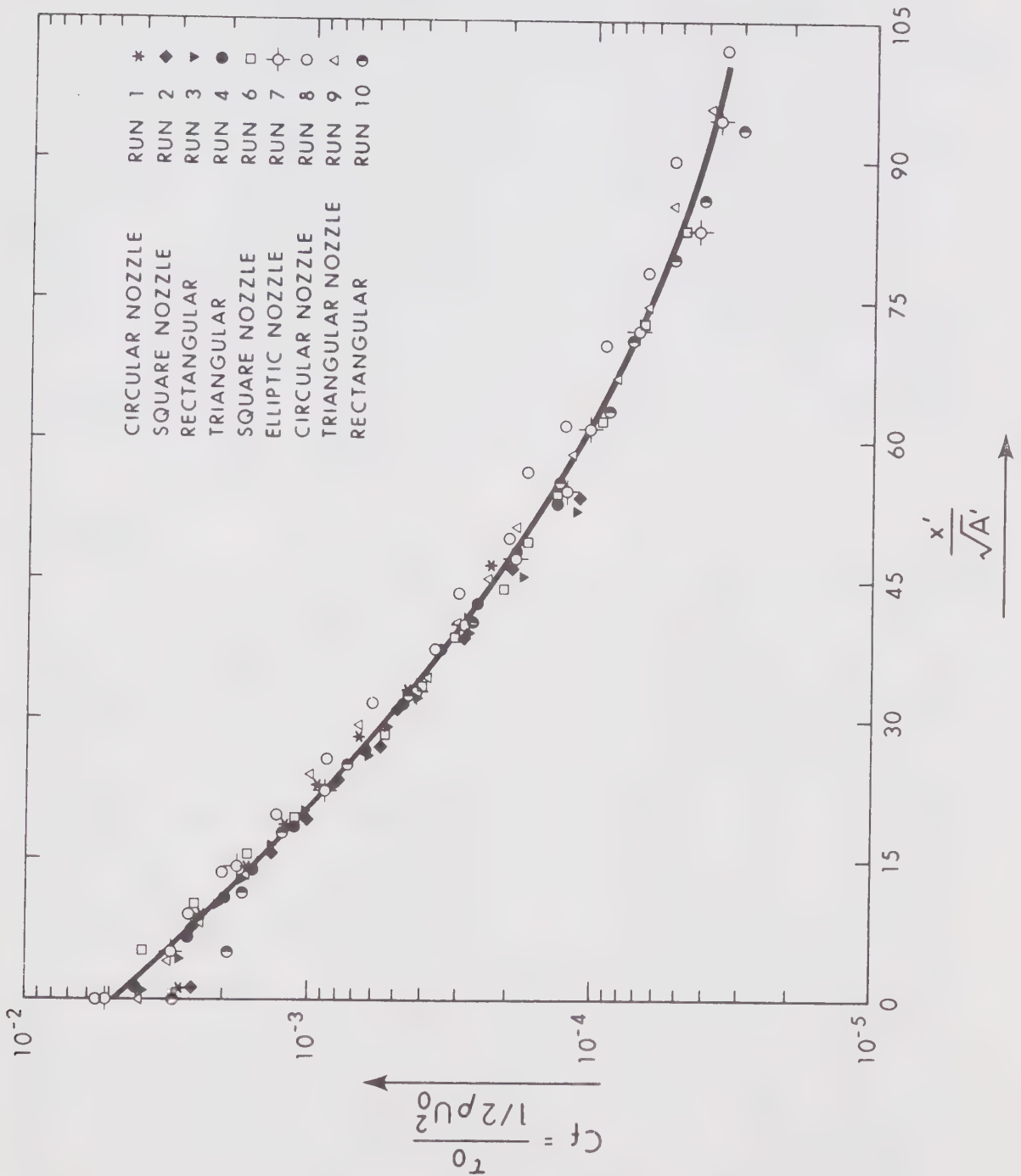


FIGURE 4.14 BED SHEAR DISTRIBUTION ALONG THE CENTER-PLANE
(ALTERNATE PLOT)

very quickly in a short distance.

4.5.8 Off-Center Boundary Shear Distribution

The distribution of the x component of boundary shear stress in the transverse direction is shown in Figure 4.3, and is for a circular nozzle 0.75" in diameter. The measurements were conducted during investigation on swirling jets and detailed discussions are presented in Chapter VII. At this stage it would suffice to say that, the distribution is similar beyond a distance of 12 times the nozzle height and is very well described by Goertler's velocity distribution curve. The length scale for shear distribution b_τ equals z at which the shear stress is $\tau_{om}/2$ and is found to vary linearly with x' .

4.6 Summary

From experimental observations on wall jets of various shapes, the velocity distribution normal to the wall and along the centerline was found to be similar and closely approximated by the classical wall jet curve. The velocity distribution in transverse directions was also found to be similar and agreed with Goertler's curve for a free circular jet. The maximum velocity at any section in the fully developed zone was inversely proportional to the distance measured from the virtual origin. This is in accordance with the theoretical predictions. However, to avoid the trouble of locating the virtual origin, an empirical curve was presented to predict u_{mo} . This curve seems to be independent of the nozzle shape, if \sqrt{A} is selected as a characteristic parameter to non-dimensionalise the distance from

the nozzle. The length scales b_y and b_z grow linearly, but at different rates. The virtual origin for the velocity scale and the two length scales were located at widely varying distances from the nozzle, which upsets any plan of comparison between theory and experiment. The distribution of boundary shear stress in the transverse direction was similar and followed the Goertler's velocity distribution curve. The centerline boundary shear coefficient defined by $\tau_{om}/\frac{1}{2} \rho u_{mo}^2$ was found to be a constant, and is around 0.0065. Convenient plots for estimating the centerline shear in terms of the nozzle efflux velocity U_0 is presented, giving a clear picture about the shear stress decay.

CHAPTER V

EFFECT OF SIDE WALLS5.1 Introduction

The case of a three dimensional wall jet growing in an infinitely wide channel is highly idealised and in most practical problems the channel is of finite width and the side walls would in some way or other affect the jet characteristics. This chapter presents an experimental study on the diffusion of a jet issuing from a circular outlet located symmetrically at the center of channels having finite widths. The bed and side walls were all smooth.

Consider the case of a circular jet of uniform velocity U_0 issuing tangentially on the bed of a channel of width W , with the tail-water depth sufficiently large so as to keep the outlet deeply submerged. On leaving the nozzle the jet expands, as in the case of a very wide channel, and depending on the width of channel the expanding jet would soon strike the side walls at some distance from the outlet. This would inhibit the transverse growth and consequently the decay of the maximum velocity. At the present time, there seems to be no information available on this aspect. Abramovich (1963) mentions about the diffusion of a free jet in a finite space, which occurs in the case of an ejector. He finds that the process of equalization of flow parameters in a cylindrical mixing chamber occurs in such a manner

that the velocity field at each of its cross-sections appears as if it were the central part, bounded by the cylindrical walls of the chamber of the universal function, which expresses the dimensionless velocity field at the corresponding cross-section of a free jet. However, the flow field is significantly changed, as eddies form and result in backflow near the solid boundary. Apparently, it would be desirable to examine the present data on a wall jet, and see to what extent its behaviour would be comparable with the free jet.

Some data on the diffusion of three dimensional jets in channels of finite width are available (Subramanya, 1967) for comparison with the present results.

5.2 Experiments

A circular nozzle 0.375" in diameter was used in channels having different widths. The bed was a smooth galvenised iron sheet and the sides were fabricated from smooth painted plywood boards, the distance of which could be varied from 5.35 to 18.7 times the nozzle diameter. These channels of required width were stationed in flume 2 and the bed elevation was adjusted to get a tangentially flowing jet. The velocity field was explored with the 0.05" diameter total head tube. The static pressures were measured by a Pitot-static tube located close to the total head probe. No pressure traverse was made normal to the wall and it was assumed that the pressure distribution is hydrostatic. The same total head tube was used to measure the boundary shear.

5.3 Results

5.3.1 Decay of Maximum Velocity

The maximum velocity at any section occurred on the center-line and its variation is shown in Figure 5.1 as $1/u_{mo}$ vs. x'/d . It is seen that $1/u_{mo}$ varies linearly with the distance, for x'/d less than about 35. Moreover, the efflux velocity being the same for all these runs, from Figure 5.1, it can be said that the velocity decay law is the same in this zone irrespective of the channel width. It is to be noted that this linear law near the outlet is different from the one derived for x'/d greater than 35, in case of a very wide channel. For x'/d greater than 35, the channel width appears as a governing parameter and the velocity decay follows different laws.

For better comparison, the data are plotted with u_{mo}/U_0 versus x'/\sqrt{A} in Figure 5.2a. For values of x'/\sqrt{A} less than about 45 (which also corresponds to $x'/d \approx 35$) the relationship is independent of the channel dimension. It is also interesting to note that the data of Subramanya (1967) on rectangular three dimensional wall jets of different aspect ratios (in the range of 0.94 to 3.7), issuing into channels of finite but different widths, follow closely the mean curve of the present investigation (Figure 5.2b). His observations were limited to $x'/\sqrt{A} \leq 27$, on the basis of which he concluded that the relative width of the channel does not appreciably affect the velocity decay. This is in accordance with the present observations on a circular jet. However, at large distances from the nozzle the entire flow would be in the forward direction and tend to behave as

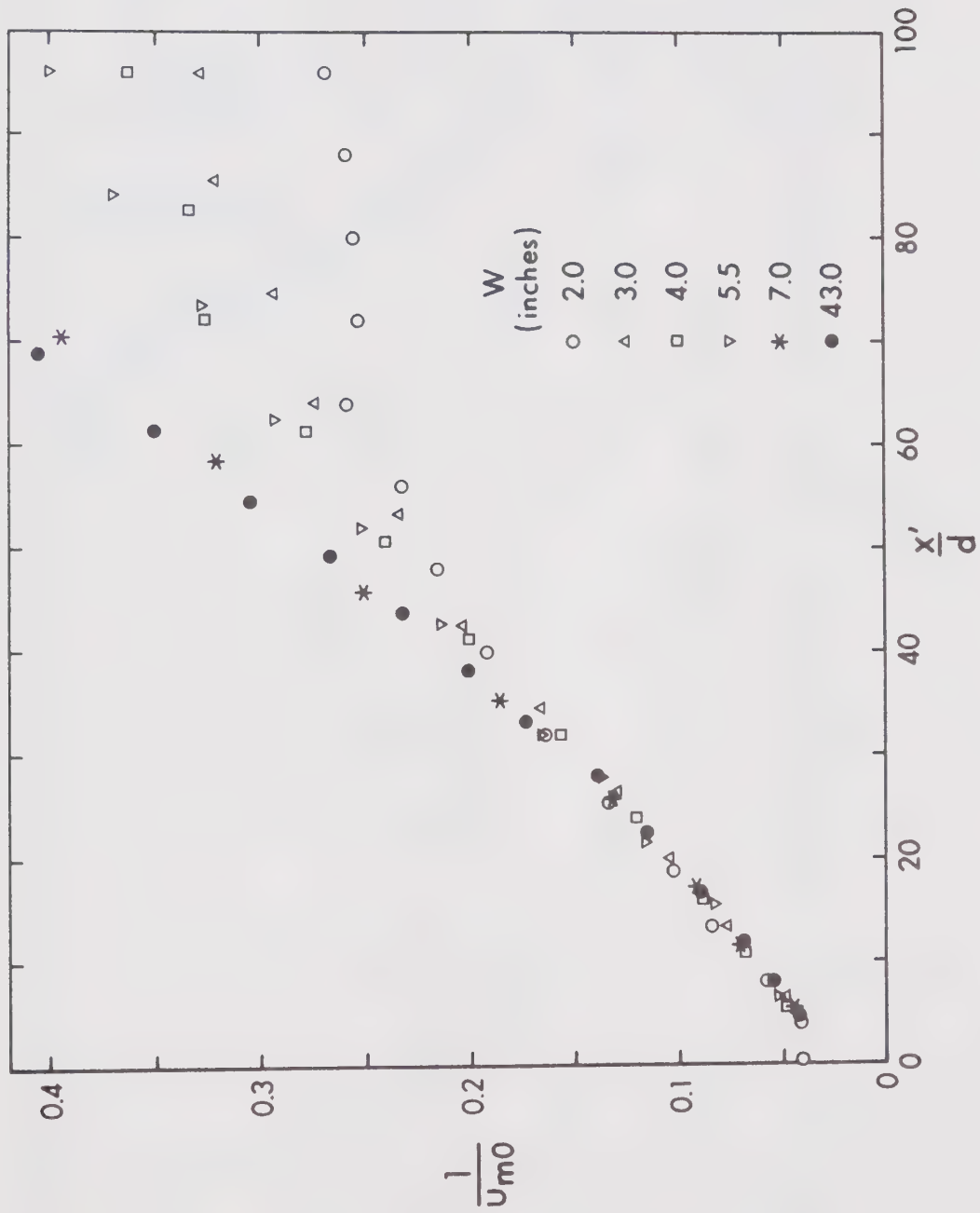


FIGURE 5.1 VIRTUAL ORIGIN FOR JETS IN FINITE WIDTH CHANNELS
(BASED ON VELOCITY SCALE)

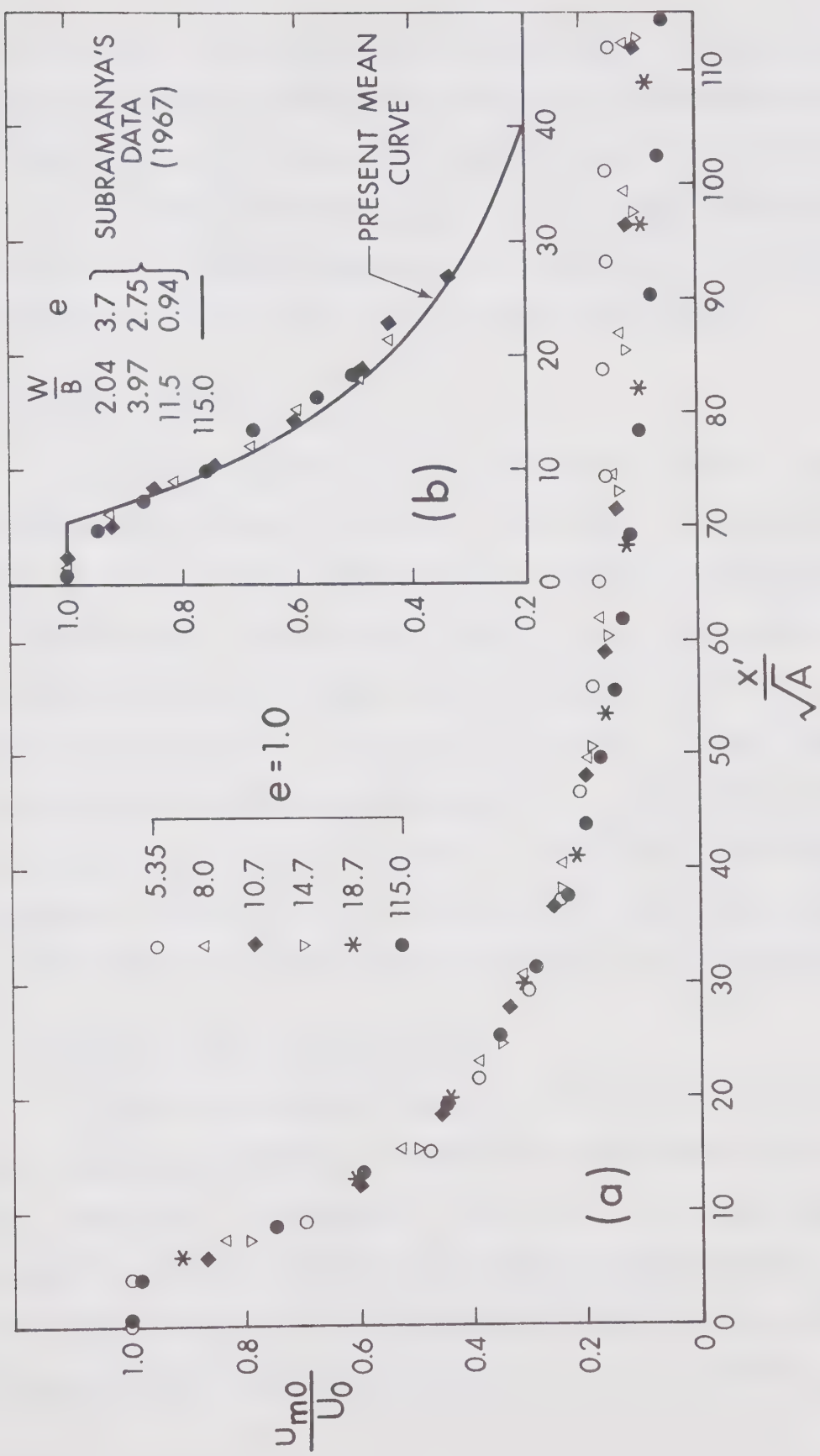


FIGURE 5.2 JET VELOCITY DECAY IN CHANNELS OF FINITE WIDTH

an open channel. This would mean that the maximum velocity at any section would tend to attain a constant value. This trend can be seen in Figure 5.2a, and is particularly clear for the narrowest channel studied. The higher values of u_{mo}/U_0 is also evident from the fact that the supply discharge remains same for all tests and therefore narrower channels will have a higher forward flow velocity.

5.3.2 Length Scale b_y

The length scale found from the velocity profiles taken along the centerline is given in Figure 5.3. Here again, the variation is linear for x'/d less than about 35 and is practically independent of the channel width. The specified limit for $x'/d = 35$ increases with an increase in the width, beyond which the growth rate is very fast and the change is abrupt. In the first instance, this was thought to be caused by the adverse pressure gradients. The measured water surface profiles are given in Figure 5.4, and as such the effect of the adverse gradient should not be felt for x'/d less than 60 to 70. No other suitable explanation could be offered for this peculiarity.

5.3.3 Velocity Profile Normal to Bed

The profiles taken along the centerline in a normal direction were checked for similarity by plotting the conventional quantities, u_m/u_{mo} versus y/b_y , in Figure 5.5. The scatter in the data was large and the velocity distributions in the narrow channels were not similar. As the channel gets wider, the distribution tends to follow the classical wall jet profile. This is seen from the tests on the channel having

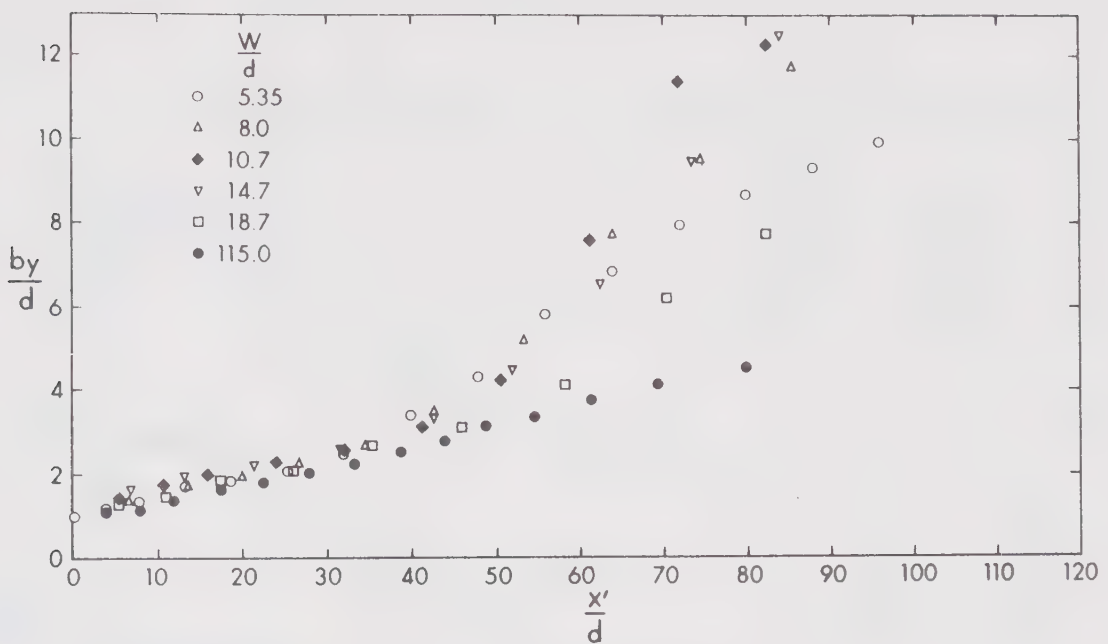


FIGURE 5.3 GROWTH OF LENGTH SCALE b_y

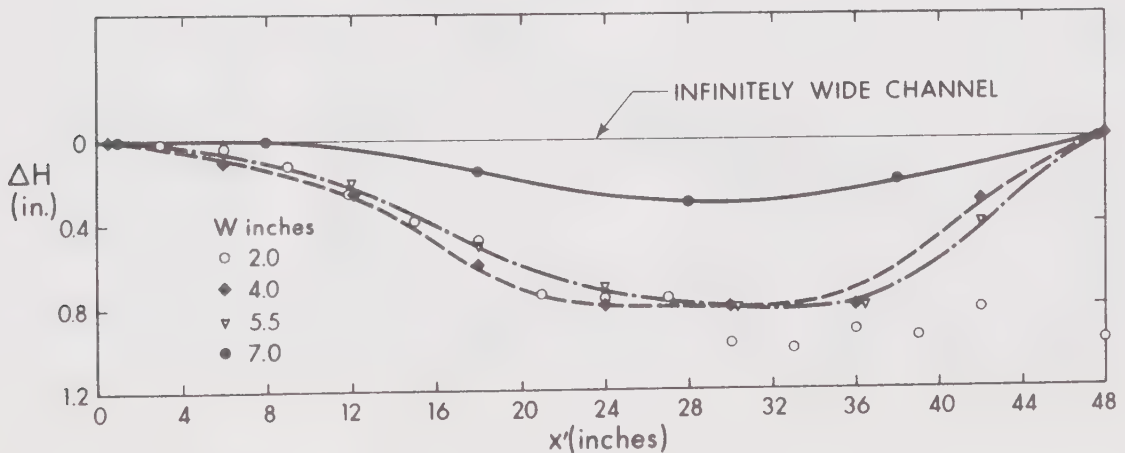


FIGURE 5.4 WATER SURFACE PROFILE

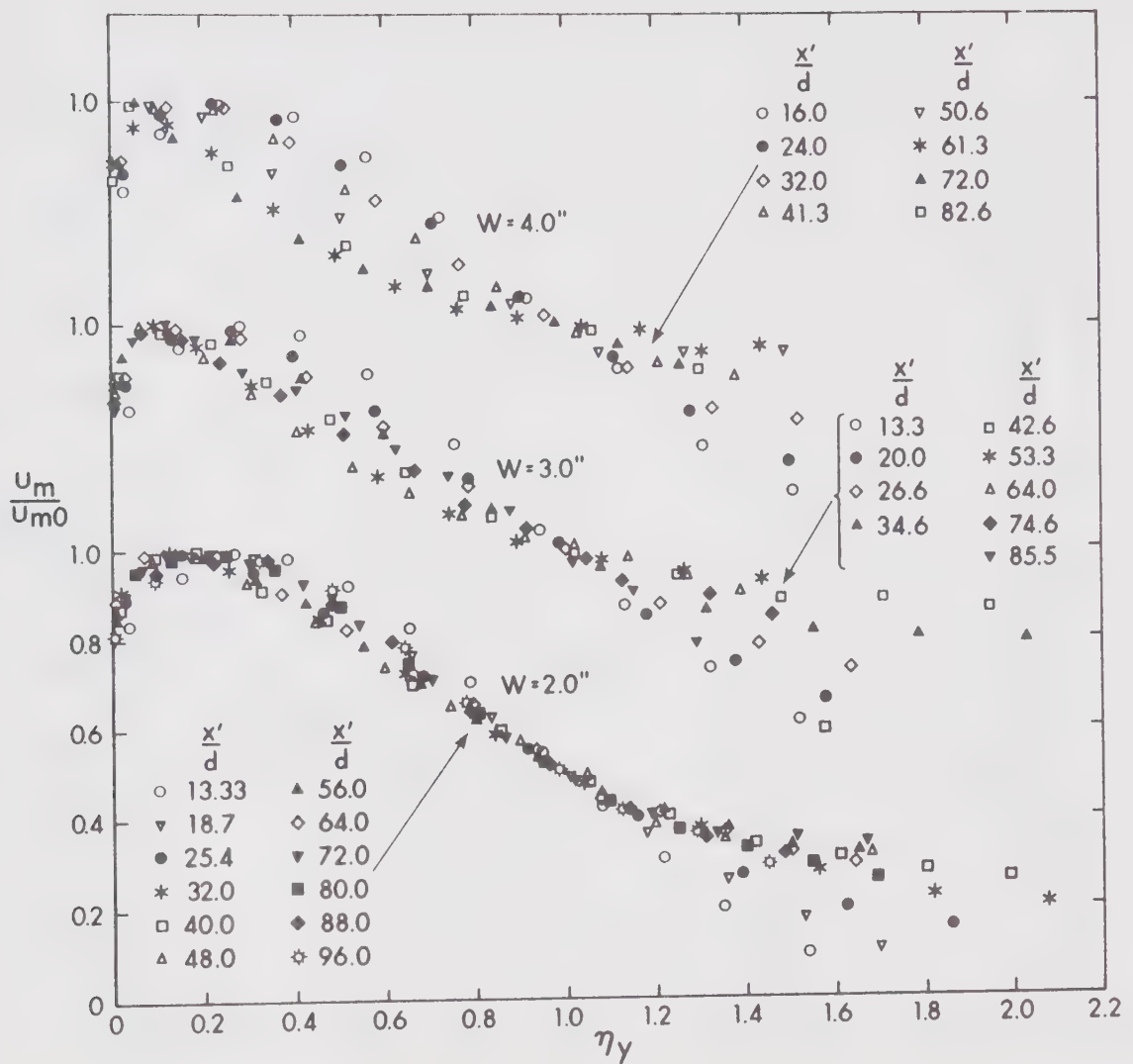


FIGURE 5.5 NON-DIMENSIONAL VELOCITY DISTRIBUTION NORMAL TO THE WALL
(CENTER-PLANE OF CHANNELS)

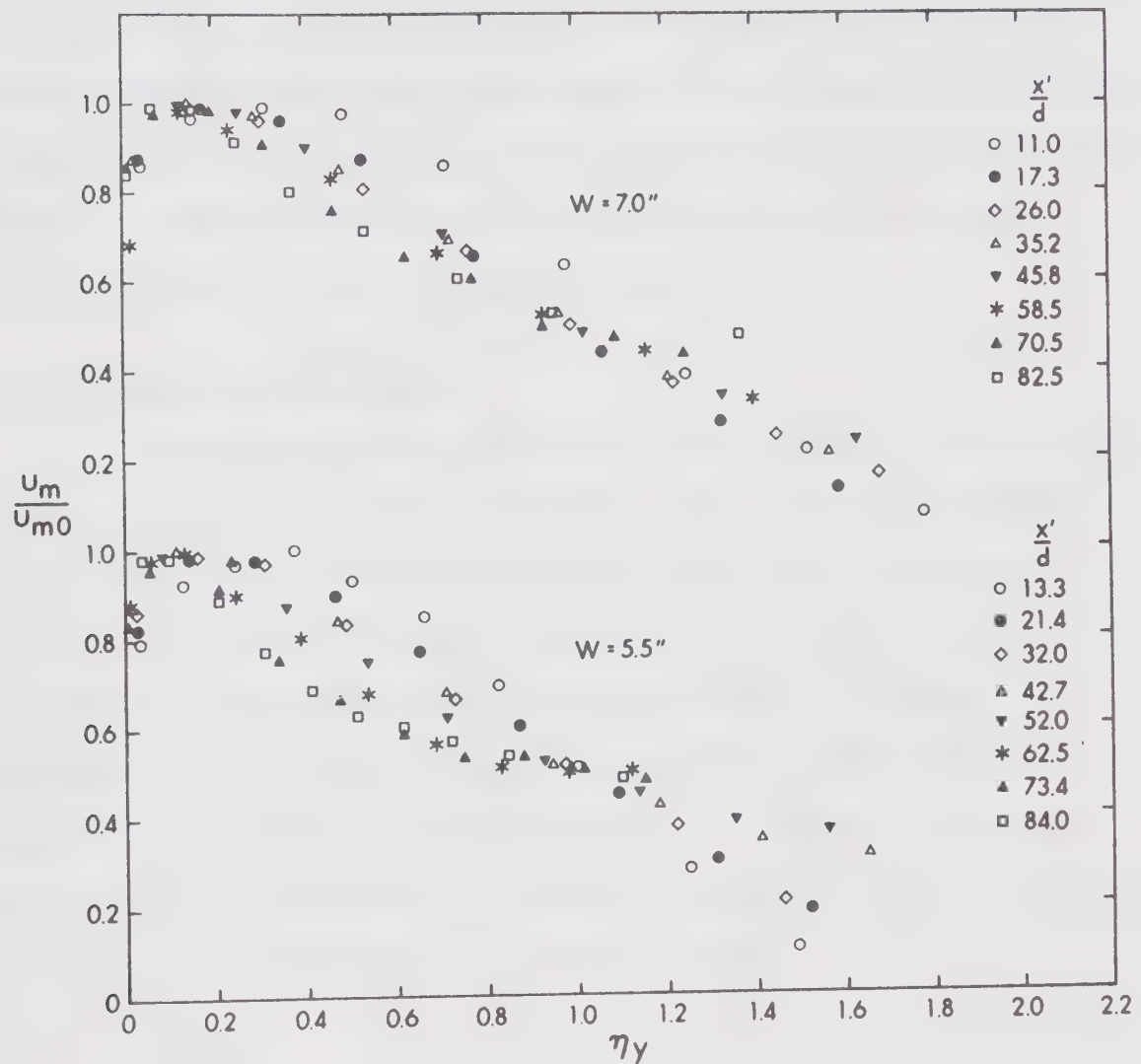


FIGURE 5.5 (CONTINUED)

$W/d = 18.7$, which is the maximum width in this series. It is hard to demarcate precisely the limiting value of W/d beyond which the velocity profiles could be considered as similar. However, for the tests conducted in flume 1 while investigating other aspects of the jet, the velocity profiles were found to be similar, the corresponding W/d value being around 33. Therefore, as a rough guide a limiting value of 30 is suggested, beyond which the results presented for a jet in a wide channel (Chapter IV) could be applied successfully.

5.3.4 Transverse Distribution

Some velocity measurements were taken in the $x-z$ plane lying close to the bed. At a short distance of $5.3d$, the velocity profiles look similar to the one found for a wide channel, but soon the entire width is occupied by the forward flow and the half-width could not be estimated, as a result of near uniform distribution of velocity. Measurements at a distance of about $35d$, for the 2" wide channel for example, show a transverse distribution that is uniform, and the same characteristic is observed for any section beyond this limit. In general all the widths tested behave in a similar fashion.

5.3.5 Bed Shear

The bed shear stress along the center of the channel was measured by the Preston tube technique. From velocity measurements taken close to the wall, and the shear estimated by a Preston tube, a check was made on the validity of the wall-law. The logarithmic law was found to be reasonably satisfied for all the tests and therefore

the shear measurement technique is satisfactory for narrow channels as well.

The variation of the local skin friction coefficient is shown in Figure 5.6. The results are compared with the mean curve for three dimensional jets on smooth beds in wide channels. The agreement looks fair for x'/\sqrt{A} less than seventy five. Beyond this distance, c_f drops from the constant value of 0.0065 and it is suspected that the adverse pressure gradient acting in this zone causes this.

Same experimental data are presented by defining a skin friction coefficient in terms of the nozzle efflux velocity, and this alternate plot is shown in Figure 5.7. For x'/\sqrt{A} greater than about 40, the coefficient is much higher for the channels having finite width. This would mean that, under identical efflux conditions of the nozzle, the centerline bed shear is higher when discharging into finite width channels. As the channel gets narrower, the shear intensity increases. As an example, for the channel having $W/d = 5.35$, the intensity of bed shear at a reference section of $x'/\sqrt{A} = 100$ is around four times larger than the corresponding value for the wide channel case.

5.4 Summary

In a certain initial reach, the velocity decay and b_y growth relations do not get affected by the channel dimensions. For narrow channels the maximum velocity along the centerline tends to attain a constant value, higher than what would be if it were to diffuse in an

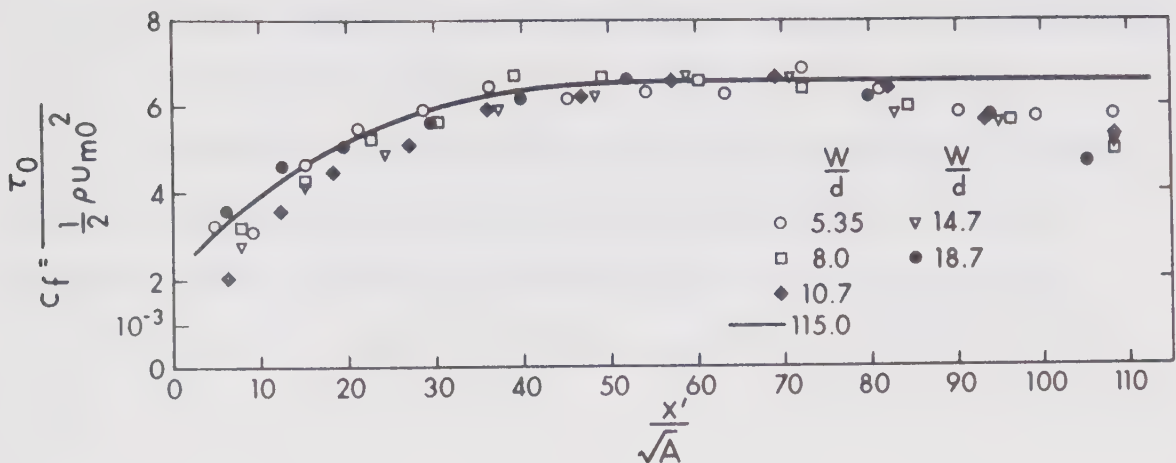


FIGURE 5.6 SKIN FRICTION COEFFICIENT (ALONG THE CENTER-PLANE)

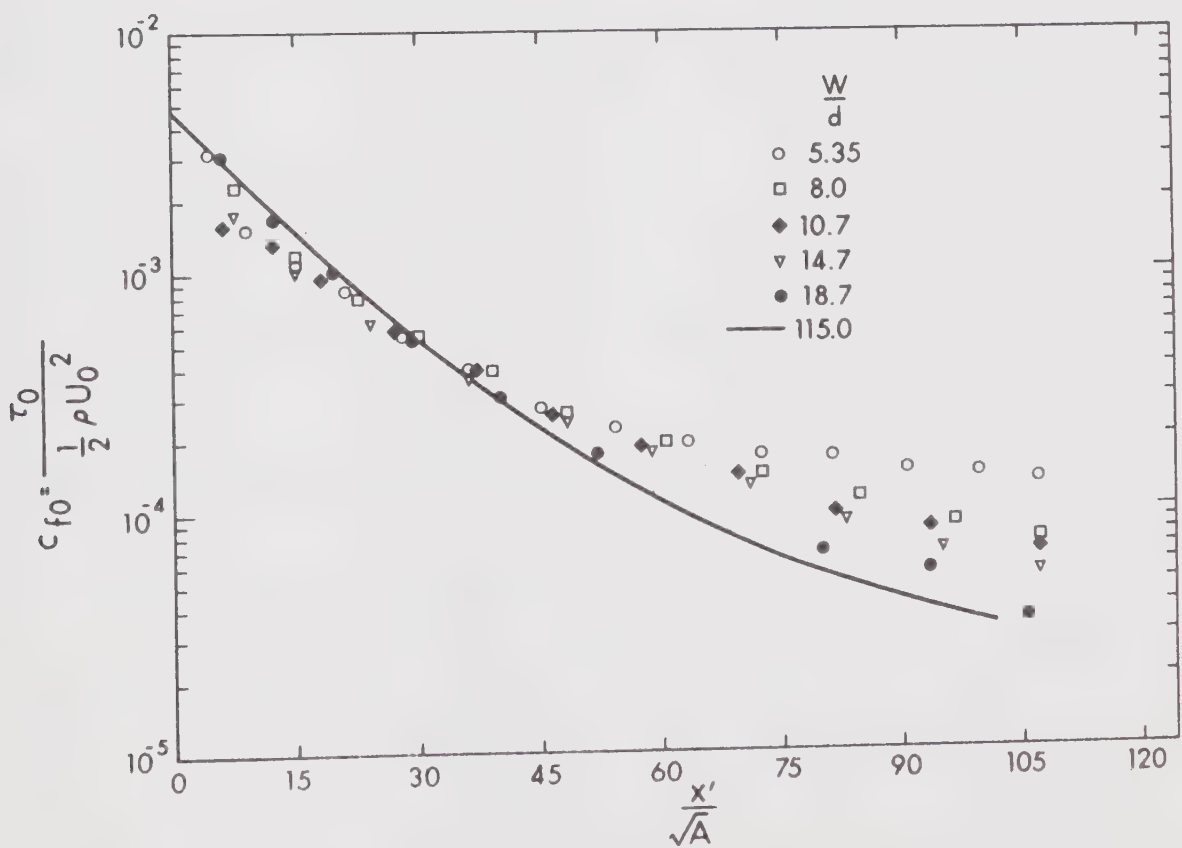


FIGURE 5.7 BED SHEAR DECAY (ON THE CENTERLINE)

infinitely wide channel. The bed shear for identical outlet conditions would be higher in the far field, for channels having finite width. As the channel gets narrower, the flow field is further complicated by the action of pressure gradients, and similarity of velocity profiles is not satisfied. A limit for W/d is roughly set at 30, beyond which most results of the wide channel investigation seem to apply.

CHAPTER VI
EFFECT OF BOUNDARY ROUGHNESS
ON CIRCULAR WALL JETS

6.1 General

Studies on diffusion of a circular jet impinging tangentially on a rough boundary, under zero pressure gradient, are presented in this section. The ambient fluid was stagnant and the outlet was deeply submerged so that the ambient could be treated as approximating a semi-infinite medium. It has been established in Chapter IV that on a smooth boundary all shapes of nozzle behave alike; moreover, the circular shape being more common in hydraulic engineering, investigations were carried out for this shape only.

The other investigations on wall jets growing on rough boundaries appear to be those of Lam Lau (1963) and Rajaratnam (1965). These treated only the two dimensional case.

6.2 Existing Work on Plane Jets

Rajaratnam conducted experiments on plane turbulent wall jets under zero pressure gradient on rough boundaries and covered a range of K_s/h varying from 0.00455 to 0.126, h being the initial depth of wall jet. It was observed that in the fully developed zone, the velocity profile should be considered in two parts, viz, the inner or the boundary layer and the outer or free-mixing region. Al-

though a single length scale does not exist, each of the parts exhibit similarity if the appropriate length scales are considered individually. The variation of the two length scales and the common velocity scale u_{mo} were presented. A power law type of equation described the velocity distribution in the boundary layer, with its exponent varying from 1/2 to 1/8. The decay of the maximum velocity was reported to be affected by the boundary roughness. Studies on momentum fall showed that for the $K_s/h = 0.126$ case, the flow could loose more than 50% of its efflux momentum by the time it travels a distance of 60h.

6.3 Dimensional Considerations

For flow over rough boundaries the loss in forward momentum is high and it is not possible anymore to assume that the efflux momentum flux is preserved. This would mean that the efflux momentum flux can no longer be considered as a single variable, but the efflux velocity U_0 and the area of the nozzle would appear as separate variables, affecting the flow field. Hence, for turbulent flow on a rough boundary, the maximum velocity at any section may be expressed as

$$u_{mo} = f(U_0, A, \rho, x, K_s) \quad (6.1)$$

or

$$\frac{u_{mo}}{U_0} = \phi\left[\frac{K_s}{\sqrt{A}}, \frac{x}{\sqrt{A}}\right] \quad (6.2)$$

For flow on a smooth boundary it has been established (Chapter II) that,

$$\frac{u_{mo}}{U_0} = \frac{C}{(x/\sqrt{A})} \quad (2.56)$$

An examination of Eqs. 6.2 and 2.56 (together with the experimental results presented later) suggests that Eq. 6.2 could possibly be re-written as

$$\frac{u_{mo}}{U_0} = \frac{C(K_s/\sqrt{A})}{x/\sqrt{A}} \quad (6.3)$$

and for a circular outlet

$$\frac{u_{mo}}{U_0} = \frac{C(K_s/d)}{(x/d)} \quad (6.4)$$

As data on plane wall jets on rough boundaries are extensive, it would be desirable to write the corresponding expression for the plane jet as

$$\frac{u_{mo}}{U_0} = \frac{C(K_s/h)}{(x/h)^{0.5}} \quad (6.5)$$

The data of Rajaratnam were analysed by plotting u_{mo}/U_0 versus x/h on a double-log plot. By drawing lines at a slope of 0.5, which would give best fit for the test data for any particular run, C was determined for various roughness heights. The variation of C for a wide range of relative roughness is shown in Figure 6.1. There is no systematic variation although there seems to be lot of scatter and C remains un-

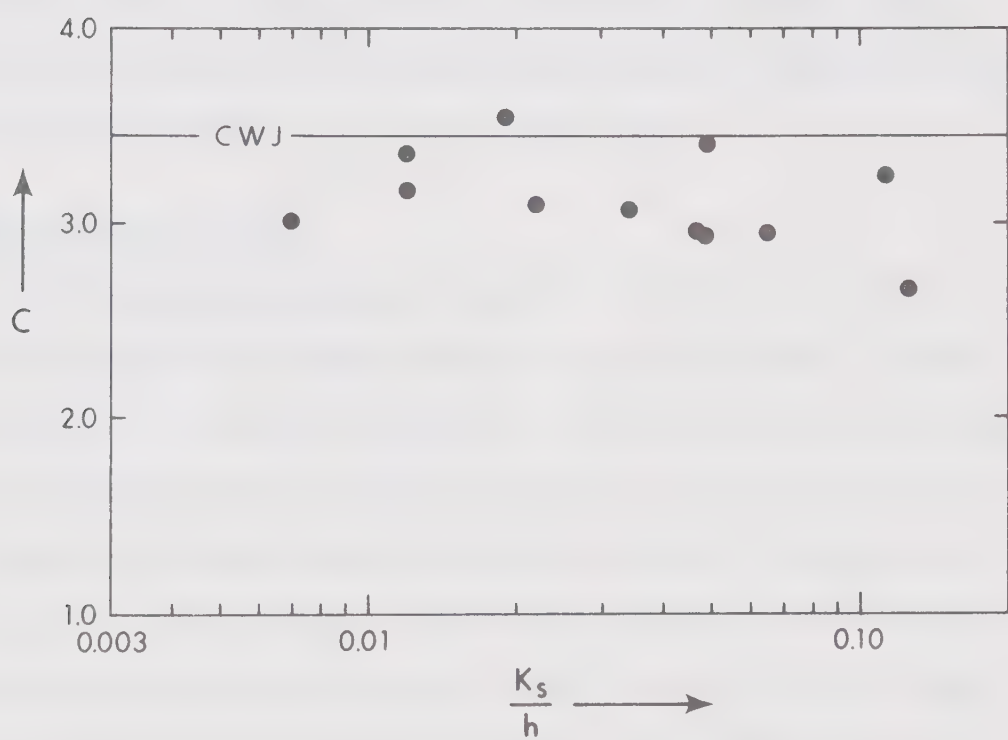


FIGURE 6.1 EFFECT OF BED ROUGHNESS ON THE MAXIMUM VELOCITY DECAY CONSTANT FOR PLANE JETS

affected by the roughness. This is contrary to the belief that C should decrease with an increase in bed roughness. Observations on the plane jet indicate that an increase in the roughness displaces farther away from the boundary the point of maximum velocity and the distribution in the boundary layer is less steep. This distribution of velocity, added with the thicker boundary layer, account for the high rate of momentum loss which is almost entirely confined to the wall region. The wall does not affect the free-mixing zone and the maximum velocity occurring at any section to any significant extent.

6.4 Present Investigation

By varying the boundary roughness systematically, design curves for predicting the gross behaviour could be prepared. However, the discussions on the plane jet (Section 6.3) dictate that the present investigation should aim at finding out whether the results for the smooth boundary are applicable as an approximation to the rough boundaries. If not, the existing order of differences should be found. Other details about dividing the flow field into the inner and outer region, the velocity distribution, boundary layer growth along the centerline and the decay of maximum shear were also studied for a circular wall jet.

6.5 Experiments

Experiments were carried out in flume 2. The rough boundary was formed by gluing a continuous strip of #36 wet-or-dry aluminium oxide cloth (described in Section 3.4) on the smooth aluminium plate.

The nozzle was 0.375" in diameter, and the jet location was adjusted till visually it could be judged to be issuing tangential to the rough boundary. For this test run, the relative roughness $K_s/d = 0.195$. In a major portion of the flow, the velocity field was explored by a total head tube 0.085" inside diameter and 0.11" outside diameter. However, detailed mean velocity measurements in the boundary layer along the centerline and the velocity measurements close to the nozzle were taken with a 0.05" total head tube. The static pressure was measured by means of a side-wall tapping.

6.6 Results

6.6.1 Similarity of Velocity Profile

Non-dimensional plots u_m/u_{m0} vs. y/b_y are shown in Figure 6.2 and indicate similarity of the profiles, for x'/d in the range of 15 to 50. Beyond the upper limit, the scatter increases and seems to be the result of inaccurate mean velocity recorded in this zone of high turbulence intensities. Comparison of the experimental similarity curve with the classical wall jet shows that the rough wall shifts outward the point of maximum velocity. Also, use of a single length scale b_y for the entire thickness gives wide scatter for the points in the boundary layer, and it should be checked as to whether division into two regions having different length scales would improve the velocity distribution for a three dimensional jet.

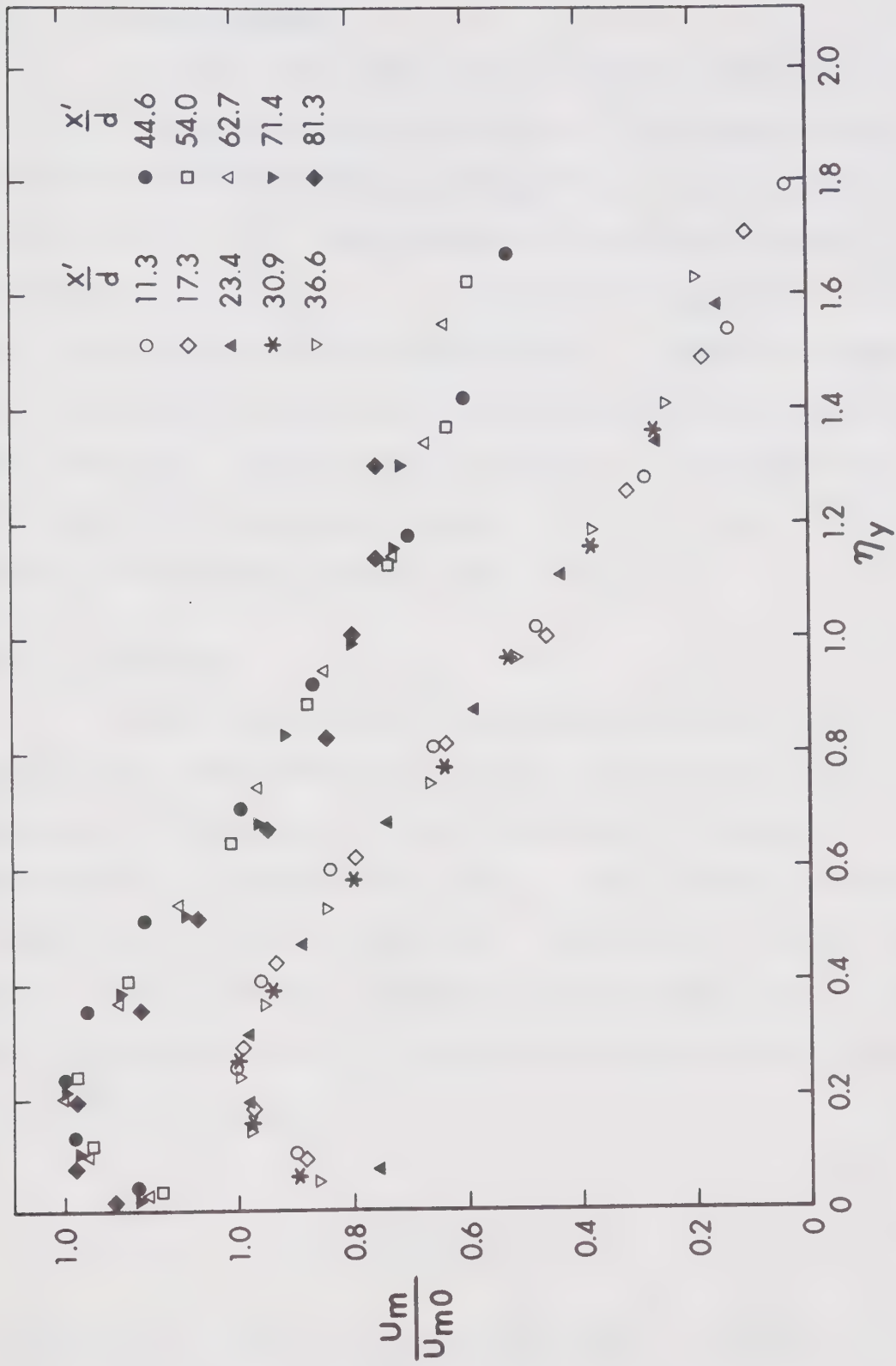


FIGURE 6.2 CENTERLINE NON-DIMENSIONAL VELOCITY PROFILE ON A ROUGH WALL

6.6.2 Free Mixing Region

The shear layer lying above the boundary layer of thickness δ is referred to as the free mixing region. The distances and the velocity scale for this zone were measured from the outer edge of the boundary layer. Hence, the non-dimensional velocity distribution is given by $f(n') (= u_m/u_{m0})$ vs. $n' (= y-\delta/b_y - \delta)$ in Figure 6.3. In the same figure, the data on the smooth boundary is plotted for comparison. In both cases, the distribution agrees closely with the classical wall jet curve. Thus the free-mixing region is unaffected by the particulars of the boundary roughness. This is identical with the results of Rajaratnam (1965) for plane wall jets.

6.6.3 Inner Region

From a knowledge on the velocity distribution in the familiar boundary layer and pipe flows, the present data are plotted as u_m/u_{m0} versus y/δ in Figure 6.4. For small distances from the nozzle, K_s/δ would be large compared to the values for large distances and therefore a single curve is not to be expected. Data indicate a two fold variation in the value of K_s/δ . However, Figure 6.4 shows that excluding the first section, the rest of the data can be described by a simple power law distribution,

$$\frac{u_m}{u_{m0}} = \left(\frac{y}{\delta}\right)^{1/n} \quad (6.6)$$

A value for $n = 8$ in the above expression gives a reasonable fit to the data. Rajaratnam found that for a plane jet, the value of n can

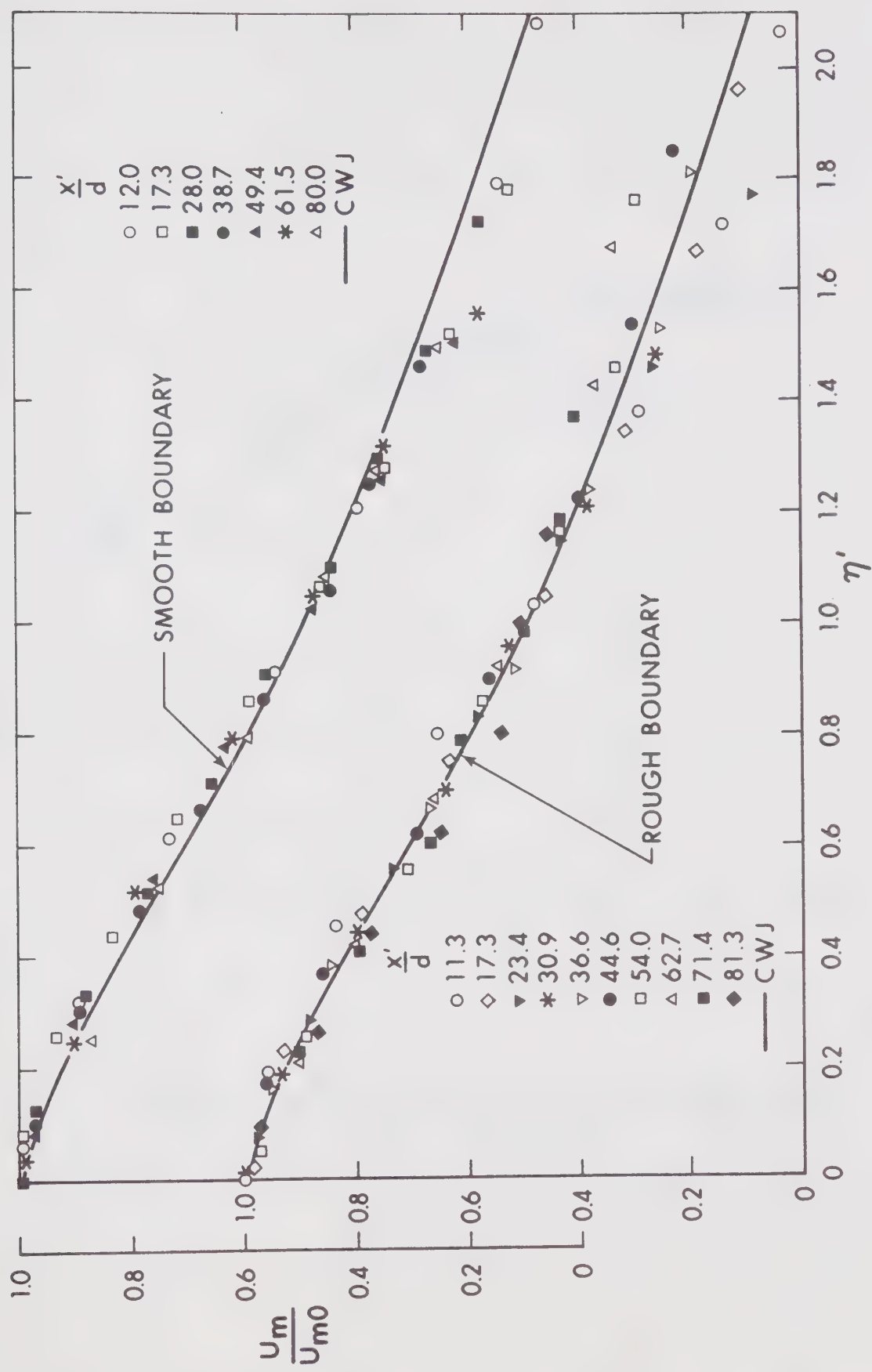


FIGURE 6.3 VELOCITY DISTRIBUTION - FREE MIXING REGION

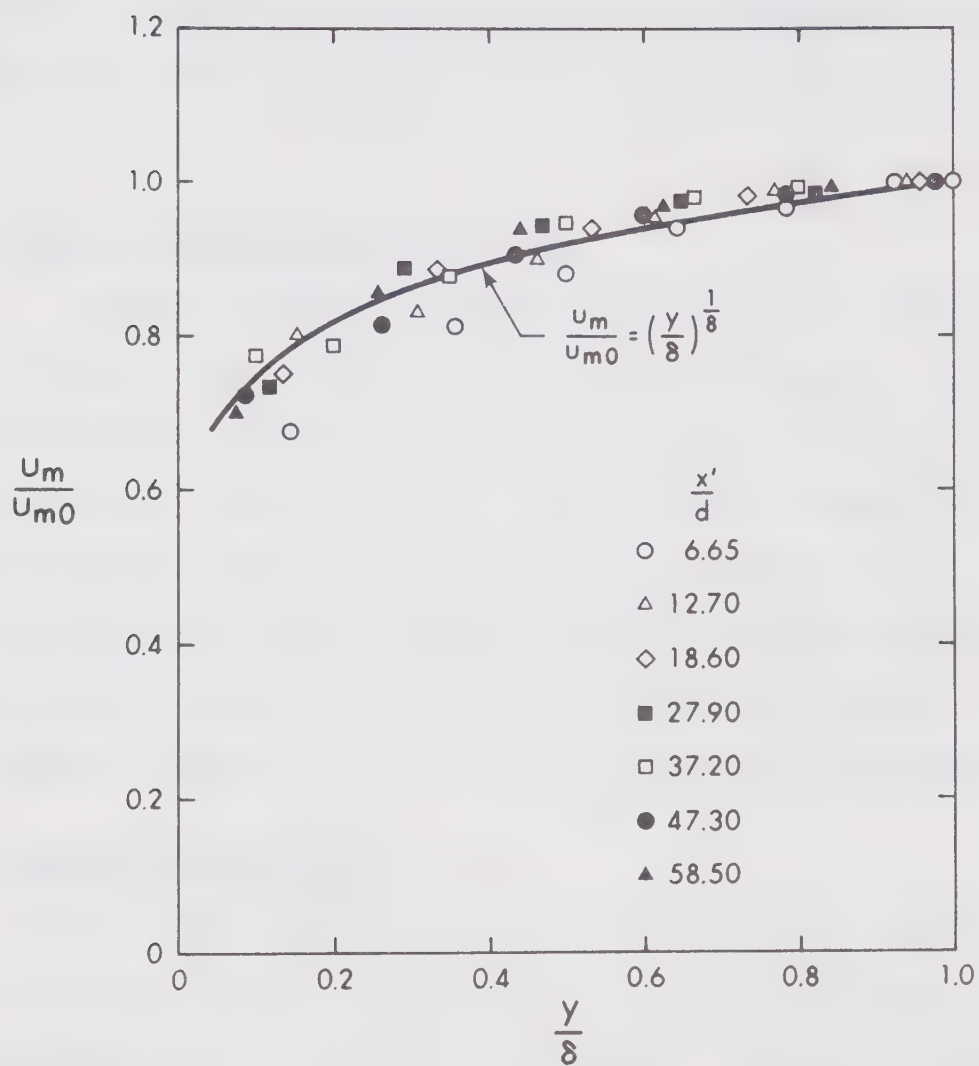


FIGURE 6.4 VELOCITY DISTRIBUTION IN THE BOUNDARY LAYER
(ROUGH WALL)

be between 2 and 8 and the lower value occurs for the higher roughness. For a three dimensional jet, the growth of the boundary layer normal to the bed is limited by the flow spreading in a transverse direction, and therefore results in a high value for n even for case of a very rough wall.

6.6.4 Velocity Distribution in x-z Plane

Velocity distribution in the transverse plane is shown in Figure 6.5 and represents the conventional quantities u/u_m vs. z/b_z . The distribution is found to be similar and for planes lying close to the boundary, the agreement is good. Goertler's free circular jet curve is compared with the data and can be seen to agree closely with the experimental results. Thus the boundary roughness does not affect the nature of this distribution to any noticeable extent. In planes lying at higher elevation from the bed, the data scatter more.

6.6.5 Maximum Velocity Decay

The maximum velocity u_{mo} along the centerline is a scale common to both the inner and the free mixing regions. The observations on the maximum velocity are given in Figures 6.6. Plot of $1/u_{mo}$ versus x'/d in Figure 6.6a for the rough and the smooth boundary, gives linear relationships. The two tests were conducted for identical efflux velocities and therefore equal slope of the two linear variations would mean that the rate of decay is the same, regardless of the boundary roughness. On a rough boundary the process of mixing is enhanced and results in a shift in the virtual origin in the up-stream

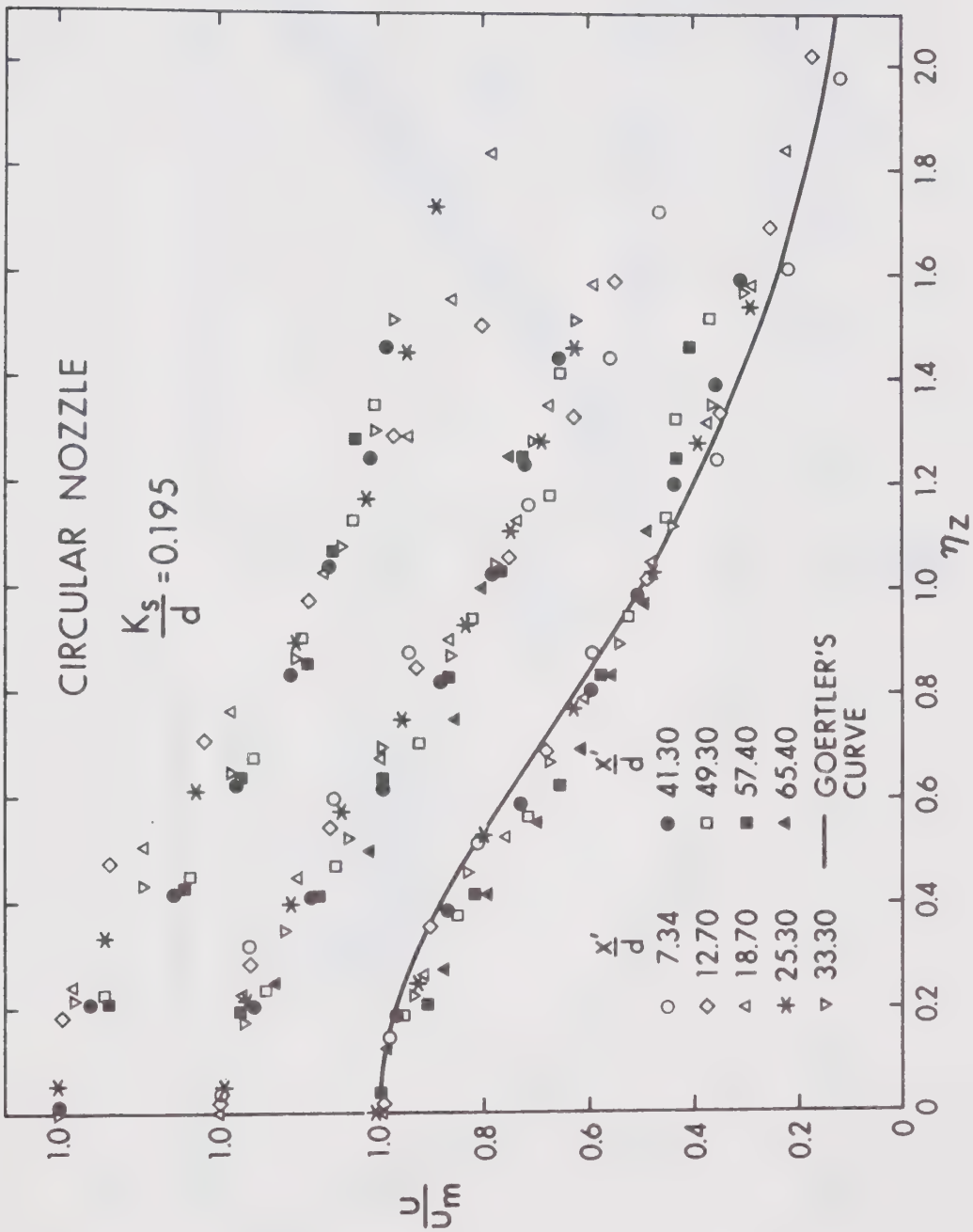


FIGURE 6.5 NON-DIMENSIONAL VELOCITY DISTRIBUTION IN z DIRECTION
(ROUGH WALL)

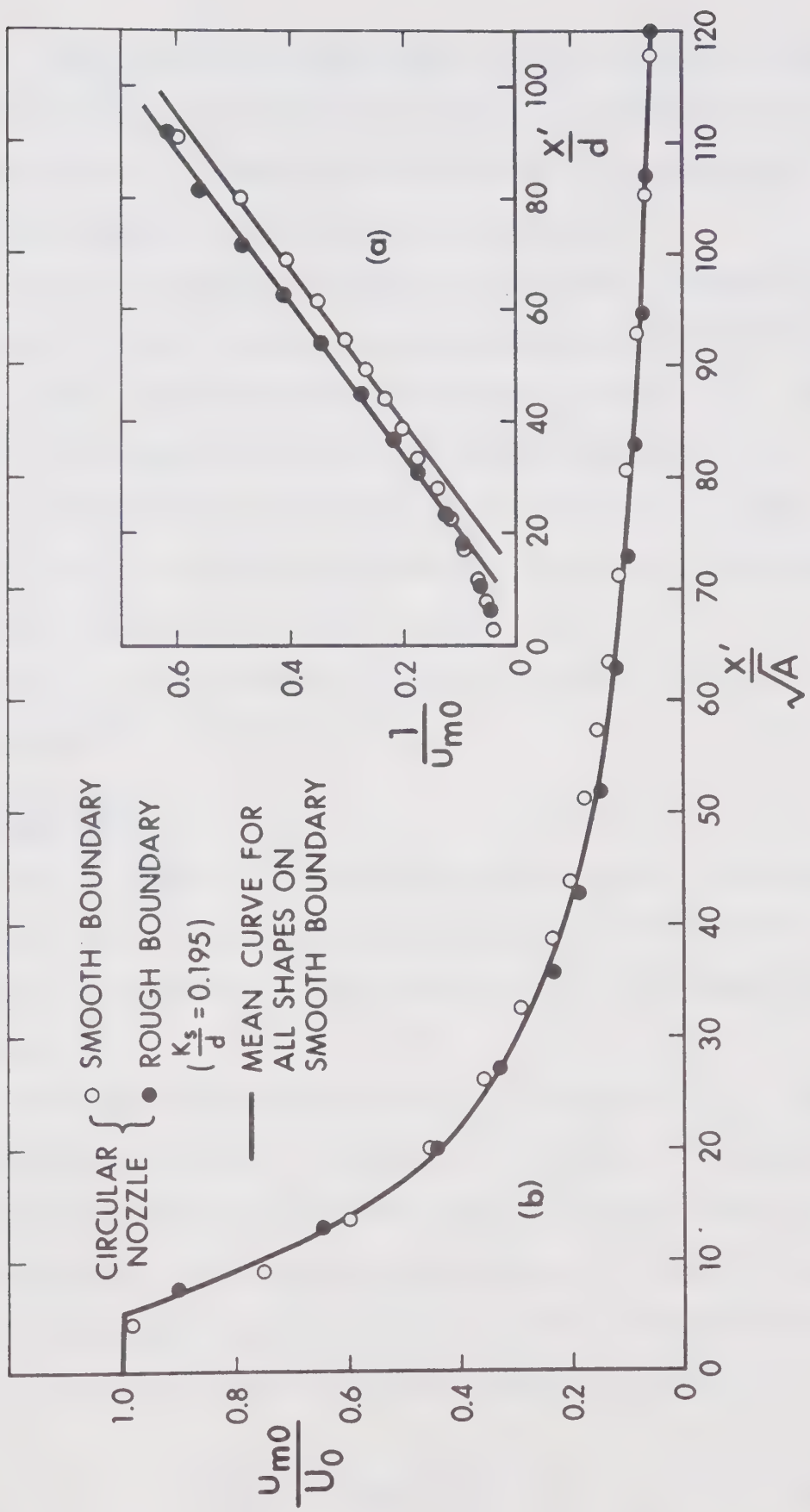


FIGURE 6.6 MAXIMUM VELOCITY DECAY OF A JET ON A ROUGH WALL

direction. Thus, at a section equidistant from two identical outlets, the velocity for the rough boundary case would be somewhat less than the smooth wall case. However, from the following discussion, it seems the differences in the two velocities are small.

As an alternative, the same data are shown in Figure 6.6b, as u_{mo}/U_0 vs. x'/\sqrt{A} . The mean curve derived from tests on all nozzle shapes is seen to describe the rough wall data extremely well. This observation, combined with the analysis of data (Section 6.3) for plane jets on rough walls, suggests that the maximum velocity decay law is the same for all kinds of boundaries. Hence, the relationships derived from extensive investigation on three dimensional wall jets on smooth walls can satisfactorily be used in practice, unless the relative roughness is excessively large.

6.6.6 Length Scales

As the centerline velocity distribution normal to the wall is considered in two parts, two length scales need to be specified. In addition, there would be a third length scale for the transverse distribution.

The length scale for the free mixing region is $(b_y - \delta)$, and its variation with distance x' is given in Figure 6.7a. The variation can be found to be linear and follows closely the data on smooth boundaries. Beyond a distance of $x'/d > 50$, the length scale for a rough wall grows fast, and no explanation could be found. A general relationship which would be valid for all types of boundary roughness is given by

$$\frac{(b_y - \delta)}{d} = 0.042 \left(\frac{x'}{d} \right) + 0.5 \quad (6.7)$$

Variation of the boundary layer thickness δ , which is the length scale for the inner region, is given in Figure 6.7b. For the smooth as well as the rough boundary the variation of δ with x' is linear, the values being higher for the rough boundary. It is to be pointed out that in all tests it was impossible to locate the outlet exactly tangent to the boundary and a small step is provided at the outlet section. As this step size is arbitrary, and is likely to be different in the two sets of experiments, no significance is given to the boundary layer thickness measured close to the outlet section.

The growth of the boundary layer for a circular outlet is given as

$$\frac{\delta}{d} = 0.01 \left(\frac{x'}{d} \right) + K \quad (6.8)$$

where K is a constant and depends on the boundary roughness and the nozzle contraction details.

Growth of b_z in three different planes was considered and its variation is given in Figure 6.8. Up to $x'/d = 30$, the growth rate is very much like the smooth boundary case, but beyond this distance the growth rate of b_z is faster. Even the data on a plane close to the rough boundary does not exhibit linear variation. Therefore, no simple expression is suggested and b_z should be read from the plot.

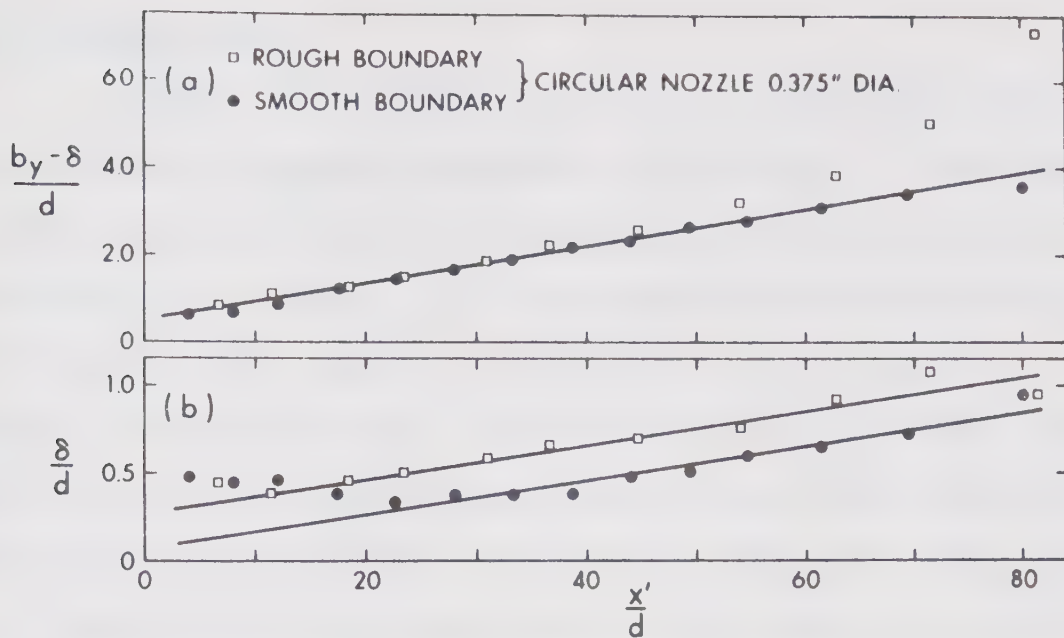
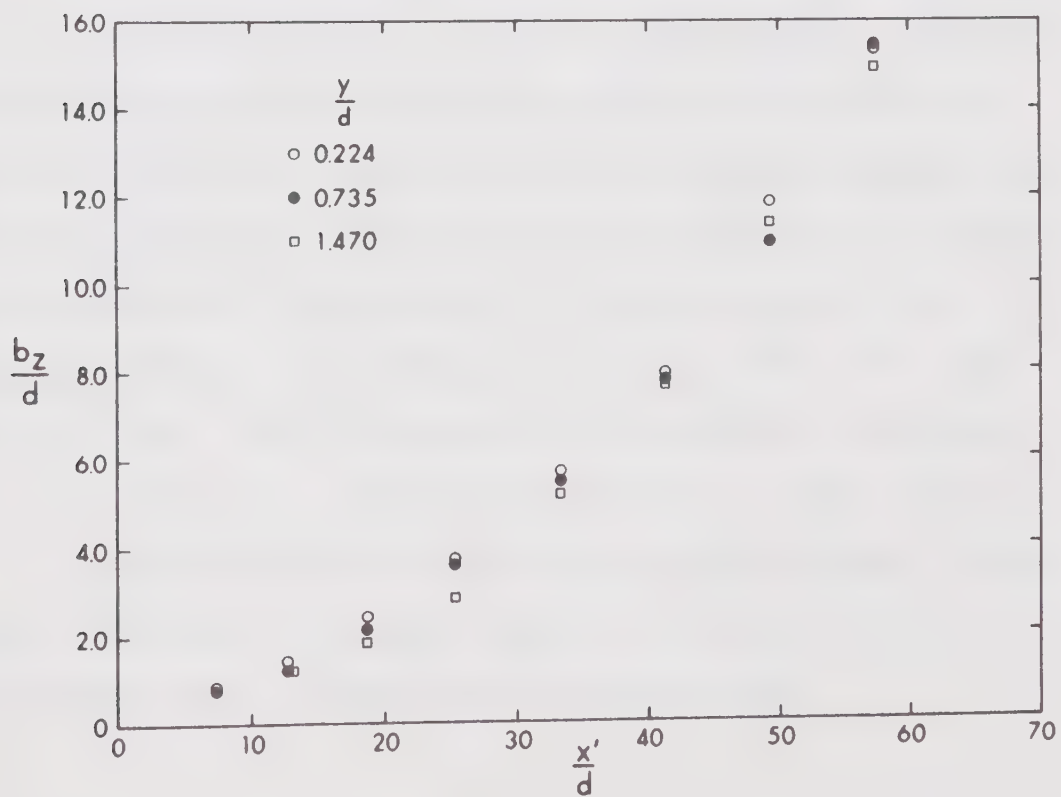


FIGURE 6.7 GROWTH OF LENGTH SCALES FOR FREE MIXING AND INNER REGION

FIGURE 6.8 GROWTH OF LENGTH SCALE b_z (ROUGH WALL)

6.6.7 Boundary Shear

Beyond an initial reach of 2.5" from the outlet, the centerline bed shear was computed from Preston tube readings. A larger tube of 0.00917' outer diameter was used to minimize the error in location of the zero datum. From Eq. 3.11, the centerline bed shear was found, and the values seemed very high and unrealistic. In the range of distances considered, the tube occupies 30 to 75% of the boundary layer thickness, so that, the displacement of the effective center would be large compared to the boundary layer thickness. This would mean that in all cases, the total head tube records a much higher pressure reading than actual.

The velocity profile in the boundary layer was then measured with a smaller total head tube of 0.0041' outside diameter. The data plotted as straight lines on a semi-log paper and the bed shear was computed from Eq. 3.13. When the tube is resting on the boundary, the displacement effects would be a maximum, and therefore, the first point should be avoided as far as possible in fitting a straight line. The boundary shear found by this method was found to be low, and in many regions the local skin friction coefficient was found to be somewhat smaller than the one for a smooth boundary, which is rather baffling.

Until more reliable results are obtained for boundary layers of larger thicknesses (using bigger nozzles), no comment could be made on the bed shear distribution on a rough boundary.

6.7 Summary

The centerline velocity profile normal to the boundary can be split into two regions - the free mixing zone, and the inner zone, which exhibit similarity. The distribution in the free mixing region closely follows the classical wall jet profile, regardless of the boundary roughness. A power law type of distribution is found to be satisfactory for the inner region. The length scale for the free mixing region and the boundary layer thickness, vary linearly with distance x . The maximum velocity $u_{mo} \propto x^{-1.0}$, and the boundary roughness does not affect the x'/\sqrt{A} vs. u_{mo}/U_0 curve to any significant extent, so that, for preliminary estimates, the curve for the three dimensional wall jet on a smooth boundary would be used.

The velocity distribution in the transverse direction can be approximated by Goertler's curve, noting that the growth of b_z can no longer be represented by a linear relationship. Both the Preston tube technique and velocity profile method, proved unsuccessful in giving a true picture of the centerline bed shear distribution.

CHAPTER VII

WALL JETS WITH SWIRL

7.1 Introduction

Giving a certain amount of swirl or rotation, before a jet comes out of a circular nozzle, helps to spread the flow more rapidly and therefore the maximum velocity decays faster. Considerable amount of work has been done on the effect of swirl on free circular jets and these swirling jets find application in combustion chambers and sprayers. Experimental observations on free swirling jets have been made by Rose (1962), Gore and Ranz (1964), Kerr and Fraser (1965), Chigier and Chervinsky (1967), Pratte and Keffer (1969) and others. In the fully developed flow region the distribution of axial and tangential velocity components were found to be similar, with the length scales varying linearly with distance x . The pressure plus momentum ($P+M$) and the angular momentum (T) were found to be preserved and were combined to form a dimensionless parameter,

$$S = \frac{T}{(P+M)r_0} \quad (7.1)$$

where S = swirl number, and

r_0 = radius of the nozzle

From a similarity analysis it is possible to show that for a free

swirling jet, when the maximum axial velocity u_{mo} is far larger than the maximum tangential velocity w_{mo} at the nozzle, the following relations are satisfied.

$$b \propto x$$

$$u_{mo} \propto \frac{1}{x} \quad (7.2)$$

$$w_{mo} \propto \frac{1}{x^2}$$

where b is a length scale.

From the experiments of Chigier and Chervinsky, even for the highest value of $S (= 0.64)$ the above expressions were found to be valid.

There appears that no information is available on the effect of swirl on a circular wall jet. In an attempt to find how effectively one can spread the flow from a circular outlet resting on a smooth boundary, some preliminary experiments were conducted. At this stage any reasonable theoretical approach is not possible because of lack of symmetry in the flow field. In this chapter the forward velocity and the bed shear distribution for $S = 0, 0.141$, and 0.265 were measured in detail.

7.2 Experiments

Experiments were conducted in flume 2 for a circular nozzle 0.75" in diameter. Selecting proper axial and tangential discharges through the swirl generator, the swirl number could be suitably adjusted in the range of 0 to 0.265. The velocity field was explored by a calibrated five hole probe 0.17" thick, and the bed shear distribution was explored by a yaw probe. The tail water depth was of the order of 28 times the nozzle diameter and resulted in a level surface.

7.3 Results and Analysis

7.3.1 Velocity Distribution Normal to the Wall

Distribution of the axial velocity component taken normal to the wall are given in the non-dimensional form η_y vs u_m/u_{mo} (Figure 7.1). Observations were limited to distances of 40 and 26 times the nozzle diameter, for $S = 0.141$ and 0.265 respectively, since beyond this distance the velocity components were small and would have introduced large errors in measurement. For both the experiments, the distributions were found to be similar and as in the case of non-swirling jets, the distribution is closely represented by the classical wall jet curve. For swirling jets, similarity was found to be satisfied beyond a short distance from the outlet. For example, for $S = 0.265$, velocity profiles were similar beyond a distance of $6d$ from the nozzle. These observations were in general similar with those on free swirling jets.

7.3.2 Velocity Distribution in the Transverse Direction

Distributions of axial velocity components are indicated in

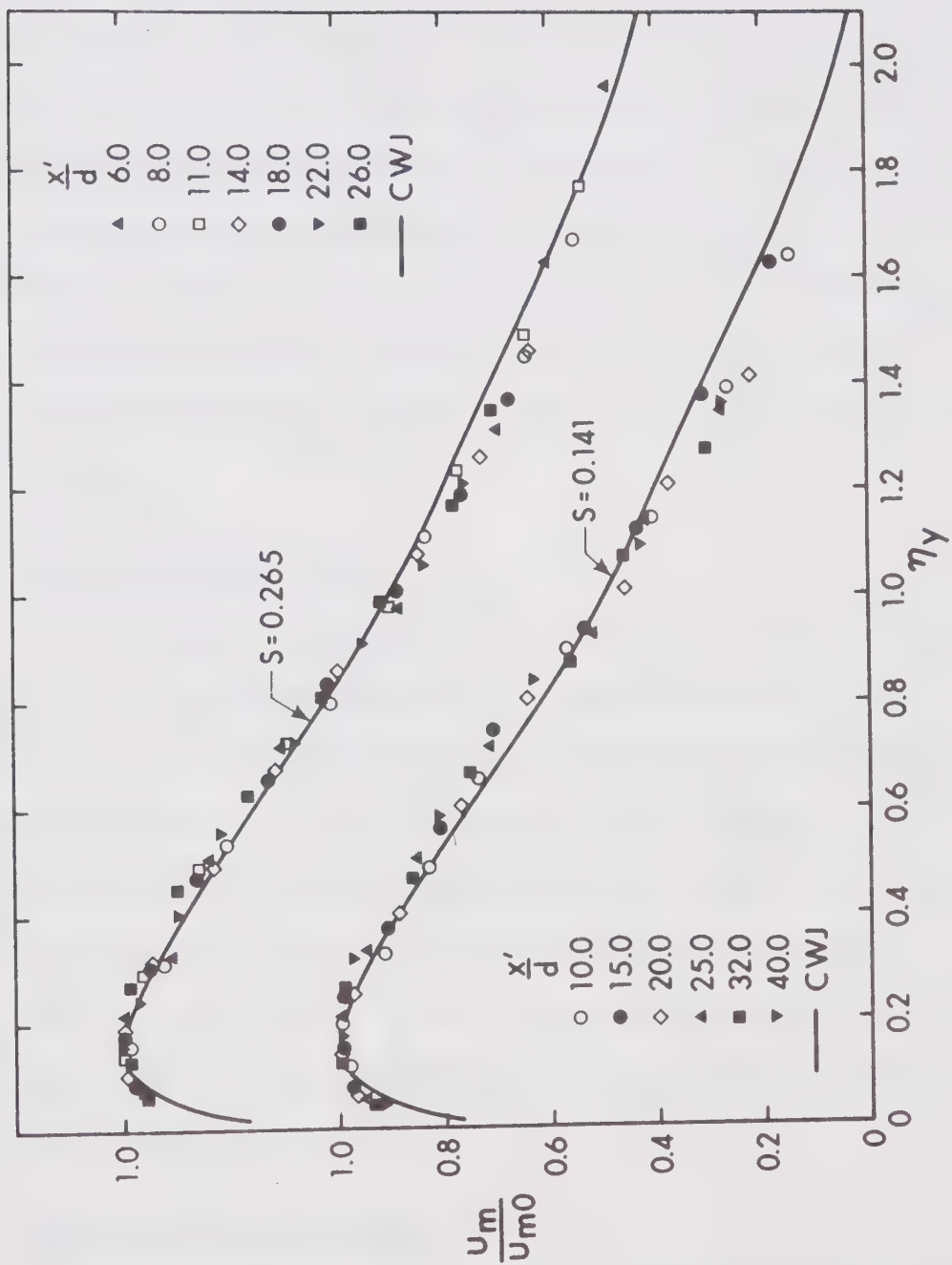


FIGURE 7.1 CENTERLINE NON-DIMENSIONAL VELOCITY DISTRIBUTION - SWIRLING JETS

Figure 7.2. For $y/d = 0.139$ and 0.512 the profiles look similar and are very well described by Goertler's curve for free circular jets. Measurements in higher planes showed a shift in the location of the maximum velocity from the centerline. This shift was of varying degrees depending on the distance of the section from the nozzle. Also, many of the profiles looked unsymmetrical and irregular. Measurements at large distances from the nozzle proved unsuccessful because the velocity components were small in the higher planes. As a result, the investigation had to be limited to locations close to the bed, and the distributions were found to be similar beyond a short distance of 4 to 6 d from the nozzle.

7.3.3 Distribution of v and w

As a typical example, the distribution of v and w components on the centerline normal to the wall are given in Figure 7.3 for $S = 0.141$. The w component decays very fast and the distribution does not look similar. The v component was also unsymmetric and the present data prevent us from drawing any definite conclusion. The same is true for the static pressure distribution (Figure 7.4). Beyond a short initial reach, all the above mentioned quantities are of very small order and their measurement with the present technique is likely to be not very reliable.

7.3.4 Decay of Maximum Velocity

Maximum velocities measured along the centerline of the jet

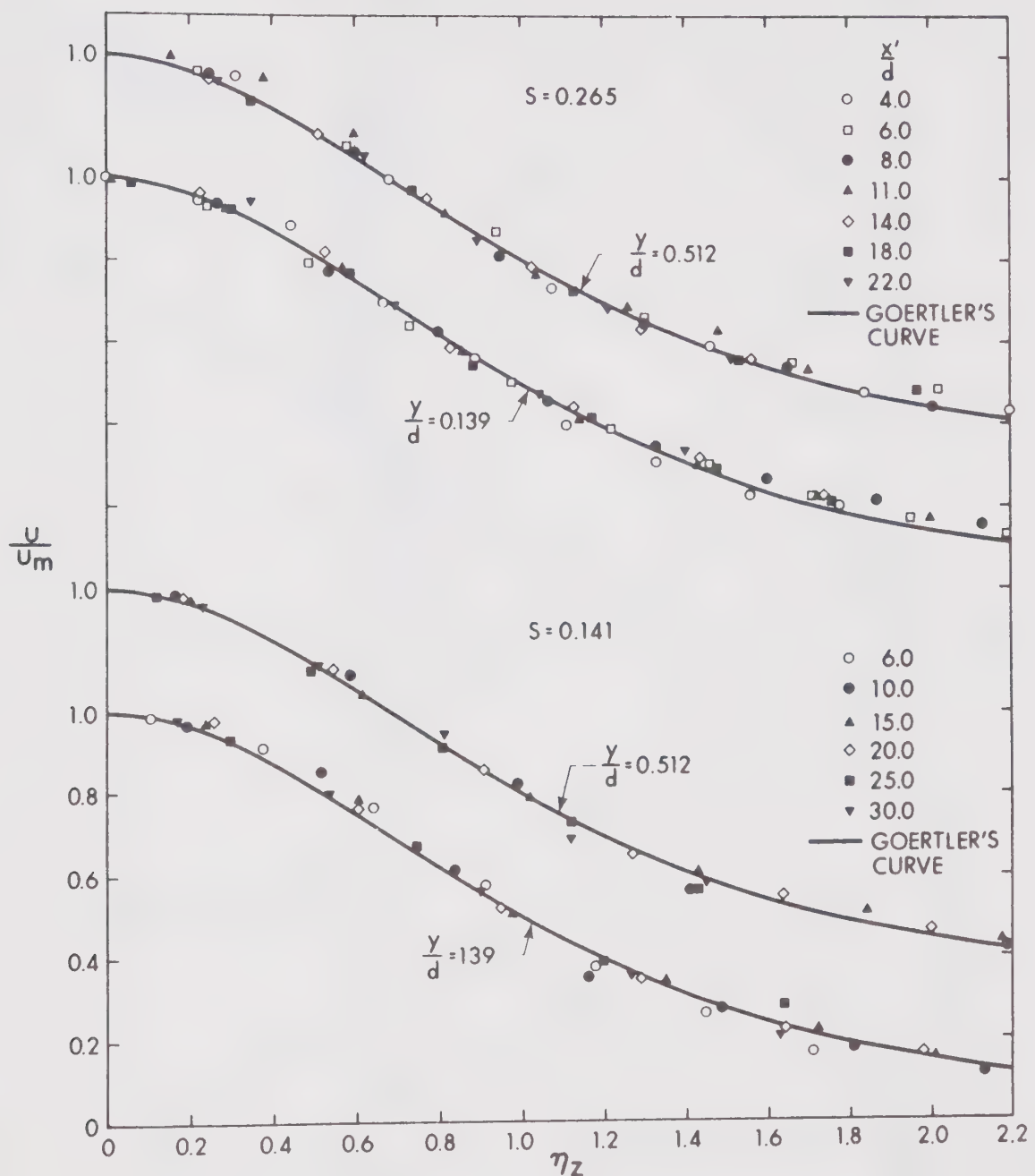
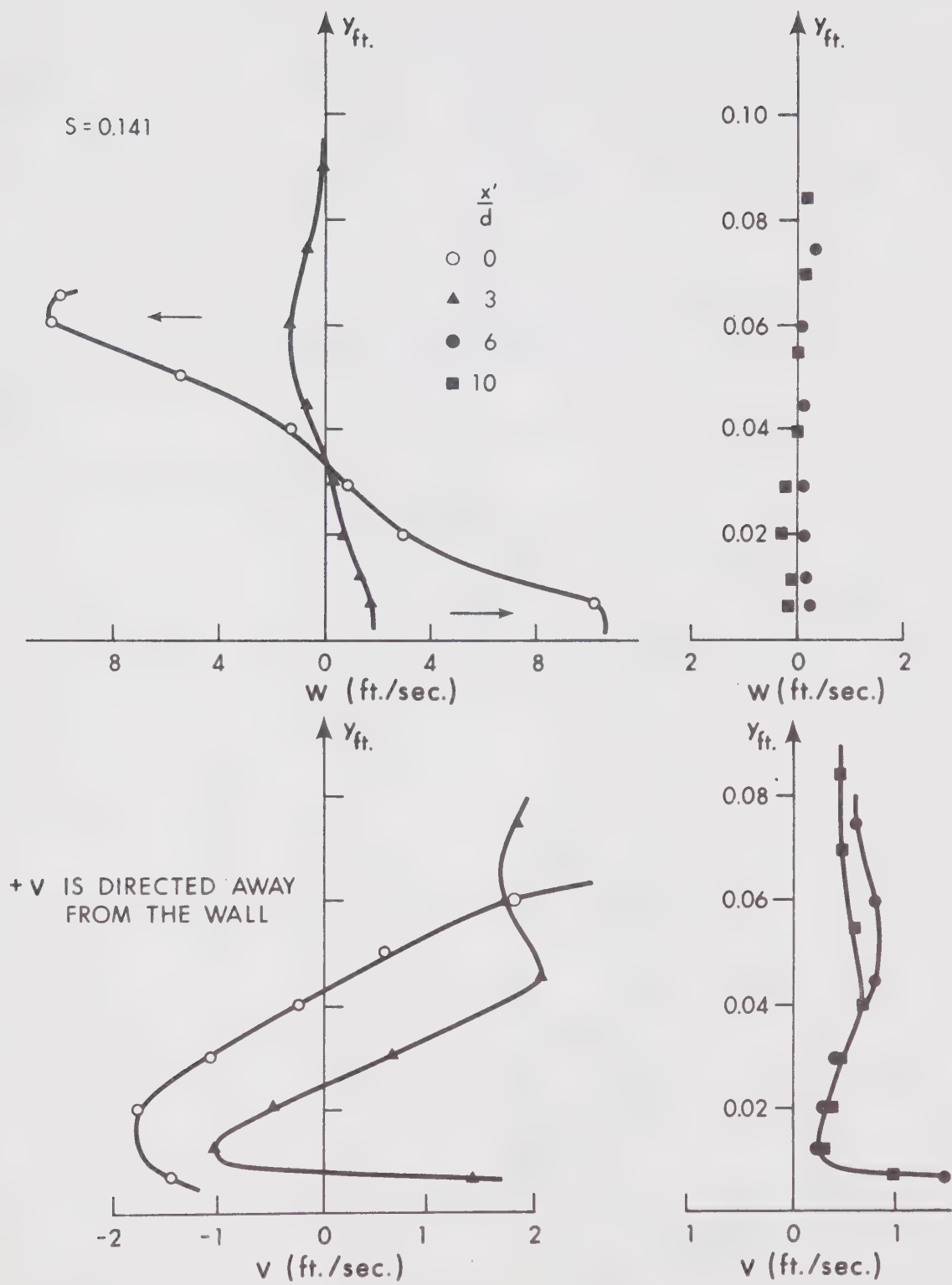


FIGURE 7.2 NON-DIMENSIONAL VELOCITY DISTRIBUTION IN TRANSVERSE PLANES OF SWIRLING JETS

FIGURE 7.3 v AND w VELOCITY COMPONENTS - A TYPICAL PLOT

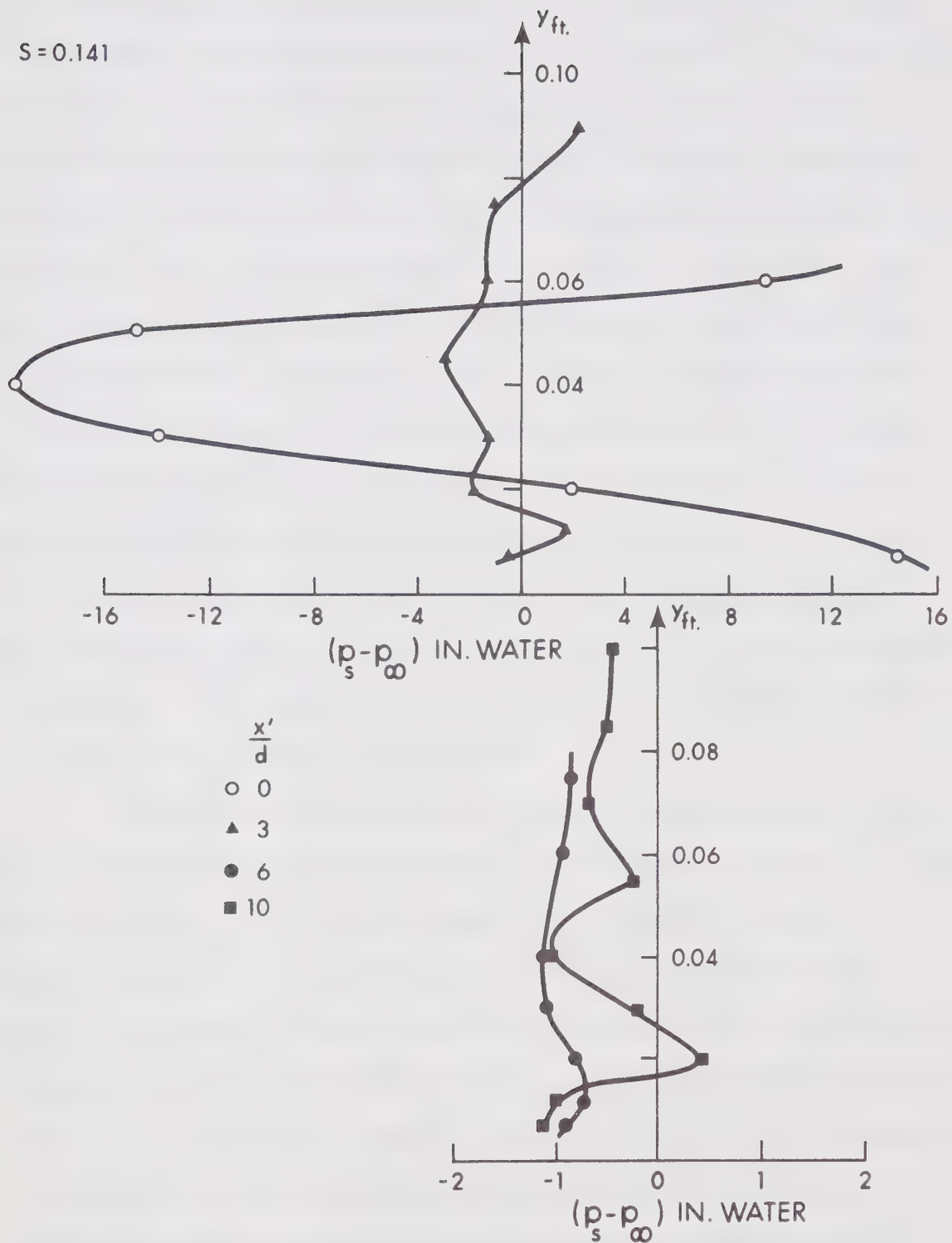


FIGURE 7.4 STATIC PRESSURE ALONG CENTER-PLANE - A TYPICAL PLOT

were non-dimensionalised with respect to the average efflux velocity at the outlet, and the variation is given in Figure 7.5. The data for zero swirl on the 0.375" and 0.75" nozzle were in close agreement. Velocity measurements at the 0.75" nozzle efflux section showed that the distribution was not uniform, but resembles the turbulent pipe flow profile. This is perhaps because of the straight length of 1" diameter pipe provided upstream of the test nozzle and the insufficient contraction ratio at the nozzle entry. First, the maximum velocity at the efflux section was selected as the reference velocity U_0 and the data showed no agreement with the results from the 0.375" diameter nozzle which had an uniform velocity distribution at the outlet. Hence, from the measured discharge rate the average velocity was computed for the 0.75" nozzle and was taken to be the representative velocity U_0 . This seems justified in the light of agreement between the results for different size nozzles.

Even for jets with swirl, U_0 was the average forward velocity and the decay of the maximum velocity u_{mo} is shown in Figure 7.5. The data indicate $u_{mo} \propto \frac{1}{x}$ for this range of swirl numbers and that the decay is faster for the swirling jets. One can clearly see that a small swirl is very effective and for higher swirls the effects do not increase proportionately. The difference in the decay rates for $S = 0$ and 0.141 is appreciable, whereas, the difference for $S = 0.141$ and 0.265 is very small. Another important feature of swirling jet is that the flow becomes similar at relatively short distances from the nozzle, and the virtual origin shifts close to the outlet section. As a result,

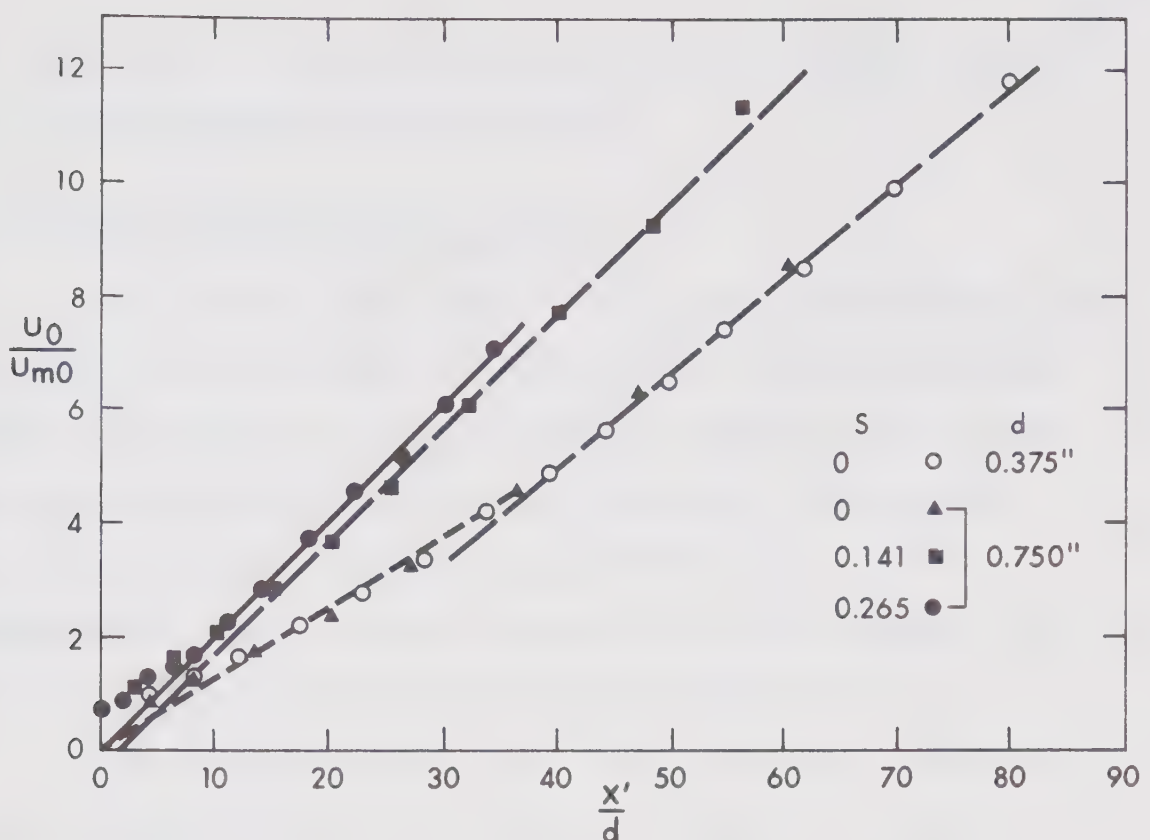
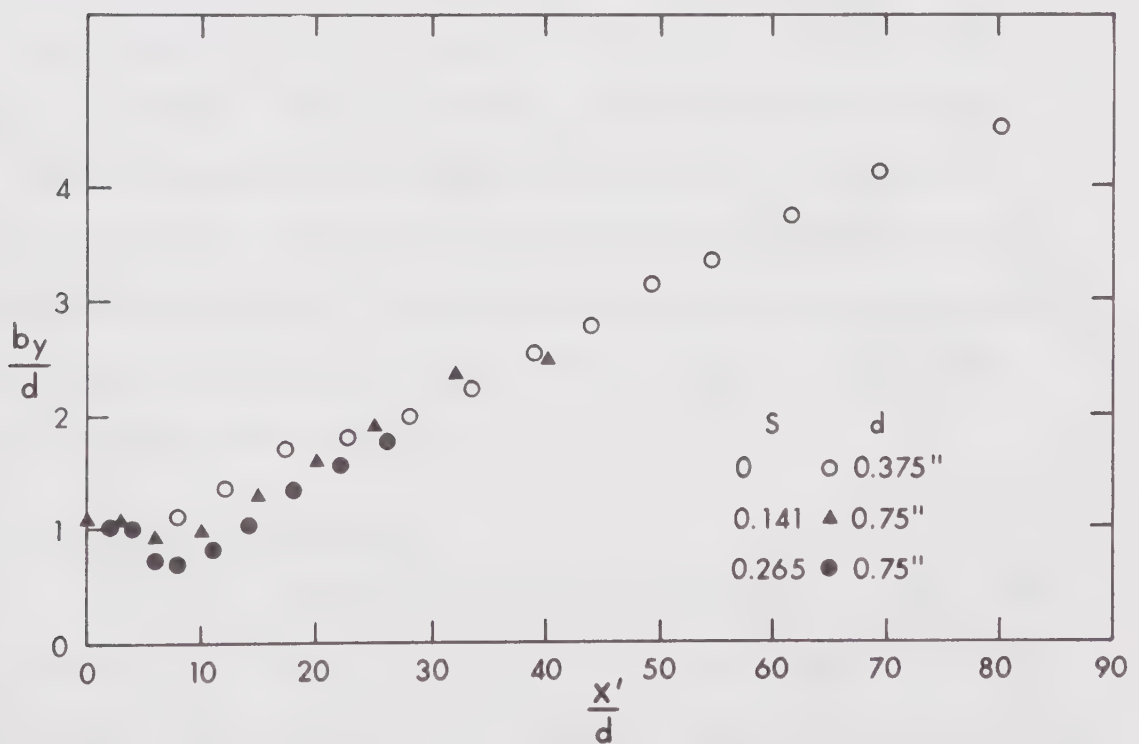


FIGURE 7.5 MAXIMUM VELOCITY DECAY FOR SWIRLING JETS

FIGURE 7.6 GROWTH OF LENGTH SCALE b_y

the overall effect of swirl is to have at identical sections velocities far less than those for non-swirling jets.

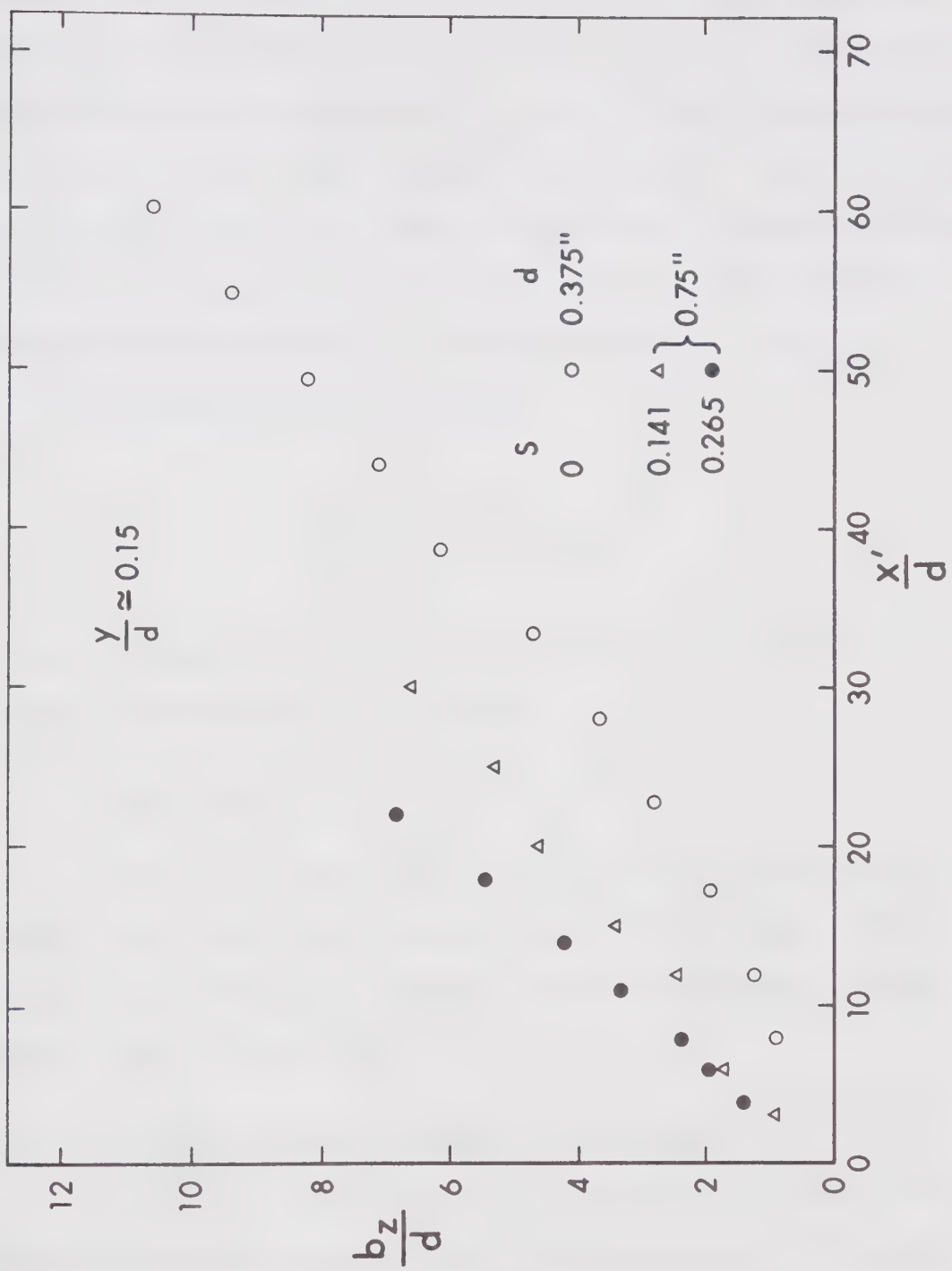
7.3.5 Growth of Length Scales b_y and b_z

For a short initial length of $3d$, b_y does not grow at all and then falls for a swirling jet. From Figure 7.6, this dip can be seen to increase with higher swirls. At around $8d$, the jet starts to grow and beyond about $20d$ the growth becomes linear and follows the data for non-swirling jets. Hence, in the far field ($x'/d > 30$) the relationship developed for three dimensional wall jets (in Chapter IV) may be used as a approximation for jets with moderate swirls.

For comparison, growth of b_z close to the wall is shown in Figure 7.7, for different swirl numbers. Here again, the expansion rate is more for swirling jets which increases with swirl number. Also, jets with swirl tend to expand right from the outlet section causing the virtual origin to lie very close to the nozzle (Figure 7.7). For the range of swirl numbers investigated, the growth of b_z close to the wall is linear, which is typical of the behaviour of b_z in higher planes as well. In the above discussion no attempt was made to give empirical expressions for b_y and b_z , since we have results for only two non-zero values of S .

7.3.6 Bed Shear Distribution

Transverse distribution of the x component of the bed shear was measured at a number of x stations and it was observed that the maximum value occurs almost on the centerline and the distribution was

FIGURE 7.7 GROWTH OF LENGTH SCALE b_z

more or less symmetrical. The maximum shear stress τ_{om} on the center-line was taken as the scale for shear stress and b_τ was taken as a length scale, being equal to z at which $\tau_0 = \tau_{om}/2$. The non-dimensional shear distribution is given by τ_0/τ_{om} vs. $n_\tau (= z/b_\tau)$ as indicated in Figure 7.8. For all cases, the shear distribution is similar in the fully developed zone and is very well described by Goertler's velocity distribution curve. For higher swirl numbers the distribution becomes similar very quickly at a distance of $3d$ from the nozzle.

A gaussian profile given by

$$\frac{\tau_0}{\tau_{om}} = \exp -\{0.693 n_\tau^2\} \quad (7.3)$$

is also indicated in Figure 7.8 and this empirical relationship does not give any improved fit to the data.

7.3.7 Length Scale b_τ

From the present investigations, the shear length scale is found to vary linearly with distance x . Also the virtual origin is located close to the nozzle and the growth rate increases with the degree of swirl (Figure 7.9).

7.3.8 Alternative form of Bed Shear Distribution

Since the virtual origin for b_τ lies close to the nozzle, it was thought that use of the shear length scale could be avoided if z is non-dimensionalised by the distance x' . The alternative way

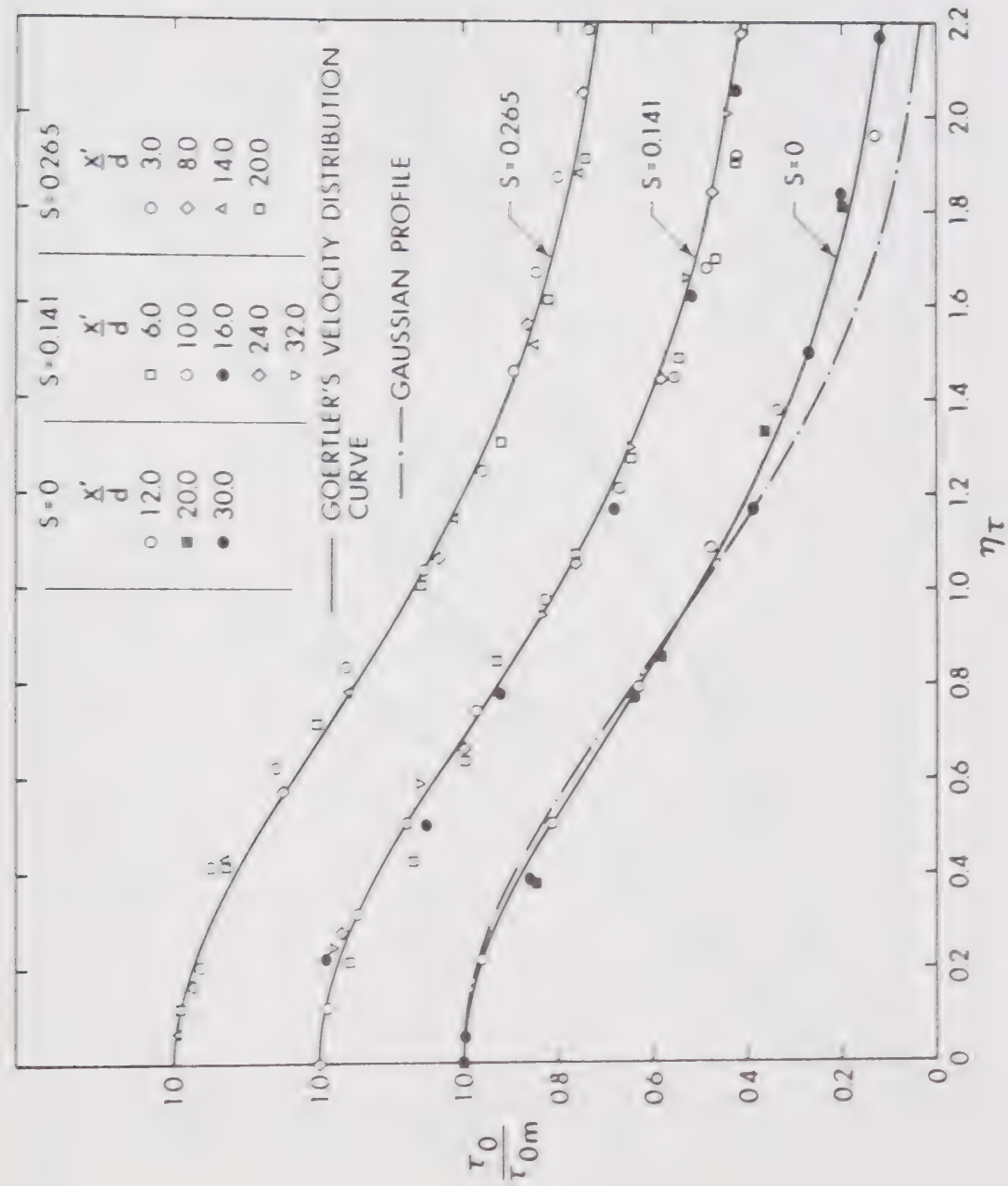
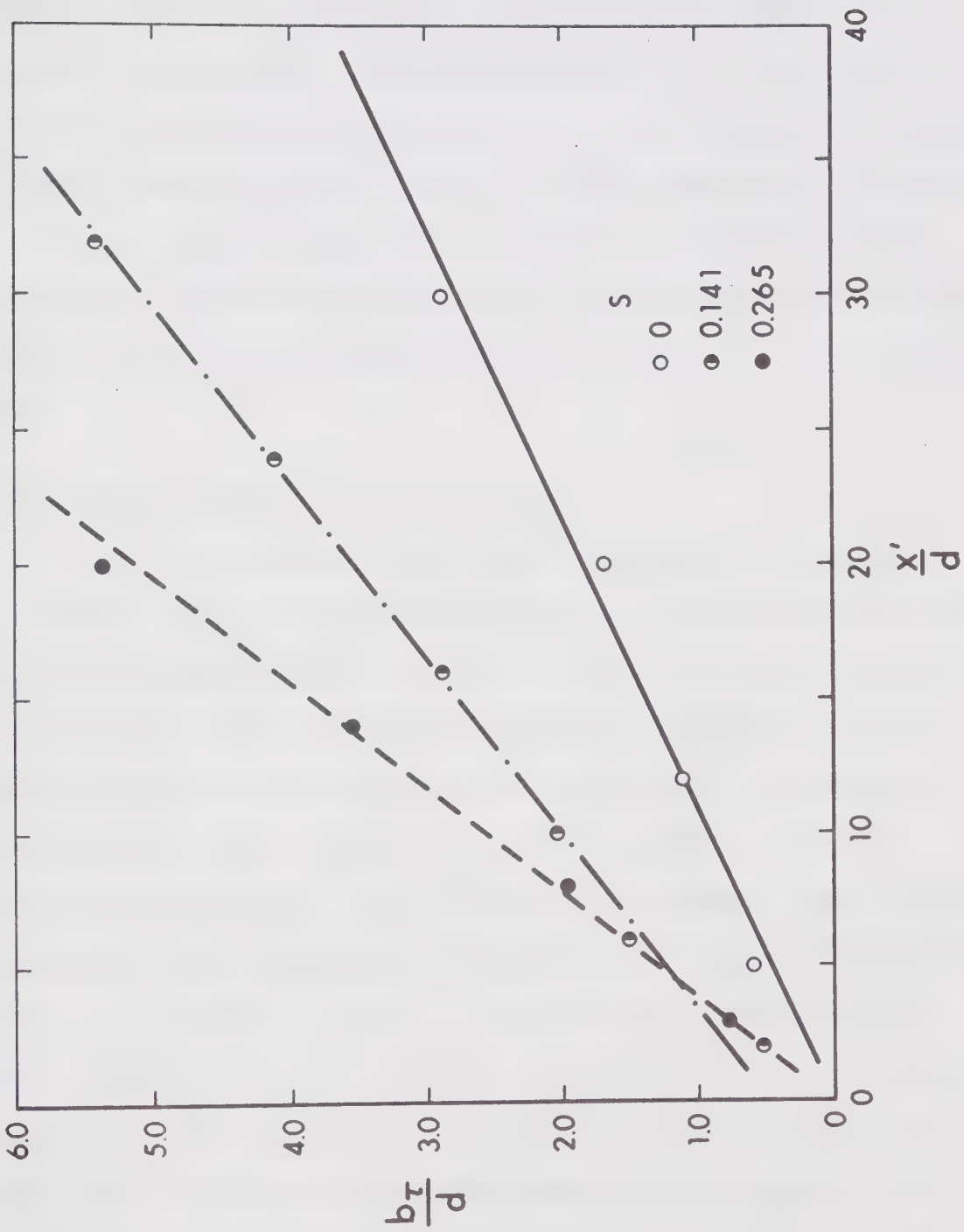


FIGURE 7.8 NON-DIMENSIONAL BED SHEAR DISTRIBUTION

FIGURE 7.9 VARIATION OF LENGTH SCALE b_τ

of representing the bed shear distribution is given in Figure 7.10. In case of $S = 0$ and 0.141 , the distribution for $x'/d < 10$ follow different curves and beyond this limit, all the test points tend to fall into a single curve. For the highest swirl ($S = 0.265$), the distribution becomes similar even at $x'/d = 3.0$. Experimental curves are drawn through the points lying on profiles that exhibit similarity and are then assembled together in Figure 7.11. This indicates that the shape of the similarity distribution changes with S and the lateral extent in which the bed shear acts increases greatly with an increase in swirl.

7.3.9 Decay of Centerline Bed Shear Stress

The centerline bed shear stress represents the maximum at any section. This is non-dimensionalised by the mean efflux velocity and the streamwise variation is given in Figure 7.12. For the case of zero swirl with the 0.75" diameter nozzle the centerline bed shear was determined by a total head tube as well as with a yaw probe, and the results are shown in Figure 7.12. The agreement of the data from the two methods was close and both follow the mean curve derived earlier for three dimensional wall jets of various shape (Chapter IV). This gives confidence in the yaw probe technique for shear measurements. For jets with swirl τ_{om} falls very rapidly right from the outlet section. The rapid fall in the intensity is expected as the lateral extent over which the bed shear acts increases very much with swirl and would therefore give a far smaller peak value on the center-

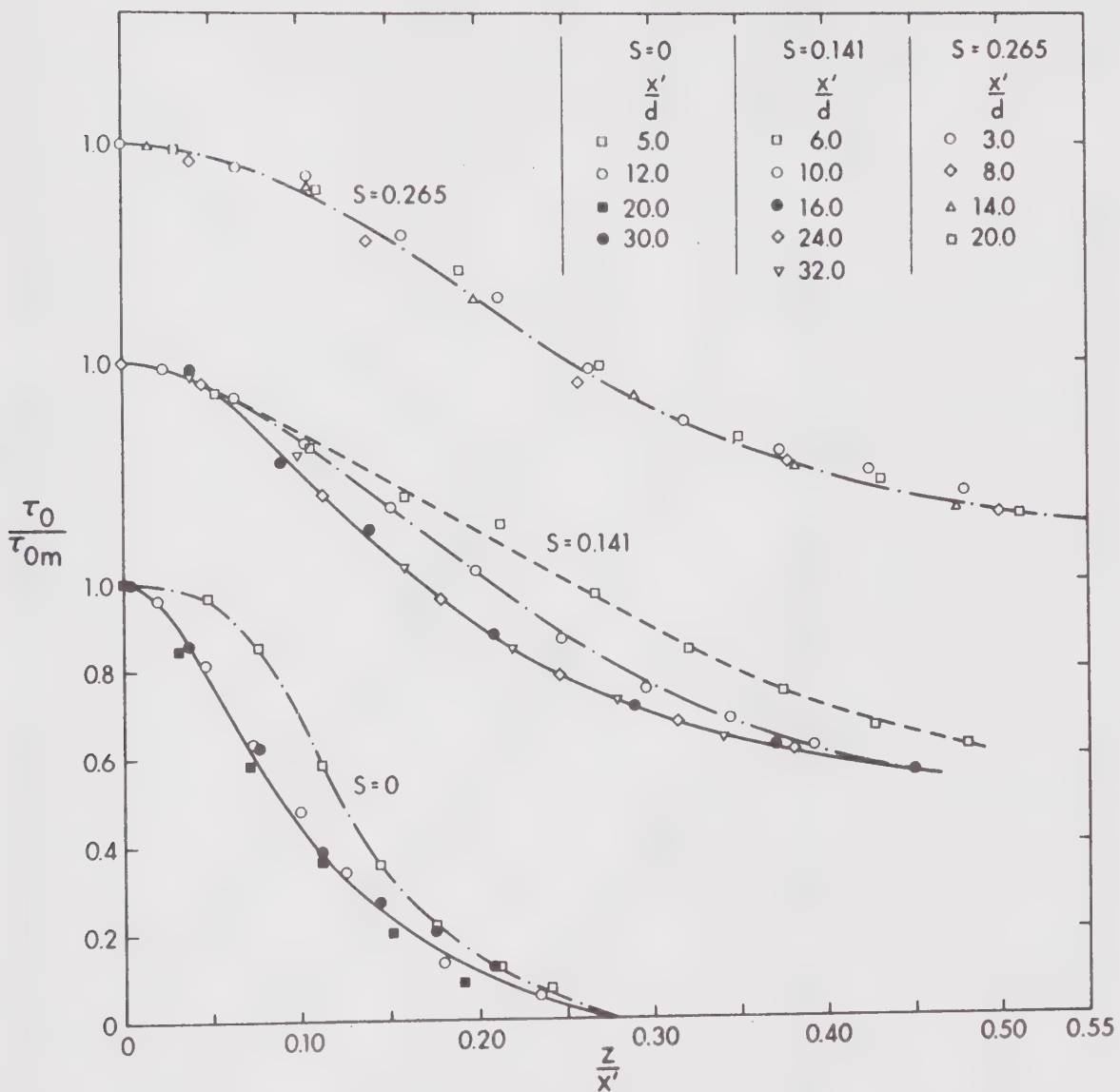


FIGURE 7.10 NON-DIMENSIONAL BED SHEAR DISTRIBUTION
(WITH x' AS THE LENGTH SCALE)

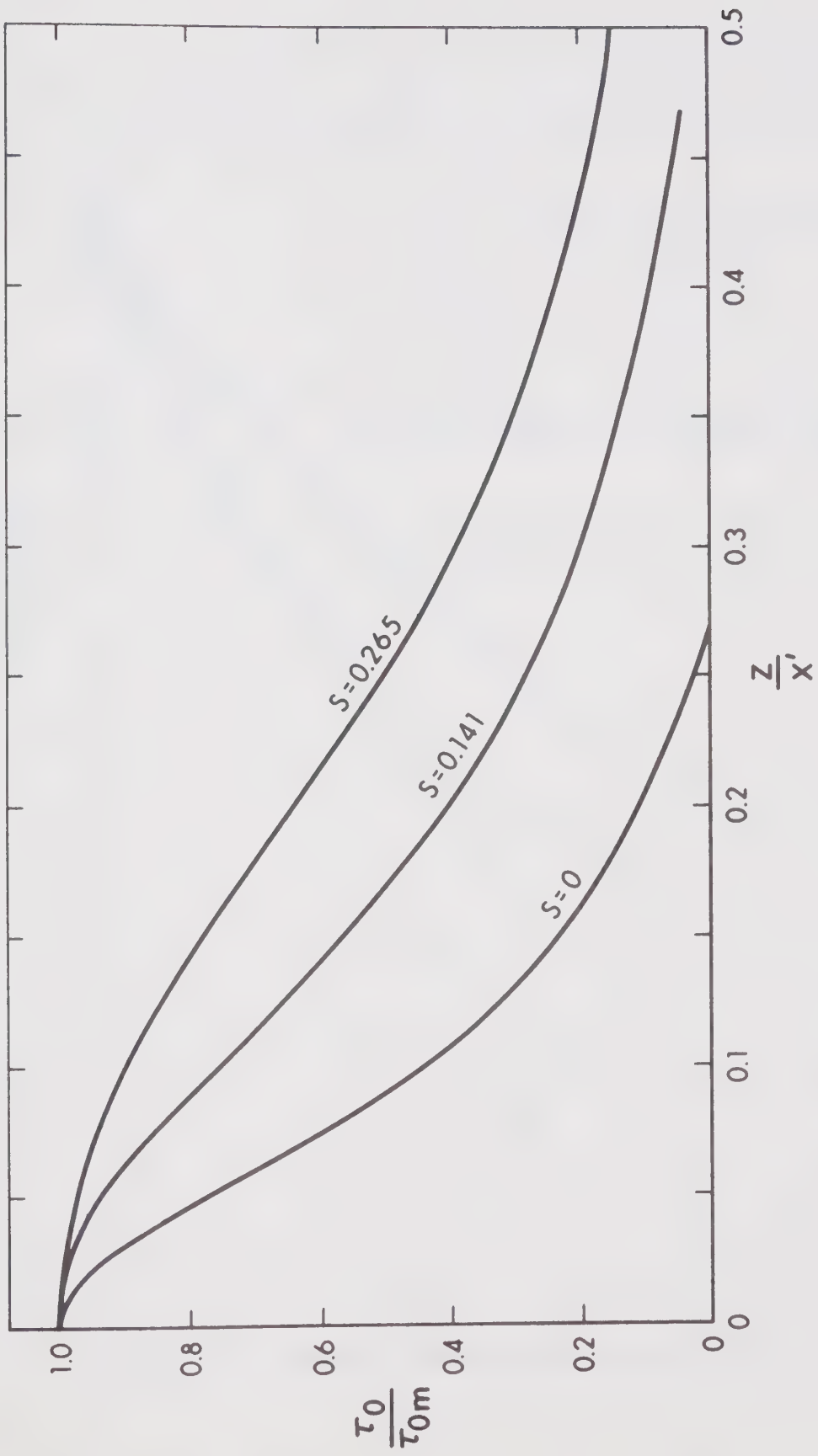


FIGURE 7.11 EFFECT OF SWIRL ON BED SHEAR DISTRIBUTION

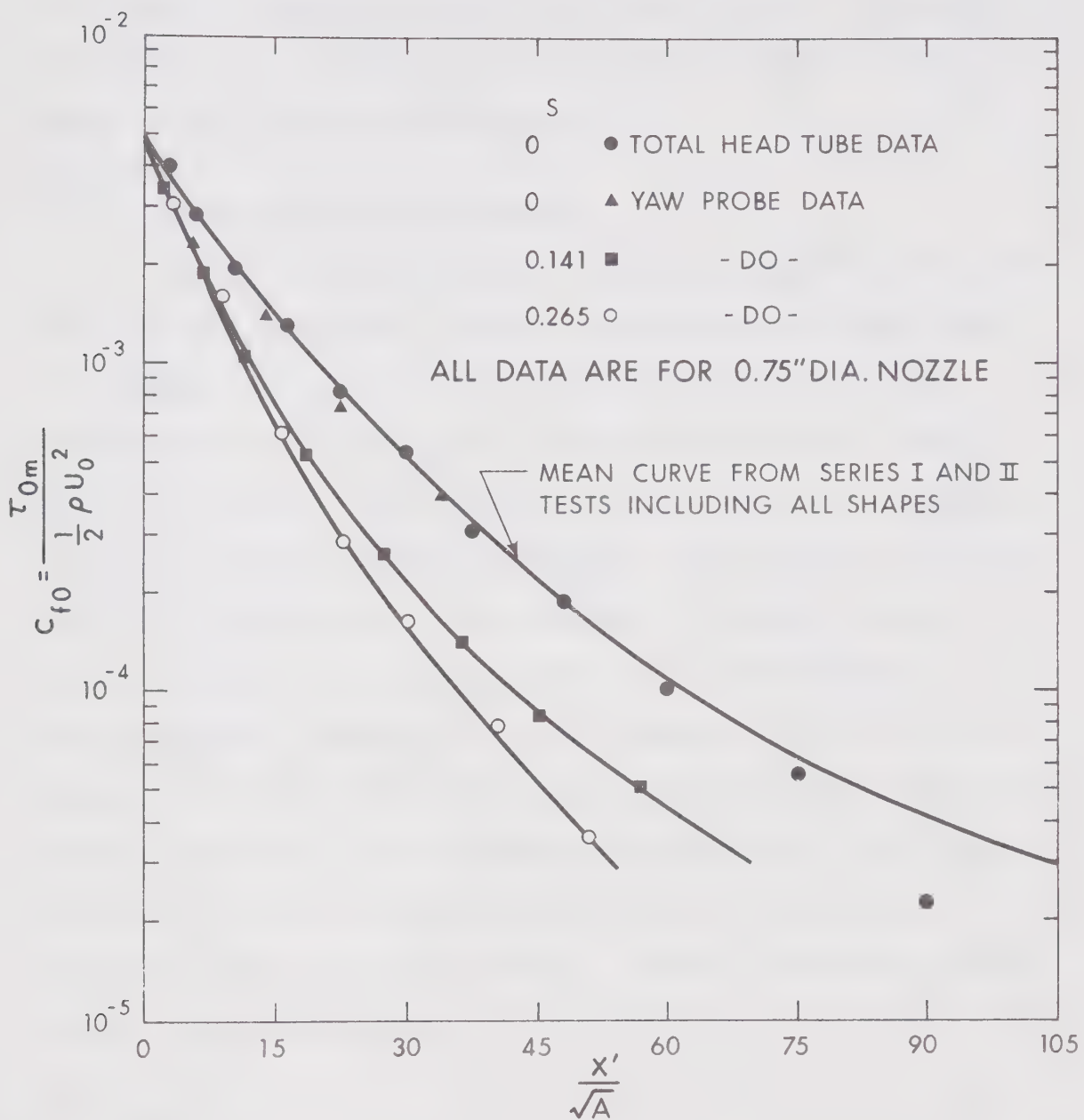


FIGURE 7.12 DECAY OF CENTERLINE SHEAR STRESS FOR SWIRLING JETS

line. Here again, a weak swirl is found to be most effective and the effects are not enhanced very much for stronger swirls. The maximum shear stress at corresponding sections of swirling jets is 2 to 2.5 times less than that for a non-swirling jet.

7.3.10 Transverse Bed Shear Component

In the discussions so far, only the x component of bed shear vector has been considered. However, some knowledge is needed about the z component if one is to have a complete picture of the shear distribution below outlets. Of all the alternative ways of representation, it was felt that an indication as to how the yaw angle would vary with z would be the simplest to get a rough estimate of the transverse shear component, once the x component τ_0 is known. Hence, for the various swirls investigated, the data for the yaw angle θ vs. z/x' were plotted for a number of x stations (Figure 7.13). As the swirl component at sections close to the nozzle were strong but unsymmetric, because of the wall, θ does not behave systematically. For distances beyond 8 to 10d, the flow looks symmetric about the x -axis and θ increases linearly with z/x' . Further, the data from various sections collapse into a single curve.

7.4 Summary

The velocity distribution along the centerline of the jet normal to the wall was found to be similar. The distribution of axial components of velocity and bed shear in the transverse direction were also found to be similar and closely followed Goertler's curve. Even

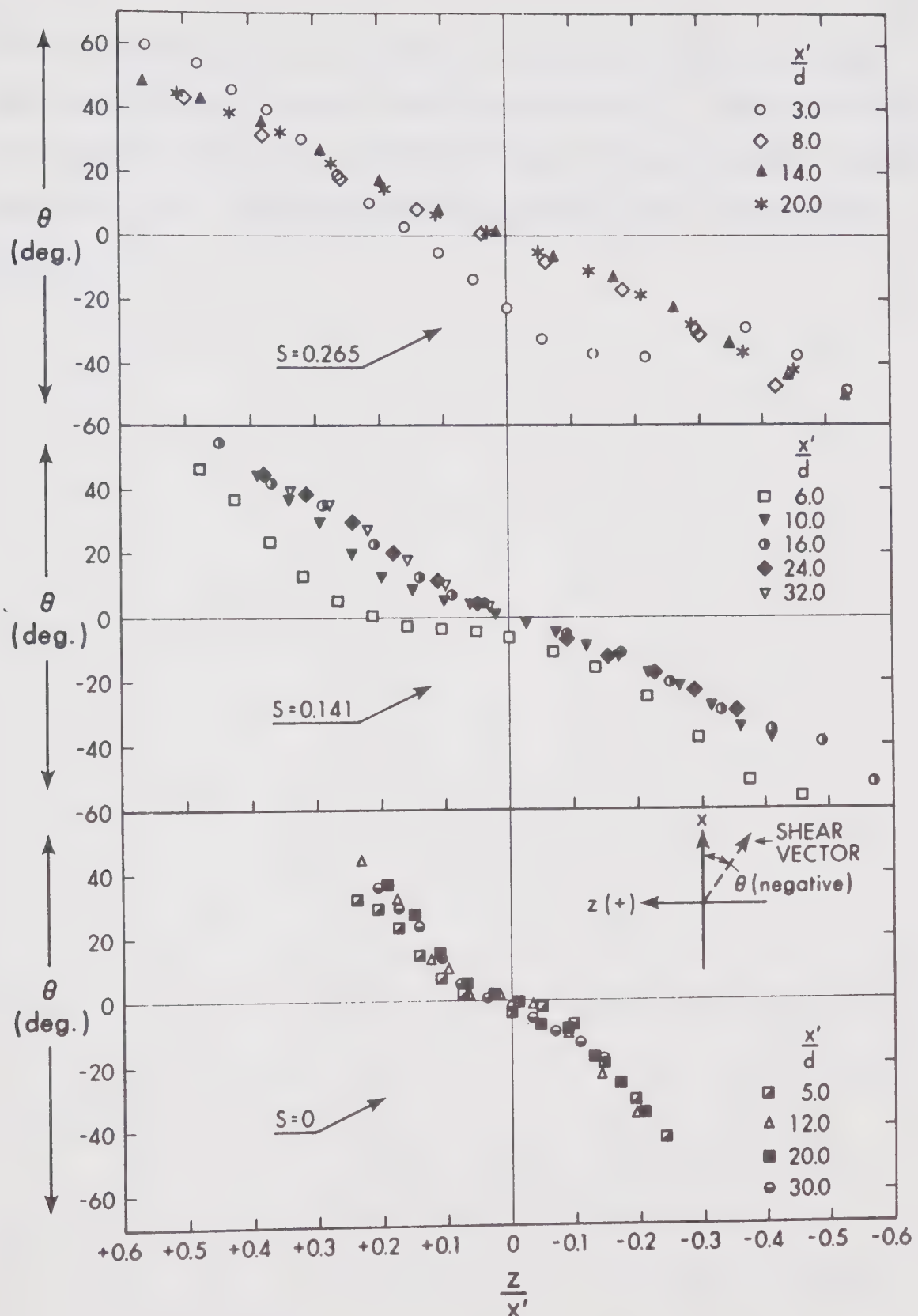


FIGURE 7.13 YAW ANGLE FOR OFF-CENTER BED SHEAR VECTOR

for the highest value of $S = 0.265$, all the length scales and the maximum velocity decay followed a linear variation with x . The growth rate of the jet and the velocity decay were faster for swirling jets. Moderate swirls were found to be very effective in reducing the centerline bed shear stress.

CHAPTER VIII

CONCLUSIONS AND RECOMMENDATIONS

8.1 Summary and Conclusions

In hydraulic engineering, flows from deeply submerged circular and rectangular outlets are often encountered. A turbulent wall jet issuing from a circular, elliptic, triangular or rectangular outlet of finite aspect ratio is three dimensional in nature. As an initial step towards understanding the mechanics of flow from submerged outlets, a simple free jet was considered for analysis. Based on the observation that the forward-momentum flux of the wall jet was not reduced to any appreciable degree, the free jet analysis was extended to three-dimensional wall jets. Extensive experimental investigations were then conducted on wall jets issuing into a wide channel from nozzles of various shapes. Aspects of practical interest, such as the effect of the channel side walls, the boundary roughness, and swirl were experimentally investigated on circular wall jets. A summary of the investigation on each aspect is included in the respective chapters. The significant conclusions drawn from the present investigation are collected and are presented below.

From a similarity analysis (Chapter II) on the boundary-layer type of equations, the maximum velocity decay and the growth of the length scales for a three dimensional wall jet were given by the following expressions.

$$u_{mo} \propto x^{-1.0}$$

$$b_y \propto x \quad (8.1)$$

$$b_z \propto x$$

Dimensional considerations also indicated the same type of variations. Moreover, dimensional considerations indicated that \sqrt{A} , the square root of the cross-sectional area of the outlet (Eq. 2.63), should be taken as a characteristic length if the shape effects of the nozzle are to be eliminated. An expression for the centerline bed shear stress variation was derived in terms of the characteristic parameter \sqrt{A} and the Reynolds number of the jet at the efflux section.

Experimental observations (Chapter IV) on wall jets of various shapes showed that in the fully developed flow ($x'/h \geq 15$), the velocity profiles satisfied similarity and the classical wall jet curve served as a good approximation for describing the data in the center-plane. The distribution in the transverse direction of the fully-developed flow were also found to be similar, following closely Goertler's free circular jet curve. The theoretical relationships given in Eq. 8.1 were in general found to be satisfied. The length scale b_z grows 4 to 5 times faster than b_y . The virtual origins for the velocity scale and the two length scales were located at widely varying distances from the nozzle, suggesting that the flow was not truly self-preserving. Use of \sqrt{A} to nondimensionalise x' , as suggested by dimen-

sional considerations, describes the maximum velocity decay relationship by a unified curve regardless of the nozzle shape. The boundary shear stress distributions in the transverse directions were similar and followed Goertler's velocity distribution curve. The centerline boundary shear stress coefficient $c_f (= \tau_{om} / \frac{1}{2} \rho u_{mo}^2)$ equalled 0.0065 in the far field and was found to be a constant.

It was observed in Chapter V that when a circular wall jet diffuses in channels of finite width, in a certain initial region ($x'/d < 35$, for the range of widths considered in the present investigation) the velocity decay and growth of b_y were not affected by the side walls of the channel. However, the similarity of the centerline velocity profiles was not satisfied. The maximum forward velocity and the centerline bed shear stress in narrow channels were higher compared to the values for a infinitely wide case. A lower limit for W/d of 30 is tentatively suggested, beyond which most results derived from investigation on a three dimensional wall jet discharging into a wide channel seem to apply.

For flow over a rough boundary (Chapter VI), the centerline velocity profile normal to the wall was considered in two parts - the free-mixing zone and the inner zone. The velocity distribution in the free-mixing region was similar and was very well described by the classical wall jet profile regardless of the boundary roughness. The distribution in the inner zone was also similar and a power-law type of representation was satisfactory for representing the data. The growth of length scales for the free-mixing region was unaffected

by the boundary roughness and the streamwise variation was linear. The velocity scale u_{mo} varied as $x^{-1.0}$ and the boundary roughness did not seem to affect the relationship x'/\sqrt{A} vs. u_{mo}/U_0 to any significant extent. This finding was also supported by the analysis of the available data for plane wall jets on rough boundaries (Section 6.3). Hence, for preliminary estimates, the curve for the three-dimensional wall jet on a smooth boundary is recommended for use in engineering practice so long as the roughness of the bed is not excessive. The growth of the length scale b_z on a rough boundary was not linear, although the distribution in the transverse direction was similar and was given by Goertler's curve.

Experiments on circular swirling wall jets (Chapter VII) with moderate swirl showed the centerline velocity distribution normal to the wall to be similar and could be described by the classical wall jet curve. For moderate swirls, all the length scales, including the one for bed shear distribution, followed a linear variation with x . Also, the maximum velocity $u_{mo} \propto x^{-1.0}$. The transverse growth rate of the jet and the decay of the maximum velocity were faster for swirling jets, and in particular moderate swirls proved to be very effective. Swirls were also found to be very effective in reducing the centerline bed shear stress.

8.2 Recommendations for Further Study

For better understanding of the flow from deeply submerged outlets, the following topics are recommended for future study.

1. A detailed investigation on the initial reach ($x'/h \lesssim 15$) of the jet. This would be very useful in engineering practice, particularly in hydraulic engineering.
2. Measurements of the velocity components u , v , w and the turbulent shear stresses for an air wall jet. This would check the basic assumptions made in the similarity analysis and might give better insight to the mechanics of the flow.
3. A satisfactory method of analysis considering the effects of the side walls. Study of this kind would in general be very useful in practice.
4. More experimental observations on swirling wall jets. This would supplement the present exploratory studies and cover a wider range of swirl numbers.

LIST OF REFERENCES

1. Abramovich, G.N., "The Theory of Turbulent Jets", M.I.T. Press, Cambridge, Mass., 1963 (English Translation).
2. Albertson, M.L., Dai, Y.B., Jensen, R.A., and Rouse, H., "Diffusion of Submerged Jets", Trans. ASCE, Vol. 115, 1950.
3. Anwar, H.O., Weller, J.A., "A Thin Rectangular Jet Discharging into a Slow-Moving Stream", Water Power, June 1969.
4. Bradbury, L.J.S., "The Structure of a Self-Preserving Turbulent Plane Jet", J. of Fluid Mechanics, Vol. 23, 1965.
5. Chigier, N.A., and Chervinsky, A., "Experimental and Theoretical Study of Turbulent Swirling Jets Issuing from a Round Orifice", Israel J. of Tech., Vol. 4, 1966.
6. Chigier, N.A., and Chervinsky, A., "Experimental Investigation of Swirling Vortex Motion in Jets", Trans. ASME, J. of Appl. Mech., June 1967.
7. Corrsin, S., "Investigation of Flow in an Axially Symmetrical Heated Jet of Air", NACA Wartime Rept., Dec. 1953.
8. Flora, J.J., and Goldschmidt, V.W., "Virtual Origins of a Free Plane Turbulent Jet", AIAA Journal, Vol. 7, Dec. 1969.
9. Forstall, W. and Shapiro, A.H., "Momentum and Mass Transfer in Coaxial Gas Jets", Trans. ASME, J. of Appl. Mech., Dec. 1950.

10. Glauert, M.B., "The Wall Jet", J. of Fluid Mech., 1956.
11. Goldstein, S., Modern Development in Fluid Dynamics", Dover Publications, New York, 1965.
12. Gore, R.W., and Ranz, W.E., "Backflows in Rotating Fluids Moving Axially Through Expanding Cross Sections", J. American Inst. of Chem. Engrs., Vol. 10, 1964.
13. Head, M.R., and Rechenberg, I., "The Preston Tube as a Means of Measuring Skin Friction", J. Fluid Mech., Vol. 14, 1962.
14. Hollingshead, A.B., "Boundary Shear Distribution in Open Channel Flow", Ph.D. Thesis, Dept. of Civil Engg., Univ. of Alberta, Edmonton, Canada, 1972.
15. Hwang, L.S., and Laursen, E.M., "Shear Measurement Technique for Rough Surfaces". Proc. ASCE, J. Hyd. Div., March 1963.
16. Joubert, P.N., Perry, A.E., and Brown, K.C., "Critical Review and Current Developments in Three Dimensional Turbulent Boundary Layers", Fluid Mechanics of Internal Flow, Edited by Gino Sovran, Elsevier Publishing Co., 1967.
17. Kerr, N.M., and Fraser, D., "Swirl Part 1 - Effect on Axisymmetrical Turbulent Jets", J. Inst. of Fuel, Vol. 38, 1965.
18. Kruka, V., and Eskinazi, S., "The Wall Jet in a Moving Stream", J. of Fluid Mech., Vol. 20, 1964.
19. Kuethe, A.M., "Investigations of the Turbulent Mixing Regions Formed by Jets", Trans. ASME, J. of Appl. Mech., 1935.
20. Lau, Lam, "Flow Characteristics of Wall Jets on Smooth, Rough and Porous Walls", M.A.Sc. Thesis, Dept. of Mech. Engrg. Univ. of Toronto, 1963.

21. Lewis, W.E., "Fixed Direction Probes for Aerodynamic Measurements", Proc. Instn. Mech. Engrs., Vol. 180, 1965-66.
22. MacMillan, F.A., "Experiments on Pitot-tubes in Shear Flow", Aeronautical Research Committee Reports and Memoranda, No. 3028, Feb. 1956.
23. Myers, G.E., Schauer, J.J., and Eustis, R.H., "Plane Turbulent Wall Jet Flow Development and Friction Factor", Trans. ASME, J. of Basic Engineering, March 1963.
24. Newman, B.G., "The Deflexion of Plane Jets by Adjacent Boundaries - Coanda Effect", Boundary-Layer and Flow Control, Vol. I, Pergamon Press, 1961.
25. Newman, B.G., "The Prediction of Turbulent Jets and Wall Jets", Canadian Aeronautics and Space Journal, Oct. 1969.
26. Newman, B.G., Patel, R.P., Savage, S.B., and Tijo, H.K., "Three Dimensional Wall Jets Originating from a Circular Orifice", McGill Univ., Montreal, Jan. 1971.
27. Patel, V.C., "Calibration of the Preston Tube and Limitations on its Use in Presusre Gradients", J. Fluid Mech., Vol. 23, 1965.
28. Pratte, B.D., and Keffer, J.F., "Swirling Turbulent Jet Flows - Part 1 - The Single Swirling Jet", Univ. of Toronto, Mech. Engrg. Dept. Rept. 6901, March 1969.
29. Preston, J.H., "The Determination of Turbulent Skin Friction by Means of Pitot Tubes", J. Royal Aeronautical Society, London, England, Vol. 58, 1954.

30. Rajaratnam, N., "Plane Turbulent Wall Jets on Rough Boundaries", Dept. of Civil Engrg. Report, Univ. of Alberta, Edmonton, Canada, July 1965.
31. Rajaratnam, N., "Theoretical Calibration Curve for the Preston Tube", J. Royal Aeronautical Society, England, Vol. 69, 1965.
32. Rajaratnam, N., and Subramanya, K., "Diffusion of Rectangular Wall Jets in Wider Channels", J. of Hyd. Research, March 1967.
33. Rajaratnam, N., and Subramanya, K., "Flow Immediately Below Submerged Sluice Gates", Proc. ASCE, J. of Hyd. Division, July 1967.
34. Rajaratnam, N., and Muralidhar, D., "Yaw Probe Used as Preston Tube", The Aeronautical J. of the Royal Aeronautical Society, Dec. 1968.
35. Rajaratnam, N., and Muralidhar, D., "Submerged Non-Rectangular Outlets", La Houille Blanche, No. 1 - 1969.
36. Rose, W.G., "A Swirling Round Turbulent Jet, 1 - Mean Flow Measurements", Trans. ASME, J. of Appl. Mechanics, Dec. 1962.
37. Rosenhead, L., "Laminar Boundary Layers", Clarendon Press, Oxford, England, 1963.
38. Sami, S., Carmody, T., and Rouse, H., "Jet Diffusion in the Region of Flow Establishment", J. of Fluid Mech., Vol. 27, 1967.
39. Schlichting, H., "Boundary Layer Theory", McGraw-Hill Book Co., Inc., N.Y., 1968.

40. Schubauer, G.B. and Tchen, C.M., "Turbulent Flow", Princeton University Press, Princeton, N.J., 1961.
41. Schwarz, W.H., Cosart, W.P., "The Two Dimensional Turbulent Wall Jet", J. of Fluid Mech., Vol. 10, 1961.
42. Sforza, P.M., Steiger, M.H., and Trentacoste, N., "Studies on Three Dimensional Viscous Jets", AIAA Journal, Vol. 5, No. 5, May 1966.
43. Sforza, P.M., Herbst, G., "A Study of Three Dimensional, Incompressible, Turbulent Wall Jets", Polytechnic Inst. of Brooklyn, Dept. of Aerospace Engrg. and Appl. Mech., PIBAL Report No. 1022, Oct. 1967.
44. Sforza, P.M., "A Quasi-Axisymmetric Approximation for Turbulent, Three Dimensional Jets and Wakes", AIAA Journal, Vol. 7, No. 7, July 1969.
45. Sigalla, A., "Measurements of Skin Friction in a Plane Turbulent Wall Jet", J. of the Royal Aeronautical Society, London, Vol. 62, Dec. 1958.
46. Spink, L.K., "Principles and Practice of Flow Meter Engineering", The Foxboro Company, Mass., U.S.A., 1958.
47. Squire, H.B., and Troucer, J., "Round Jets in a General Stream", R & M, 1974 of the Aeronautical Research Council, England, Jan. 1944.
48. Subramanya, K., "Some Studies on Turbulent Wall Jets in Hydraulic Engineering", Ph.D. Thesis, Dept. of Civil Engg., Univ. of Alberta, Edmonton, Canada, 1967.

49. Trentacoste, N., and Sforza, P., "Further Experimental Results for Three Dimensional Free Jets", AIAA Journal, Vol. 5, No. 5, May 1967.

Also see Trentacoste, N., and Sforza, P.M., "An Experimental Investigation of Three Dimensional Free Mixing in Incompressible, Turbulent, Free Jets", Polytechnic Inst. of Brooklyn, Dept. of Aerospace Engrg. and Appl. Mech., PIBAL Report No. 871, March 1966.

50. Viets, H., and Sforza, P.M., "An Experimental Investigation of a Turbulent, Incompressible, Three Dimensional Wall Jet", Polytechnic Inst. of Brooklyn, Dept. of Aerospace Engg. and Appl. Mech., PIBAL Report No. 968, April 1966.

51. Wygnanski, I. and Fiedler, H., "Some Measurements in the Self Preserving Jet", J. of Fluid Mech., Vol. 38, 1969.

52. Yevdjevich, V.M., "Diffusion of Slot Jets with Finite Orifice Length-Width Ratios", Hydraulics Papers, Colorado State Univ., Fort Collins, Colorado, March 1966.

APPENDIX A
TURBULENT COMPOUND ANNULAR SHEAR LAYERS

APPENDIX A

TURBULENT COMPOUND ANNULAR SHEAR LAYERSA.1 Introduction

Consider a circular jet of diameter d issuing from a nozzle with an uniform velocity U_0 into a large stagnant mass of the same fluid. Due to the velocity discontinuity on the periphery of the jet, shear stresses are set up and a shear layer originates at the plane of the nozzle. In most practical cases, these shear layers become turbulent very close to the nozzle itself. This shear layer is termed as a simple shear layer. If the surrounding fluid is also in motion, then the shear layers are referred to as the turbulent compound annual shear layers. A schematic representation of such a shear layer is shown in Figure A.1, in which U_1 is the velocity of the surrounding fluid, \bar{x} is the axial distance measured from the nozzle, x is axial distance measured from a virtual origin, r is the radial distance, r_1 and r_2 are the radial distances to the inner and outer edges of the shear layer, u is the turbulent mean velocity in the axial direction, $u_m = U_0$, $U = u - U_1$ and $U_m = U_0 - U_1$.

A similarity type of analysis is presented to show that r_1 and r_2 vary linearly with x . This greatly simplifies computation in the existing relationship derived by Squire and Trouncer (1944). These predicted linear variations were then checked experimentally for four values of jet velocity to secondary stream velocity ratios. The be-

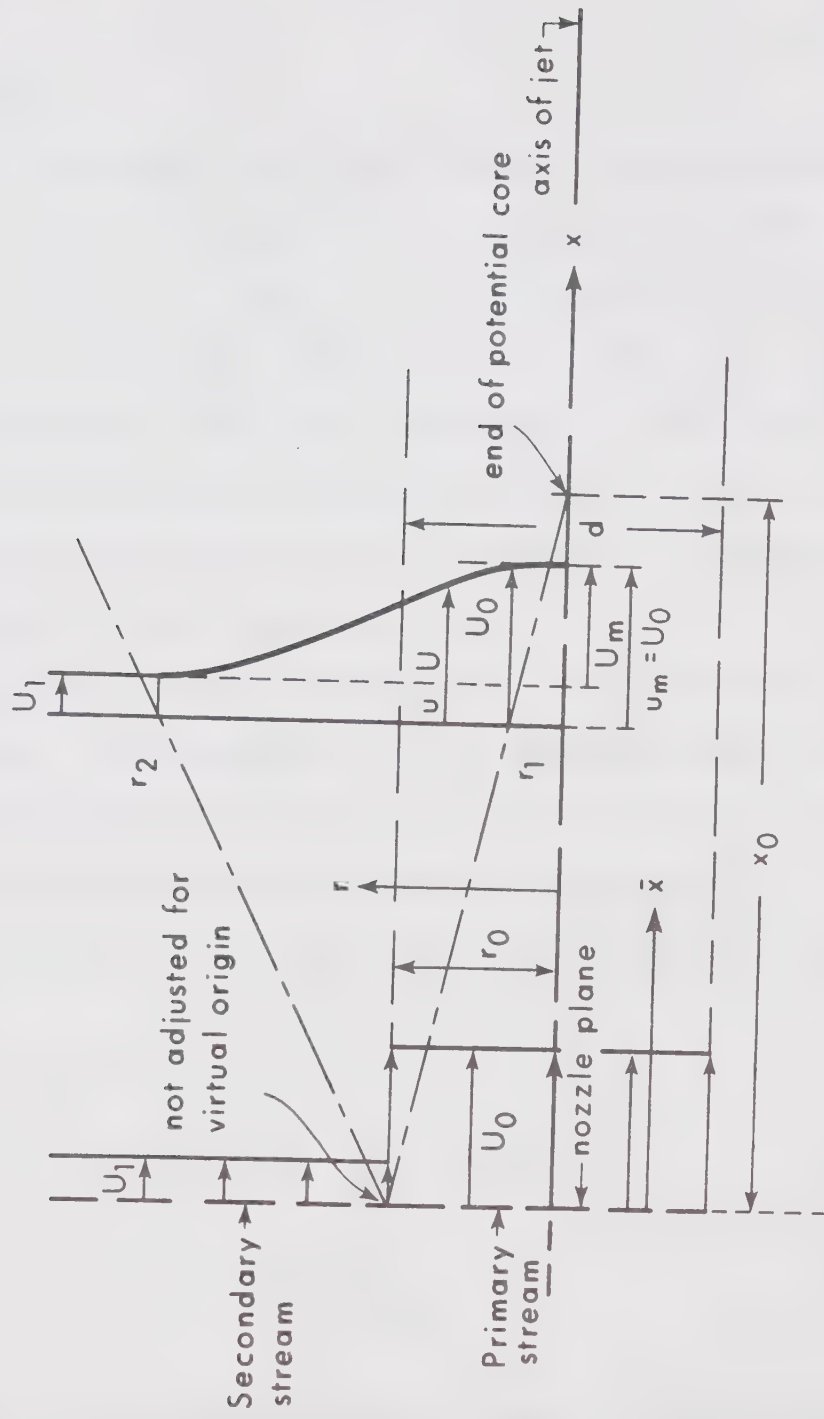


FIGURE A.1 DEFINITION SKETCH OF COMPOUND ANNULAR SHEAR LAYER

haviour of constant c in the mixing length relationship (Eq. A.6) is also discussed.

A.2 Existing Work

The simple annular shear layer has been studied by Kuethe (1935), Corrsin (1953), Abramovich (1963), Albertson et al (1950) and more recently by Sami et al (1967). Similarity analysis as well as experimental observations have shown that both r_1 and r_2 vary linearly in the axial direction. The velocity distribution in the shear layer can be represented by a Gaussian expression (Albertson et al), cosine expression (Squire and Trouncer) or by the expression developed by Schlichting (1968) for the turbulent far wake.

The compound annular shear layer has received only very little attention. On the experimental side, Abramovich quotes the results of Yakovlovskiy for $\lambda = U_1/U_0 = 0.4$, for an isothermal case which showed that for this particular value of the velocity ratio the velocity distribution was similar and can be represented by the expression,

$$\frac{U}{U_m} = \frac{u-U_1}{U_0-U_1} = [1 - \bar{n}^{3/2}]^2 \quad (A.1)$$

where

$$\bar{n} = \frac{r-r_1}{r_2-r_1}$$

Squire and Trouncer developed an integral method for predicting the growth of the compound annular shear layer. Assuming

c^2 (Eq. A.7) to be a constant quantity, results have been presented for various values of λ . However, the main predictions of Squire and Trouncer have not been checked experimentally. The length of potential core given by their method does not agree with the experimental results of Forstall and Shapiro(1950).

The expressions derived by Squire and Trouncer are briefly indicated below, as these results would be needed in computing r_1 and r_2 by the simplified procedure suggested in the present analysis.

The equations of motion for the axisymmetric jet can be written as

$$u \frac{\partial u}{\partial x} + v \frac{\partial u}{\partial r} = \frac{1}{\rho} \frac{1}{r} \frac{\partial}{\partial r} (r\tau) \quad (\text{A.2})$$

$$\frac{\partial}{\partial x} (ru) + \frac{\partial}{\partial r} (rv) = 0 \quad (\text{A.3})$$

where v is the turbulent mean velocity in the radial direction, τ is the turbulent shear stress and ρ is the mass density of the fluid. The viscous shear stress has been neglected in Eq. A.2.

Multiplying Eq. A.2 by ρr and on integration,

$$\frac{\partial}{\partial x} \int_0^r \rho u^2 r dr - \rho u \frac{\partial}{\partial x} \int_0^r u r dr = r\tau \quad (\text{A.4})$$

It was assumed that the velocity distribution in the annular shear is described by a cosine function of the form

$$\frac{U}{U_m} = \frac{1}{2} [1 - \cos\pi\zeta] \quad (A.5)$$

where

$$\zeta = \frac{r_2 - r}{r_2 - r_1}$$

Prandtl's mixing length was assumed to be proportional to the width of the mixing region, so that

$$\ell = c(r_2 - r_1) \quad (A.6)$$

and the turbulent shear stress is given by,

$$\tau = \rho [c(r_2 - r_1)]^2 \left(\frac{\partial u}{\partial r} \right)^2 \quad (A.7)$$

where ℓ is the mixing length and c is an empirical constant. At this point, Squire and Trouncer assumed c^2 to be invariant with the velocity ratio U_1/U_0 and assigned a constant value of 0.0067, which they obtained from experiments on a circular jet issuing into a stagnant environment.

Equation A.4 was evaluated for $r = r_2$ and $r = (r_1 + r_2)/2$ and the following two equations were derived.

$$a_{11} r_1^2 + 2a_{10}r_1r_2 + a_{00}r_2^2 = r_0^2 \quad (A.8)$$

$$\frac{d}{dx} [A_{11}r_1^2 + 2A_{10}r_1r_2 + A_{00}r_2^2] = B[r_1+r_2] \quad (A.9)$$

where r_0 is the radius of the nozzle, and

$$\begin{aligned} a_{11} &= 2 \left[\frac{5-\lambda}{16} - \frac{1}{\pi^2} \right]; \quad a_{10} = \frac{2}{\pi^2} \\ a_{00} &= 2 \left[\frac{3+\lambda}{16} - \frac{1}{\pi^2} \right]; \quad A_{11} = \frac{13+3\lambda}{16} - \frac{1+\lambda}{2\pi} - \frac{5+3\lambda}{4\pi^2} \\ A_{10} &= \frac{1-\lambda}{16} + \frac{5+3\lambda}{4\pi^2}; \quad A_{00} = \frac{1-\lambda}{16} + \frac{1+\lambda}{2\pi} - \frac{5+3\lambda}{4\lambda^2} \\ B &= -\frac{\pi^2}{2} [1-\lambda] c^2 \end{aligned} \quad (A.10)$$

From Eqs. A.8 and A.9, r_1/r_0 and r_2/r_0 were evaluated in a rather laborious manner and were plotted against c^2x/r_0 for various values of λ . These results are discussed later.

A.3 Present Analysis

A similarity analysis was performed on the equations of motion, making the following assumptions,

$$\frac{U}{U_m} = f\left(\frac{r-r_1}{b}\right) = f(\eta) \quad (A.11)$$

$$\frac{v}{U_m} = h(\eta) \quad (A.12)$$

$$\frac{-\tau}{\rho U_m^2} = g(\eta) \quad (A.13)$$

where b is a length scale, defined as the radial length from the inner edge of the shear layer to the point where $U = \frac{1}{2} U_m$, and v is the radial velocity. Regarding Eq. A.12, one could develop an expression for v/U_m from Eq. A.3, which would be rather tedious. From the experience on a number of free turbulent shear flows (Anwar and Weller, 1969) it appears reasonable to assume the form given by Eq. A.12.

Introducing the above expressions into Eq. A.2, it can be shown that,

$$\begin{aligned} [ng' + g - nhf'] &= - r_1' [\eta ff' + \frac{U_1}{U_m} \eta f'] + b' [\eta^2 ff' - \frac{U_1}{U_m} \eta^2 f'] \\ &+ \frac{r_1 r_1'}{b} [- ff' - \frac{U_1}{U_m} f'] + \frac{r_1 b'}{b} [\eta ff' - \frac{U_1}{U_m} \eta f'] + \frac{r_1}{b} [\eta f' - g] \quad (\text{A.14}) \end{aligned}$$

In Eq. A.14, the primes on r_1 and b represent differentiation with respect to x and the primes on f , h and g denote differentiation with respect to η . For similarity of flow, the coefficients of η functions on the right hand side of the above equations will have to be independent of x . They could be constants or zero. Thus

$$r_1' \propto x^0$$

$$b' \propto x^0$$

$$\frac{r_1 r_1'}{b} \propto x^0 \quad (\text{A.15})$$

$$\frac{r_1 b'}{b} \propto x^0$$

$$\frac{r_1}{b} \propto x^0$$

If one assumes that

$$\begin{aligned} b &\propto x^q \\ (r_0 - r_1) &\propto x^{q_1} \end{aligned} \quad (\text{A.16})$$

Then in the latter part of the shear layer it is possible to have similarity with $q = q_1 = 1$, whereas in the earlier part, it does not appear feasible to obtain simple values for the exponents in Eq. A.16. This places a restriction on the similarity relationships. Further, if a cosine distribution (Eq. A.5) is adopted for the velocity, it can be seen that $b = (r_1 + r_2)/2$, and therefore r_2 as well varies linearly with x .

Let $R_1 = r_1/r_0$, $R_2 = r_2/r_0$ and $X = x/r_0$. Then Eqs. A.8 and A.9 can be written as

$$a_{11}R_1^2 + 2a_{10}R_1R_2 + a_{00}R_2^2 = 1 \quad (\text{A.17})$$

$$\text{and } A_{11}R_1^2 + 2A_{10}R_1R_2 + A_{00}R_2^2 = B \int (R_1 + R_2) dX + K \quad (\text{A.18})$$

$$\text{If } R_1 = 1 - m_1 X \quad (\text{A.19})$$

$$R_2 = 1 + m_2 X$$

where \bar{x} has been taken to be the same as x , and m_1 and m_2 are the un-

known slopes, substitution of Eq. A.19 into Eq. A.18, with the boundary condition that $R_1 = 1$ and $R_2 = 1$ at $X = 0$, would yield

$$\begin{aligned} A_{11}R_1^2 + 2A_{10}R_1R_2 + A_{00}R_2^2 - R_1 \frac{BX}{2} - R_2 \frac{BX}{2} \\ = BX + A_{11} + 2A_{10} + A_{00} \end{aligned} \quad (\text{A.20})$$

For a given λ , the coefficients in Eq. A.17 and A.20 are constants and the two equations can be solved simultaneously for R_1 and R_2 for given values of X .

It was found that the results obtained by this procedure agree closely with the earlier computations of Squire and Trouncer as shown in Figure A.2.

A.4 Experiments

The primary jet was produced by a nozzle of inside diameter of 0.92", receiving its air supply from the compressed air line of the laboratory. The velocity of the primary jet was varied from 125.5 to 225.2 ft./sec. The nozzle was located in a rectangular air duct 9" wide, 15" deep and 13'-0" long, with suitable entrance arrangements (Figure A.3) and an exit diffuser, at the end of which a 1.5 H.P. blower was located. Four experiments were conducted with the velocity of the secondary stream U_1 equal to approximately zero, 58.0, 93.5 and 94.1 ft./sec. The value of $\lambda = U_1/U_0$ was respectively 0, 0.257, 0.496 and 0.75.

The velocity distribution in the axial vertical plane was

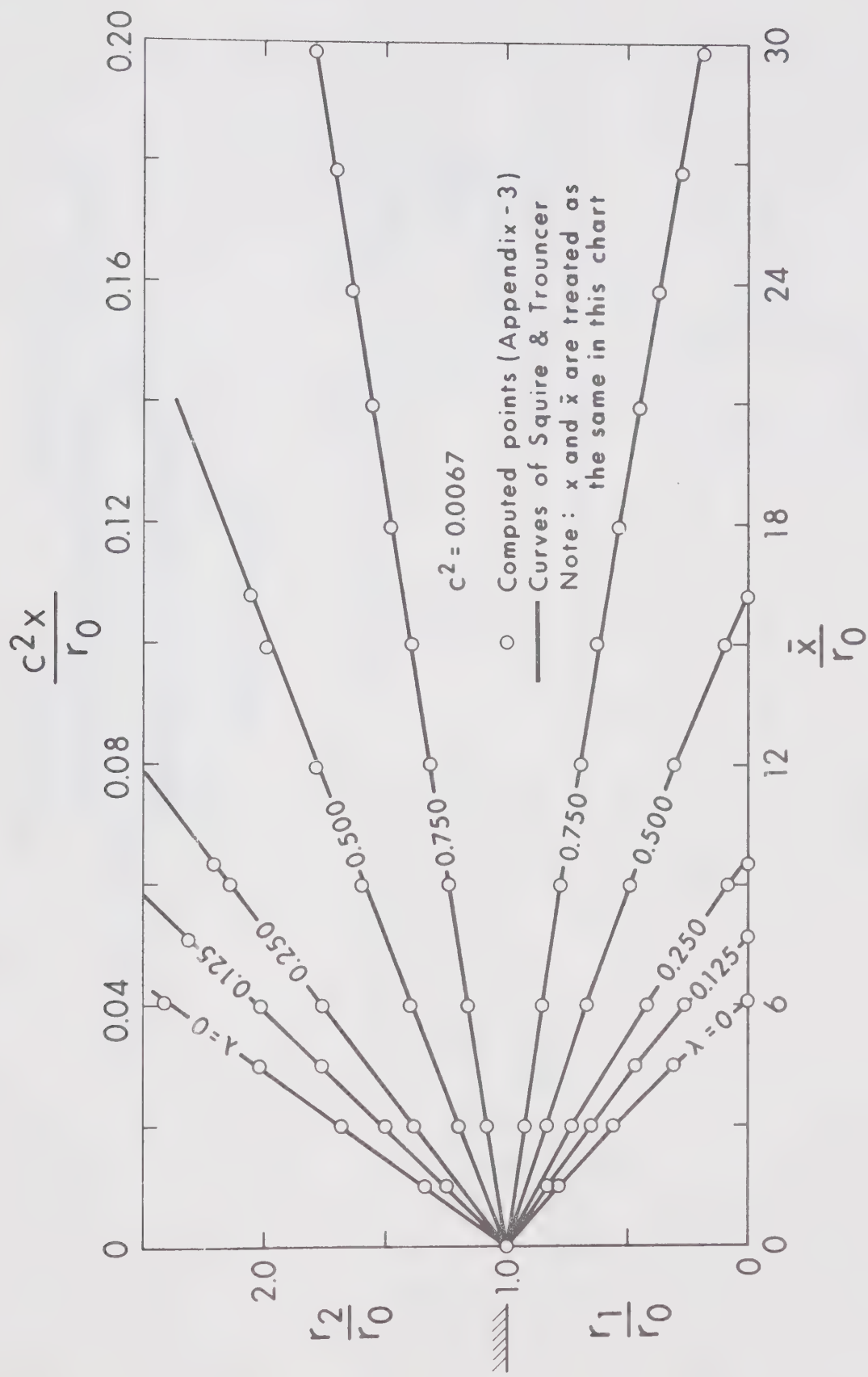


FIGURE A.2 VARIATION OF THE INNER AND OUTER EDGES OF THE SHEAR LAYER

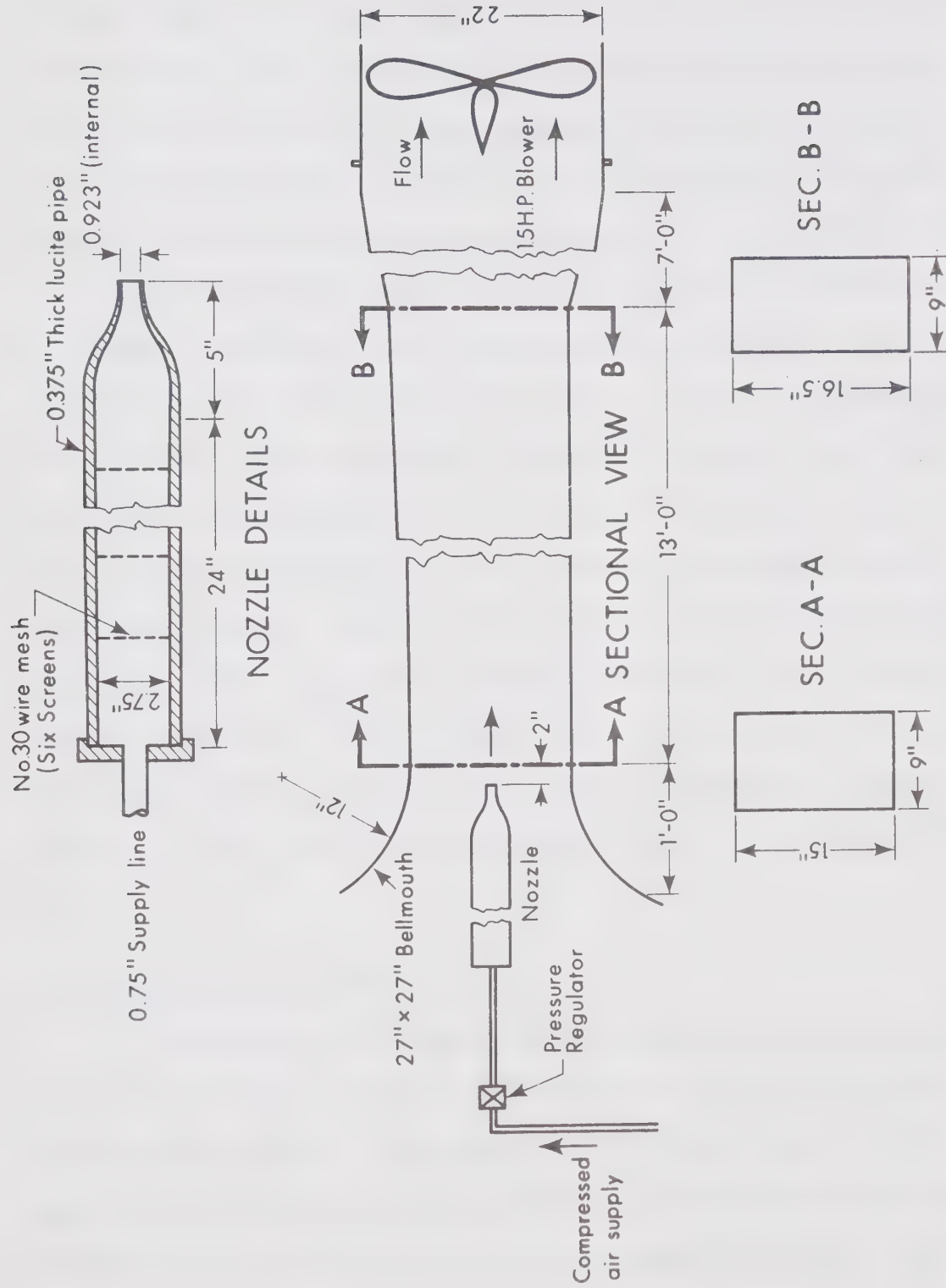


FIGURE A.3 EXPERIMENTAL ARRANGEMENT

measured with a total head tube of diameter 0.05", connected to a Göttingen type 655 inclined manometer which could be inclined in the range of 1:2 to 1:25. The manometer could read within an accuracy of ± 0.5 mm of water for the higher slope and the accuracy could be of the order of ± 0.05 mm of water for the lowest slope. The static pressure in the secondary stream was measured with a streamlined probe. In all four experiments, the velocity of the secondary stream did not vary to any significant extent in the zone of measurements. There was a maximum increase of 3% for the case with $\lambda = 0.75$. The measurements were continued close to the end of the potential core of the primary jet in the first three cases. However, in the fourth case, for $x/r_0 > 15.7$, long term fluctuations in the differential manometer reading over a wide range was observed. Hence measurements were not continued beyond $x/r_0 = 15.7$. A typical velocity distribution for $\lambda = 0.496$ is shown in Figure A.4. It can be seen that the non-uniformity observed in the secondary stream at the nozzle plane, disappears for larger values of x . The significant experimental results are given in Table A.1.

A.5 Analysis of Experimental Results

The velocity distribution data for the four velocity ratios were plotted with U/U_m versus ξ in Figure A.5 along the cosine curve of Squire and Trouncer. It is seen that in Figures A.5a to 5c, the experimental observations agree reasonably well with the cosine curve. For the case of $\lambda = 0.75$, the experimental observations show large

TABLE A.1

EXPERIMENTAL RESULTS ON LENGTH SCALE OF ANNULAR SHEAR LAYERS

λ	$\frac{\bar{x}}{r_0}$	$\frac{r_1}{r_0}$	$\frac{r_2}{r_0}$	$\frac{b}{r_0}$	λ	$\frac{\bar{x}}{r_0}$	$\frac{r_1}{r_0}$	$\frac{r_2}{r_0}$	$\frac{b}{r_0}$		
$(U_0 \approx 0, U_1 = 155.75 \text{ ft./sec.})$	0	0	0.935	1.08	0.083	0	0.496	0	0.86	1.04	0.149
	1.08	0.857	1.285	0.195	$(U_0 = 93.5 \text{ ft./sec., } U_1 = 188.3 \text{ ft./sec.})$		3.25	0.727	1.18	0.244	
	2.17	0.765	1.43	0.32			5.42	0.625	1.25	0.312	
	3.8	0.598	1.65	0.512			7.58	0.467	1.365	0.455	
	5.42	0.495	1.925	0.629			9.75	0.40	1.46	0.515	
	7.05	0.273	2.28	0.875			11.92	0.234	1.61	0.678	
	8.67	0.104	2.39	1.065			13.55	0.167	1.66	0.715	
							15.2	0.091	1.77	0.795	
$(U_0 = 58.0 \text{ ft./sec., } U_1 = 225.2 \text{ ft./sec.})$	0	0.922	1.04	0.078	0.75	0	0.987	1.012	0.078		
	1.63	0.805	1.26	0.221	$(U_0 = 94.1 \text{ ft./sec., } U_1 = 125.5 \text{ ft./sec.})$		5.42	0.715	1.04	0.151	
	3.26	0.662	1.43	0.372			8.13	0.61	1.08	0.221	
	4.87	0.558	1.56	0.458			11.84	0.506	1.17	0.262	
	6.5	0.403	1.69	0.636			13.3	0.415	1.18	0.327	
	8.14	0.312	1.87	0.74			15.7	0.364	1.235	0.40	
	10.3	0.156	2.08	0.896							

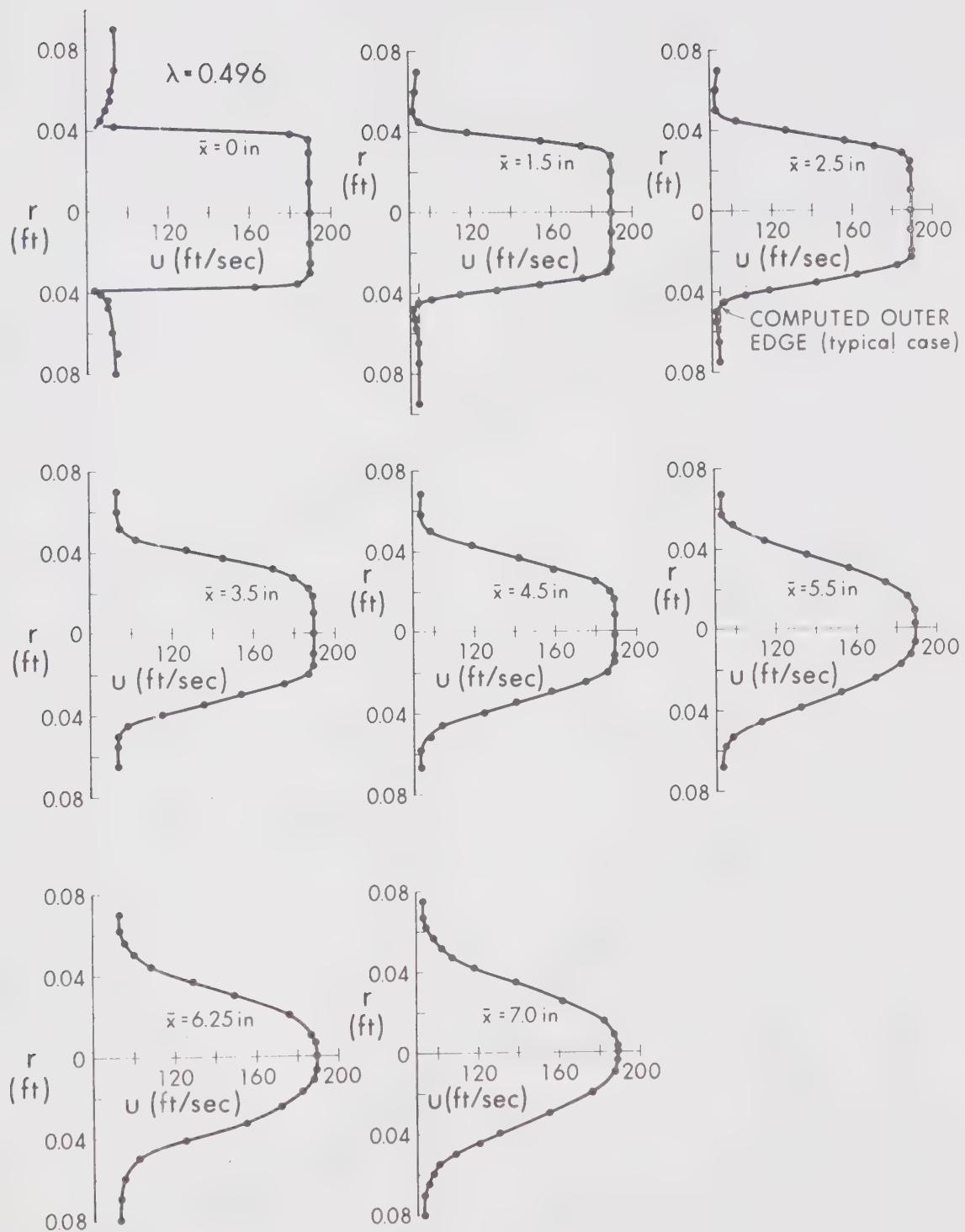


FIGURE A.4 TYPICAL VELOCITY DISTRIBUTION

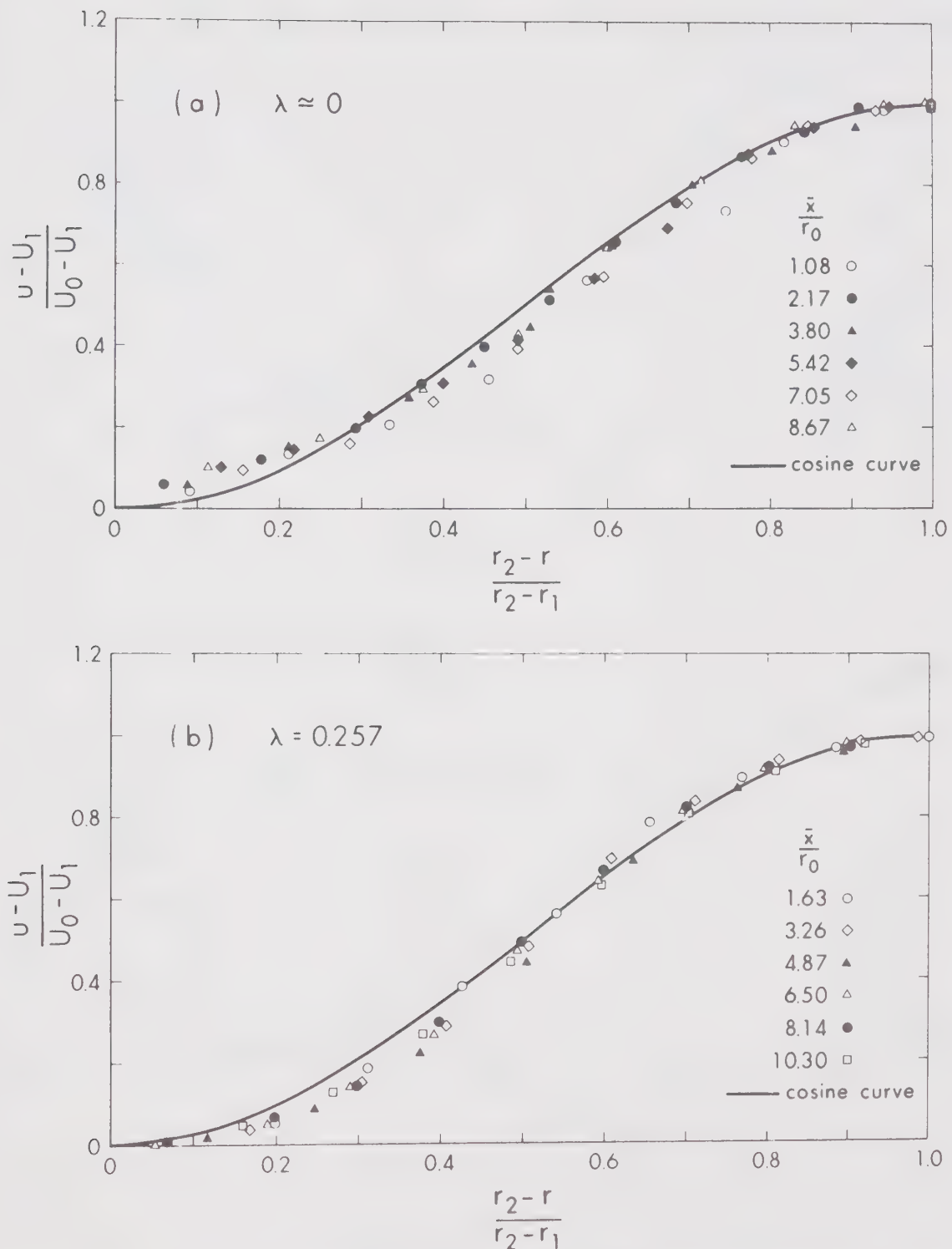


FIGURE A.5 COMPARISON OF EXPERIMENTAL OBSERVATIONS WITH THE COSINE CURVE

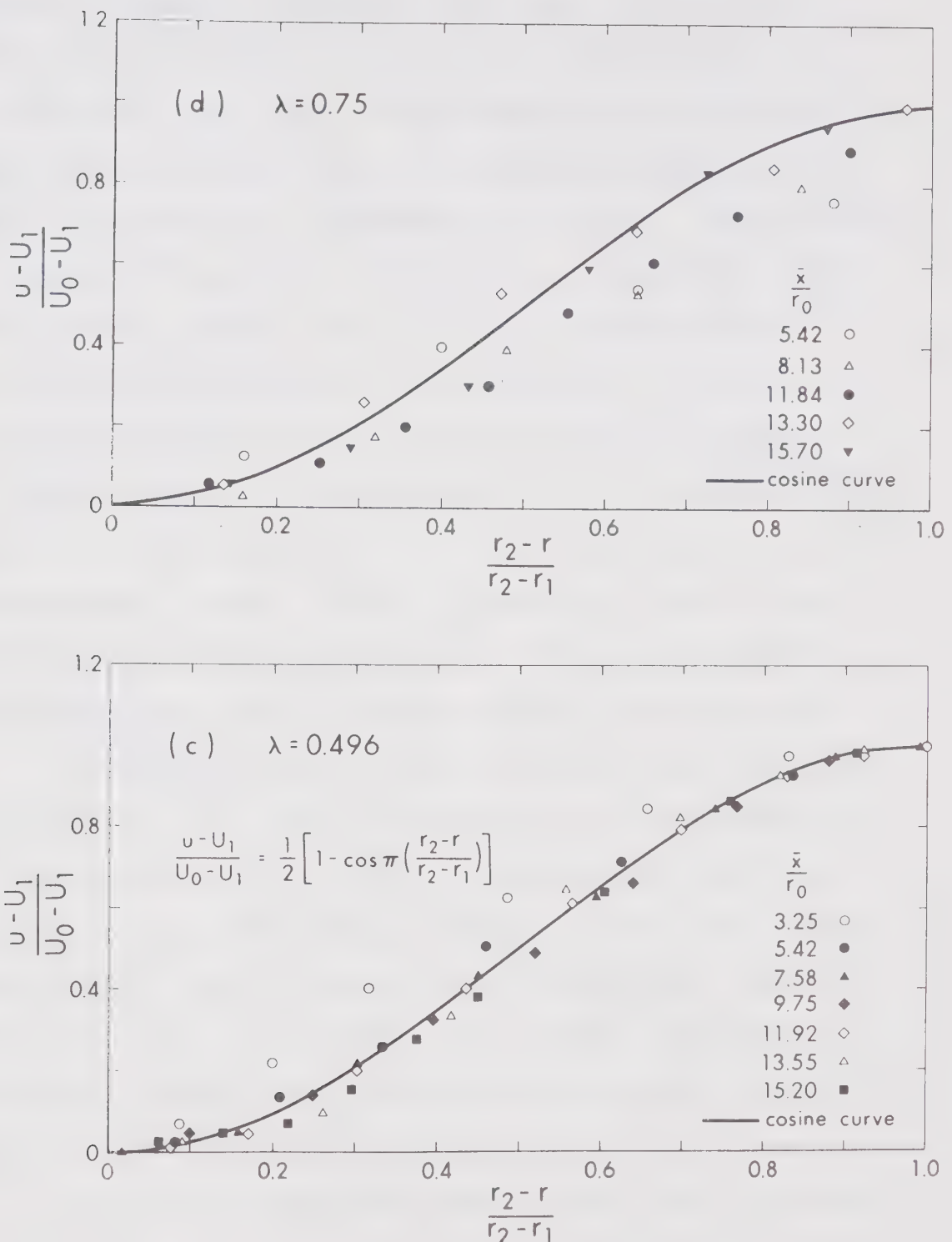


FIGURE A.5 (CONTINUED)

scatter and some departure from the cosine curve. In the plots of Figure A.5, the outer radius r_2 was used in the calculation of the total width of the shear layer. It was somewhat difficult to locate the outer edge of the shear layer and some personal judgement had to be used in this operation. To overcome this difficulty, the half-width b was computed and the velocity distributions are replotted in Figure A.6a to d with U/U_m versus $\eta = (r-r_1)/b$. For all the four velocity ratios, the velocity profiles are seen to be similar. In Figure A.6a the solutions of Tollmien and Goertler for the circular jet (Abramovich, 1963) are shown. It is seen that for $\eta < 1.0$, the Goertler curve is closer to the data whereas for $\eta > 1.0$, the Tollmien curve is closer to the experimental points. For more accurate use, a curve is drawn through the points of Figure A.6a for $\lambda \approx 0$. This curve described reasonably well the velocity distribution for the other values of λ .

The invasion of the shear layer into the primary jet is shown in Figure A.7 with r_1/r_0 versus \bar{x}/r_0 along with the data of Sami et al (1967), and Corrsin (1953) for $\lambda = 0$. The experimental data of this work show that r_1/r_0 varies linearly with \bar{x}/r_0 . If the virtual origin for the r_1 line is fixed at the section where the straight lines of Figure A.7 meet the $r_1/r_0 = 1.0$ axis, then, it could be seen that virtual origin is located behind the nozzle and its distance varies from $0.4 r_0$ for $\lambda \approx 0$ to about $2.5 r_0$ for $\lambda = 0.75$.

If x_0 is the length of the potential core, that is the axial length from the nozzle to the section where r_1 is zero, the variation of x_0/r_0 , as found by extrapolation from Figure A.7 is shown plotted

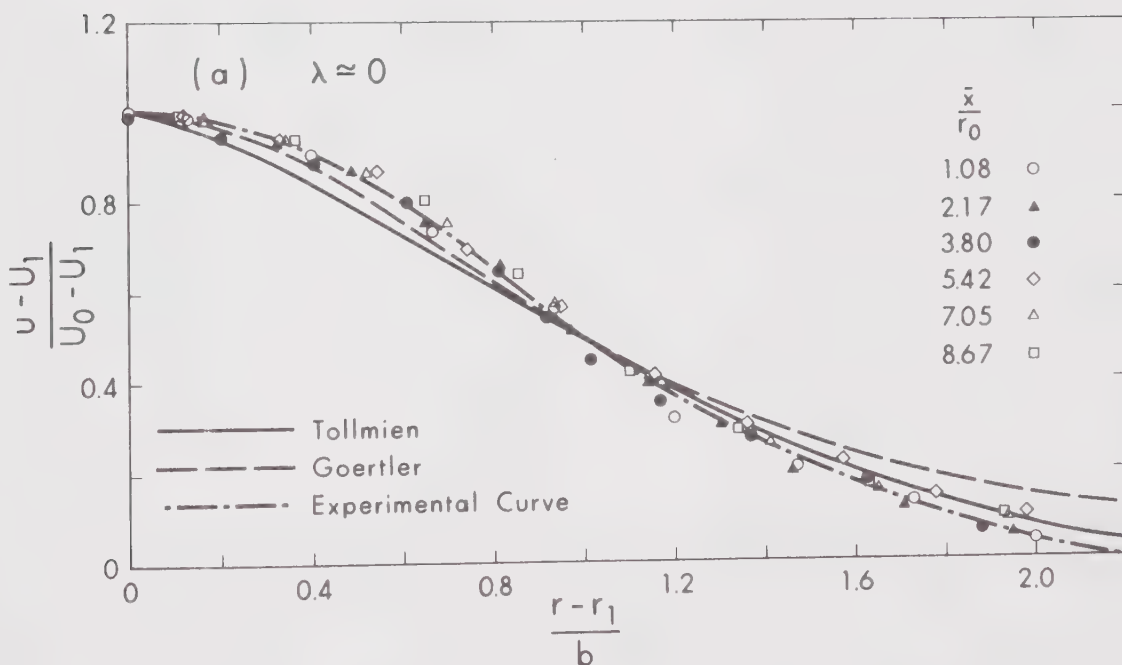
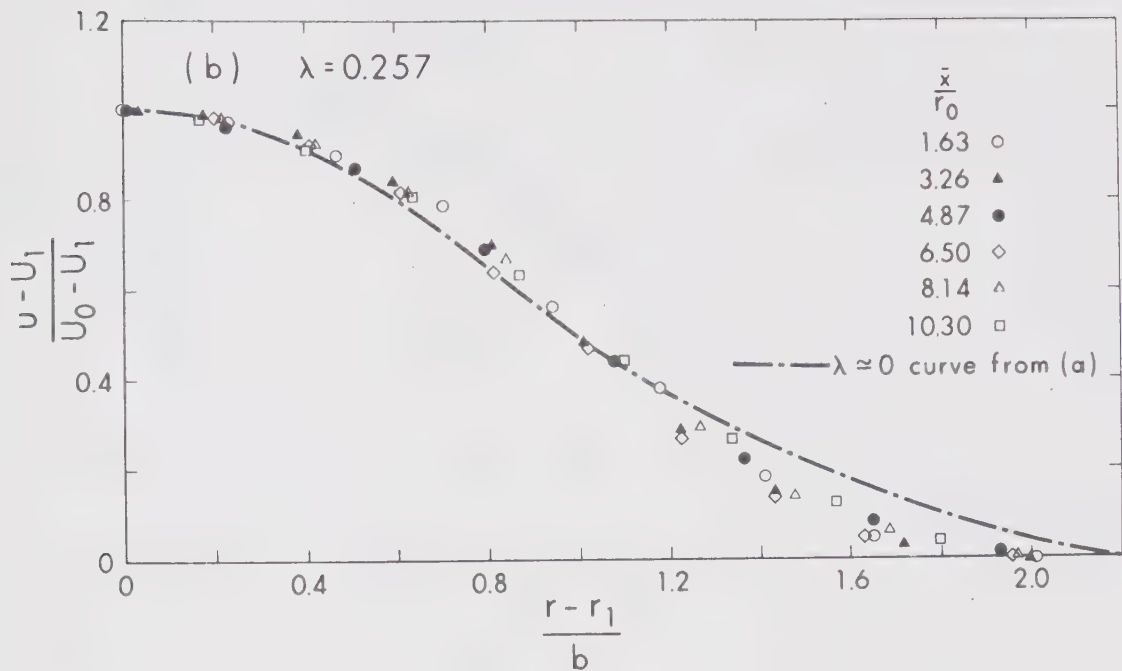
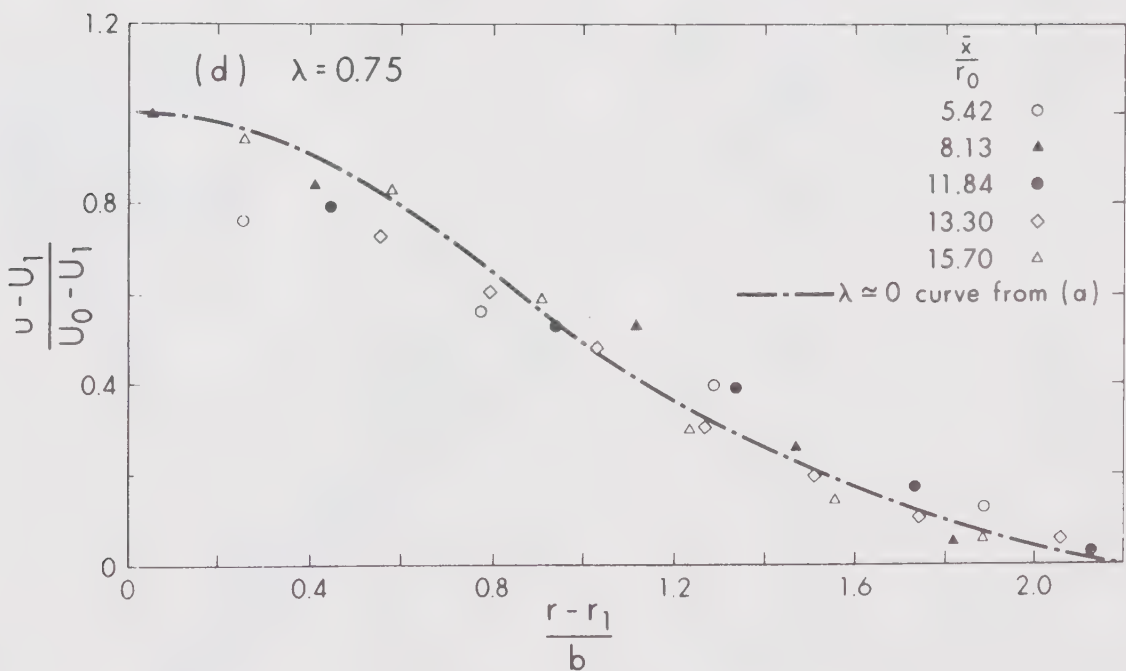
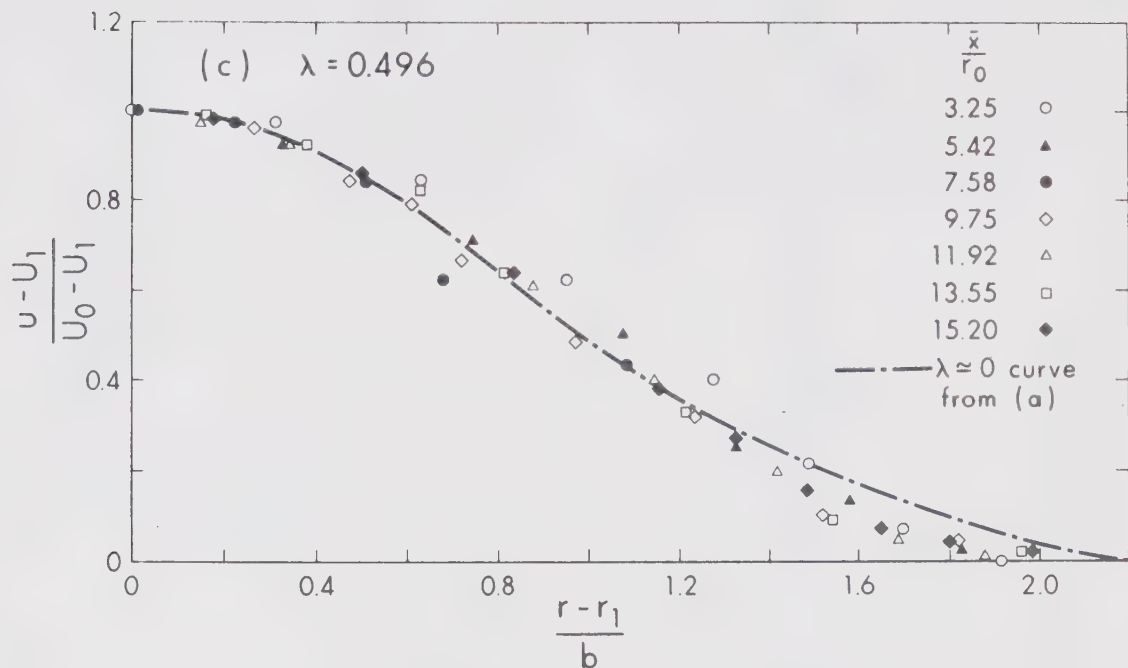


FIGURE A.6 SIMILARITY IN VELOCITY DISTRIBUTION



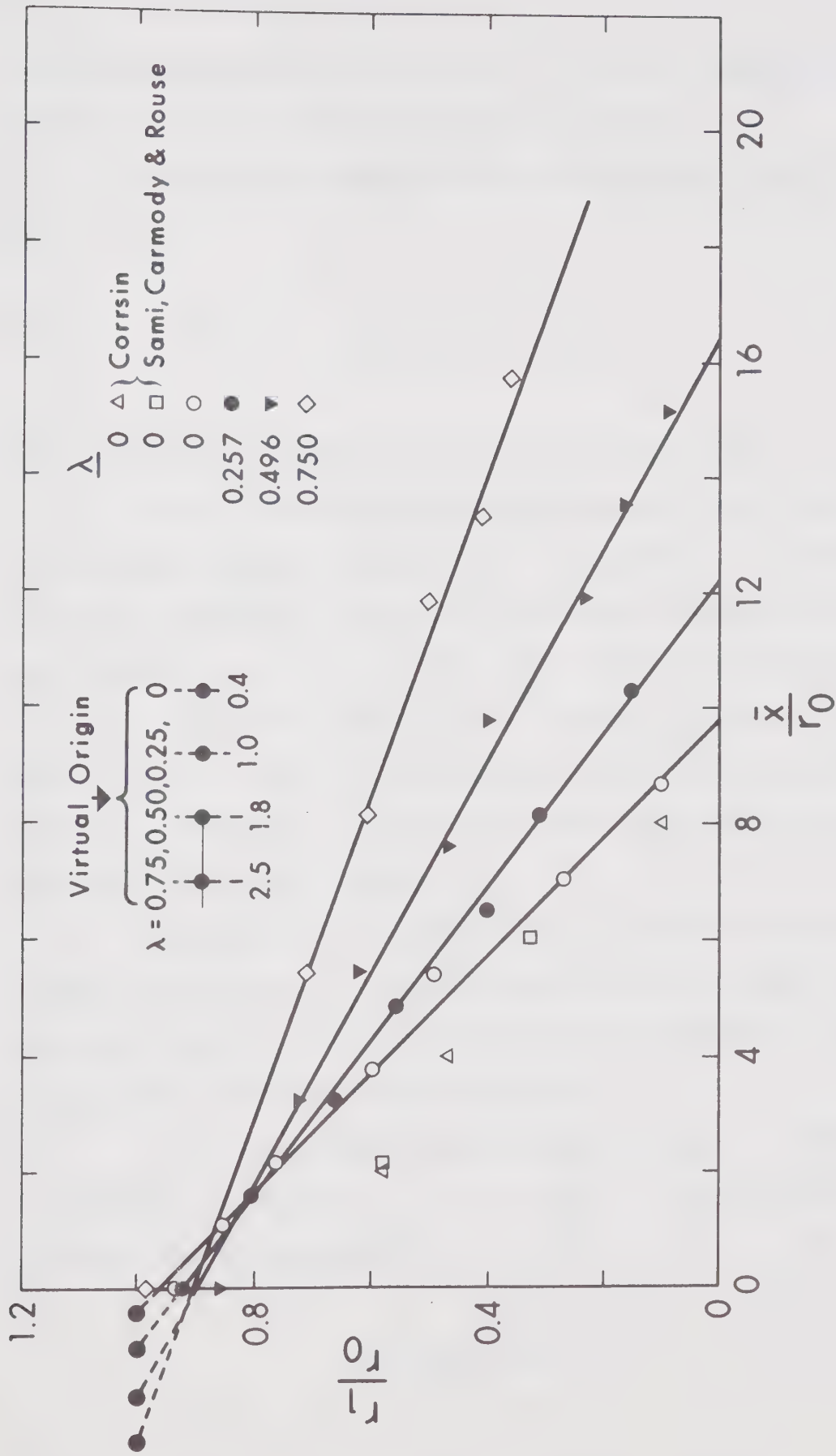


FIGURE A.7 GROWTH OF THE INNER EDGE OF THE SHEAR LAYER

in Figure A.8 with the velocity ratio λ . It is seen that x_0/r_0 increases from 10 at $\lambda \approx 0$ to about 25 at $\lambda = 0.75$.

The empirical equation given by Forstall and Shapiro (1950) as

$$\frac{x_0}{d} = 4.0 + 12 \frac{U_1}{U_0} \quad (\text{A.21})$$

does not agree well with the present results (Figure A.8).

To find out the variation of the empirical coefficient c^2 used by Squire and Trouncer, the value of $c^2 x_0/r_0$ given by the analysis of Squire and Trouncer was matched with the present observations and c^2 was determined. The variation of c^2 with λ obtained by this procedure is shown in Figure A.9. For $\lambda \approx 0$, c^2 is equal to 0.0042 and increases to 0.0096 for $\lambda = 0.75$. It should be mentioned that Kuethe (1935) found $c^2 = 0.00496$ for $\lambda = 0$, whereas Squire and Trouncer used the value of 0.0067 for all values of λ .

The growth of the length scale b is shown in Figure A.10 in a dimensionless form. As predicted by the similarity analysis, b increases linearly with the axial distance, with the virtual origin located about one radius behind the nozzle.

If $b = C_1 x$, then the data plotted in Figure A.11 show that C_1 decreases linearly with λ for λ up to 0.75. This variation could be represented by the equation

$$C_1 = 0.115 [0.96 - \lambda] \quad (\text{A.22})$$

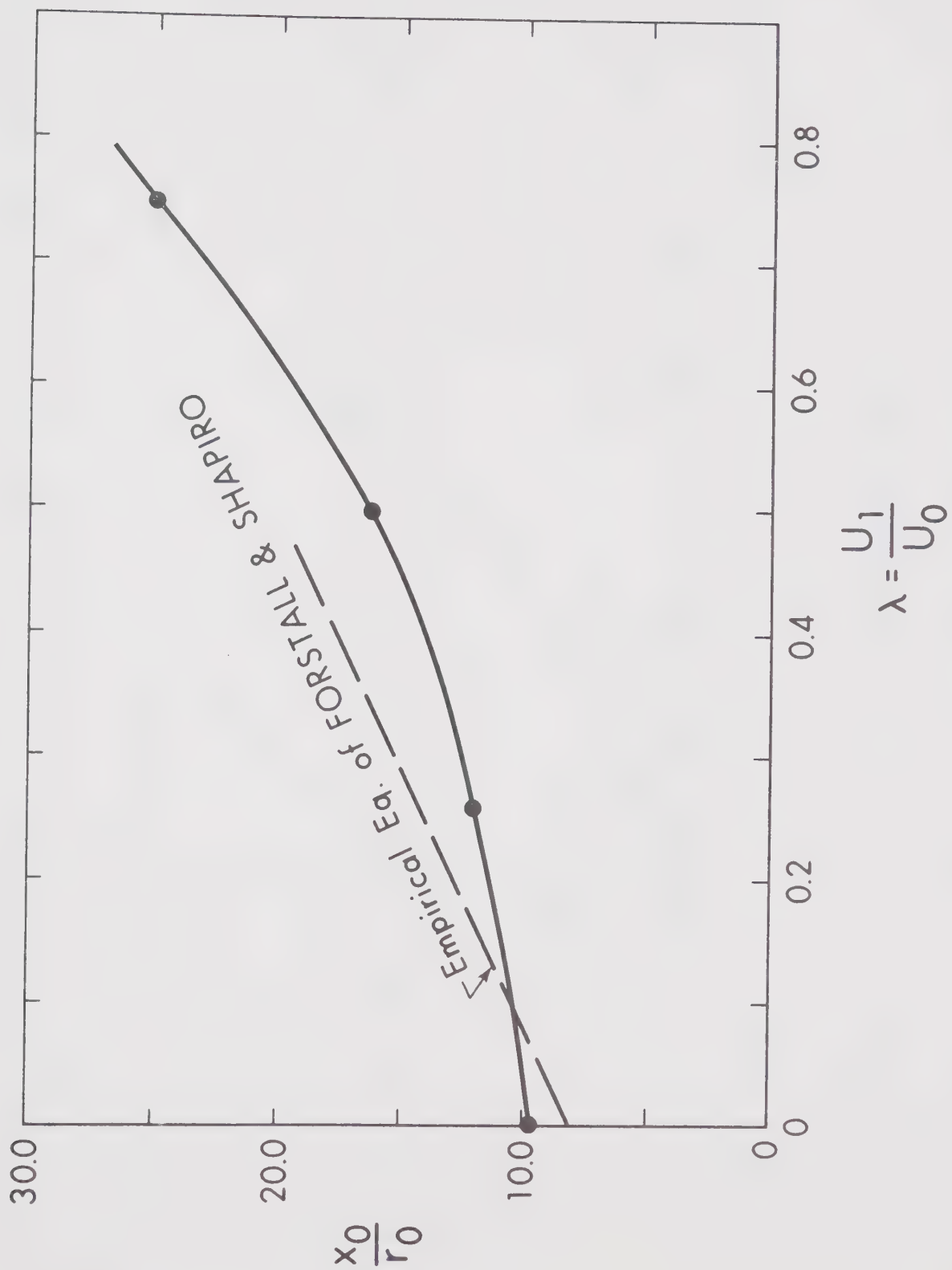


FIGURE A.8 LENGTH OF POTENTIAL CORE

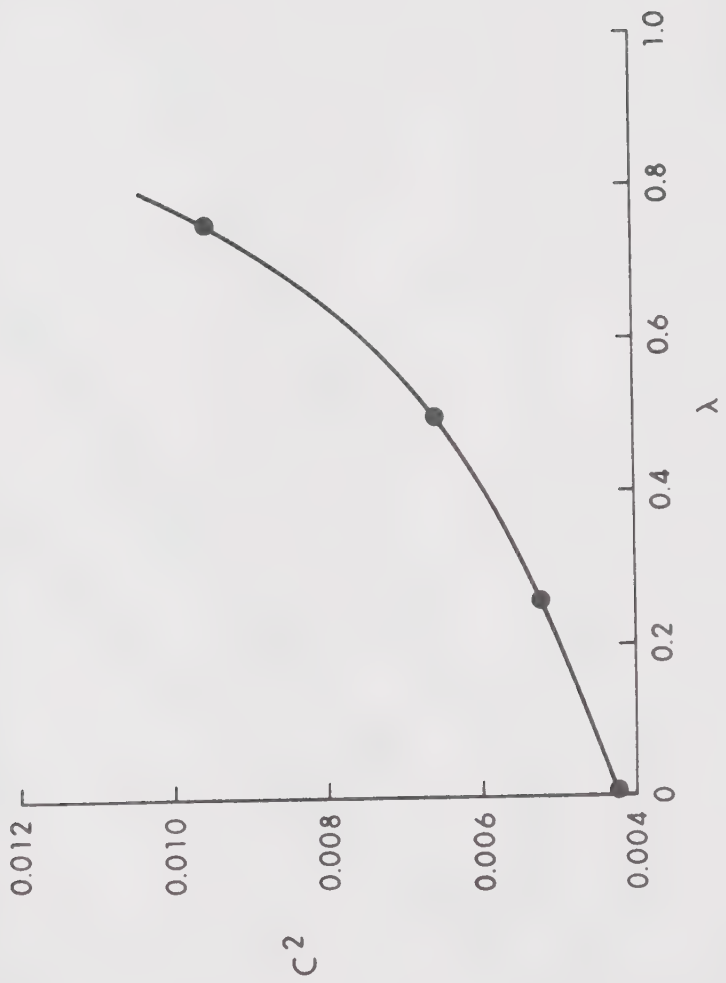


FIGURE A9 VARIATION OF c^2 WITH λ

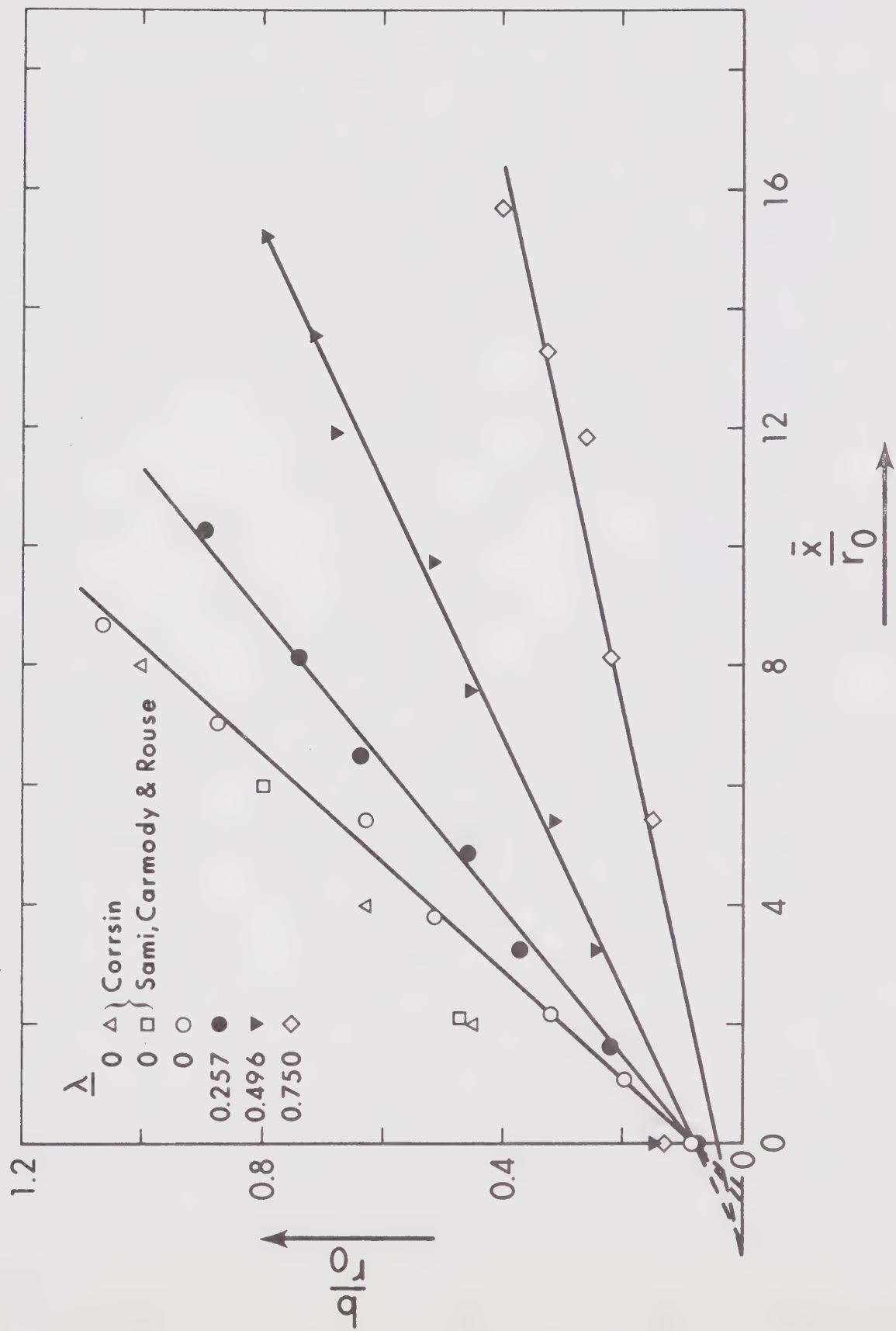
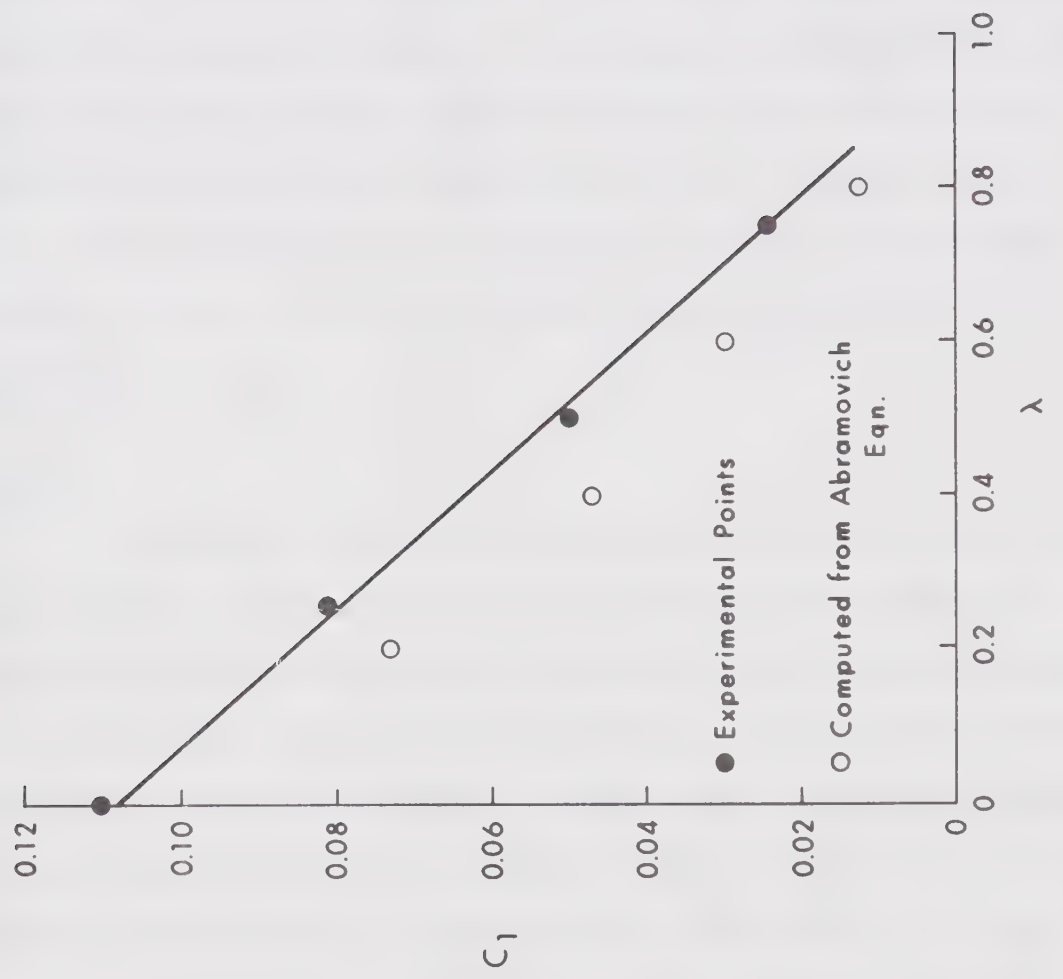


FIGURE A.10 GROWTH OF LENGTH SCALES

FIGURE A11 VARIATION OF C_1 WITH λ

The values of C_1 predicted by the equation of Abramovich (1963) are less than the experimental values (see Figure A.11).

As mentioned earlier, it is somewhat difficult to determine the outer limit of the shear layer precisely. The observations on the growth of r_2 are shown in Figure A.12, where the increase is seen to be linear with the axial distance. If α_1 and α_2 are the angles in degrees made by the inner and outer edges of the shear layer with the axial direction, the variation of these angles with λ is shown in Figure A.13. From Figure A.13, it is seen that α_1 decreases linearly from 5.6° at $\lambda \approx 0$ to 2.1° at $\lambda = 0.75$ and α_2 decreases from 8.9° at $\lambda \approx 0$ to 0.75° at $\lambda = 0.75$.

Summary

A similarity analysis of the turbulent compound annular shear layer has shown that the length characteristics of this layer vary linearly with the axial distance. When this linear relation was used, it was found that the earlier results of Squire and Trouncer could be obtained in a much simpler manner. Based on the experimental results for four values of the velocity ratio λ from about zero to 0.75, the empirical coefficient c^2 was found to vary from 0.0042 at $\lambda \approx 0$ to 0.0096 for $\lambda = 0.75$ whereas Squire and Trouncer assumed a constant value of 0.0067 for c^2 for all the velocity ratios. The length of the potential core was found to increase from $10 r_0$ at $\lambda \approx 0$ to $25 r_0$ at $\lambda = 0.75$, where r_0 is the radius of the nozzle. Further, some experimental results have also been obtained regarding the variation of the angle of the inner and outer edges of the shear layer with λ and the growth of the half width.

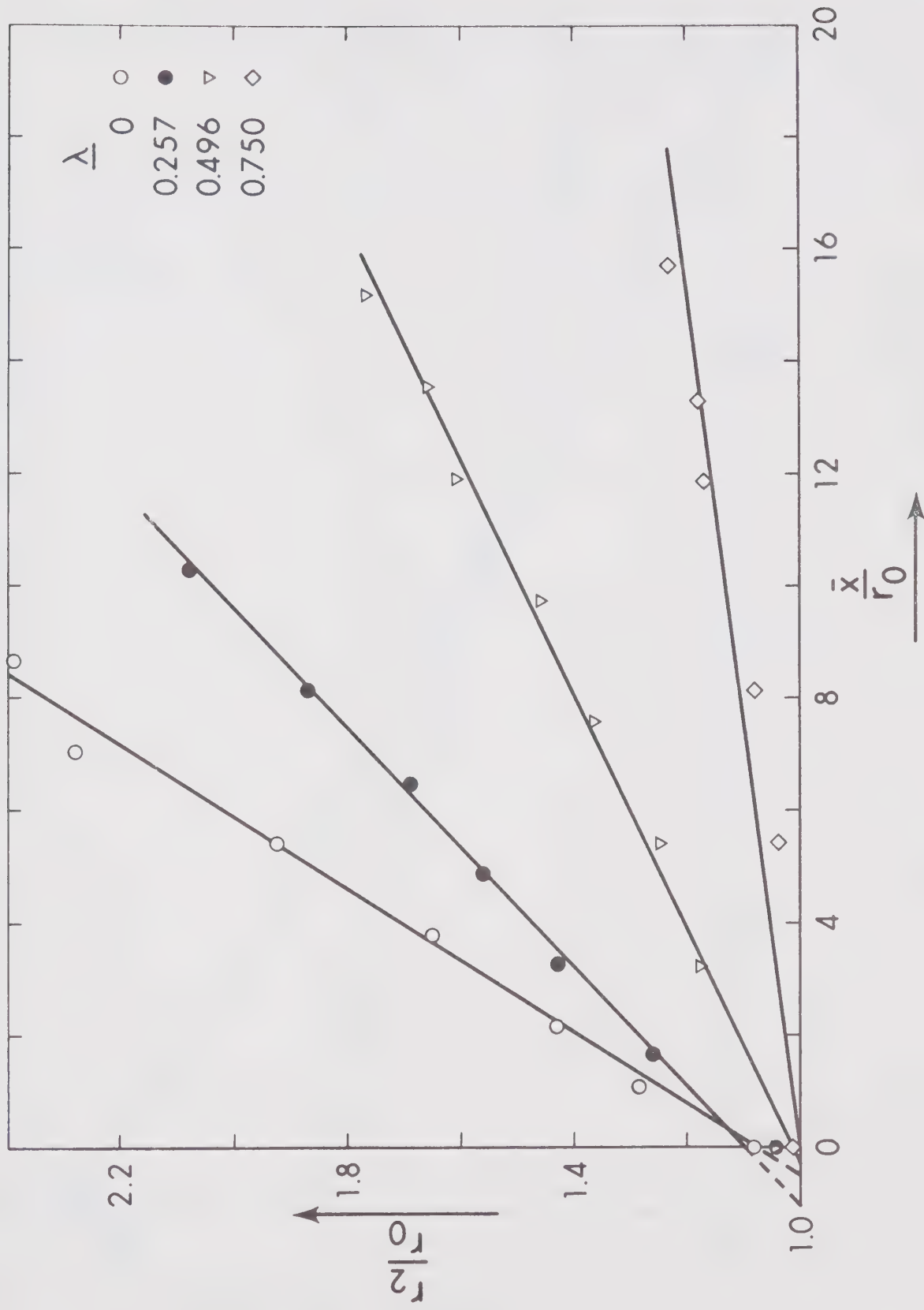


FIGURE A. 12 GROWTH OF THE OUTER EDGE OF THE SHEAR LAYER

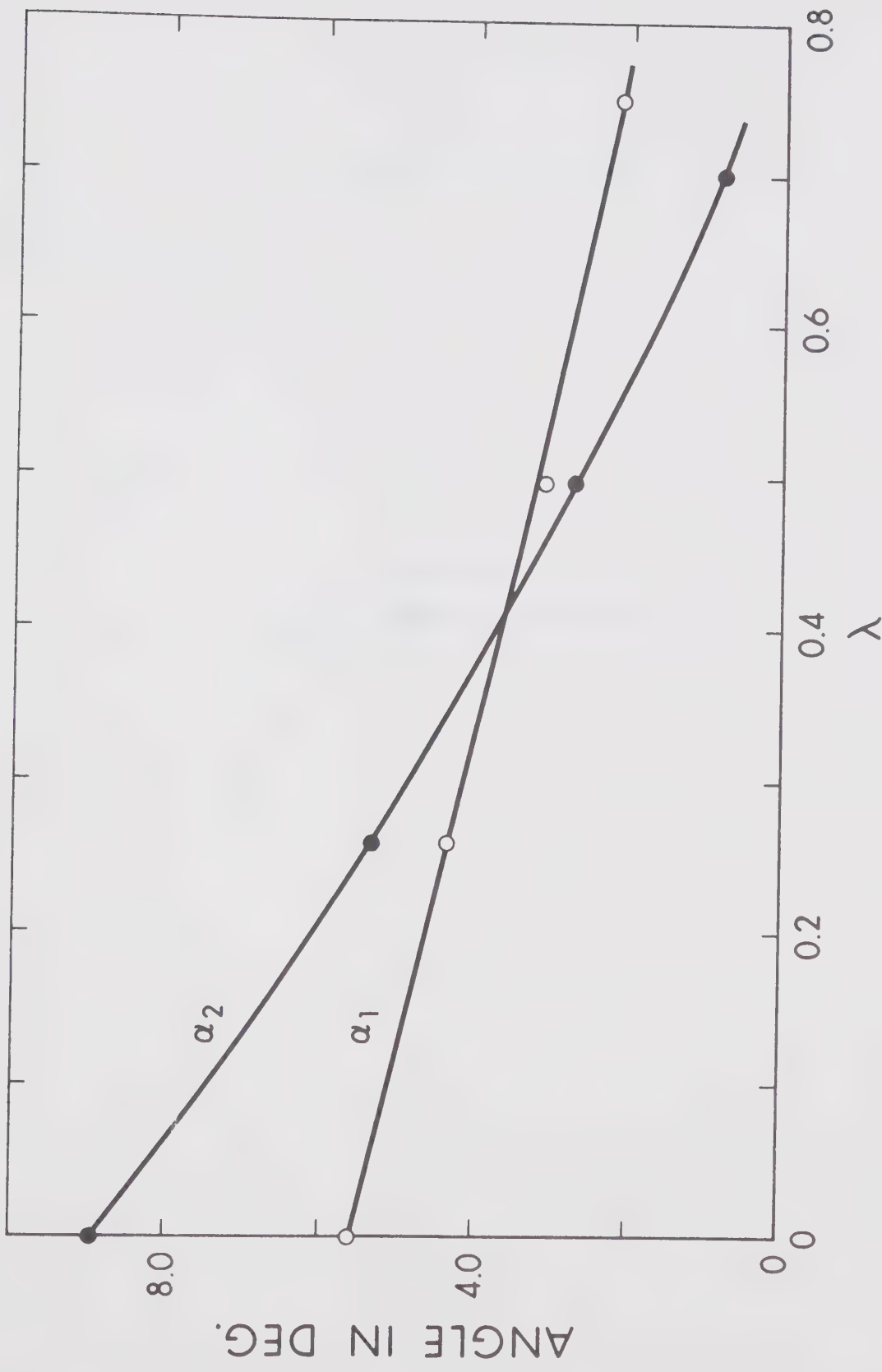


FIGURE A.13 ANGLES OF THE INNER AND OUTER EDGES

APPENDIX B
THREE DIMENSIONAL FREE JETS

APPENDIX B

THREE DIMENSIONAL FREE JETSB.1 Introduction

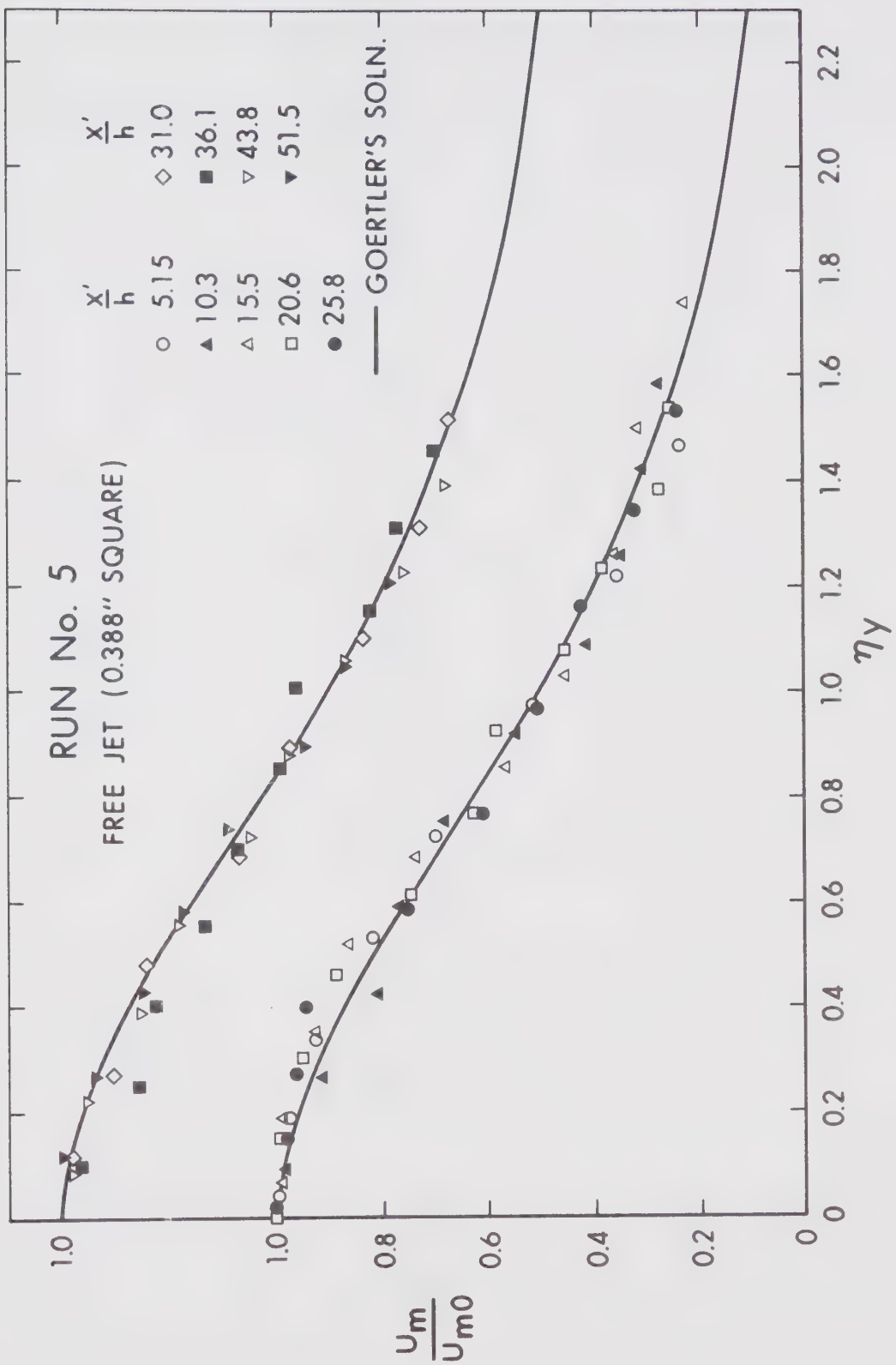
In Chapter II growth laws and maximum velocity decay for three dimensional free jets were worked out from theoretical considerations. From dimensional analysis it was shown that if \sqrt{A} is taken as a characteristic length parameter to non-dimensionalise the stream-wise distance x , the velocity decay relation would be the same regardless of the nozzle shape. In an attempt to find this, some of the available data of Trentacoste and Sforza (1966) together with the data on a free square jet investigated presently are analysed. The experiments on the free square jet were conducted in flume 2 and the velocity field explored with a total head tube 0.05 inches diameter. The significant data are given in Table B-1.

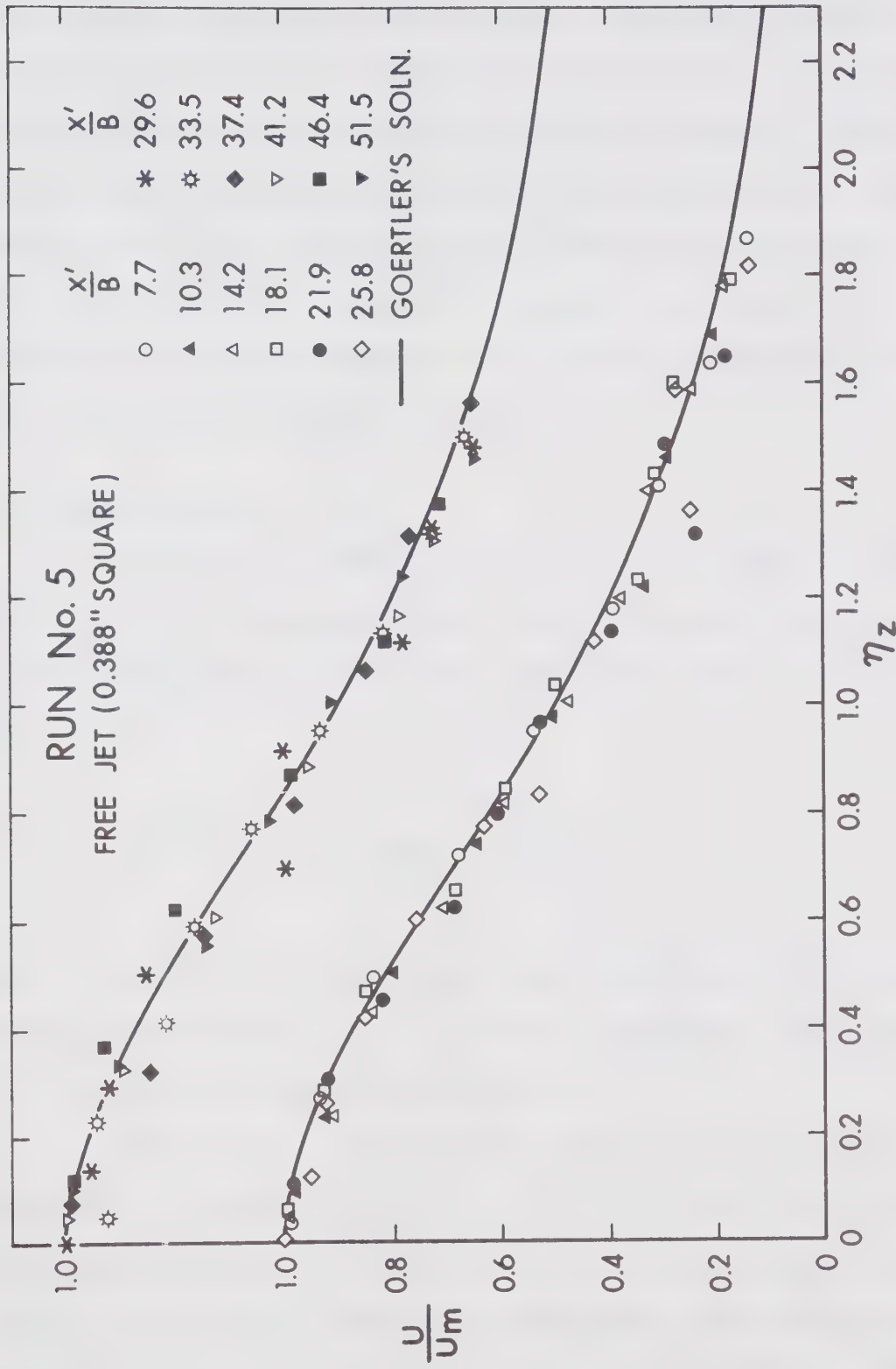
B.2 Similarity

Velocity profiles taken along planes passing through the axis of the nozzle are plotted in the conventional non-dimensional forms, u_m/u_{m0} vs. η_y and u/u_m vs. η_z . From Figure B.1 and B.2, the two distributions are found to be similar for distances greater than 5 to 6 times the nozzle height and closely follow Goertler's free circular jet profile. During measurements it was noted that the jet was some-

TABLE B.1
VELOCITY AND LENGTH SCALES FOR A FREE JET
RUN # 5 0.388" SQUARE NOZZLE

Distance inches	u_{mo} ft./sec.	b_y ft.	Distance inches	$y/B = 0$	b_z ft. $y/B = 0.5$
0	24.16	--	1.5	0.0180	--
2.0	23.1	0.0205	3.0	0.0220	0.0230
4.0	16.0	0.0303	4.0	0.0295	0.0295
6.0	11.1	0.0420	5.5	0.0419	0.0410
8.0	8.17	0.0650	7.0	0.0530	0.0515
10.0	6.74	0.0795	8.5	0.0700	0.0740
12.0	5.64	0.0970	10.0	0.0860	0.0870
14.0	4.70	0.1330	11.5	0.0970	0.0950
17.0	3.96	0.1500	13.0	0.1110	--
20.0	3.40	0.1940	13.5	--	0.1150
24.0	2.85	--	14.5	0.1220	--
28.0	2.37	--	15.0	--	0.1260
32.0	2.04	--	16.0	0.1440	--
38.0	1.84	--	18.0	0.1600	--
			20.0	0.1780	--

FIGURE B.1 NON-DIMENSIONAL VELOCITY DISTRIBUTION IN y DIRECTION

FIGURE B.2 NON-DIMENSIONAL VELOCITY DISTRIBUTION IN z DIRECTION

what unsteady and changes direction after noticeable intervals, making it hard to get consistent readings for the velocities. However, at any particular section the profiles are taken a number of times and the one looking consistent was taken as the correct profile. This explains the reason for getting some scatter in the experimental data. The unsteadiness was believed to be caused by the large recirculating eddies in the tank and therefore this is likely to happen with experiments conducted in ambients of finite extent.

B.3 Velocity Decay

Variation of maximum velocity u_{mo} with distance is given in Figure B.3, which indicates a linear relationship with the virtual origin lying at the outlet section. The present data is represented by

$$\frac{u_{mo}}{U_0} = 7.25 \left[\frac{x}{h} \right]^{-1.0} \quad (B.1)$$

and the constant coefficient on the right hand side of this expression is comparable with the value 7.0 quoted by Yevdjevich (1966). Also from Figure B.3, the difference looks small.

The available data on various shapes were then studied in Figure B.4, by plotting u_{mo}/U_0 vs. x'/\sqrt{A} . The shape includes a slender nozzle having aspect ratio as high as 10 and considering the odd shapes involved, the agreement among the different data looks remarkable. Further it is observed that use of \sqrt{A} as a characteristic length

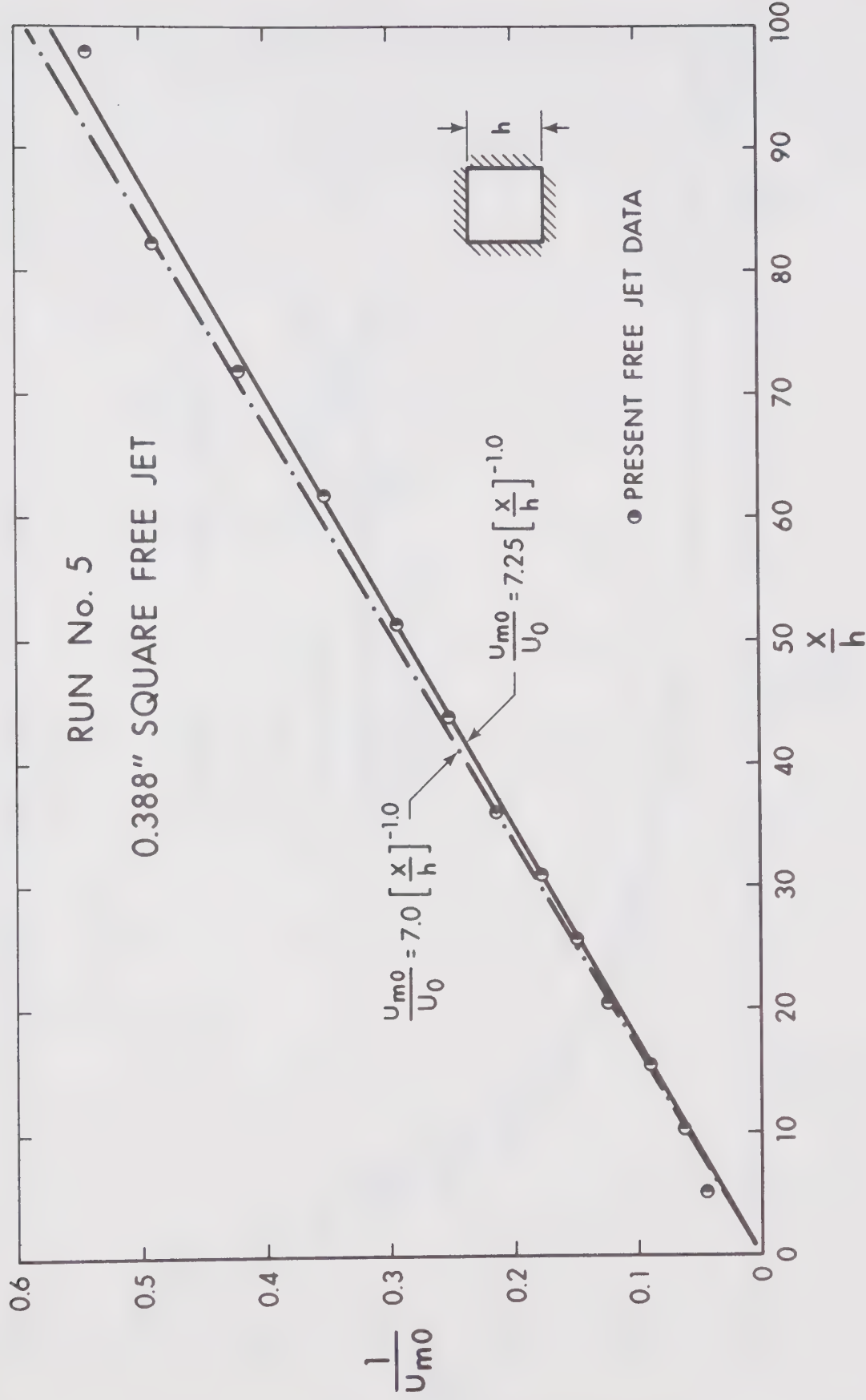


FIGURE B.3 MAXIMUM VELOCITY DECAY FOR A SQUARE NOZZLE

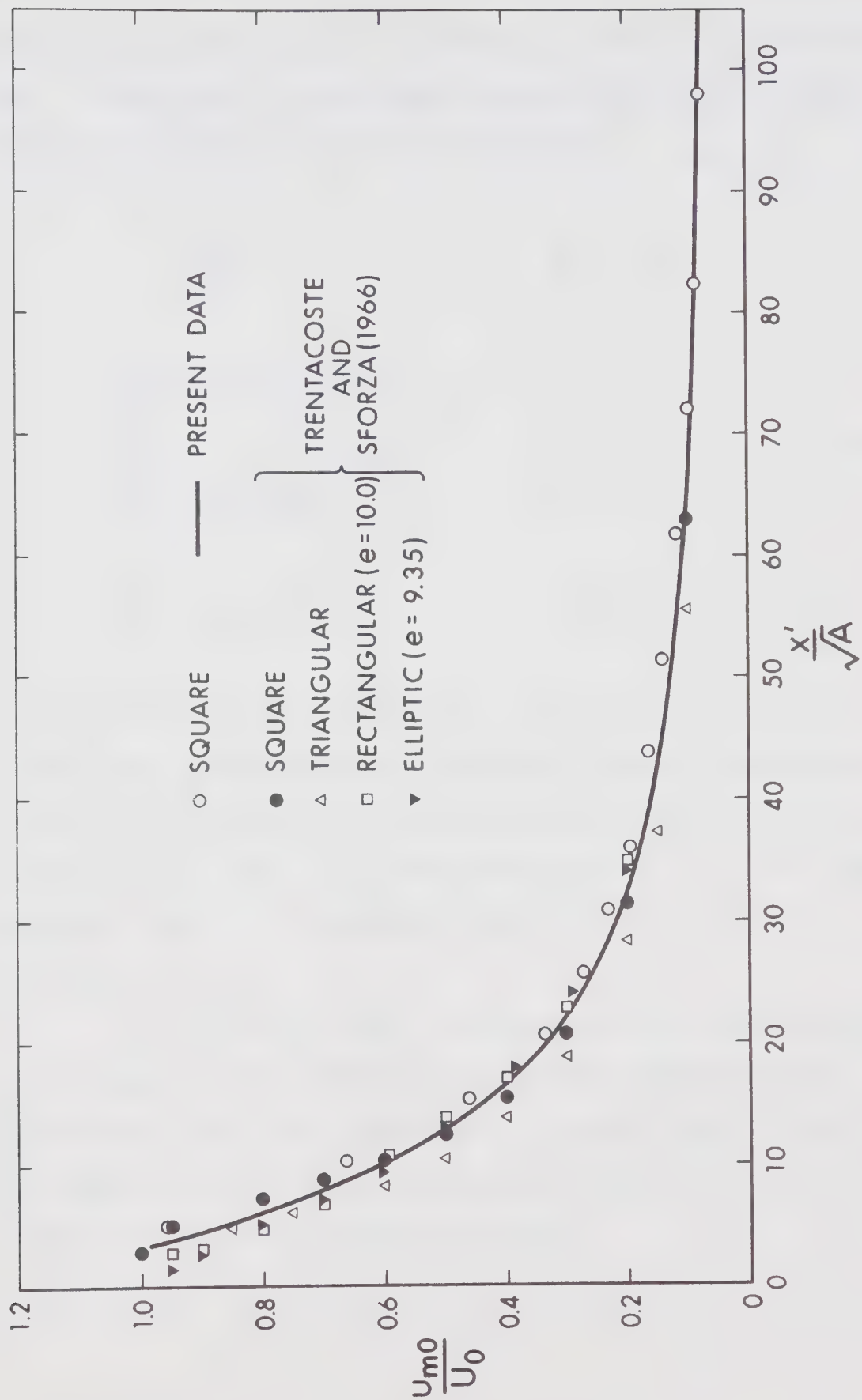


FIGURE B.4 MAXIMUM VELOCITY DECAY FOR THREE DIMENSIONAL FREE JETS

rather than hydraulic radius r' (Subramanya, 1967) gives closer agreement. A mean curve is drawn through the test points and is represented by the following set of empirical relationships.

$$\frac{u_{mo}}{U_0} = 1.0 \quad \frac{x'}{\sqrt{A}} < 4.0$$

$$\frac{u_{mo}}{U_0} = 2.04 \left[\frac{x'}{\sqrt{A}} \right]^{-0.511} \quad 4.0 \leq \frac{x'}{\sqrt{A}} \leq 8.3 \quad (B.2)$$

$$\frac{u_{mo}}{U_0} = 3.27 \left[\frac{x'}{\sqrt{A}} \right]^{-0.785} \quad 8.3 \leq \frac{x'}{\sqrt{A}} \leq 14$$

$$\frac{u_{mo}}{U_0} = 6.6 \left[\frac{x'}{\sqrt{A}} \right]^{-1.0} \quad 14 < \frac{x'}{\sqrt{A}}$$

For most free jets the virtual origin lies very close to the nozzle, so that x and x' are more or less identical. From the last expression, which is valid in the fully developed region, we find $u_{mo} \propto x^{-1.0}$ as predicted in Eq. 2.38. For a three dimensional free jet of arbitrary shape use of Eq. B.2 is recommended when more detail and precise values are not known.

It is to be noted that the exponents on the right hand side of the second and third expression of Eq. B.2 are same as the ones appearing for a wall jet. Comparison of Figures B.4 and 4.9 shows that the maximum velocity decay for a free jet is faster than the decay in a wall jet under identical outlet conditions.

B.4 Length Scale b_y

Abramovich (1963) indicates that the data on length scale of axisymmetric and plane jets can be described by a common equation

$$\frac{b_y}{h} = 0.097 \frac{x}{h} \quad (\text{B.3})$$

where, h is the height of the nozzle and would be the diameter for an axisymmetric case. Since the aspect ratios are 1 and ∞ for these shapes and represent extreme cases, it might be expected that the same relationship be valid for three dimensional jets as well.

Subramanya (1967) analysed some of Trentacoste and Sforza's data for various shapes and concluded that the above expression remains valid. The results of the present investigation are shown in Figure B.5, and are compared with Eq. B.3. The growth of b_y is found to be faster than given by the equation and the virtual origin is located at a distance of $3.3h$ in the downstream direction. In any case, the variation is linear and is in accordance with Eq. 2.38.

B.5 Length Scale b_z

Transverse length scales in the x - z plane passing through the axis of the jet, as well as in a plane at 0.5 times the nozzle height above the axis were found out. Both sets of values are plotted in Figure B.5 and are seen to be in agreement with the b_y scale, which is expected. There seems to be no data available on growth of b_z for any other shape. One set of values for a rectangular jet of aspect

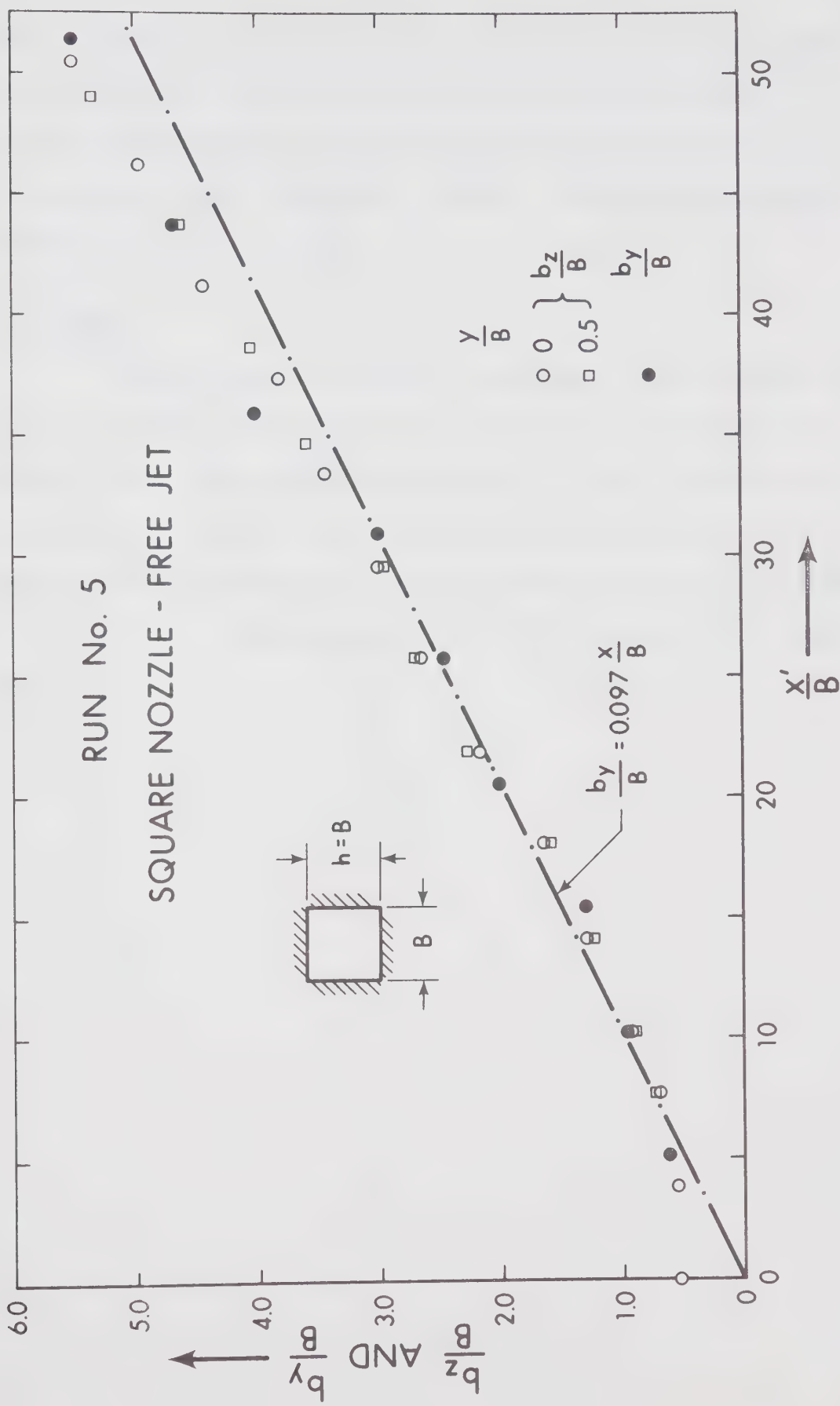


FIGURE B.5 GROWTH OF LENGTH SCALES b_y AND b_z

ratio 10, measured in a plane passing through the axis of the nozzle has been given by Trentacoste and Sforza. They observe that in a certain initial length b_z decreases and then starts growing in the far field in a manner similar to b_y growth. This peculiarity seems to prevail for slender nozzles.

B.6 Summary

Velocity decay relationship can be described by single curve regardless of the outlet shape, if \sqrt{A} is used as a characteristic length. In the fully developed flow zone, $u_{mo} \propto x^{-1.0}$ in accordance with similarity analysis. The length scale b_y was found to grow linearly with distance and the velocity profiles in the fully developed flow were similar, following closely Goertler's curve for an axisymmetric case.

APPENDIX C
VELOCITY PLOTS AND EXPERIMENTAL DATA

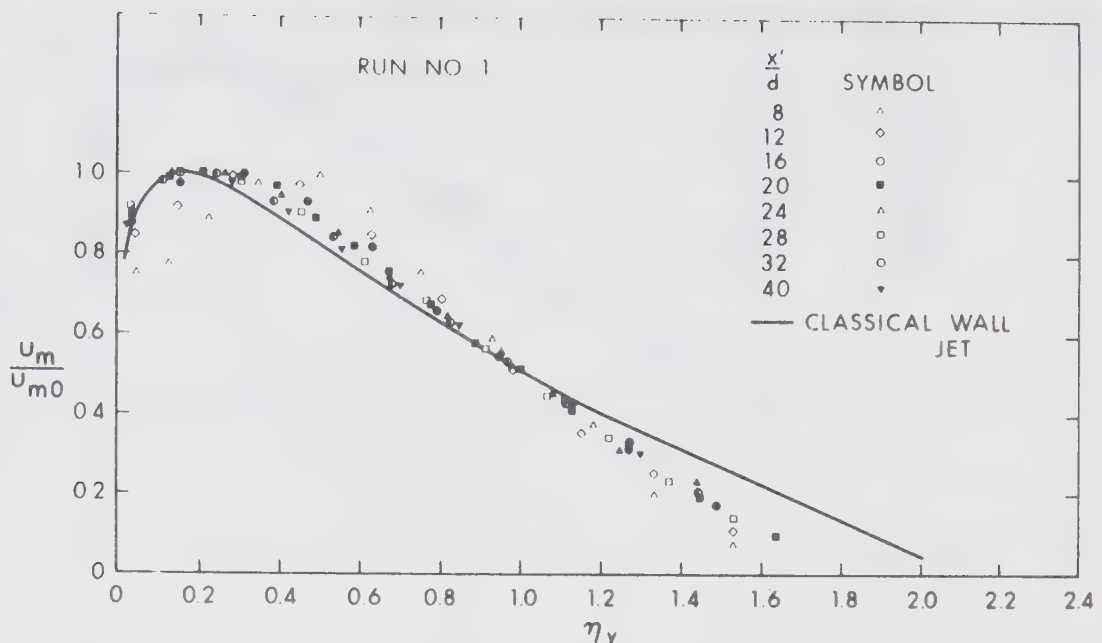


FIGURE C.1 NON-DIMENSIONAL VELOCITY DISTRIBUTION IN THE CENTER-PLANE -CIRCULAR NOZZLE

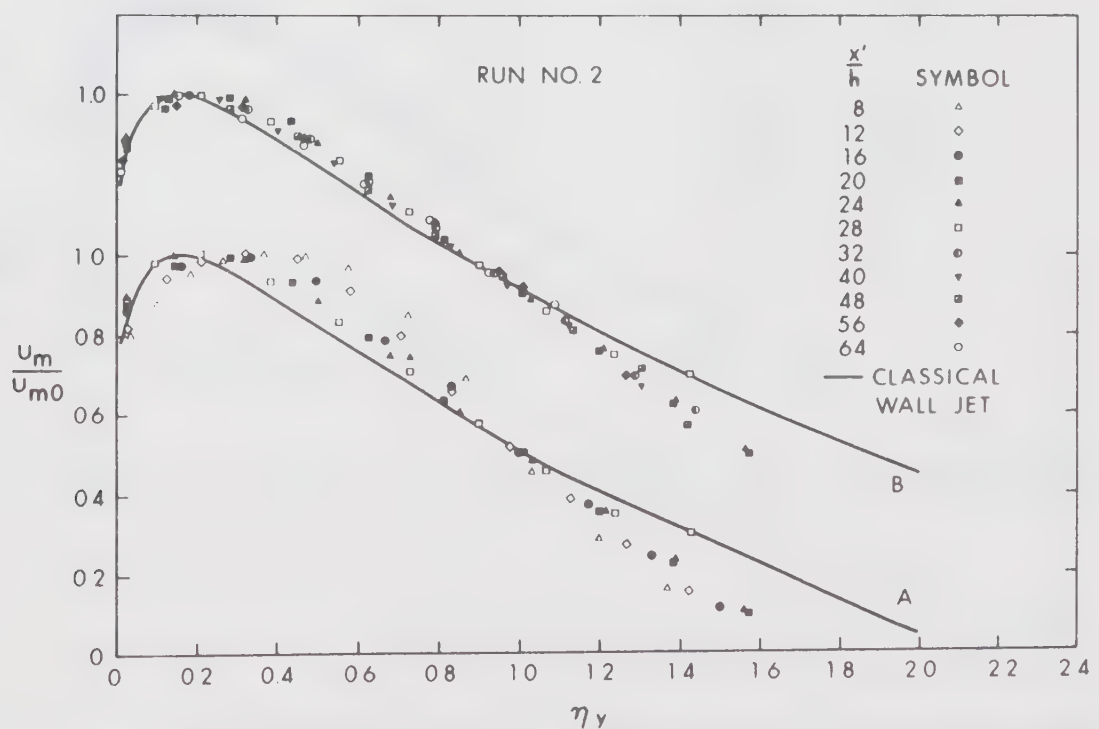


FIGURE C.2 NON-DIMENSIONAL VELOCITY DISTRIBUTION IN THE CENTER-PLANE - SQUARE NOZZLE

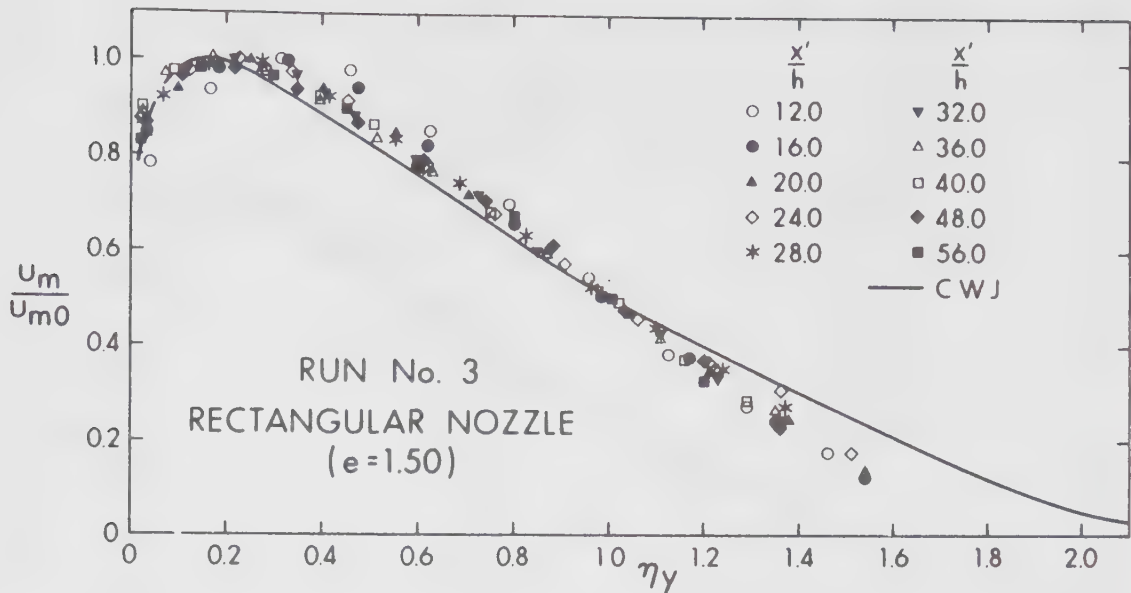


FIGURE C.3 NON-DIMENSIONAL VELOCITY DISTRIBUTION IN THE CENTER-PLANE
- RECTANGULAR NOZZLE ($e=1.50$)

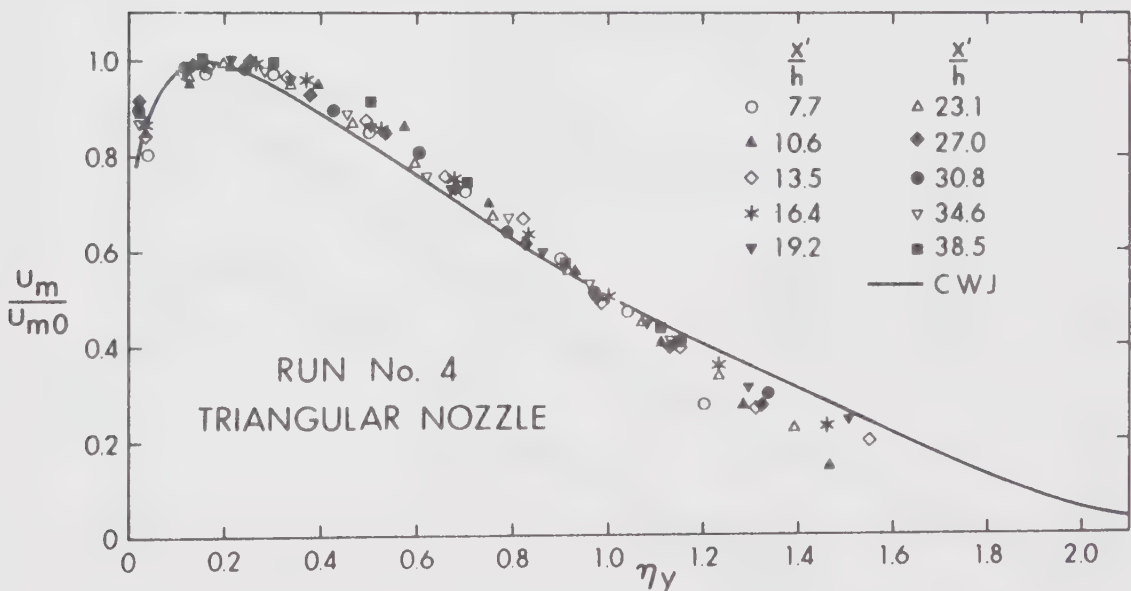


FIGURE C.4 NON-DIMENSIONAL VELOCITY DISTRIBUTION IN THE CENTER-PLANE
- TRIANGULAR NOZZLE

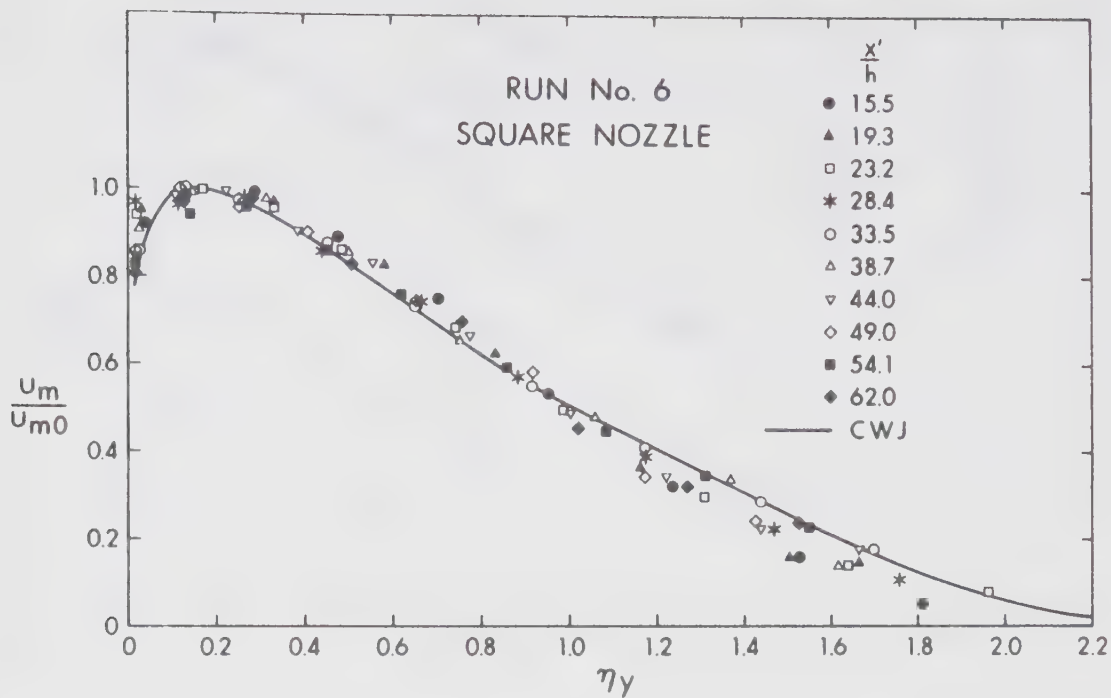


FIGURE C.5 NON-DIMENSIONAL VELOCITY DISTRIBUTION IN THE CENTER-PLANE
- SQUARE NOZZLE

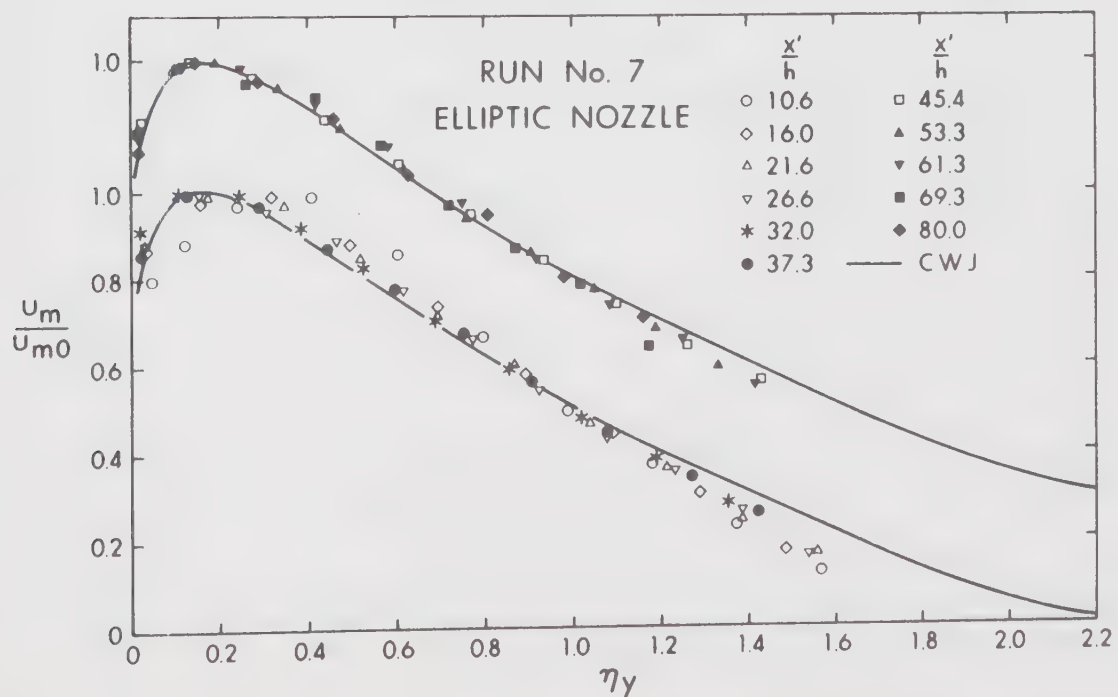


FIGURE C.6 NON-DIMENSIONAL VELOCITY DISTRIBUTION IN THE CENTER-PLANE
- ELLIPTIC NOZZLE ($e = 1.62$)

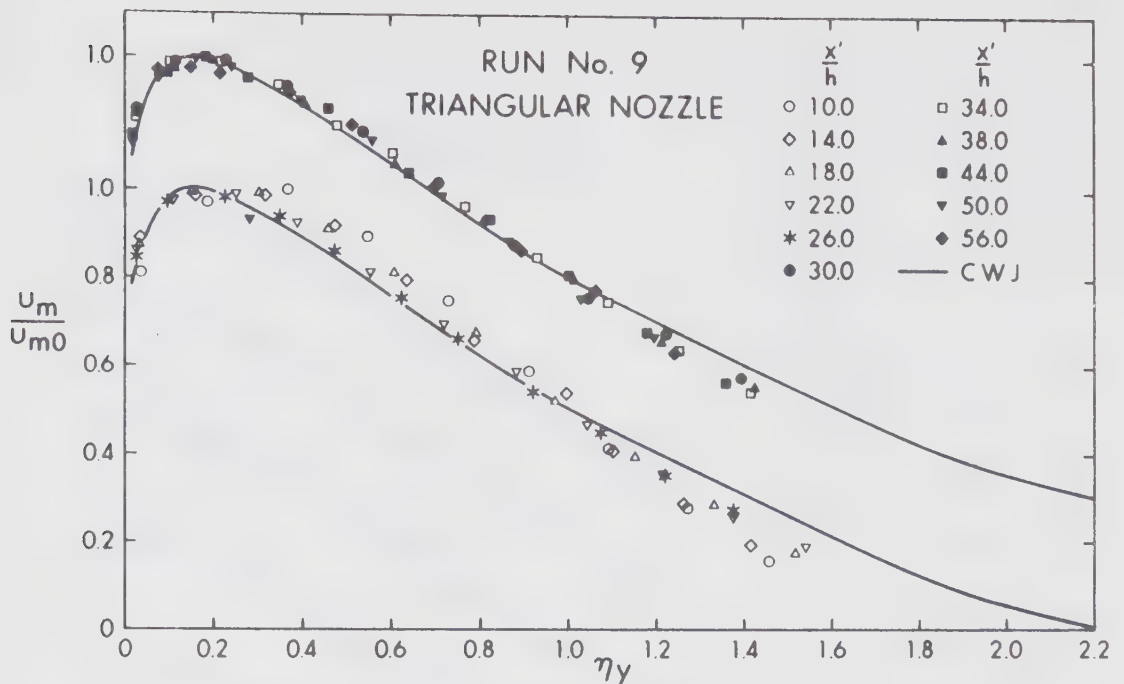


FIGURE C.7 NON-DIMENSIONAL VELOCITY DISTRIBUTION IN THE CENTER-PLANE
- TRIANGULAR NOZZLE

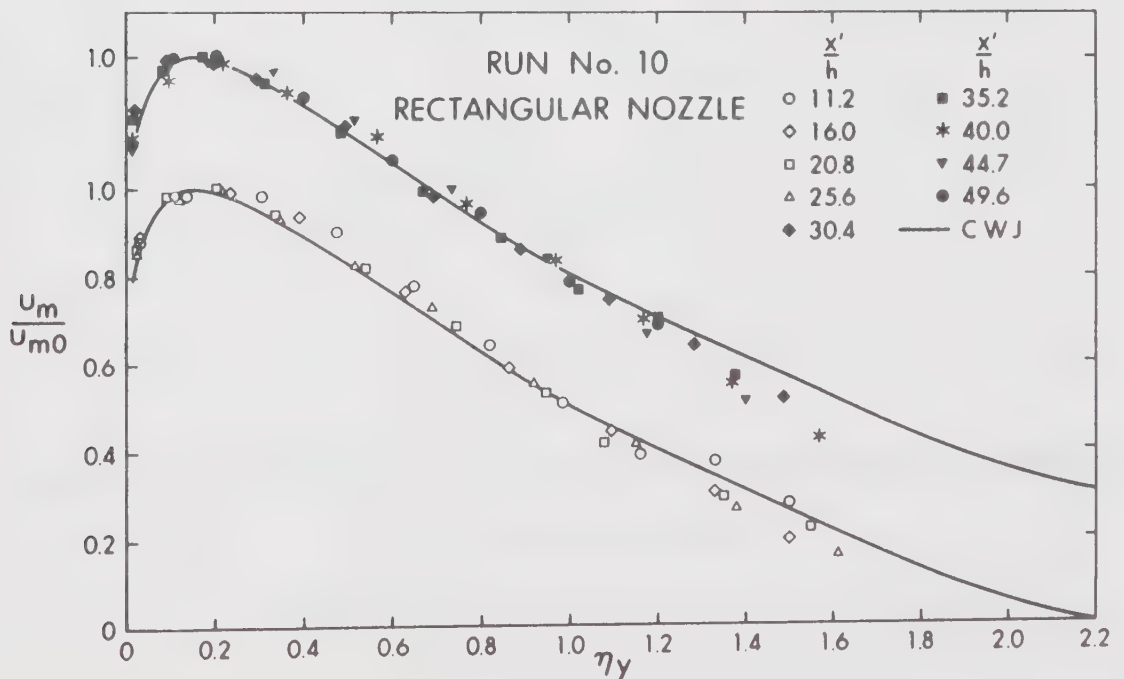


FIGURE C.8 NON-DIMENSIONAL VELOCITY DISTRIBUTION IN THE CENTER-PLANE
- RECTANGULAR NOZZLE ($e = 0.4$)

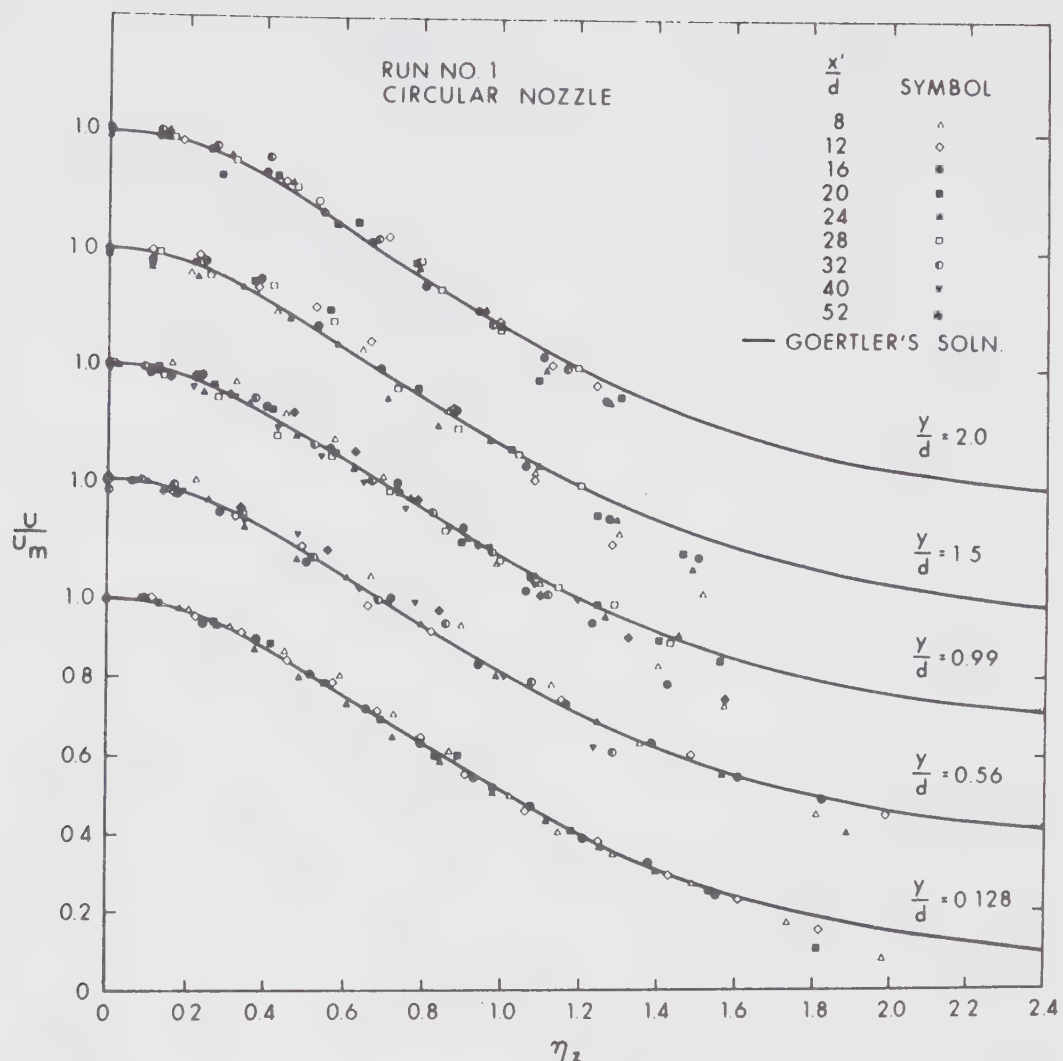


FIGURE C.9 NON-DIMENSIONAL VELOCITY DISTRIBUTION IN THE z DIRECTION
- CIRCULAR NOZZLE

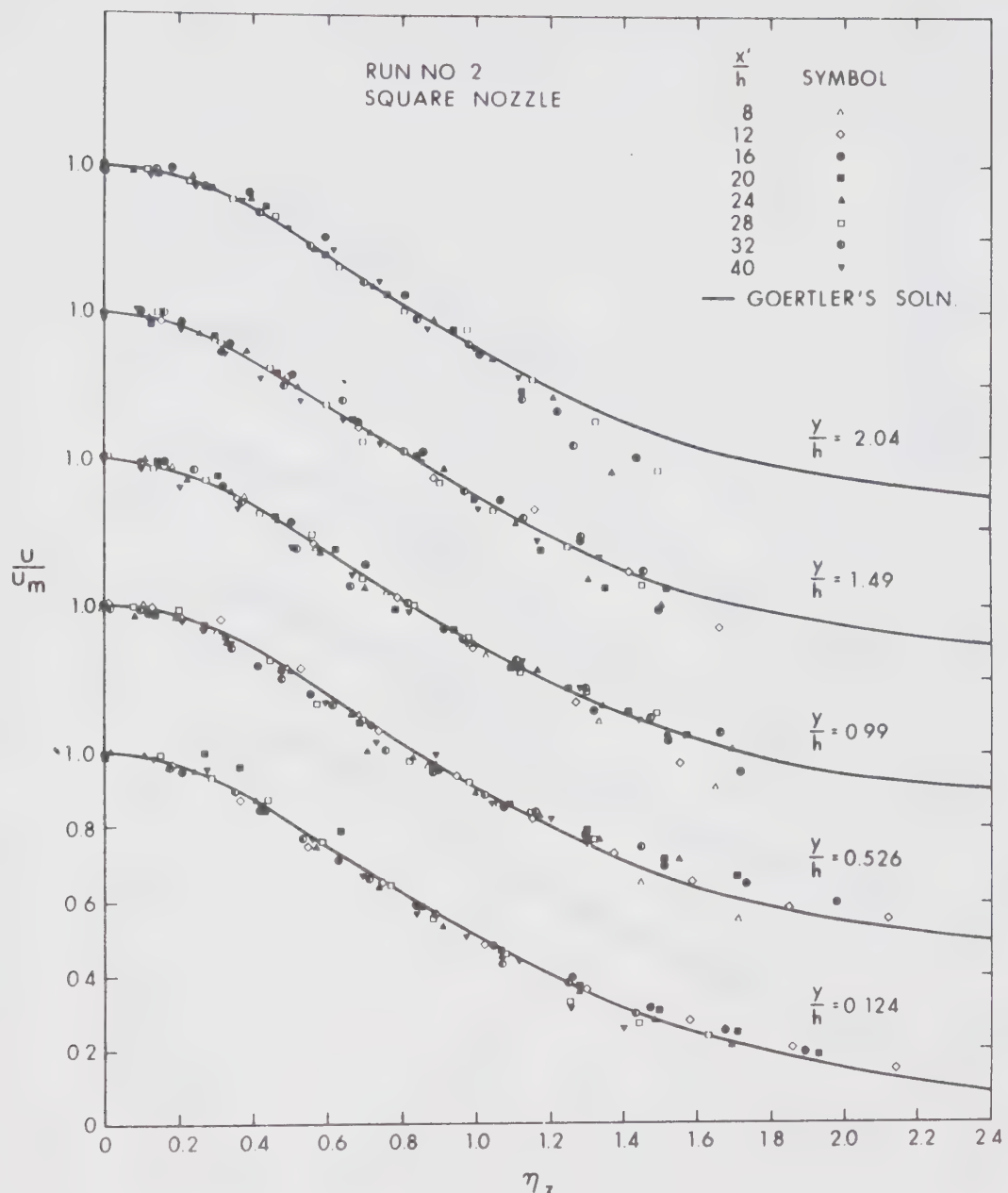


FIGURE C.10 NON-DIMENSIONAL VELOCITY DISTRIBUTION IN THE z DIRECTION
- SQUARE NOZZLE

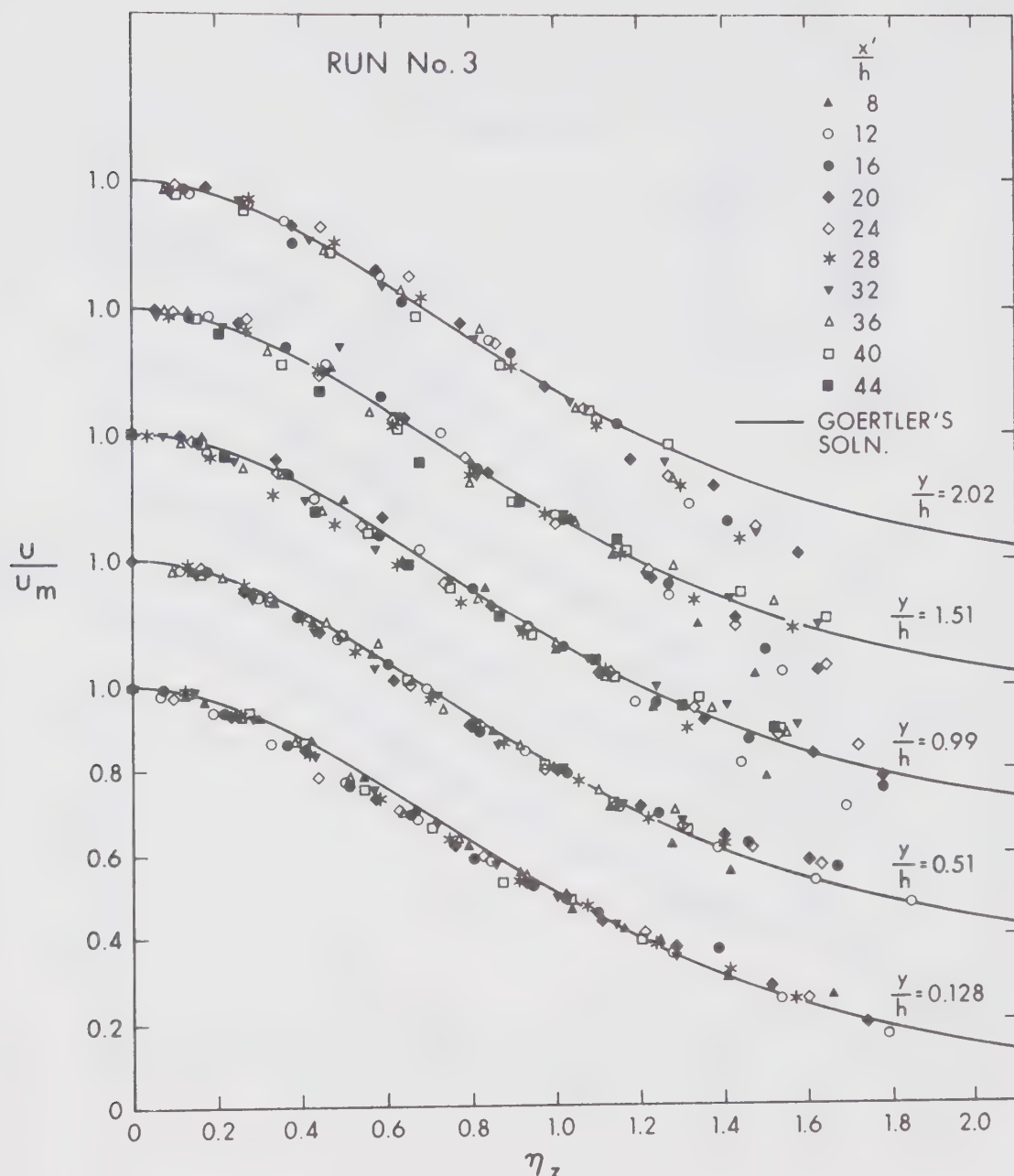


FIGURE C.11 NON-DIMENSIONAL VELOCITY DISTRIBUTION IN THE z DIRECTION
- RECTANGULAR NOZZLE ($e = 1.50$)

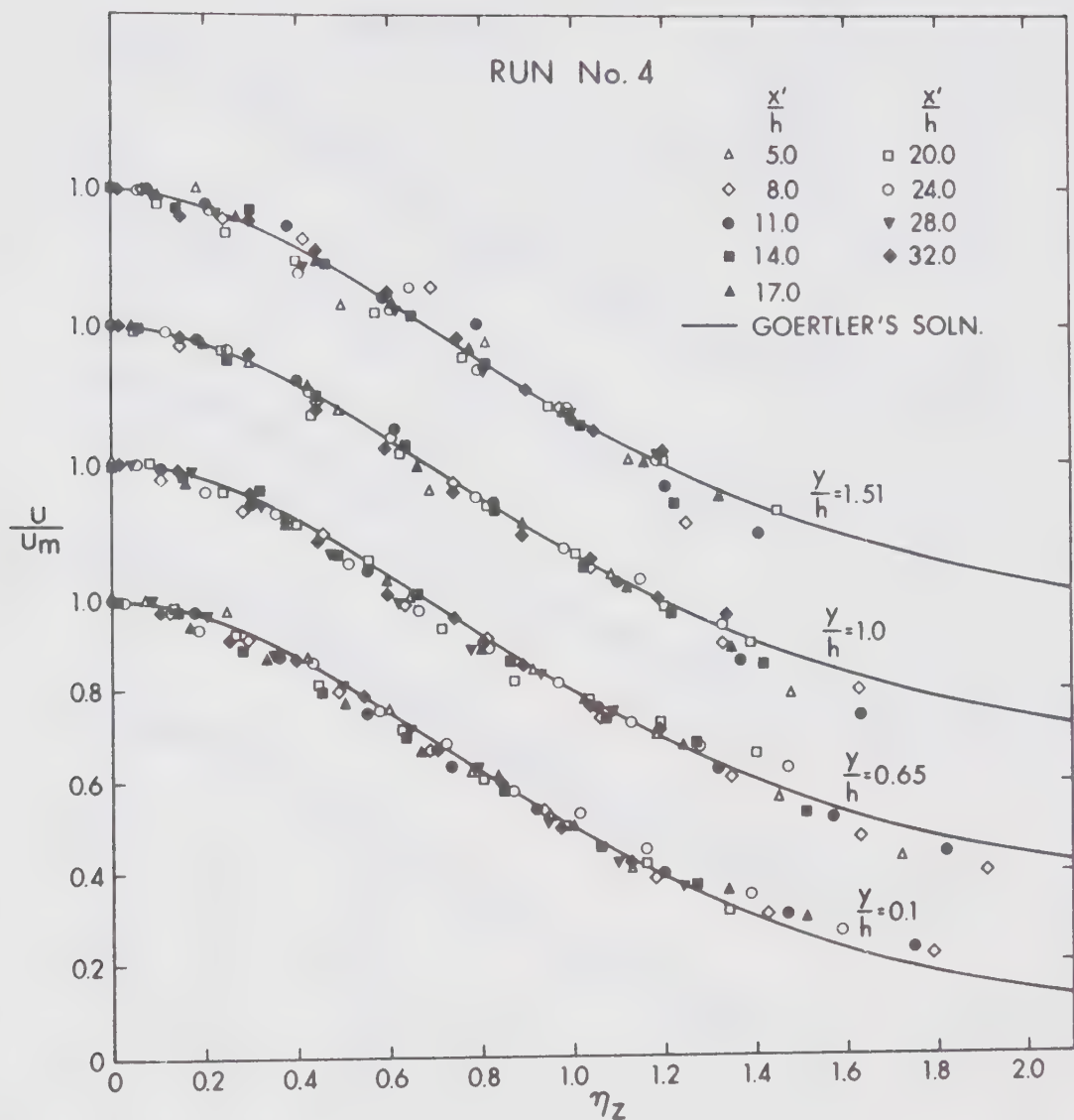


FIGURE C.12 NON-DIMENSIONAL VELOCITY DISTRIBUTION IN THE z DIRECTION
- TRIANGULAR NOZZLE

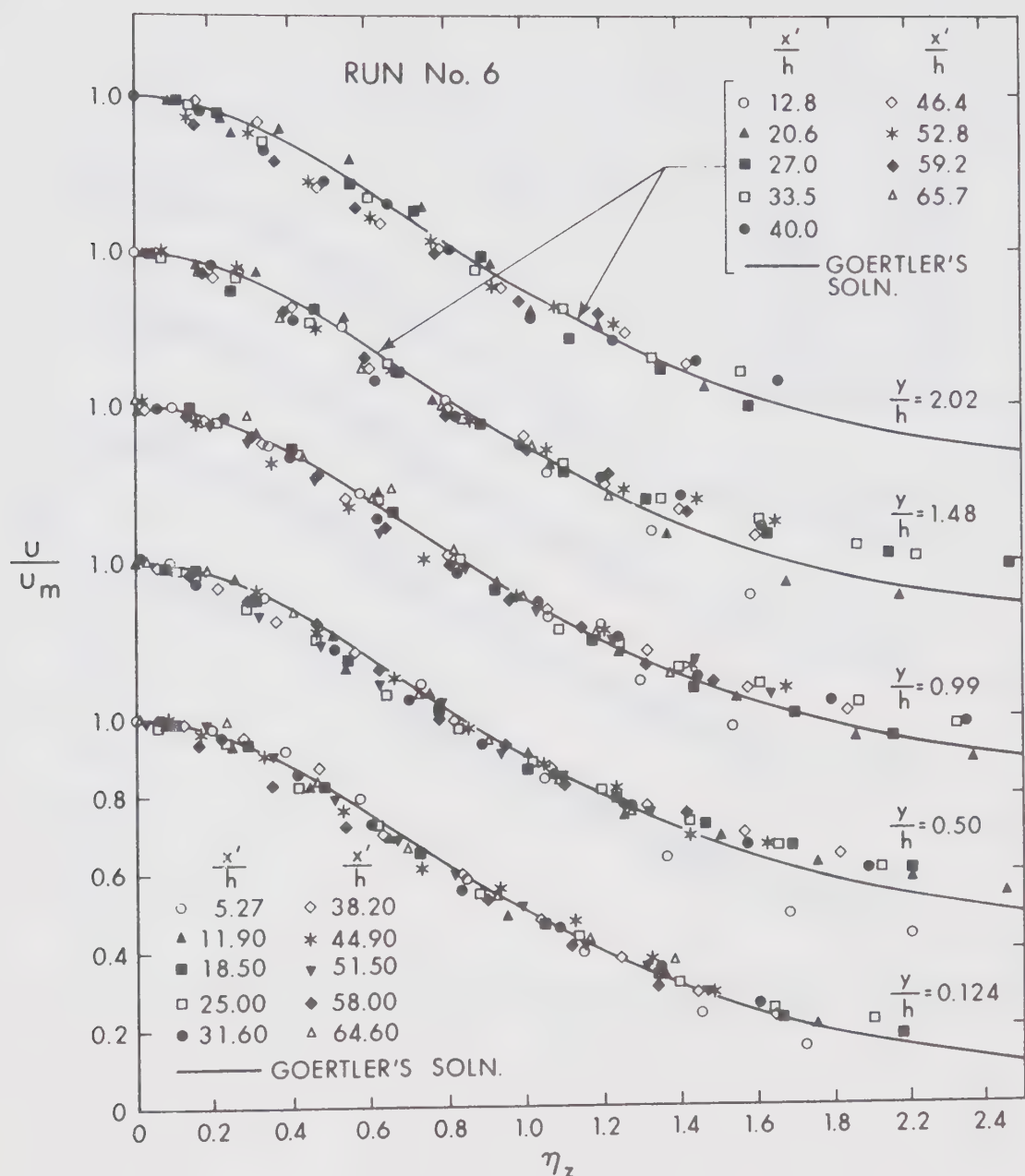


FIGURE C.13 NON-DIMENSIONAL VELOCITY DISTRIBUTION IN THE z DIRECTION
- SQUARE NOZZLE

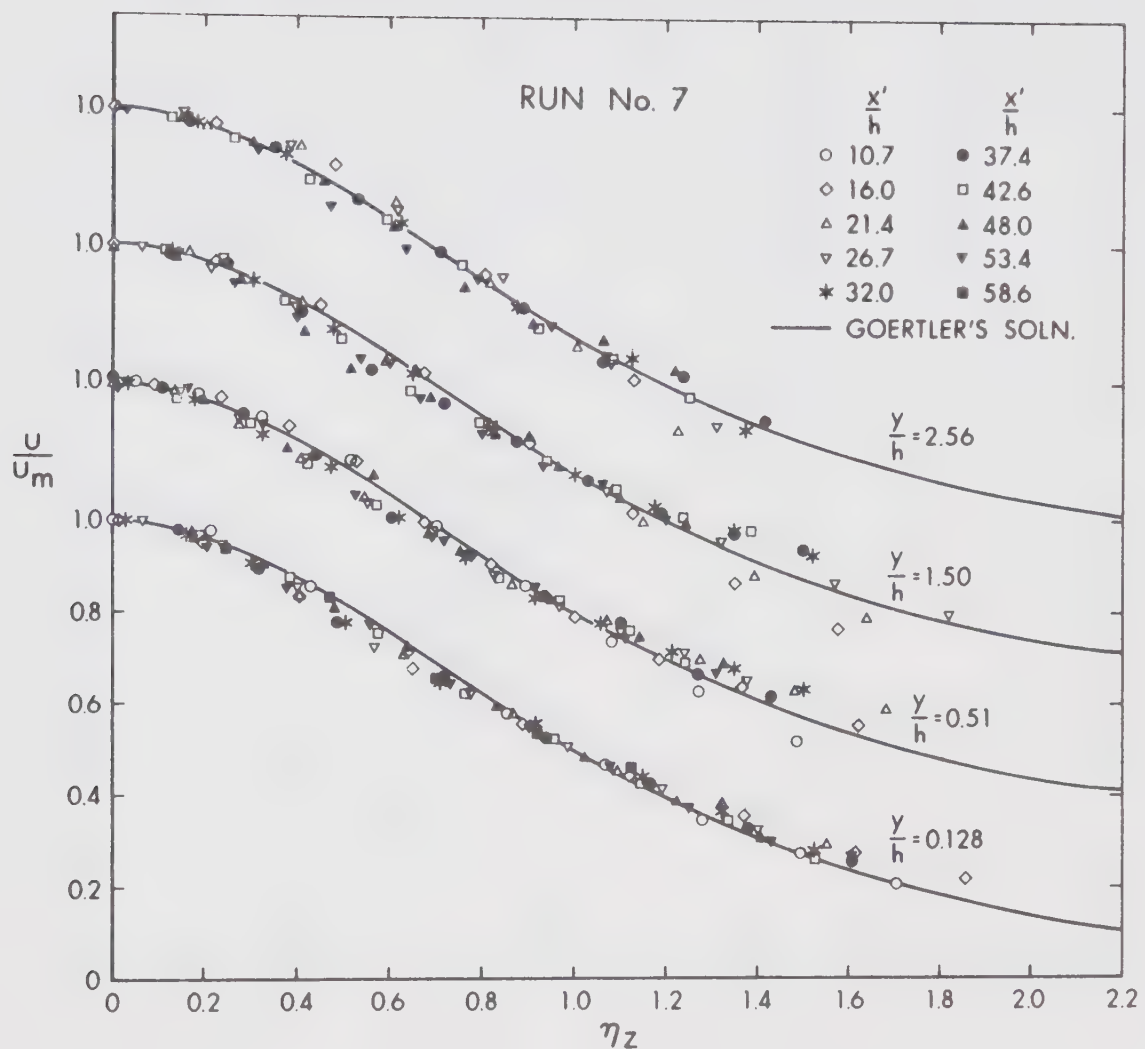


FIGURE C.14 NON-DIMENSIONAL VELOCITY DISTRIBUTION IN THE z DIRECTION
- ELLIPTIC NOZZLE

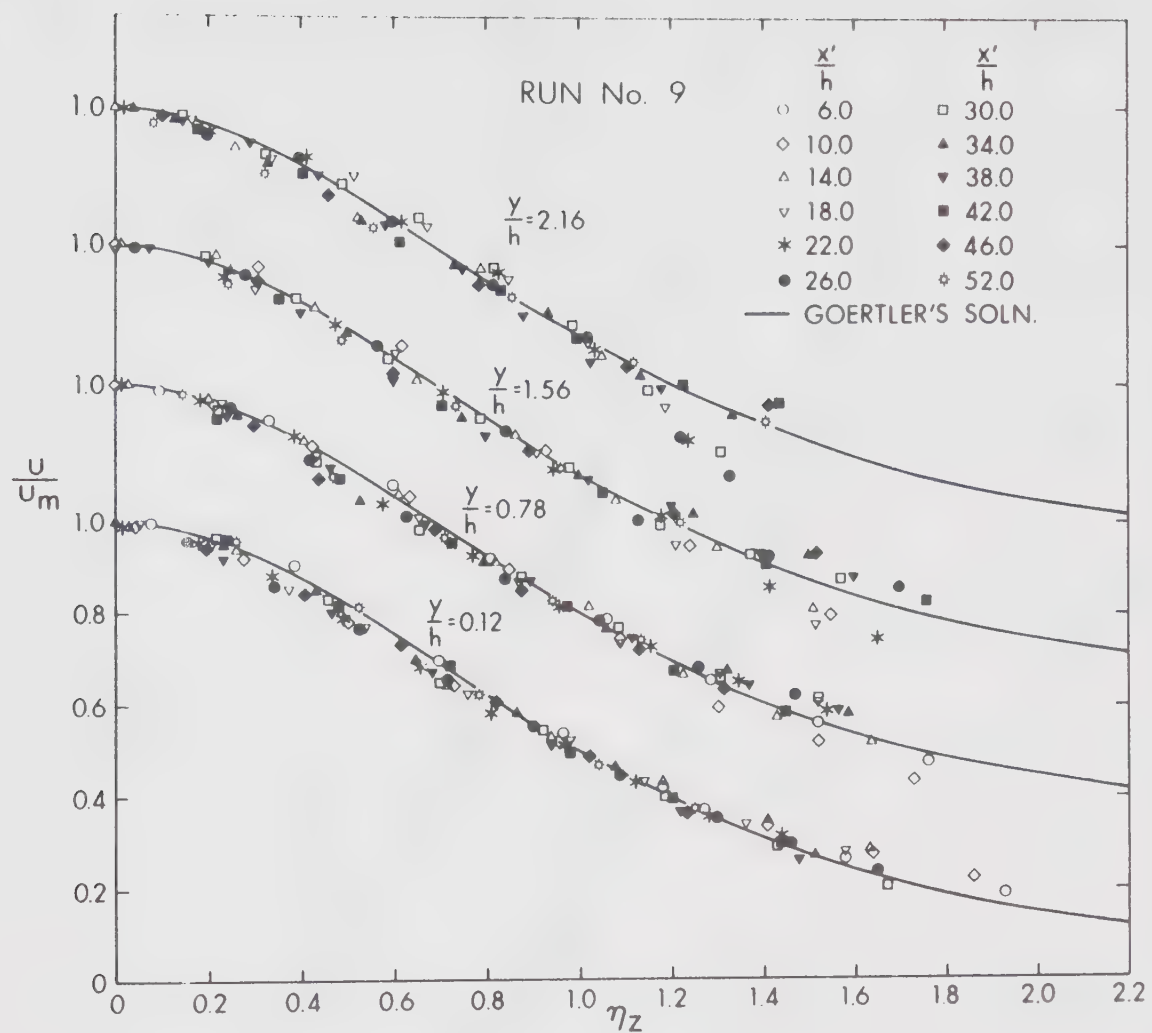


FIGURE C.15 NON-DIMENSIONAL VELOCITY DISTRIBUTION IN THE z DIRECTION
- TRIANGULAR NOZZLE

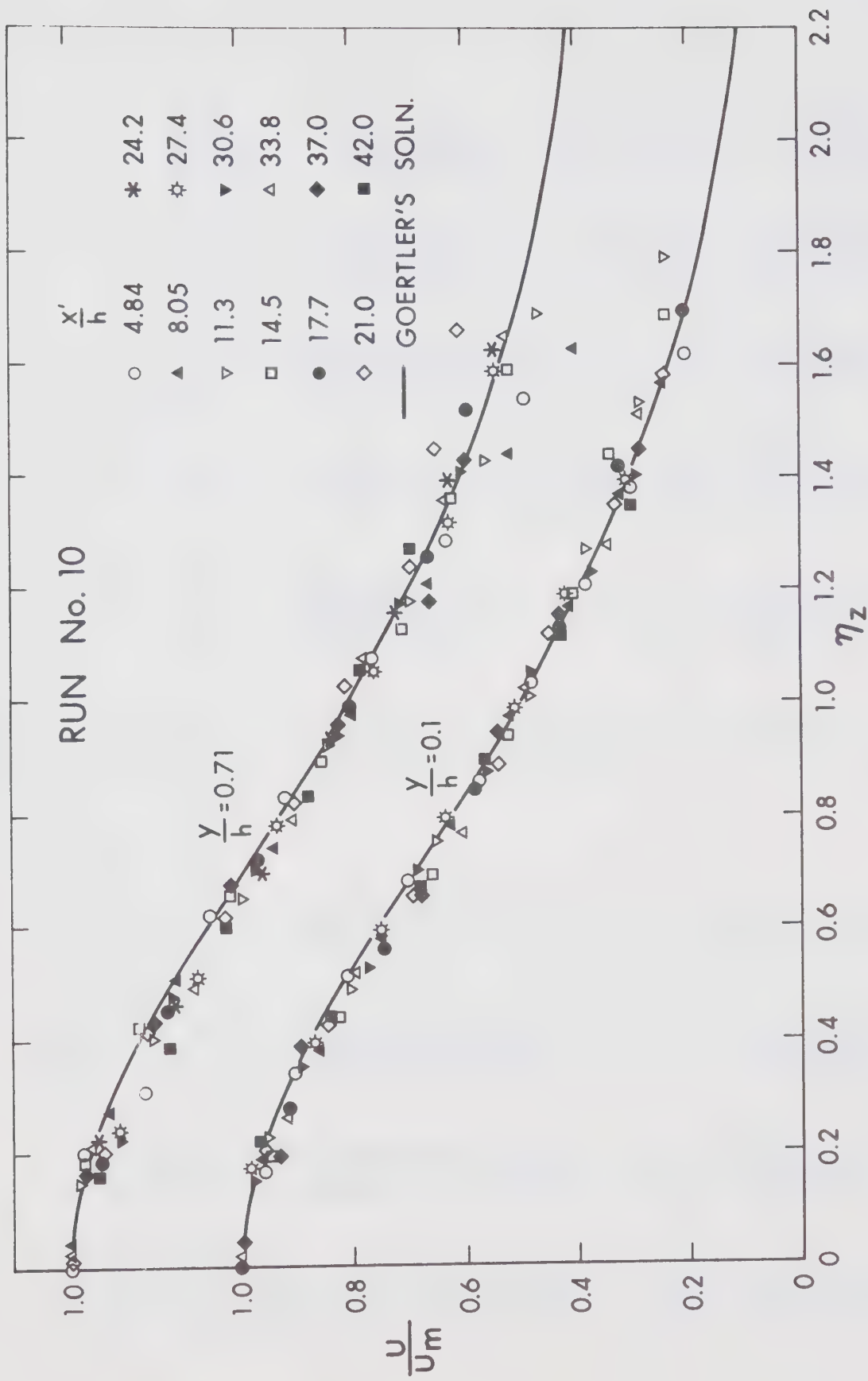
FIGURE C.16 NON-DIMENSIONAL VELOCITY DISTRIBUTION IN THE z DIRECTION- RECTANGULAR NOZZLE ($e = 0.4$)

TABLE C.1

IMPORTANT FLOW PARAMETERS FOR THREE DIMENSIONAL WALL JETS

x' Inches	u_{mo} ft/sec	b_y ft.	τ_0 lbs/sq.ft.	x' Inches	$\frac{y}{h} = 0.128$	0.56	0.99	b_z ft.	1.5	2.0
<u>Expt. No. 1</u>										
0.4	25.95	0.0398	1.84	0.4	0.0108			0.0136		
3.0	22.02	0.046	1.57	3.0	0.0288	0.022		0.024	0.023	
4.5	16.57	0.0505	1.156	4.5	0.044	0.030	0.0314	0.034	0.0265	
6.0	13.02	0.055	0.808	6.0	0.058	0.045	0.0415	0.043	0.037	
7.5	10.78	0.055	0.602	7.5	0.072		0.0614	0.053	0.048	
9.0	8.84	0.059	0.436	9.0	0.1075	0.078	0.082	0.077	0.0625	
10.5	7.31	0.0655	0.323	10.5	0.125		0.1035	0.095	0.075	
12.0	6.33	0.0692	0.245	12.0		0.115	0.132		0.102	
15.0	4.84	0.077	0.151	13.5						
19.5	3.34		0.129	15.0						
				18.0						
				19.5						
<u>Expt. No. 2</u>										
0.4	25.95	0.0483	1.68	0.4	0.034	0.0263	0.026			
3.0	21.32	0.055	1.65	3.0	0.0537	0.0378	0.035	0.0315		
4.5	16.91	0.060	1.35	4.5	0.0714	0.0555	0.0488	0.0464	0.0385	
6.0	13.80	0.0635	0.87	6.0	0.0935	0.073	0.063	0.0587	0.0554	
7.5	11.6	0.0677	0.655	7.5	0.121	0.090	0.0845	0.076	0.0624	
9.0	9.73	0.070	0.51	9.0						
10.5	8.44		0.365	10.5	0.135	0.122	0.106	0.099	0.0870	
				18.0						
				19.5						
				20.0						
				21.0						
				22.0						
				23.0						
				24.0						
				25.0						
				26.0						
				27.0						
				28.0						
				29.0						
				30.0						
				31.0						
				32.0						
				33.0						
				34.0						
				35.0						
				36.0						
				37.0						
				38.0						
				39.0						
				40.0						
				41.0						
				42.0						
				43.0						
				44.0						
				45.0						
				46.0						
				47.0						
				48.0						
				49.0						
				50.0						
				51.0						
				52.0						
				53.0						
				54.0						
				55.0						
				56.0						
				57.0						
				58.0						
				59.0						
				60.0						
				61.0						
				62.0						
				63.0						
				64.0						
				65.0						
				66.0						
				67.0						
				68.0						
				69.0						
				70.0						
				71.0						
				72.0						
				73.0						
				74.0						
				75.0						
				76.0						
				77.0						
				78.0						
				79.0						
				80.0						
				81.0						
				82.0						
				83.0						
				84.0						
				85.0						
				86.0						
				87.0						
				88.0						
				89.0						
				90.0						
				91.0						
				92.0						
				93.0						
				94.0						
				95.0						
				96.0						
				97.0						
				98.0						
				99.0						
				100.0						
				101.0						
				102.0						
				103.0						
				104.0						
				105.0						
				106.0						
				107.0						
				108.0						
				109.0						
				110.0						
				111.0						
				112.0						
				113.0						
				114.0						
				115.0						
				116.0						
				117.0						
				118.0						
				119.0						
				120.0						
				121.0						
				122.0						
				123.0						
				124.0						
				125.0						
				126.0						
				127.0						
				128.0						
				129.0						
				130.0						
				131.0						
				132.0						
				133.0						
				134.0						
				135.0						
				136.0						
				137.0						
				138.0						
				139.0						
				140.0						
				141.0						
				142.0						
				143.0						
				144.0						
				145.0						
				146.0						
				147.0						
				148.0						
				149.0						
				150.0						
				151.0						
				152.0						
				153.0						
				154.0						
				155.0						
				156.0						
				157.0						
				158.0						
				159.0						
				160.0						
				161.0						
				162.0						
				163.0						
				164.0						
				165.0						
				166.0						
				167.0						
				168.0						
				169.0						
				170.0						
				171.0						
				172.0						
				173.0						
				174.0						
				175.0						
				176.0						
				177.0						
				178.0						
				179.0						
				180.0						
				181.0						
				182.0						
				183.0						
				184.0						
				185.0						
				186.0						
				187.0						
				188.0						
				189.0						
				190.0						
				191.0						
				192.0						
				193.0						
				194.0						
				195.0						
				196.0						
				197.0		</				

TABLE C.1 (continued)

x' Inches	u_{mo} ft./sec	b_y ft.	τ_0 lbs/sq. ft.	x' Inches	$\frac{y}{h} = 0.124$	0.526	0.99	1.49	2.04
10.5	8.44	0.070	0.365	10.5	0.135	0.122	0.106	0.099	0.0870
12.0	7.15	0.0744	0.296	12.0	0.168	0.146	0.134	0.123	0.1075
15.0	5.52	0.0844	0.192	15.0	0.214	0.191	0.192	0.186	0.1620
18.0	4.4	0.088	0.129						
21.0	3.5	0.095	0.073						
24.0	2.64	0.128	0.035						
27.0	1.93	0.02							
Expt. No. 3				$\frac{y}{h} = 0.128$	0.5	0.99	1.45	1.95	
0.4	25.95	0.0374	2.49	3.0	0.0404	0.0353	0.030	0.0294	
2.0	25.95	1.84	1.84	4.5	0.0580	0.0434	0.0396	0.037	
3.0	24.20	0.0403		5.0					
4.5	19.60	0.048	1.374	6.0	0.0685	0.0562	0.046	0.044	
6.0	16.25	0.0548	1.11	7.5	0.086	0.075	0.059	0.0512	0.0501
7.5	14.25	0.0596	0.90	9.0	0.10	0.092	0.076	0.0698	0.0582
9.0	12.06	0.0662	0.678	10.5	0.121	0.114	0.102	0.085	0.0728
10.5	10.40	0.0728	0.53	12.0	0.140	0.139	0.120	0.0995	0.090
12.0	8.85	0.0787	0.40	13.5	0.157	0.164	0.136	0.125	0.1082
13.5	7.80	0.084	0.343	15.0	0.184	0.184	0.153	0.147	0.124
15.0	6.80	0.089	0.275	16.5					
18.0	5.55	0.092	0.185						
21.0	4.45	0.10	0.115						
24.0	3.60	0.074							

TABLE C.1 (continued)

<u>Expt. No. 4</u>	x' Inches	u_{mo} ft/sec	b_y ft.	τ_0 lbs/sq.ft.	x' Inches	$\frac{y}{h} = 0.1$	b_z ft.	b_z ft.	y Inches	$\frac{y}{h} = 0.65$	b_z ft.	b_z ft.
0.5	25.89	0.0415	2.655		2.5	0.0284		0.0186	0.0203	0.016		
2.5	22.02	0.040	1.71		4.0	0.0406		0.0283	0.0207	0.0288		
4.0	18.30	0.05	1.275		5.5	0.0544		0.0395	0.0373	0.039		
5.5	15.20	0.056	1.02		7.0	0.0706		0.0590	0.0515	0.049		
7.0	12.60	0.061	0.73		8.5	0.0895		0.0690	0.065	0.059		
8.5	10.50	0.065	0.54		10.0	0.112		0.095	0.0785	0.08		
10.0	8.99	0.0695	0.417		12.0	0.138		0.131	0.111	0.103		
12.0	7.30	0.0755	0.306		14.0	0.169		0.163	0.153	0.157		
14.0	5.96	0.0795	0.227		16.0	0.205		0.202	0.202	0.20		
16.0	5.20	0.0825	0.170									
18.0	4.36	0.	0.12									
20.0	3.66	0.0995	0.086									
<u>Expt. No. 6</u>						$\frac{y}{h} = 0.124$		0.5	0.99	1.54	2.01	
0.0	25.16		3.40			2.0	0.0262		0.022	0.021		
2.0	23.0	0.037	2.375			4.5	0.0495		0.040	0.0325		
4.0	18.55	0.0435	1.55			5.0					0.038	
6.0	14.0	0.0525	1.025			7.0	0.080		0.068	0.058		
7.5	10.65	0.060	0.68			8.0					0.066	0.055
9.0	9.55	0.061	0.55			9.5	0.117		0.110	0.097		
11.0	7.80	0.068	0.332			10.5					0.094	0.088
13.0	6.60	0.0765	0.2475			12.0	0.156		0.159	0.144		
15.0	5.42	0.084	0.195								0.156	0.11

TABLE C.1 (continued)

x' Inches	u_{mo} ft/sec	b_y ft.	τ_0 lbs/sq. ft.	x' Inches	$\frac{y}{h} = 0.124$	0.5	0.99	1.54	2.01
17.0	4.60	0.090	0.128	14.5	0.197	0.200	0.194	0.190	0.188
19.0	4.0	0.098	0.105	15.5					
21.0	3.5	0.110	0.081	17.0	0.252	0.260	0.258	0.252	0.252
24.0	2.94	0.118	0.0575	18.0					
28.0	2.54		0.0412	19.5	0.315	0.322	0.297	0.305	0.318
32.0	2.10		0.0285	20.5					
				22.0	0.375	0.380	0.355	0.385	0.385
				23.0					
				24.5	0.435	0.445	0.425	0.475	0.475
				25.5					
<hr/>									
<u>Expt. No. 7</u>				$\frac{y}{h} = 0.128$	0.513	1.51	2.56		
0.0	24.55			3.125	0.032	0.0276			
2.0	24.40	0.0364	1.775	4.0	0.047	0.037			
4.0	20.20	0.0415	1.445	6.0	0.062	0.055	0.0445	0.031	
6.0	15.20	0.0505	1.05	8.0	0.087	0.073	0.061	0.049	
8.0	11.84	0.0577	0.69	10.0	0.120	0.109	0.0795	0.065	
10.0	9.66	0.0648	0.50	12.0	0.147	0.136	0.115	0.080	
12.0	7.82	0.0724	0.37	14.0	0.117	0.182	0.160	0.113	
14.0	6.6	0.0785	0.255	16.0	0.210	0.218	0.202	0.152	
17.0	5.24	0.091	0.165	18.0	0.258	0.264	0.254	0.197	
20.0	4.24	0.105	0.110	20.0	0.286	0.306	0.30	0.252	
23.0	3.54	0.120	0.0775	22.0	0.338				
26.0	3.0	0.132	0.060						
30.0	2.52	0.143	0.040						
35.0	2.06		0.025						
40.0	1.78		0.0212						

TABLE C.1 (continued)

<u>Expt. No. 8</u>	x' Inches	u_{mo} ft/sec	b_y ft.	τ_0 lbs/sq. ft.	x' Inches	$\frac{y}{h} = 0.16$	b_z ft	$\frac{y}{h} = 0.512$	b_z ft	$\frac{y}{h} = 1.52$	b_z ft	$\frac{y}{h} = 2.5$
0.0	24.34	0.0345	3.187		1.5		0.029		0.0188			
1.5	24.34	0.0345	1.81		3.0		0.029		0.021			
3.0	21.8	0.035	1.525		4.5		0.0403		0.031			
4.5	16.8	0.0424	1.15		6.5		0.062		0.051		0.041	
4.5	12.4	0.0503	0.75		8.5		0.090		0.078		0.060	0.049
6.5	9.62	0.0562	0.50		10.5		0.116		0.112		0.082	0.062
8.5	7.70	0.0626	0.3475		12.5		0.149		0.153		0.120	0.087
10.5	6.25	0.0696	0.2075		14.5		0.195		0.186		0.161	0.120
12.5	5.16	0.079	0.173		16.5		0.225		0.229		0.208	0.162
14.5	4.4	0.087	0.120		18.5		0.260		0.263		0.253	0.208
16.5	3.74	0.098	0.100		20.5		0.296		0.302		0.308	0.264
18.5	3.28	0.105	0.073		22.5		0.332		0.348		0.360	
20.5	2.85	0.117	0.053									
23.0	2.45	0.129	0.0375									
26.0	2.05	0.1415	0.0251									
30.0	1.67	0.1415	0.020									
34.0	1.37	0.1415	0.016									
38.0												

<u>Expt. No. 9</u>	x' Inches	u_{mo} ft/sec	b_y ft.	τ_0 lbs/sq. ft.	x' Inches	$\frac{y}{h} = 0.12$	b_z ft	$\frac{y}{h} = 0.78$	b_z ft	$\frac{y}{h} = 1.56$	b_z ft	$\frac{y}{h} = 2.16$
0.0	24.41	0.0442	2.275		1.5		0.021		0.013			
1.5	24.28	0.0442	1.825		3.0							
3.0	21.35	0.048	1.40		5.0		0.044		0.033		0.0323	
5.0	15.25	0.055	0.97		7.0		0.0655		0.049		0.0462	0.038

TABLE C.1 (continued)

x' Inches	u_{mo} ft/sec	b_y ft.	τ_0 lbs/sq.ft.	x' Inches	$\frac{y}{h} = 0.12$	0.78	1.56	2.16	b_z ft.
7.0	11.80	0.0635	0.675	9.0	0.091	0.069	0.066	0.059	
9.0	9.20	0.066	0.45	11.0	0.127	0.104	0.085	0.0725	
11.0	7.60	0.0728	0.325	13.0	0.161	0.143	0.106	0.098	
13.0	6.30	0.0805	0.222	15.0	0.206	0.184	0.153	0.122	
15.0	5.30	0.088	0.170	17.0	0.232	0.227	0.200	0.150	
17.0	4.6	0.093	0.135	19.0	0.278	0.269	0.250	0.204	
19.0	4.07	0.099	0.1085	21.0	0.292	0.330	0.284	0.244	
22.0	3.35	0.110	0.0685	23.0	0.342	0.365	0.332	0.306	
25.0	2.80	0.126	0.050	26.0	0.424	0.41	0.340		
28.0	2.42	0.137	0.0375	27.0	0.384				
32.0	2.08		0.025						
36.0	1.75		0.0225						
$\frac{y}{h} = 0.10$									
$\frac{y}{h} = 0.71$									
<u>Expt. No. 10</u>									
0.0	24.41		1.73	1.5	0.014	0.016			
2.0	19.60	0.0555	1.11	3.0	0.029	0.024			
4.5	15.20	0.0585	0.985	5.0	0.0512	0.043			
7.0	11.85	0.0587	0.72	7.0	0.077	0.0585			
10.0	8.72	0.064	0.425	9.0	0.101	0.086			
13.0	6.58	0.074	0.2585	11.0	0.141	0.113			
16.0	5.12	0.087	0.1575	13.0	0.174	0.145			
19.0	4.12	0.101	0.110	15.0	0.204	0.215			

TABLE C.1 (continued)

x' Inches	u_{mo} ft./sec.	b_t ft.	τ_0 lbs/sq. ft.	x' Inches	$\frac{y}{h} = 0.10$	b_z ft.
22.0	3.42	0.112	0.0775	17.0	0.252	0.260
25.0	2.90	0.124	0.051	19.0	0.285	0.298
28.0	2.45	0.136	0.0375	21.0	0.3175	0.352
31.0	2.13	0.150	0.030	23.0	0.380	0.40
34.0	1.90	0.024	0.024	26.0	0.445	0.455
37.0	1.67		0.0175			

TABLE C-2
FLOW PARAMETERS FOR CIRCULAR WALL JETS
DIFFUSING IN CHANNELS OF FINITE WIDTH

Nozzle Diameter = 0.375"

Tailwater Depth \approx 55d

Width of channel	x' inches	u_{mo} ft/sec	τ_{om} lbs/sft	Width of channel	x' inches	u_{mo} ft/sec	τ_{om} lbs/sft
2.0"	1.5	24.2	1.85	3.0"	2.5	20.6	1.34
($U_0 = 24.62$ ft/sec)	3.0	17.1	0.894	($U_0 = 24.62$ ft/sec)	5.0	13.0	0.71
	5.0	11.82	0.635		7.5	9.62	0.475
	7.0	9.68	0.50		10.0	7.75	0.33
	9.5	7.45	0.32		13.0	5.98	0.234
	12.0	6.12	0.235		16.0	4.90	0.153
	15.0	5.20	0.162		20.0	4.26	0.117
	18.0	4.64	0.132		24.0	3.69	0.085
	21.0	4.30	0.113		28.0	3.40	0.0675
	24.0	3.86	0.100		32.0	3.10	0.053
	27.0	3.96	0.097		36.0	3.04	0.045
	30.0	3.90	0.086				
	33.0	3.84	0.082				
	36.0	3.71	0.077				

TABLE C-2 (continued)

Width of channel	x' inches	u_{mo} ft/sec	τ_{om} lbs/sft	Width of channel	x' inches	u_{mo} ft/sec	τ_{om} lbs/sft
$(U_0=24.62 \text{ ft/sec})$	2.0	21.4	0.928	$(U_0=24.48 \text{ ft/sec})$	19.5	3.96	0.102
	4.0	14.8	0.766		23.5	3.40	0.075
	6.0	11.28	0.56		27.5	3.05	0.053
	9.0	8.28	0.343		31.5	2.70	0.040
	12.0	6.35	0.231		36.0	2.50	0.032
	15.5	4.98	0.151		7.0"	2.0	22.25
	19.0	4.15	0.11		$(U_0=24.48 \text{ ft/sec})$	4.12	14.8
	23.0	3.58	0.082		6.5	10.9	0.59
	27.0	3.06	0.058		9.75	7.55	0.31
	31.0	3.0	0.05		13.25	5.36	0.173
$(U_0=24.48 \text{ ft/sec})$	36.0	2.75	0.039		17.25	3.98	0.1025
	5.5"	2.5	19.3	22.0	3.10	0.035	
	5.0	12.12	0.603	26.5	2.54	0.039	
	8.0	8.65	0.36	31.0	2.40	0.0325	
	12.0	6.07	0.21	35.0	2.10	0.020	
	16.0	4.68	0.136				

TABLE C-3

FLOW PARAMETERS FOR CIRCULAR WALL JET ON A ROUGH BOUNDARY

Diameter of nozzle = 0.375" $K = 0.00183 \text{ ft.}$

$$K_s = 0.006 \text{ ft.} \quad U_0 = 24.6 \text{ ft/sec}$$

x' inches	u_{mo} ft/sec	b_y ft.	δ ft.	x' inches	τ_{om}^* lbs/sft	$\frac{y}{d} = 0.224$	$b_z \cdot \text{ft.}$
2.50	22.1	0.0405	--	2.5	4.46	--	--
4.25	15.8	0.0468	0.0120	2.75	--	--	--
6.50	10.8	0.0550	0.0145	4.75	--	0.0273	0.0250
8.75	8.0	0.0640	0.0160	1.825	0.045	0.0385	0.038
11.50	5.7	0.0775	0.0185	7.0	0.50	0.076	0.0665
13.75	4.6	0.0910	0.0210	9.5	--	0.117	0.1130
16.75	3.65	0.1020	0.0220	10.5	0.1223	--	--
20.25	2.90	0.1240	0.0240	12.5	--	0.179	0.1720
23.5	2.42	0.1490	0.0290	14.0	0.0623	--	--
26.75	2.06	0.1920	0.0340	15.5	--	0.249	0.2430
30.5	1.78	0.2540	0.030	18.0	0.0538	--	--
34.5	1.62	--	--	18.5	--	0.370	0.340
38.74	1.45	--	--	21.5	--	0.480	0.465
				22.0	0.0254	--	--
				24.5	--	0.72	0.60

*Computed from velocity profile in boundary layer

TABLE C-4
FLOW PARAMETERS FOR SWIRLING WALL JETS

Diameter of nozzle = 0.75"

Tailwater Depth \approx 28D

(a)

Swirl No.	x' inches	u_{mo} ft/sec	b_y ft.	x' inches	$\frac{y}{d} = 0.139$	0.512
0	3.0	22.92	--	--	--	--
$(u_0^* = 21.13$ ft/sec)	6.0	17.30	--	--	--	--
	10.0	11.90	--	--	--	--
	15.0	8.75	--	--	--	--
	20.0	6.50	--	--	--	--
	27.0	4.59	--	--	--	--
0.141	0	25.0	0.066	2.25	0.058	0.048
$(u_0^* = 21.4$ ft/sec)	2.25	18.9	0.068	4.5	0.112	0.099
	4.50	13.2	0.057	7.5	0.155	0.121
	7.50	10.2	0.061	11.25	0.215	0.196
	11.25	7.45	0.08	15.0	0.290	0.275
	15.0	5.73	0.099	18.75	0.335	0.384
	18.75	4.58	0.119	22.5	0.410	0.490
	24.0	3.5	0.145			
	30.0	2.69	0.155			
	36.0	2.08	--			

TABLE C-4 (continued)

Swirl No.	x' inches	u_{mo} ft/sec	b_y ft.	x' inches	$\frac{y}{d} = \frac{b_z}{0.139}$	ft. 0.512
0.265	0	29.6	--	3.0	0.09	0.052
($U_0^* = 21.4$ ft/sec)	1.5	24.3	0.0637	4.5	0.123	0.083
	3.0	16.4	0.063	6.0	0.150	0.142
	4.5	14.4	0.046	8.25	0.210	0.227
	6.0	12.4	0.045	10.5	0.265	0.305
	8.25	9.35	0.051	13.5	0.342	0.380
	10.5	7.3	0.065	16.5	0.430	0.480
	13.5	5.65	0.084			
	16.5	4.62	0.099			
	19.5	3.90	0.111			
	22.5	3.50	--			
	25.5	3.0	--			

*Average velocity at nozzle section

(b)

TABLE C-4 (continued)

Swirl No.	x' inches	τ_{om} lbs/sft	b_τ ft.
0	2.0	1.74	--
	3.75	--	0.037
	4.0	1.23	--
	7.0	0.85	--
	9.0	--	0.069
	11.0	0.575	--
	15.0	0.360	0.105
	20.0	0.2375	--
	22.5	--	0.180
	25.0	0.135	--
	32.0	0.0832	--
	40.0	0.045	--
	50.0	0.025	--
	60.0	0.01	--

TABLE C-4 (continued)

Swirl No.	x' inches	τ_{om} lbs/sft	b_τ ft.
0.141	1.5	1.49	0.0325
	4.5	0.84	0.094
	7.5	0.465	0.1275
	12.0	0.238	0.179
	18.0	0.1172	0.256
	24.0	0.063	0.338
	30.0	0.038	--
	37.5	0.023	--
0.265	2.25	1.36	0.048
	6.0	0.715	0.122
	10.5	0.272	0.221
	15.0	0.128	0.336
	20.0	0.0721	--
	27.0	0.0312	--
	34.0	0.0159	--

B30042